UNIVERSIDAD
DE ANTIOQUIA
1 8 0 3

Theoretical study of thermoelectric and optical properties in molecular and quantum systems

Thesis

Rafael Guillermo Toscano Negrette

University of Antioquia
Faculty of Exact and Natural Sciences, Institute of Physics
Medellín, Colombia
2024

Theoretical study of thermolectric and optical properties in molecular and quantum systems

Rafael Guillermo Toscano Negrette

Submitted to the University of Antioquia in fulfillment of the Physics PhD requirements program

Advisor:
PhD Carlos Alberto Duque Echeverri
Co-Advisors:
PhD Alvaro Morales Aramburo
PhD Judith Helena Ojeda Silva

Research line:
Condensed Matter
Research group:
Condensed Matter-UdeA

University of Antioquia
Faculty of Exact and Natural Sciences, Institute of Physics
Medellín, Colombia
2024

Abstract

In this thesis, we analyze the electronic and optical properties in semiconductor heterostructures with zero dimension, that is, a quantum dot, which has a spherical symmetry based on materials such as CdS, ZnS, CdSe, and ZnTe. The calculations are made under the effective mass approximation, considering the effects of external electric and magnetic fields, the effect of surface donor impurity states, and electron-hole interaction with excitonic contribution. These properties are analyzed using the finite element method to solve the time-independent Schrödinger equation. We also analyze the thermoelectric properties in circuits formed from a single molecule connected between two metallic electrodes. To obtain the results, first, an analytical process is carried out in which a renormalization of the system to be studied is done using the Dyson equation for first neighbors, and the Green's function formalism. Then the Fisher-Lee relation is used to calculate the probability of transmission. Calculations of the current-voltage characteristic curve and thermoelectric properties (Seebeck coefficient, thermal and electrical conductance, and ZT) are made using the Landauer relation.

The first part of this thesis is dedicated to the theoretical details that support the equations and the numerical method used in the calculations, beginning with the section on the Landauer-Buttiker electronic transport theory, the Landauer relation, obtaining the integrals of Landauer for the calculation of thermoelectric properties, a section dedicated to the development of electronic and optical properties in semiconductor heterostructures, where the theory of effective mass is analyzed, the Hamiltonian for systems subjected to external electric and magnetic fields, the theory of optical absorption (linear and nonlinear) and finally a brief description of the finite element method. The main details of each chapter are:

Chapter 3: A theoretical analysis of optical properties in a ZnS/CdS/ZnS core/shell/shell spherical quantum dot was carried out within the effective mass approximation. The corresponding Schrödinger equation was solved using the finite element method via the 2D axis-symmetric module of COMSOL-Multiphysics software. Calculations included variations of internal dot radius, the application of electric and magnetic fields (both oriented along z-direction), as well as the presence of on-center donor impurity. Reported optical properties are the absorption and relative refractive index change coefficients. These quantities are related to transitions between the ground and first excited states, with linearly polarized incident radiation along the z-axis.

Chapter 4: A theoretical analysis was conducted to examine the electronic and optical properties of a confined electron and a hole in a type-II core-shell spherical quantum dot composed of CdSe/ZnTe and ZnTe/CdSe. The Schrödinger equation for the electron and the hole was numerically solved using COMSOL-Multiphysics software in the 2D axisymmetric module, which employs the finite element method under the effective mass approximation. A Fortran code was utilized to calculate excitonic energy, specifically designed to solve the Coulomb integral. The calculations encompassed variations in the inner radius (R_1), as well as variations in the electric (F_z) and magnetic (B) fields along the z-axis. The absorption coefficients were determined for transitions between the hole and electron ground states, considering z-polarized incident radiation.

Chapter 5: Taking into consideration the research that has been done on the optical, and electrical properties of molecular systems, especially the good thermoelectric energy conversion at a nanometric scale that such systems have presented, here we present a new alternative by using a particular Diphenyl-ether molecule as a functional device. Such a molecular system is modeled as a planar segment coupled to two electrodes in the first-neighbor approximation within a tight-binding Hamiltonian. We study the electrical and thermal properties of Diphenyl-ether molecules like the electric current, electrical and thermal conductance, Seebeck coefficient, and figure of merit, in the strong and weak coupling regimes, considering different structural configurations and variations with temperature.

Chapter 6: A theoretical analysis was performed to investigate the transport properties of the Zinc Porphyrin molecule and its response to thermal fluctuations. The renormalization method was used for this analysis, using the Green's functions technique through the Dyson equation, focusing on first-neighbor interactions. This study produced various results, including energy-dependent transmission probability, voltage-current characteristic curves, electrical and thermal conductance assessments, Seebeck coefficient, and figure of merit (ZT).

Publications

[1] Toscano-Negrette, R. G.; León-González, J. C.; Vinasco, J. A.; Morales, A. L.; Koc, F.; Kavruk, A. E.; Sahin, M.; Mora-Ramos, M. E.; Sierra-Ortega, J.; Martínez-Orozco, J. C.; Restrepo, R. L.; Duque, C. A. *Optical Properties in a ZnS/CdS/ZnS Core/Shell/Shell Spherical Quantum Dot: Electric and Magnetic Field and Donor Impurity Effects.* Nanomaterials (**Q1** in scimago), **13**, 550 (2023).

[2] Toscano-Negrette, R.G.; León-González, J.C.; Vinasco, J.A.; Morales, A.L.; Mora-Ramos, M.E.; Duque, C.A. *Effect of External Fields on the Electronic and Optical Properties in ZnTe/CdSe and CdSe/ZnTe Spherical Quantum Dots.* Condens. Matter (**Q2** in scimago), **8**, 66 (2023).

[3] Toscano-Negrette, R.G.; León-González, J.C.; Vinasco, J.A.; Ojeda Silva, J.H.; Morales, A.L.; Duque, C.A. *Theoretical Study of Thermoelectric Properties of a Single Molecule of Diphenyl-Ether.* Condens. Matter (**Q2** in scimago), **8**, 55 (2023).

[4] Toscano-Negrette, R.G.; León-González, J.C.; Gil-Corrales, J.A.; Ojeda Silva, J.H.; Morales, A.L.; Eramo, G.; Vinasco, J.A.; Duque, C.A. *Theoretical study of the thermoelectric properties through a single-molecule junction of Zinc Porphyrin.* Physica E (**Q2** in scimago), **161**, 115970 (2024).

Collaborations and Contributions in Other Publications:

[1] León-González, J.C.; Toscano-Negrette, R.G.; Morales, A.L.; Vinasco, J.A.; Yücel, M.B.; Sari, H.; Kasapoglu, E.; Sakiroglu, S.; Mora-Ramos, M.E.; Restrepo, R.L.; Duque, C.A. *Spin–Orbit and Zeeman Effects on the Electronic Properties of Single Quantum Rings: Applied Magnetic Field and Topological Defects.* Nanomaterials (**Q1** in scimago), **13**, 1461 (2023).

[2] León-González, J.C.; Toscano-Negrette, R.G.; Vinasco, J.A.; Morales, A.L.; Mora-Ramos, M.E.; Duque, C.A. *Influence of a Non-Resonant Intense Laser and Structural Defect on the Electronic and Optical Properties of a GaAs Quantum Ring under Inversely Quadratic Potential.* Condens. Matter (**Q2** in scimago), **8**, 52 (2023).

Event Participation

[1] *Zn-porphyrin molecule renormalization*, First Postgraduate Symposium, University of Antioquia, speaker, june (2021).

[2] *Effect of external fields on the electronic and optical properties in ZnTe/CdSe and CdSe/ZnTe spherical quantum dot*, 23^{rd} International Conference on Physics of Light-Matter Coupling in Nanostructures PLMCN, University of Antioquia, poster presentation, april (2023).

[3] *Theoretical study of the thermoelectric properties of a Zinc Porphyrin*, VI International Meeting of the Faculty of Sciences-IMFaS-2023, Pedagogical and Technological University of Colombia, poster presentation, october (2023).

Contents

List of Figures

List of Tables

1 Introduction

The theoretical and experimental study of low-dimensional structures has been the focus of study in recent decades for scientists focused on this area since these structures present unique and interesting properties that can be applied to increase the efficiency of existing electronic devices. As i the case of optoelectronics, photonics, electrical circuits at the nanometric scale, etc. [1–6]. In the case of semiconductor structures, we have the case of wells, wires, and quantum dots (QDs), the first is achieved by confining the charge carriers (electrons or holes) in one dimension, the second in two dimensions, and the third confines the carriers in three spatial dimensions, and each one presents unique properties that are of great technological interest. Currently, there is a bibliographic record of the study of electronic and optical properties in QDs, using different geometries such as cylinders, pyramidal, conical, and spherical, among others [7–10]. An interesting aspect in the study of properties in QDs is the possibility of controlling, changing, or obtaining new properties using external fields, such as electric and magnetic, considering donor or acceptor impurities, hydrostatic pressure, and temperature [11–15].

There are various theoretical and experimental methods for the study of QDs, in the experimental part we can find the following methods that allow us to control the manufacturing of these structures such as molecular beam epitaxy (MBE), ultrasonic sol-gel, and the hydrothermal method, among others; with nanostructure sizes less than 10 nm, which has enabled applications in areas such as nanophotonics and nanoelectronics [16–18]. In the theoretical part, we can find the development of the Schrödinger equation in many analytical and numerical methods, which include perturbation theory, finite differences, finite element method (FEM), etc. [19–21], being the last one used in this work. To solve the Schrödinger equation proposed with the effective mass approximation with the finite element method, the COMSOL-Multiphysics software is used, which requires a paid license [22–24].

In the QDs, the energies are discrete and depend on the size, if there are no external electromagnetic fields, of the prohibited bands, etc., and the physical and optical properties can be controlled and used for applications in fields such as electronics, medicine, chemistry, and biology [25–27]. The most commonly used semiconductors for the fabrication of quantum dots (QDs) are compounds from groups II–VI, III–V, and IV–VI of the periodic table. For instance, in 2022, Kuzyk et al. investigated the potential applications of deformation effects in QDs with a CdSe/ZnS/CdS/ZnS multi-shell core structure in the field of nanomedicine. They analyzed the interaction between these QDs and human serum albumin and found

that QDs with three shells are more sensitive to deformation. Moreover, in some cases, the deformation was found to be independent of the core radius, suggesting that such QDs could be used as bio-nanosensors to detect and quantify albumin concentrations. [28].

In molecular electronics there has also been much interest in recent decades, aiming to increase the density of the components that contain a microchip, following Moore's law. With current technologies focus on miniaturization, the idea of molecular electronics can replace current electronic components, based on semiconductors, by monomolecular devices which are among the smallest nanometer-scale structures [29,30]. The study of molecular electronics, which is centered on the behavior of the charging ports when it comes to a molecule that is found between two or more electrodes, which depend on its structure, can have the natural properties of electronic devices, like rectifiers, transistors, diodes, among others. Today we can meet many technical and experimental studies on electronic devices based on a single molecule, such as cables, interruptors, power devices, amplification, and logic, to mention some of them [31–34]. We first informed you theoretically about the rectifying properties of a molecule based on tetratia-fulvaleno (donate) and tetracianoquinodimetano (acceptor), united by a saturated molecule source, proposed by Aviram and Ratner in 1974 [35].

In molecular systems, various experimental and theoretical techniques are available today to determine the structural, electronic, and transport properties of systems formed by a single molecule. Among the experimental techniques you can find is scanning Tunneling Microscopy (STM), which uses individual molecular junctions on surfaces to manipulate and characterize molecules at the nanometer scale. In this process, charge carriers generated by a potential difference feel the tunneling mechanism. Scanning probe microscopy (SPM) consists of breaking the joints of a probe with a sharp tip, facilitating the surface of a sample to be scanned, and measuring its topography, conductivity, magnetic field, etc. [36–38]. Mechanically controlled rupture joints (MCBJ), which are characterized by having two metal electrodes separated by a small distance, on the order of nanometers, which allows the spacing of the electrodes to be precisely adjusted, which can be mechanically moved and a molecule between them to act as a bridge. By varying the distance between the metal tips, the conductance of the molecule can be studied as a function of the separation of the electrodes [39, 40].

Among the theoretical methods for the study of molecular systems, such as density functional theory (DFT), with the non-equilibrium Green's function formalism (NEGF), renormalization method with the tight-binding approximation, and the equation from Dyson to first neighbors with Green's function formalism to describe the system. With these methods, studies can be carried out on the electronic, transport, and optical properties of molecular systems, such as transmission probability, current-voltage characteristic curve, electrical and thermal conductance, Seebeck coefficient, figure of merit (ZT), and absorption, among others, all the above, considering variations in temperatures, external fields, etc. [41–44]. The

method used in this work is renormalization, which consists of decimating the molecular system using the tight-binding approximation, Dyson equation, and Green's functions, which translates into going from a 2D system with many atomic sites to a linear one with effective sites but maintaining the information of the original system.

In this work, the transport and thermoelectric properties of a Diphenyl-Ether and Zinc-Porphyrin molecule are studied, for which the system is decimated (going from a 2D system to a linear system) using a tight-binding model, which allows us to establish interactions between sites in the molecular system, and the coupling between the molecule and the contacts. The transmission probability will be calculated using the Fisher-Lee relationship, which is the basis for the analysis of the other properties studied, the calculation of the current-voltage characteristic curve will be carried out using the Landauer-Büttiker formalism and, finally, the electrical and thermal conductance, Seebeck coefficient and figure of merit, ZT, will be calculated using Landauer integrals.

The motivation to study the thermoelectric properties in these molecules is found in the following experimental works: the study reported by Perrin *et al.* in 2013, where they studied the current curve as a function of voltage in a Zn(5) molecule,15-di(p-thiolphenyl)-10,20-di(p-tolyl)porphyrin) (ZnTPPdT), for different electrode distances, using the MCBJ method. By increasing the electrode separation, they observed a substantial increase in the transport gap with level changes of several hundred meV for displacements of a few angstroms [45]. Another experimental study is the one carried out by Tali Dadosh *et al.* in 2005, where they studied the electrical conductance as a function of voltage in three short organic molecules: conjugated molecule of 4,4-biphenyldithiol (BPD), a bis-(4-mercaptophenyl)-ether (BPE) molecule, in which the conjugate is broken in the center by an oxygen atom, and the 1,4-benzenedimethanethiol (BDMT) molecule. The method used is based on synthesizing a dimer structure, which consists of two colloidal gold particles connected by a short organic molecule and trapping it electrostatically between two metal electrodes. Finding that the conjugation of the molecules is broken near the contacts by a methylene group, concluding that the oxygen in BPE and the methylene groups in BDMT suppress the electrical conduction relative to BPD [46].

The order of the thesis is as follows: Chapter 2 is dedicated to the theoretical framework. Chapter 3 contains optical properties in a ZnS/CdS/ZnS core/shell/shell spherical quantum dot: electric and magnetic field and donor impurity effects. Chapter 4 has the effect of external fields on the electronic and optical properties in ZnTe/CdSe and CdSe/ZnTe spherical quantum dots. Chapter 5 shows the results of the theoretical study of thermoelectric properties of a single molecule of diphenyl-ether. Chapter 6 shows the theoretical study of the thermoelectric properties through a single-molecule junction of Zinc Porphyrin.

References

[1] Heyn, C.; Radu, A.; Vinasco, J.A.; Laroze, D.; Restrepo, R.L.; Tulupenko, V.; Hieu, N.N.; Phuc, H.V.; Mora-Ramos, M.E.; Ojeda, J.H.; et al. Exciton states in conical quantum dots under applied electric and magnetic fields. *Opt. Laser Technol.* **2021**, *139*, 106953.

[2] Mora-Ramos, M.E.; Vinasco, J.A.; Laroze, D.; Radu, A.; Restrepo, R.L.; Heyn, C.; Tulupenko, V.; Hieu, N.N.; Phuc, H.V.; Ojeda, J.H.; et al. Electronic structure of vertically coupled quantum dot-ring heterostructures under applied electromagnetic probes. A finite-element approach. *Sci. Rep.* **2021**, *11*, 4015.

[3] Babin, H.G.; Ritzmann, J.; Bart, N.; Schmidt, M.; Kruck, T.; Zhai, L.; Löbl, M.C.; Nguyen, G.N.; Spinnler, C.; Ranasinghe, L.; et al. Charge tunable GaAs quantum dots in a photonic n-i-p diode. *Nanomaterials* **2021**, *11*, 2703.

[4] Joachim, C.; Gimzewski, J.; Aviram, A. Electronics using hybrid-molecular and monomolecular devices. *Nature* **2000**, *408*, 541–548.

[5] Aviram, A. Molecules for memory, logic, and amplification. *J.A.C.S.* **1988**, *110*, 5687–5692.

[6] Khireddine, A.; Bouhemadou, A.; Maabed, S.; Bin-Omran, S.; Khenata, R.; Al-Douri, Y. Elastic, electronic, optical and thermoelectric properties of the novel Zintl-phase Ba_2ZnP_2. *Solid State Sci.* **2022**, *128*, 106893.

[7] Aouami, A.E.; Feddi, E.; El-Yadri, M.; Aghoutane, N.; Dujardin, F.; Duque, C.A.; Phuc, H.V. Electronic states and optical properties of single donor in GaN conical quantum dot with spherical edge. *Superlattices Microstruct.* **2018**, *114*, 214–224.

[8] Heyn, C.; Duque, C.A. Donor impurity related optical and electronic properties of cylindrical GaAs-Al_xGa_{1-x} As quantum dots under tilted electric and magnetic fields. *Sci. Rep.* **2020**, *10*, 9155.

[9] Pulgar-Velásquez, L.; Sierra-Ortega, J.; Vinasco, J.A.; Laroze, D.; Radu, A.; Kasapoglu, E.; Restrepo, R.L.; Gil-Corrales, J.A.; Morales, A.L.; Duque, C.A. Shallow donor impurity states with excitonic contribution in GaAs/AlGaAs and CdTe/CdSe truncated conical quantum dots under applied magnetic field. *Nanomaterials* **2021**, *11*, 2832.

[10] Rodríguez-Magdaleno, K.A.; Pérez-Álvarez, R.; Ungan, F.; Martínez-Orozco, J.C. Strain effect on the intraband absorption coefficient for spherical CdSe/CdS/ZnSe core–shell–shell quantum dots. *Mater. Sci. Semicond. Process.* **2022**, *141*, 106400.

[11] Portacio, A.A.; Jiménez, A.F.; Urango, M.P. Theoretical study on the change of index of refraction and the optical absorption in a quantum dot in the presence of a uniform magnetic field. *Rev. Mex. Fis.* **2016**, *62*, 330–335.

[12] Holovatsky, V.; Chubrey, M.; Voitsekhivska, O. Effect of electric field on photoionisation cross-section of impurity in multilayered quantum dot. *Superlattices Microstruct. 2020*, *145*, 106642.

[13] Niculescu, E.C.; Cristea, M. Impurity states and photoionization cross section in CdSe/ZnS core–shell nanodots with dielectric confinement. *J. Lumin.* **2013**, *135*, 120–127.

[14] Chnafi, M.; Belamkadem, L.; Mommadi, O.; Boussetta, R.; Hadi, M.E.; Moussaouy, A.E.; Falyouni, F.; Vinasco, J.A.; Laroze, D.; Mora-Rey, F.; et al. Hydrostatic pressure and temperature effects on spectrum of an off-center single dopant in a conical quantum dot with spherical edge. *Superlattices Microstruct.* **2021**, *159*, 107052.

[15] Duque, C.A.; Porras-Montenegro, N.; Barticevic, Z.; Pacheco, M.; Oliveira, L.E. Electron-hole transitions in self-assembled InAs/GaAs quantum dots: Effects of applied magnetic fields and hydrostatic pressure. *Microelectron. J.* **2005**, *36*, 231–233.

[16] Heyn, C.; Zocher, M.; Küster, A.; Hansen, W. Droplet etching during semiconductor epitaxy for single and coupled quantum structures. *Quantum Dots Nanostructures Growth, Charact. Model. XV* **2018**, *10543*, 38–47.

[17] Yang, W.; Zhang, B.; Ding, N.; Ding, W.; Wang, L.; Yu, M.; Zhang, Q. Fast synthesize ZnO quantum dots via ultrasonic method. *Ultrason. Sonochem.* **2016**, *30*, 103–112.

[18] Valizadeh, A.; Mikaeili, H.; Samiei, M.; Farkhani, S.M.; Zarghami, N.; kouhi, M.; Akbarzadeh, A.; Davaran, S. Quantum dots: Synthesis, bioapplications, and toxicity. *Nanoscale Res. Lett.* **2012**, *7*, 1–14.

[19] Gong, L.; Shu, Y.-C.; Xu, J.; Zhu, Q.; Wang, Z. Numerical analysis on quantum dots-in-a-well structures by finite difference method. *Superlattices Microstruct.* **2013**, *60*, 311–319.

[20] Koller, S.; Grifoni, M.; Leijnse, M.; Wegewijs, M. R. Density-operator approaches to transport through interacting quantum dots: Simplifications in fourth-order perturbation theory. *Phys. Rev. B.* **2010**, *82*, 235307.

[21] Heyn, C.; Duque, C.A. Donor impurity related optical and electronic properties of cylindrical GaAs-Al_xGa_{1-x} As quantum dots under tilted electric and magnetic fields. *Sci. Rep.* **2020**, *10*, 9155.

[22] COMSOL. *Multiphysics*; v. 5.4; COMSOL AB: Stockholm, Sweden, 2018.

[23] COMSOL. *Multiphysics Reference Guide*; COMSOL AB: Stockholm, Sweden, 2012.

[24] COMSOL. *Multiphysics Users Guide*; COMSOL AB: Stockholm, Sweden, 2012

[25] Sahu, A.; Kumar, D. Core-shell quantum dots: A review on classification, materials, application, and theoretical modeling. *J. Alloys Compd.* **2022**, *924*, 166508.

[26] Huang, X.; Tong, X.; Wang, Z. Rational design of colloidal core/shell quantum dots for optoelectronic applications. *J. Electron. Sci. Technol.* **2020**, *18*, 100018.

[27] Zeiri, N.; Naifar, A.; Nasrallah, S.A.B.; Said, M. Third nonlinear optical susceptibility of CdS/ZnS core-shell spherical quantum dots for optoelectronic devices. *Optik* **2019**, *176*, 162–167.

[28] Kuzyk, O.; Stolyarchuk, I.; Dan'kiv, O.; Peleshchak, R. Baric properties of quantum dots of the type of core (CdSe)-multilayer shell (ZnS/CdS/ZnS) for biomedical applications. *Appl. Nanosci.* **2022**, 1–10.

[29] Marqués-González, S.; Low, P.J. Molecular electronics: history and fundamentals. *Aust. J. Chem.* **2016**, *69*, 244–253.

[30] Xin, N.; Guo, X. Catalyst: the renaissance of molecular electronics. *Chem.* **2017**, *3*, 373–376

[31] Mendoza-Uribe, G.; Rodriguez-Lopez, J. Nanoscience and nanotechnology: a revolution in progress. *Perf. latinoam.* **2007**, *14*, 161–186.

[32] Charles, P.; Frank, O. *Introduction to nanotechnology*; John Wiley & Sons, 2003.

[33] Joachim, C.; Gimzewski, J.; Aviram, A. Electronics using hybrid-molecular and mono-molecular devices. *Nature* **2000**, *408*, 541–548.

[34] Aviram, A. Molecules for memory, logic, and amplification. *J.A.C.S.* **1988**, *110*, 5687–5692.

[35] Aviram, A.; Ratner, M. Molecular rectifiers. *Chemical Physics Letters* **1974**, *29*, 277–283.

[36] Han, W.; Durantini, E.; Moore, T.; Moore, A.; Gust, D.; Rez, P.; Leatherman, G.; Seely, G.; Tao, N.; Lindsay, S.M. STM contrast, electron-transfer chemistry, and conduction in molecules. *J. Phys. Chem. B.* **1997**, *101*, 10719–10725.

[37] Xue, Y.; Datta, S.; Hong, S.; Reifenberger, R.; Henderson, J.; Kubiak, C. Negative differential resistance in the scanning-tunneling spectroscopy of organic molecules. *Phys. Rev. B.* **1999**, *59*, R7852.

[38] Li, Z.; Borguet, E. Determining charge transport pathways through single porphyrin molecules using scanning tunneling microscopy break junctions. *JACS. 2012*, *134*, 63–66.

[39] Wang, L.; Wang, L.; Zhang, L.; Xiang, D. Advance of mechanically controllable break junction for molecular electronics. *Molecular-Scale Electronics: Current Status and Perspectives.* **2017**, 45–86.

[40] Perrin, M.L.; Burzurí, E.; Van der Zant, H.S. Single-molecule transistors. *Chem. Soc. Rev. 2015*, *44*, 902–919.

[41] Xu, K.; Yi, G.; Wang, W.; Wang, J.; Wang, C.; Li, Q. Theoretical insights into the diverse and tunable charge transport behavior of stilbene-based single-molecule junctions. *Chem. Phys.* **2022**, *556*, 111478.

[42] Ojeda, J.H.; Duque, C.A.; Laroze, D. Electron–phonon interaction in quantum transport through quantum dots and molecular systems. *Physica B.* **2016**, *502*, 73–81.

[43] Albrecht, K.F.; Wang, H.; Mühlbacher, L.; Thoss, M.; Komnik, A. Bistability signatures in nonequilibrium charge transport through molecular quantum dots. *Phys. Rev. B.* **2012**, *86*, 081412.

[44] Ojeda, J.H.; Duque, C.A.; Laroze, D. Shot noise and thermopower in aromatic molecules. *Physica E.* **2014**, *62*, 15–20.

[45] Perrin, M.L.; Verzijl, C.; Martin, C.; Shaikh, A.; Eelkema, R.; Van Esch, J.; Van Ruitenbeek, J.; Thijssen, J.; Van Der Zant, H.; Dulić, D. Large tunable image-charge effects in single-molecule junctions. *Nat. Nanotechnol.* **2013**, *8*, 282–287.

[46] Dadosh, T.; Gordin, Y.; Krahne, R.; Khivrich, I.; Mahalu, D.; Frydman, V.; Sperling, J.; Yacoby, A.; Bar-Joseph, I. Measurement of the conductance of single conjugated molecules. *Nature* **2005**, *436*, 677–680.

2 General theoretical framework

2.1 Quantum transport through a single molecule

2.1.1 Time-independent Green's functions.

Green's functions ($G(\boldsymbol{r}, \boldsymbol{r}'; z)$) can be defined as the solutions of inhomogeneous differential equations of the form:

$$[z - L(\boldsymbol{r})]G(\boldsymbol{r}, \boldsymbol{r}'; z) = \delta(\boldsymbol{r} - \boldsymbol{r}'). \tag{2-1}$$

Equation 2-1 is subject to certain boundary conditions for $\boldsymbol{r}$ or $\boldsymbol{r}'$, which lie on the surface S of the domain Ω. Here we assume that z is a complex variable with $\lambda \equiv Re\{z\}$ and $s \equiv Im\{z\}$ and that $L(\boldsymbol{r})$ is a linear, hermitian differential operator, independent of time that has a complete set of eigenfunctions $\phi_n(\boldsymbol{r})$, i.e.

$$L(\boldsymbol{r})\phi_n(\boldsymbol{r}) = \lambda_n \phi_n(\boldsymbol{r}), \tag{2-2}$$

where $\phi_n(\boldsymbol{r})$ satisfies the same boundary conditions as $G(\boldsymbol{r}, \boldsymbol{r}'; z)$, the subscript n specifies each eigenfunction with its respective eigenvalue λ_n and the set $\{\phi_n\}$ is considered orthonormal, satisfying the condition:

$$\int_\Omega \phi_n^*(\boldsymbol{r})\phi_m(\boldsymbol{r})d\boldsymbol{r} = \delta_{nm}. \tag{2-3}$$

The completeness relation of the set $\{\phi_n(\boldsymbol{r})\}$ is given by the following relation:

$$\sum_n \phi_n(\boldsymbol{r})\phi_n^*(\boldsymbol{r}') = \delta(\boldsymbol{r} - \boldsymbol{r}'). \tag{2-4}$$

Using Green's functions allows us to introduce an abstract vector space, whose particular representation is the various functions we deal with. The most convenient way to achieve this is to use Dirac's bra and ket notation, which can be written as follows:

$$\phi_n(\boldsymbol{r}) = \langle \boldsymbol{r}|\phi_n\rangle, \qquad \phi_n^*(\boldsymbol{r}) = \langle \phi_n|\boldsymbol{r}\rangle, \tag{2-5}$$

$$\delta(\boldsymbol{r} - \boldsymbol{r}')L(\boldsymbol{r}) \equiv \langle \boldsymbol{r}|L|\boldsymbol{r}'\rangle, \tag{2-6}$$

$$G(\boldsymbol{r}, \boldsymbol{r}'; z) \equiv \langle \boldsymbol{r}|G(z)|\boldsymbol{r}'\rangle, \tag{2-7}$$

$$\langle \boldsymbol{r}|\boldsymbol{r}'\rangle = \delta(\boldsymbol{r}-\boldsymbol{r}'), \tag{2-8}$$

$$\int d\boldsymbol{r}|\boldsymbol{r}\rangle\langle\boldsymbol{r}| = 1, \tag{2-9}$$

where $|\boldsymbol{r}\rangle$ is the eigenvector of the position operator. Now, we can rewrite the expressions from (2-1) to (2-4) with Dirac notation:

$$(z-L)G(z) = 1, \tag{2-10}$$

$$L|\phi_n\rangle = \lambda_n|\phi_n\rangle, \tag{2-11}$$

$$\langle\phi_n|\phi_m\rangle = \delta_{nm}, \tag{2-12}$$

$$\sum_n |\phi_n\rangle\langle\phi_n| = 1. \tag{2-13}$$

If all the eigenvalues of $(z-L)$ are non-zero, i.e., if $z \neq \{\lambda_n\}$, then the solution of the differential equations given in equation (2-10) can be written as:

$$G(z) = [z-L]^{-1}. \tag{2-14}$$

Applying the completeness condition (equation (2-13)) to the previous expression, we obtain:

$$G(z) = \frac{1}{z-L}\sum_n |\phi_n\rangle\langle\phi_n| = \sum_n \frac{|\phi_n\rangle\langle\phi_n|}{z-L}. \tag{2-15}$$

The Green's function formalism can be directly applied to physical systems. For example, considering the time-independent, non-relativistic, single-particle Schrödinger equation, which has the form:

$$[E-H(\boldsymbol{r})]\psi(\boldsymbol{r}) = 0, \tag{2-16}$$

by making the following substitutions $L(\boldsymbol{r}) \to H(\boldsymbol{r})$, $\lambda \to E$, and $z = \lambda + is \to z = E + is$, it is possible to rewrite with the Green's functions using the equation:

$$[E-H(\boldsymbol{r})]G(\boldsymbol{r},\boldsymbol{r}',E) = \delta(\boldsymbol{r}-\boldsymbol{r}'), \tag{2-17}$$

here, $H(r)$ is the Hamiltonian operator in the $\boldsymbol{r}$-representation, E is the energy eigenvalue, and $G(\boldsymbol{r},\boldsymbol{r}';E)$ that satisfies the same boundary conditions of the wave function $\psi(\boldsymbol{r})$, i.e., the continuity of $\psi(\boldsymbol{r})$ and $\nabla\psi(\boldsymbol{r})$, and finite (or zero) value at infinity.

Expressing $G(\boldsymbol{r},\boldsymbol{r}';E)$ in terms of the eigenvalues E_n and the complete set of orthonormal eigenfunctions ϕ_n of H is

$$G(\boldsymbol{r},\boldsymbol{r}';E) = \sum_n \frac{\phi_n(\boldsymbol{r})\phi_n^*(\boldsymbol{r}')}{z-E_n}, \tag{2-18}$$

or, in Dirac's bra and ket notation,

$$G(\boldsymbol{r}, \boldsymbol{r}'; E) = \sum_n \frac{|\phi_n\rangle\langle\phi_n|}{z - E_n} = [z - H]^{-1}, \tag{2-19}$$

where z has the form $z \to E \mp i\eta$. In the limit where the imaginary part has an infinitesimal contribution, i.e., $\eta \to 0$, the advanced Green's functions G^a and retarded G^r can be defined as follows:

$$G^{a(r)}(E) \equiv \lim_{\eta \to 0}[(E \mp i\eta)I - H]^{-1} \tag{2-20}$$

where the sign $(+)$ is attributed to the advanced Green's function and the sign $(-)$ to the delayed Green's function, and I is the identity operator.

Although time does not appear explicitly in the expression (2-20), the delayed Green's function G^r can be related to the propagation of an electron forward in time (making physical sense), while G^a is the corresponding time-inverted function, which would describe the propagation of the electron backward in time (mathematical sense). Therefore, the equation (2-20) can be written in terms of the eigenfunctions and eigenvalues as:

$$G^{a(r)}(E) = \sum_n \frac{|\phi_n\rangle\langle\phi_n|}{E - E_n \mp i\eta}, \tag{2-21}$$

in the limit when $\eta \to 0$ is implicitly assumed in all expressions in which the parameter η will appear. This last expression shows that the Green's functions (for a non-interacting case) have poles in the self-energies E_n, of the system, which is part of the information contained in these functions [1, 2].

2.1.2 Tight-Binding Hamiltonian

The Green's function, as defined in equation (2-19), serves as the propagator for a specific physical system characterized by a Hamiltonian. This Hamiltonian describes a particle capable of being confined within a particular site or transitioning to its nearest neighboring site. In this context, the Hamiltonian employed is commonly known as the tight-binding Hamiltonian.

The tight-binding method is defined as a linear combination of atomic orbitals located in the atoms of a system (Equation 2-22), where the coefficients represent the amplitudes of the plane wave $\exp(i\boldsymbol{k} \cdot \boldsymbol{R})$ of atoms located at position $\boldsymbol{R}$, and with wave vector $\boldsymbol{k}$. With this approximation, space can be represented in a discrete way, where there is an atomic orbital of the form $\phi_n(\boldsymbol{r} - \boldsymbol{R}_j)$ located on an atom in position $\boldsymbol{R}_j$ and a band quantum number n, which represents the n-th atomic energy level. This combination can be represented by:

$$B_{n,\boldsymbol{k}}(\boldsymbol{r}) = \frac{1}{\sqrt{N}} \sum_j \exp(i\boldsymbol{k}\cdot\boldsymbol{R}_j)\phi_n(\boldsymbol{r}-\boldsymbol{R}_j), \tag{2-22}$$

the above sum extends over all positions of the atoms in the unit cell of the material. The expression (2-22) is called a Bloch sum, because it produces a function that satisfies the Bloch condition, $B_{n,\boldsymbol{k}}(\boldsymbol{r}) = B_{n,\boldsymbol{k}}(\boldsymbol{r}+\boldsymbol{R}_0)$, for the wave vector $\boldsymbol{k}$, where the following condition is met:

$$\sqrt{N}B_{n,\boldsymbol{k}}(\boldsymbol{r}+\boldsymbol{R}_0) = \sum_j \exp(i\boldsymbol{k}\cdot\boldsymbol{R}_j)\phi_n(\boldsymbol{r}+\boldsymbol{R}_0-\boldsymbol{R}_j),$$

$$\sqrt{N}B_{n,\boldsymbol{k}}(\boldsymbol{r}-\boldsymbol{R}_0) = \sum_j \exp(i\boldsymbol{k}\cdot\boldsymbol{R}_j)\phi_n(\boldsymbol{r}-(\boldsymbol{R}_0+\boldsymbol{R}_j)),$$

changing $\boldsymbol{R}_j \to \boldsymbol{R}'_j = \boldsymbol{R}_j - \boldsymbol{R}_0$, with $\boldsymbol{R}_0$ a lattice vector, we have:

$$\sqrt{N}B_{n,\boldsymbol{k}}(\boldsymbol{r}-\boldsymbol{R}_0) = \sum_j \exp\left(i\boldsymbol{k}\cdot(\boldsymbol{R}'_j+\boldsymbol{R}_0)\right)\phi_n(\boldsymbol{r}-\boldsymbol{R}'_j),$$

$$\sqrt{N}B_{n,\boldsymbol{k}}(\boldsymbol{r}-\boldsymbol{R}_0) = \exp\left(i\boldsymbol{k}\cdot\boldsymbol{R}_0\right)\sum_j \exp\left(i\boldsymbol{k}\cdot\boldsymbol{R}'_j\right)\phi_n(\boldsymbol{r}-\boldsymbol{R}'_j),$$

thus fulfilling the property

$$B_{n,\boldsymbol{k}}(\boldsymbol{r}-\boldsymbol{R}_0) = \exp\left(i\boldsymbol{k}\cdot\boldsymbol{R}_0\right)B_{n,\boldsymbol{k}}(\boldsymbol{r}). \tag{2-23}$$

When considering tight binding, the states of the atomic sites with orbitals (s, p or d) mix with each other, which is known as hybridization, due to the overlap of neighboring atomic orbitals within of the valence band, therefore, the valence wavefunction in the system is one of the atomic functions with real quantities determined by the solution of the Schrödinger equation. With the above, the electron wave functions of the system are expressed as a quantity $b_{n,\boldsymbol{k}}$ of each of the Bloch sums, of the form:

$$\psi_{\boldsymbol{k}}(\boldsymbol{r}) = \sum_n b_n(\boldsymbol{k})B_{n,\boldsymbol{k}}(\boldsymbol{r}), \tag{2-24}$$

where the coefficient b_n indicates the amplitudes of each of the Bloch states (B_n) in the wave function of the particle moving in the system. The Bloch sums become the basis functions, with which the wave functions of the electrons are expressed. To find the wavefunctions, we need these to be solutions of the Schrödinger equation. On the other hand, these Bloch functions can be expressed in Dirac notation of the form $|n\rangle \equiv B_n$, and taking into account that $|n\rangle$ must be orthonormal functions, that is, they satisfy $\langle n|\beta\rangle = \delta_{n\beta}$, the strong bond Hamiltonian in the Hilbert space formed by $B_{n,\boldsymbol{k}}$ can be written as:

$$H = \sum_{n}(E_n + e\varphi_n)|n\rangle\langle n| + \sum_{n,\beta} v_{n,\beta}|n\rangle\langle\beta| + \sum_{n\beta,\lambda\gamma} V_{n\beta,\lambda\gamma}|n\rangle|\beta\rangle\langle\lambda|\langle\gamma| + \cdots, \tag{2-25}$$

where the first term in the Hamiltonian describes the localized states with energies E_n, φ_n is the electrostatic potential, the second term is known as the tight-binding coupling and determines the jump between first neighbors, where $v_{n,\beta}$ represents the matrix elements of the energy between the nearest neighbors, the third term is an interaction between two or more particles in conduction, and the following terms are taken into account in case of considering more interactions.

The tight-binding model is reasonable only when the local states can be orthogonalized, however, the method turns out to be of particular importance for describing small molecules when atomic orbitals form the basis. Mathematically, this model is a discrete version of the Schrödinger equation, which is why it is frequently used in numerical calculations. Considering the simplest model where there is no interaction between electrons, and there is only one particle in conduction, therefore, the electrostatic potential interactions in the n states are ignored, so only the first term of (2-25) is maintained, along with the first neighbor coupling term. In this way, the Hamiltonian reduces to:

$$H = \sum_{n} E_n|n\rangle\langle n| + \sum_{n\neq\beta} v_{n,\beta}|n\rangle\langle\beta|, \tag{2-26}$$

the Hamiltonian above represents a single particle that goes from a state n to a state β. To solve the single-particle problem, it is necessary to introduce a new representation, where the coefficients b_n in the expansion (2-24) are the vector components of the wavefunction ψ.

$$\{\psi\} = \begin{pmatrix} b_1 \\ b_2 \\ b_3 \\ \vdots \\ b_N \end{pmatrix} \tag{2-27}$$

These components are obtained from the Schrödinger matrix equation:

$$[H]\{\psi\} = E\{\psi\}, \tag{2-28}$$

the matrix elements are given by:

$$H_{n,\beta} = \langle n|H|\beta\rangle = \int \psi_n^*(\boldsymbol{r})H\psi_\beta(\boldsymbol{r})d\boldsymbol{r}. \tag{2-29}$$

This Hamiltonian is applied in some very common examples such as: a linear chain that is made up of coupled sites between first neighbors (see figure 2-1), the Hamiltonian of this system will have the form:

$$[H] = \begin{pmatrix} E_1 & v & 0 & \dots & 0 \\ v & E_2 & v & \dots & 0 \\ 0 & v & \ddots & \ddots & \vdots \\ \vdots & \vdots & \ddots & E_{N-1} & v \\ 0 & 0 & \dots & v & E_N \end{pmatrix} \tag{2-30}$$

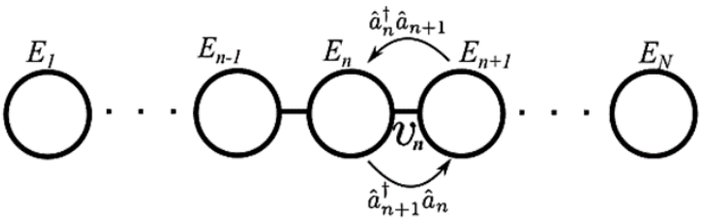

Figure **2-1**: Linear chain described by a tight-binding Hamiltonian, where the action of the creation and destruction operators in the system is shown.

Also for a single quantum dot, where the basis is formed by its eigenstates, the matrix Hamiltonian is diagonal, similar to that of the linear chain, with the difference that the coupling to its neighbors, v, is zero.

The tight-binding Hamiltonian can be rewritten in new operator notation using the second quantization, substituting the product of the states $\{|n\rangle\}$ into the expression (2-26). These are the annihilation operator $\hat{a}$ and the creation operator $\hat{a}^\dagger$, which act at the site n. These operators correspond to the lattice and obey the switching rules:

$$[\hat{a}_n, \hat{a}_\beta^\dagger] = \delta_{n\beta}, \tag{2-31}$$

$$[\hat{a}_n, \hat{a}_\beta] = [\hat{a}_n^\dagger, \hat{a}_\beta^\dagger] = 0. \tag{2-32}$$

Using the new notation, the Hamiltonian can be expressed in terms of those new operators as:

$$H = \sum_n E_n \hat{a}_n^\dagger \hat{a}_n + \sum_{n \neq \beta} v_{n\beta} \hat{a}_n^\dagger \hat{a}_\beta, \tag{2-33}$$

where the ladder operators $\hat{a}^\dagger$ and $\hat{a}$, create and destroy an electron in the n site or in the β site.

Another consideration of great importance in the tight-binding Hamiltonian is that only interactions with nearest neighbors are important (first neighbor interaction), i.e., if Δ_n represents the vectors from n to all neighboring sites closest, then the Hamiltonian can be written as:

$$H = \sum_{n} E_n \hat{a}_n^{\dagger} \hat{a}_n + \sum_{n \neq \beta} v_{n,\Delta_n} (\hat{a}_n^{\dagger} \hat{a}_{n+\Delta_n} + \hat{a}_{n+\Delta_n}^{\dagger} \hat{a}_n), \tag{2-34}$$

the above expression has diagonal contributions given by the eigenenergies of the site E_n, and hopping energy contributions, which create and annihilate the excitations in neighboring lattice sites and annihilate or create them respectively in the site n, (see figure 2-1) [2–5].

2.1.3 Dyson equation

To analyze the electronic behavior of a molecule connected between two electrodes (left, right), considering the formulation of the tight-binding Hamiltonian, the molecular system will first be studied independently to establish the equation of motion using the Green's function formalism, based on the following relation:

$$G = \frac{1}{E - \hat{H}}, \tag{2-35}$$

where G is the Green's function of the particle and $\hat{H}$ is the Hamiltonian of the molecular system. The matrix components of the Green's function are given by:

$$G_{ij} = \langle i|G|j\rangle, \tag{2-36}$$

applying the relationship (2-36) in the equation (2-35), we have:

$$\langle i|G(E - \hat{H})|j\rangle = \delta_{i,j}, \tag{2-37}$$

now, the completeness relation is applied, we obtain:

$$\sum_{k} \langle i|G|k\rangle\langle k|(E - \hat{H})|j\rangle = \delta_{i,j},$$

$$\sum_{k} G_{ik}(E\delta_{kj} - H_{kj}) = \delta_{ij}. \tag{2-38}$$

Using the Hamiltonian of equation (2-26), to obtain the matrix elements H_{kj}

$$\langle k|\hat{H}|j\rangle = \sum_{n} E_n \langle k|n\rangle\langle n|j\rangle + \sum_{n \neq \beta} v_{n,\beta}\langle k|n\rangle\langle \beta|j\rangle,$$

$$H_{kj} = \sum_{n} E_n \delta_{kn}\delta_{nj} + \sum_{n \neq \beta} v_{n\beta}\delta_{kn}\delta_{\beta j},$$

from the previous equation the first summation for $n = k$ is expanded, and for the second summation for $n = k$ and $\beta = j$, nothing remains of the above:

$$H_{kj} = E_k\delta_{kj} + v_{kj}, \tag{2-39}$$

replacing (2-39) into (2-38)

$$\sum_k G_{ik}(E\delta_{kj} - E_k\delta_{kj} - v_{kj}) = \delta_{ij},$$

$$\sum_k G_{ik}(E\delta_{kj} - E_k\delta_{kj}) = \delta_{ij} + \sum_k v_{kj}G_{ik},$$

expanding the first sum to $k = j$

$$(E - E_j)G_{ij} = \delta ij + \sum_k v_{kj}G_{ik}, \tag{2-40}$$

the second term on the right of the previous expression shows the interaction of the particle with its first neighbors, which in the case of the Hamiltonian (2-26), represents the hopping term of the electron to one of the two possible sites i or j, therefore, the expression (2-40) can be written as:

$$G_{ij} = \frac{1}{E - E_j}\delta_{ij} + \frac{1}{E - E_j}\sum_k v_{kj}G_{ik},$$

$$G_{ij} = G_0\delta_{ij} + G_0\sum_k v_{kj}G_{ik}, \tag{2-41}$$

assuming that site i has two nearest neighbors, the sum of the previous expression can be expanded as:

$$G_{ij} = G_0\delta_{ij} + G_0v_{j-1,j}G_{i,j-1} + G_0v_{j+1,j}G_{i,j+1}. \tag{2-42}$$

This equation is generalized by introducing a term, in which all the possible effects of the interactions on the system's dynamics are assumed. This quantity, called irreducible self-energy, is represented as $\Sigma(E)$. With this term the equation (2-42) can be written in the form:

$$G(E) = G_0(E) + G_0(E)\Sigma(E)G(E). \tag{2-43}$$

This equation is known as the Dyson equation (equation of motion), where the irreducible self-energy can be written for our system as $\Sigma = \Sigma_L + \Sigma_R$; Σ_L is the irreducible self-energy due to all interactions produced by the left electrode, and Σ_R is the self-energy due to the right electrode:

$$G(E) = G_0(E) + G_0(E)(\Sigma_L(E) + \Sigma_R(E))G(E). \tag{2-44}$$

The Dyson equation will be the starting point for the determination of physical properties (such as electrical, thermal and magnetic) in some one-dimensional and quasi-one-dimensional models [1, 5, 6].

2.1.4 Landauer-Büttiker formalism

This section shows the Landauer relation, which allows us to characterize the tunnel current through a single molecule, semiconductor system, or any other nanoscale structure, which is connected to two metallic electrodes, which are semi-infinite pieces of conductors that intersperse the central region C (see Fig. 2-2).

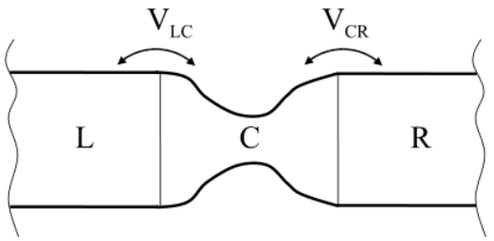

Figure **2-2**: Finite device (C) coupled to two semi-infinite conductive electrodes (right, left) through the operators V_{LC} and V_{CR}. There is no coupling between the electrodes.

The Hamiltonian of the central region, the right electrode, and the left electrode are represented as follows: $\hat{H}_C$, $\hat{H}_R$, and $\hat{H}_L$, respectively. Which can be associated with the Green function $G_C(z)$, $G_R(z)$, and $G_L(z)$, according to equation 2-35. The Schrödinger equation for the system shown in Fig. 2-1 is given by:

$$\hat{H}|\psi\rangle = E|\psi\rangle, \tag{2-45}$$

where E is the system energy, $|\psi\rangle$ the wavefunction, and $\hat{H}$ is the Hamiltonian of the complete system, in which is the Hamiltonian of the central zone, of the electrodes (right, left), and the coupling of the electrodes and zone C, the regions L and C are coupled by the potentials $\hat{V}_{LC}$ and $\hat{V}_{LC}^{\dagger}$, while the regions C and R, by the potentials $\hat{V}_{CR}$ and $\hat{V}_{CR}^{\dagger}$. It will also be assumed that the regions L and R are not coupled to each other, that is, there is physically no direct tunneling effect between the two regions. Taking the above into account, the total Hamiltonian can be represented as follows:

$$\hat{H} = \hat{H}_C + \hat{H}_R + \hat{H}_L + \hat{V}_{LC} + \hat{V}_{LC}^{\dagger} + \hat{V}_{CR} + \hat{V}_{CR}^{\dagger}. \tag{2-46}$$

The Schrödinger equation can be formally written in matrix form as follows:

$$\begin{bmatrix} \hat{H}_L & \hat{V}_{LC} & 0 \\ \hat{V}_{LC}^{\dagger} & \hat{H}_C & \hat{V}_{CR}^{\dagger} \\ 0 & \hat{V}_{CR} & \hat{H}_R \end{bmatrix} \begin{bmatrix} |\psi_L\rangle \\ |\psi_C\rangle \\ |\psi_R\rangle \end{bmatrix} = E \begin{bmatrix} |\psi_L\rangle \\ |\psi_C\rangle \\ |\psi_R\rangle \end{bmatrix}. \tag{2-47}$$

The following definition of the Green's function will be used for the total Hamiltonian of the system:

$$(E - \hat{H})\hat{G} \equiv \hat{I}, \tag{2-48}$$

It will be assumed that Green's functions of the C region and the electrodes are exactly known. The objective is to determine the Green's function $\hat{G}(z)$, not $\hat{H}_C$, since $\hat{G}(z)$ has the presence of the information of the coupling of the central region with the electrodes. This is done because it is easier to calculate Green's function than to solve the entire problem of eigenvalues, to do this we proceed to write the previous equation in matrix form:

$$\begin{bmatrix} E-\hat{H}_L & -\hat{V}_{LC} & 0 \\ -\hat{V}_{LC}^{\dagger} & E-\hat{H}_C & -\hat{V}_{CR}^{\dagger} \\ 0 & -\hat{V}_{CR} & E-\hat{H}_R \end{bmatrix} \begin{bmatrix} \hat{G}_L & \hat{G}_{LC} & \hat{G}_{LR} \\ \hat{G}_{CL} & \hat{G}_C & \hat{G}_{CR} \\ \hat{G}_{RL} & \hat{G}_{RC} & \hat{G}_R \end{bmatrix} = \begin{bmatrix} I & 0 & 0 \\ 0 & I & 0 \\ 0 & 0 & I \end{bmatrix}, \tag{2-49}$$

to find the expression for $\hat{G}_C(z)$ from the previous matrix equation, the equations that emerge when multiplying the first matrix, with the second column of the second matrix, will be taken, obtaining the following system of equations:

$$(E-\hat{H}_L)\hat{G}_{LC} - \hat{V}_{LC}\hat{G}_C = 0, \tag{2-50}$$

$$-\hat{V}_{LC}^{\dagger}\hat{G}_{LC} + (E-\hat{H}_C)\hat{G}_C - \hat{V}_{CR}^{\dagger}\hat{G}_{RC} = I, \tag{2-51}$$

$$(E-\hat{H}_R)\hat{G}_{RC} - \hat{V}_{CR} = 0, \tag{2-52}$$

solving $\hat{G}_{LC}$ from the equation 2-50,

$$\hat{G}_{LC} = \frac{1}{E-\hat{H}_L}\hat{V}_{LC}\hat{G}_C,$$

$$\hat{G}_{LC} = \hat{G}_L\hat{V}_{LC}\hat{G}_C, \tag{2-53}$$

performing the same procedure for $\hat{G}_{RC}$ of equation 2-52

$$\hat{G}_{RC} = \frac{1}{E-\hat{H}_R}\hat{V}_{CR}\hat{G}_C,$$

$$\hat{G}_{RC} = \hat{G}_R\hat{V}_{CR}\hat{G}_C, \tag{2-54}$$

$\hat{G}_L$ and $\hat{G}_L$ are defined as $(E-\hat{H}_{L(R)})^{-1}$. Now, we replace 2-53 and 2-54 into 2-51

$$-\hat{V}_{LC}^{\dagger}(\hat{G}_L\hat{V}_{LC}\hat{G}_C) + (E-\hat{H}_C)\hat{G}_C - \hat{V}_{CR}^{\dagger}(\hat{G}_R\hat{V}_{CR}\hat{G}_C) = I,$$

$$(-\hat{V}_{LC}^{\dagger}\hat{G}_L\hat{V}_{LC} + E - \hat{H}_C - \hat{V}_{CR}^{\dagger}\hat{G}_R\hat{V}_{CR})\hat{G}_C = I,$$

$$\hat{G}_C = (E-\hat{H}_C - \hat{V}_{CR}^{\dagger}\hat{G}_R\hat{V}_{CR} - \hat{V}_{LC}^{\dagger}\hat{G}_L\hat{V}_{LC})^{-1}, \tag{2-55}$$

the third and fourth terms on the right side of the equality are known as the self-energies of the system, and are defined as follows:

$$\hat{\Sigma}_L = \hat{V}_{LC}^{\dagger}\hat{G}_L\hat{V}_{LC},$$

$$\hat{\Sigma}_R = \hat{V}_{CR}^{\dagger}\hat{G}_R\hat{V}_{CR},$$

replacing $\hat{\Sigma}_L$ and $\hat{\Sigma}_R$ in 2-55, we have:

$$\hat{G}_C = (E - \hat{H}_C - \hat{\Sigma}_R - \hat{\Sigma}_L)^{-1}, \tag{2-56}$$

the previous expression gives us an account of the effect of the metal electrodes (leads) on the central region (or device) since calculating the Green's function of the device implies calculating the Green's function of an effective Hamiltonian, which is adding the self-energies to the Hamiltonian of the device ($\hat{H}_{eff} = \hat{H}_d + \hat{\Sigma}_L + \hat{\Sigma}_R$).

Non-equilibrium case

Before studying the non-equilibrium case, we will consider the case where the contact L is isolated from the contact R and the central region C (see Fig. **2-2**). At a given energy we have solutions of an incoming wave function that is completely reflected at the end of the contact. We will denote the solutions of the wave functions as $|\psi_{L,n}\rangle$, where L is the name of the contact, and n is a quantum number associated with the different modes in the contact. When the electrodes are connected to the device, and the system is non-equilibrium, implying that the electrodes are at different chemical potentials (or different Fermi functions), they inject electrons as plane waves, occupying the states corresponding to the waves incident on the electrodes. Therefore, we want to find the solutions corresponding to these incoming waves.

To calculate the wave function in the entire system due to the incoming wave at the contact L. First, a wave function must be proposed that must have the following form $|\psi_{L,n}\rangle + |\psi^R\rangle$, where $|\psi_{L,n}\rangle$ is the completely reflected wave and $|\psi^R\rangle$ It is the delayed response of the entire system. Substituting into the Schrödinger equation gives the following:

$$\begin{aligned}
\hat{H}(|\psi_{L,n}\rangle + |\psi^R\rangle) &= E(|\psi_{L,n}\rangle + |\psi^R\rangle),\\
\left(\hat{H}_C + \hat{H}_R + \hat{H}_L + \hat{V}_{LC} + \hat{V}_{LC}^{\dagger} + \hat{V}_{CR} + \hat{V}_{CR}^{\dagger}\right)\left(|\psi_{L,n}\rangle + |\psi^R\rangle\right) &= E\left(|\psi_{L,n}\rangle + |\psi^R\rangle\right),\\
\left(\hat{H}_C + \hat{H}_R + \hat{H}_L + \hat{V}_{LC} + \hat{V}_{LC}^{\dagger} + \hat{V}_{CR} + \hat{V}_{CR}^{\dagger}\right)|\psi_{L,n}\rangle \;+\; \hat{H}|\psi^R\rangle &= E\left(|\psi_{L,n}\rangle + |\psi^R\rangle\right),\\
\hat{H}_C|\psi_{L,n}\rangle + \hat{H}_R|\psi_{L,n}\rangle + \hat{H}_L|\psi_{L,n}\rangle + \hat{V}_{LC}|\psi_{L,n}\rangle + \hat{V}_{LC}^{\dagger}|\psi_{L,n}\rangle + \hat{V}_{CR}|\psi_{L,n}\rangle +&\\
\hat{V}_{CR}^{\dagger}|\psi_{L,n}\rangle + \hat{H}|\psi^R\rangle &= E\left(|\psi_{L,n}\rangle + |\psi^R\rangle\right),\\
E|\psi_{L,n}\rangle + \hat{V}_{LC}^{\dagger}|\psi_{L,n}\rangle + \hat{H}|\psi^R\rangle &= E\left(|\psi_{L,n}\rangle + |\psi^R\rangle\right),\\
\hat{H}|\psi^R\rangle &= E|\psi^R\rangle - \hat{V}_{LC}^{\dagger}|\psi_{L,n}\rangle,
\end{aligned} \tag{2-57}$$

In the previous expression, it can be seen that $|\psi^R\rangle$ is the response of the entire system to a perturbation of the type $-V_{CL}^{\dagger}|\psi_{L,n}$. From the equation 2-57 we can have an expression for $|\psi^R\rangle$, in the following form:

$$\left(\hat{H} - E\right)|\psi^R\rangle = -\hat{V}_{LC}^{\dagger}|\psi_{L,n}\rangle,$$
$$|\psi^R\rangle = -\frac{1}{\hat{H} - E}\hat{V}_{LC}^{\dagger}|\psi_{L,n}\rangle,$$
$$|\psi^R\rangle = \hat{G}\hat{V}_{LC}^{\dagger}|\psi_{L,n}\rangle, \tag{2-58}$$

This equation represents the scattering states of an incident electron, using all possible incoming wave states from each contact. With the previous procedure, the expression of the wave function of the device $|\psi_C\rangle$ can be obtained as a function of the contact wave $|\psi_{L,n}\rangle$, which is given by:

$$|\psi_C\rangle = \hat{G}_C\hat{V}_{LC}^{\dagger}|\psi_{L,n}\rangle. \tag{2-59}$$

From the equation 2-47 we can know the response of the wave function of the electrode R, in terms of the wave function of the device in the following way:

$$|\psi_R\rangle = \hat{G}_R(z)V_{CR}|\psi_C\rangle, \tag{2-60}$$

replacing the equation 2-59, into the equation 2-60, we have:

$$|\psi_R\rangle = \hat{G}_R(z)V_{CR}(\hat{G}_C\hat{V}_{LC}^{\dagger}|\psi_{L,n}\rangle),$$
$$|\psi_R\rangle = \hat{G}_R(z)V_{CR}\hat{G}_C\hat{V}_{LC}^{\dagger}|\psi_{L,n}\rangle, \tag{2-61}$$

to find the wave function for the contact L, a similar process is carried out as for the contact R, with the difference that it must contain the incoming wave therefore it must be added to the expression obtained:

$$|\psi_L\rangle = |\psi_{L,n}\rangle + \hat{G}_L(z)V_{LC}|\psi_C\rangle,$$
$$|\psi_L\rangle = |\psi_{L,n}\rangle + \hat{G}_L(z)V_{LC}(\hat{G}_C\hat{V}_{LC}^{\dagger}|\psi_{L,n}\rangle),$$
$$|\psi_L\rangle = |\psi_{L,n}\rangle + \hat{G}_L(z)V_{LC}\hat{G}_C\hat{V}_{LC}^{\dagger}|\psi_{L,n}\rangle,$$
$$|\psi_L\rangle = \left(1 + \hat{G}_L(z)V_{LC}\hat{G}_C\hat{V}_{LC}^{\dagger}\right)|\psi_{L,n}\rangle. \tag{2-62}$$

With what has been done above, it is possible to know the wave functions of the electrodes in terms of the incident disturbance, with which it is possible to calculate the complete set of solutions for the Schrödinger equation for the central dispersion region, for the contact L and R. This provides a tool with which it is possible to study and analyze the behavior of the electrons that enter the central region at a certain energy, and how these modify the properties of the system.

Charge density

When the system is in non-equilibrium, the electronic current that passes through the entire system can be calculated. Still, first, it is necessary to know the charge density on each electrode, which is different in each contact. The charge density matrix is defined as:

$$\rho = \sum_k f(E_k, \mu)|\psi_k\rangle\langle\psi_k|, \tag{2-63}$$

in the previous expression, the sum covers all states with occupation numbers given by the Fermi-Dirac distribution, in this case, the occupation number is determined by the reservoirs, which fill the incoming waves through the contacts, so that:

$$f(E_k, \mu_L) = \frac{1}{1 + e^{(E_k - \mu_L)/k_B T}}, \tag{2-64}$$

the equation 2-64 represents the Fermi-Dirac function of the contact L with a chemical potential (μ_L) and at a fixed temperature T.

The wave function in the device as a function of the incoming contact wave L is given in equation 2-59, which is redefined as:

$$|\psi_{C,k}\rangle = \hat{G}_C \hat{V}_{LC}^{\dagger} |\psi_{L,k}\rangle, \tag{2-65}$$

if we take into account all the states of the contact L and add them up, we have:

$$\rho_{C,L} = \int_{-\infty}^{\infty} \sum_k f(E, \mu_L)\delta(E - E_k)|\psi_{C,k}\rangle\langle\psi_{C,k}|dE, \tag{2-66}$$

now, we replace the ket and bra from the equation 2-65 into the equation 2-66:

$$\rho_{C,L} = \int_{-\infty}^{\infty} \sum_k f(E, \mu_L)\delta(E - E_k)\hat{G}_C \hat{V}_{LC}^{\dagger}|\psi_{L,k}\rangle\langle\psi_{L,k}|\hat{V}_{LC}\hat{G}_C^{\dagger}dE,$$

$$\rho_{C,L} = \int_{-\infty}^{\infty} \hat{G}_C \hat{V}_{LC}^{\dagger} f(E, \mu_L) \left(\sum_k \delta(E - E_k)|\psi_{L,k}\rangle\langle\psi_{L,k}| \right) \hat{V}_{LC}\hat{G}_C^{\dagger}dE, \tag{2-67}$$

the term in parentheses, in the previous expression, is known as the spectral function, and can be redefined as follows:

$$\hat{D}(E) = \sum_k \delta(E - E_k)|\psi_{L,k}\rangle\langle\psi_{L,k}| \equiv i\left(\frac{\hat{G}^{+} - \hat{G}^{-}}{2\pi}\right), \tag{2-68}$$

where $\hat{G}^{+}$ is the leading and $\hat{G}^{-}$ is the lagging Green's functions. Considering the above in the equation 2-67, we have:

$$\rho_{C,L} = \int_{-\infty}^{\infty} f(E,\mu_L)\hat{G}_C\hat{V}_{LC}^{\dagger}\hat{D}(E)\hat{V}_{LC}\hat{G}_C^{\dagger}dE, \tag{2-69}$$

from the previous expression, it is possible to rewrite the term $\hat{V}_{LC}^{\dagger}\hat{D}(E)\hat{V}_{LC}$ in the following way:

$$\hat{V}_{LC}^{\dagger}\hat{D}(E)\hat{V}_{LC} = i\hat{V}_{LC}^{\dagger}\left(\frac{\hat{G}^{+}-\hat{G}^{-}}{2\pi}\right)\hat{V}_{LC} = \frac{1}{2\pi}\left(\hat{V}_{LC}^{\dagger}\hat{G}^{+}\hat{V}_{LC} - \hat{V}_{LC}^{\dagger}\hat{G}^{-}\hat{V}_{LC}\right), \tag{2-70}$$

From the expression 2-55, we know that the product $\hat{V}_{LC}^{\dagger}\hat{G}^{+}\hat{V}_{LC} = \Sigma_L^{+}$, substituting we have:

$$\hat{V}_{LC}^{\dagger}\hat{D}(E)\hat{V}_{LC} = \frac{1}{2\pi}\left(\Sigma_L^{+} - \Sigma_L^{-}\right) \equiv \frac{1}{2\pi}\hat{\Gamma}_L, \tag{2-71}$$

where the term $\hat{\Gamma}_L$ corresponds to the coupling potential between the central scattering region with the contact L and is a definition in terms of self-energies. Substituting this result into equation 2-69, we have:

$$\rho_{C,L} = \frac{1}{2\pi}\int_{-\infty}^{\infty} f(E,\mu_L)\hat{G}_C\hat{\Gamma}_L\hat{G}_C^{\dagger}dE. \tag{2-72}$$

Following the same steps, a similar expression can be found for the charge density for the contact R

$$\rho_{C,R} = \frac{1}{2\pi}\int_{-\infty}^{\infty} f(E,\mu_R)\hat{G}_C\hat{\Gamma}_R\hat{G}_C^{\dagger}dE. \tag{2-73}$$

To know the total contribution of the charge density due to the contacts L and R, both contributions must be added, taking into account the double degeneracy of the electron spin:

$$\begin{gathered}
\rho = 2(\rho_{C,L} + \rho_{C,R}), \\
\rho = 2\left(\frac{1}{2\pi}\int_{-\infty}^{\infty} f(E,\mu_L)\hat{G}_C\hat{\Gamma}_L\hat{G}_C^{\dagger}dE + \frac{1}{2\pi}\int_{-\infty}^{\infty} f(E,\mu_R)\hat{G}_C\hat{\Gamma}_R\hat{G}_C^{\dagger}dE\right), \\
\rho = \frac{1}{\pi}\left(\int_{-\infty}^{\infty} f(E,\mu_L)\hat{G}_C\hat{\Gamma}_L\hat{G}_C^{\dagger}dE + \int_{-\infty}^{\infty} f(E,\mu_R)\hat{G}_C\hat{\Gamma}_R\hat{G}_C^{\dagger}dE\right).
\end{gathered} \tag{2-74}$$

Probability Current

So far, we have described a system of two contacts, which have different chemical potentials, which in turn have different populations of electrons, these conditions give rise to a tunnel current. To know the expression of the current, the temporal conservation of the total probability density of the complete system (contacts and scattering region) will be used,

since, in the steady state, the probability of finding the electron in the central region is conserved.

$$0 = \frac{\partial \sum_s |\psi_s|^2}{\partial t} = \sum_s \frac{\partial \langle\psi|s\rangle\langle s|\psi\rangle}{\partial t} = \sum_s \left(\frac{\partial \langle\psi|s\rangle}{\partial t}\langle s|\psi\rangle + \langle\psi|s\rangle \frac{\partial \langle s|\psi\rangle}{\partial t} \right), \tag{2-75}$$

To know the terms of the derivatives in the previous expression, we will use the time-dependent Schrödinger equation:

$$\begin{aligned} i\hbar \frac{\partial |\psi\rangle}{\partial t} &= \hat{H}|\psi\rangle, \\ \langle s| i\hbar \frac{\partial |\psi\rangle}{\partial t} &= \langle s|\hat{H}|\psi\rangle, \\ \frac{\partial \langle s|\psi\rangle}{\partial t} &= -\frac{i}{\hbar}\langle s|\hat{H}|\psi\rangle, \end{aligned} \tag{2-76}$$

and,

$$\begin{aligned} -i\hbar \frac{\partial \langle\psi|}{\partial t} &= \langle\psi|\hat{H}, \\ -i\hbar \frac{\partial \langle\psi|}{\partial t}|s\rangle &= \langle\psi|\hat{H}|s\rangle, \\ \frac{\partial \langle\psi|s\rangle}{\partial t} &= \frac{i}{\hbar}\langle\psi|\hat{H}|s\rangle, \end{aligned} \tag{2-77}$$

replacing the expressions 2-76, and 2-77 into 2-75, we have:

$$\begin{aligned} 0 &= \sum_s \left(\frac{i}{\hbar}\langle\psi|\hat{H}|s\rangle\langle s|\psi\rangle - \langle\psi|s\rangle \frac{i}{\hbar}\langle s|\hat{H}|\psi\rangle \right), \\ 0 &= \frac{i}{\hbar}\left(\langle\psi|\hat{H}\left\{ \sum_s |s\rangle\langle s|\psi\rangle \right\} - \left\{ \sum_s \langle\psi|s\rangle\langle s| \right\} \hat{H}|\psi\rangle \right), \end{aligned} \tag{2-78}$$

since we want to know the response of the device to the incoming wave, to do so we change the terms in braces to the wave function of the device, considering the following:

$$|\psi_C\rangle = \left(\sum_s |s\rangle \langle s| \right) |\psi_C\rangle = \sum_s |s\rangle \langle s|\psi_C\rangle, \tag{2-79}$$

$$\langle\psi_C| = \langle\psi_C| \left(\sum_s |s\rangle \langle s| \right) = \sum_s \langle\psi_C|s\rangle \langle s|, \tag{2-80}$$

substituting equations 2-79 and 2-80 into equation 2-78:

$$0 = \frac{i}{\hbar}\left(\langle\psi|\hat{H}|\psi_C\rangle - \langle\psi_C|\hat{H}|\psi\rangle \right), \tag{2-81}$$

expanding the Hamiltonian of the system, we have:

$$0 = \frac{i}{\hbar}\left(\langle\psi|(\hat{H}_C + \hat{V}_{LC} + \hat{V}_{CR})|\psi_C\rangle - \langle\psi_C|(\hat{H}_C + \hat{V}_{LC}^\dagger + \hat{V}_{CR}^\dagger)|\psi\rangle\right),$$

$$0 = \frac{i}{\hbar}\left(\langle\psi|\hat{H}_C|\psi_C\rangle + \langle\psi|\hat{V}_{LC}|\psi_C\rangle + \langle\psi|\hat{V}_{CR}|\psi_C\rangle - \langle\psi_C|\hat{H}_C|\psi\rangle - \langle\psi_C|\hat{V}_{LC}^\dagger|\psi\rangle - \langle\psi_C|\hat{V}_{CR}^\dagger|\psi\rangle\right),$$

$$0 = \frac{i}{\hbar}\left(E_C\langle\psi|\psi_C\rangle + \langle\psi|\hat{V}_{LC}|\psi_C\rangle + \langle\psi|\hat{V}_{CR}|\psi_C\rangle - E_C\langle\psi_C|\psi\rangle - \langle\psi_C|\hat{V}_{LC}^\dagger|\psi\rangle - \langle\psi_C|\hat{V}_{CR}^\dagger|\psi\rangle\right),$$

$$0 = \frac{i}{\hbar}\left(\langle\psi|\hat{V}_{LC}|\psi_C\rangle + \langle\psi|\hat{V}_{CR}|\psi_C\rangle - \langle\psi_C|\hat{V}_{LC}^\dagger|\psi\rangle - \langle\psi_C|\hat{V}_{CR}^\dagger|\psi\rangle\right),$$

$$0 = \frac{i}{\hbar}\left(\langle\psi|\hat{V}_{LC}|\psi_C\rangle - \langle\psi_C|\hat{V}_{LC}^\dagger|\psi\rangle\right) + \frac{i}{\hbar}\left(\langle\psi|\hat{V}_{CR}|\psi_C\rangle - \langle\psi_C|\hat{V}_{CR}^\dagger|\psi\rangle\right), \tag{2-82}$$

the previous expression represents the probability of current entering the device through the contact on the left (first parenthesis), and through the contact on the right (second parenthesis). The expression of the equation 2-82 can be generalized for any contact k, and multiplied by the charge of the electron $(-e)$ the electric current is obtained:

$$i_k = -\frac{ie}{\hbar}\left(\langle\psi_k|\,\hat{V}_{Ck}\,|\psi_C\rangle - \langle\psi_C|\,\hat{V}_{Ck}^\dagger\,|\psi_k\rangle\right), \tag{2-83}$$

i_k is defined as positive for a current coming from the contacts to the device.

Electrical Current

Now we can calculate the total current passing through the central region, for that we need to take into account all the contributions of the wave function of the device and the contacts (L and R) given by the equations 2-59, 2-61 and 2-62. Taking the relationship 2-83, we can calculate the current from the contact L to R, as follows:

$$i_{L\to R} = -\frac{ie}{\hbar}\left(\langle\psi_R|\,\hat{V}_{CR}\,|\psi_C\rangle - \langle\psi_C|\,\hat{V}_{CR}^\dagger\,|\psi_R\rangle\right),$$

$$i_{L\to R} = -\frac{ie}{\hbar}\left(\langle\psi_R|\,\hat{V}_{CR}\hat{G}_C\hat{V}_{LC}^\dagger\,|\psi_{L,n}\rangle - \langle\psi_{L,n}|\,\hat{V}_{LC}\hat{G}_C^\dagger\hat{V}_{CR}^\dagger\,|\psi_R\rangle\right),$$

$$i_{L\to R} = -\frac{ie}{\hbar}\left(\langle\psi_{L,n}|\,\hat{V}_{LC}\hat{G}_C^\dagger\hat{V}_{CR}^\dagger\hat{G}_R^\dagger\hat{V}_{CR}\hat{G}_C\hat{V}_{LC}^\dagger\,|\psi_{L,n}\rangle - \langle\psi_{L,n}|\,\hat{V}_{LC}\hat{G}_C^\dagger\hat{V}_{CR}^\dagger\hat{G}_R\hat{V}_{RC}\hat{G}_C\hat{V}_{LC}^\dagger\,|\psi_{L,n}\rangle\right),$$

$$i_{L\to R} = -\frac{ie}{\hbar}\left(\langle\psi_{L,n}|\,\hat{V}_{LC}\hat{G}_C^\dagger\hat{V}_{CR}^\dagger\left[\hat{G}_R^\dagger - \hat{G}_R\right]\hat{V}_{RC}\hat{G}_C\hat{V}_{LC}^\dagger\,|\psi_{L,n}\rangle\right), \tag{2-84}$$

from the equation 2-71 we can define $\hat{V}_{CR}^\dagger\left[\hat{G}_R^\dagger - \hat{G}_R\right]\hat{V}_{RC}$:

$$\hat{\Gamma}_R = i\left[\Sigma_R^+ - \Sigma_R^-\right]$$

$$\hat{\Gamma}_R = i\left[\hat{V}_{CR}^\dagger\hat{G}_R^\dagger\hat{V}_{CR} - \hat{V}_{CR}^\dagger\hat{G}_R^-\hat{V}_{CR}\right],$$

$$
\begin{aligned}
-i\hat{\Gamma}_R &= \hat{V}_{CR}^{\dagger}\left[\hat{G}_R^{\dagger} - \hat{G}_R^{-}\right]\hat{V}_{CR},\\
-i\hat{\Gamma}_R &= \hat{V}_{CR}^{\dagger}\left[\hat{G}_R^{\dagger} - \left[\hat{G}_R^{\dagger}\right]^{\dagger}\right]\hat{V}_{CR},\\
-i\hat{\Gamma}_R &= \hat{V}_{CR}^{\dagger}\left[\hat{G}_R - \left[\hat{G}_R\right]^{\dagger}\right]\hat{V}_{CR},\\
i\hat{\Gamma}_R &= \hat{V}_{CR}^{\dagger}\left[\hat{G}_R^{\dagger} - \hat{G}_R\right]\hat{V}_{CR},
\end{aligned}
\tag{2-85}
$$

replacing 2-85 in 2-84, we have:

$$
\begin{aligned}
i_{L\to R} &= -\frac{ie}{\hbar}\left(\langle\psi_{L,n}|\,\hat{V}_{LC}\hat{G}_C^{\dagger}\left[i\hat{\Gamma}_R\right]\hat{G}_C\hat{V}_{LC}^{\dagger}\,|\psi_{L,n}\rangle\right),\\
i_{L\to R} &= \frac{e}{\hbar}\left(\langle\psi_{L,n}|\,\hat{V}_{LC}\hat{G}_C^{\dagger}\hat{\Gamma}_R\hat{G}_C\hat{V}_{LC}^{\dagger}\,|\psi_{L,n}\rangle\right),
\end{aligned}
\tag{2-86}
$$

the above equation represents the electron current entering the device at an energy (E) and a mode n at the contact L through the coupling $\hat{V}_{CR}$.
Now all the modes n are added and considering that the levels are filled with electrons entering through the reservoir connected to the contact L (2 for spin),

$$
I_{L\to R} = \frac{2e}{\hbar}\int_{-\infty}^{\infty} f(E,\mu_L)\sum_n \delta(E-E_n)\,\langle\psi_{L,n}|\,\hat{V}_{LC}\hat{G}_C^{\dagger}\hat{\Gamma}_R\hat{G}_C\hat{V}_{LC}^{\dagger}\,|\psi_{L,n}\rangle\,dE,
$$

$$
I_{L\to R} = \frac{2e}{\hbar}\int_{-\infty}^{\infty} f(E,\mu_L)\sum_n \delta(E-E_n)\,\langle\psi_{L,n}|\,\hat{V}_{LC}\left(\sum_m |m\rangle\langle m|\right)\hat{G}_C^{\dagger}\hat{\Gamma}_R\hat{G}_C\hat{V}_{LC}^{\dagger}\,|\psi_{L,n}\rangle\,dE,
$$

$$
I_{L\to R} = \frac{2e}{\hbar}\int_{-\infty}^{\infty} f(E,\mu_L)\sum_{n,m} \delta(E-E_n)\,\langle\psi_{L,n}|\,\hat{V}_{LC}\,|m\rangle\langle m|\,\hat{G}_C^{\dagger}\hat{\Gamma}_R\hat{G}_C\hat{V}_{LC}^{\dagger}\,|\psi_{L,n}\rangle\,dE,
$$

$$
I_{L\to R} = \frac{2e}{\hbar}\int_{-\infty}^{\infty} f(E,\mu_L)\sum_{n,m} \langle m|\,\hat{G}_C^{\dagger}\hat{\Gamma}_R\hat{G}_C\hat{V}_{LC}^{\dagger}\delta(E-E_n)\,|\psi_{L,n}\rangle\langle\psi_{L,n}|\,\hat{V}_{LC}\,|m\rangle\,dE,
$$

$$
I_{L\to R} = \frac{2e}{\hbar}\int_{-\infty}^{\infty} f(E,\mu_L)\sum_{n,m} \langle m|\,\hat{G}_C^{\dagger}\hat{\Gamma}_R\hat{G}_C\hat{V}_{LC}^{\dagger}\left[\delta(E-E_n)\,|\psi_{L,n}\rangle\langle\psi_{L,n}|\right]\hat{V}_{LC}\,|m\rangle\,dE,
$$

$$
I_{L\to R} = \frac{2e}{\hbar}\int_{-\infty}^{\infty} f(E,\mu_L)\sum_{m} \langle m|\,\hat{G}_C^{\dagger}\hat{\Gamma}_R\hat{G}_C\hat{V}_{LC}^{\dagger}\left[\sum_n \delta(E-E_n)\,|\psi_{L,n}\rangle\langle\psi_{L,n}|\right]\hat{V}_{LC}\,|m\rangle\,dE,
\tag{2-87}
$$

taking into account the equations 2-68 and 2-71, the previous equation can be rewritten:

$$
I_{L\to R} = \frac{2e}{\hbar}\int_{-\infty}^{\infty} f(E,\mu_L)\sum_{m} \langle m|\,\hat{G}_C^{\dagger}\hat{\Gamma}_R\hat{G}_C\left[\frac{1}{2\pi}\hat{\Gamma}_L\right]|m\rangle\,dE,
$$

$$
I_{L\to R} = \frac{e}{\pi\hbar}\int_{-\infty}^{\infty} f(E,\mu_L)\sum_{m} \langle m|\,\hat{G}_C^{\dagger}\hat{\Gamma}_R\hat{G}_C\hat{\Gamma}_L\,|m\rangle\,dE,
$$

$$I_{L\to R} = \frac{e}{\pi\hbar}\int_{-\infty}^{\infty} f(E,\mu_L)\mathrm{Tr}\left(\hat{G}_C^{\dagger}\hat{\Gamma}_R\hat{G}_C\hat{\Gamma}_L\right)dE, \tag{2-88}$$

to know the total current that passes through the device, you must subtracted the currents when it is from the $L \to R$ contacts, and from the $R \to L$:

$$I = I_{L\to R} - I_{R\to L}, \tag{2-89}$$

$$I = \frac{2e}{\pi\hbar}\int_{-\infty}^{\infty} \{f(E,\mu_L) - f(E,\mu_R)\}\,\mathrm{Tr}\left(\hat{G}_C^{\dagger}\hat{\Gamma}_R\hat{G}_C\hat{\Gamma}_L\right)dE, \tag{2-90}$$

the trace of what is in parentheses is the transmission probability of the system, which is known as the Fischer-Lee relationship.

$$T(E) = \mathrm{Tr}\left(\hat{G}_C^{\dagger}\hat{\Gamma}_R\hat{G}_C\hat{\Gamma}_L\right), \tag{2-91}$$

with the above we can rewrite the equation 2-90 as:

$$I = \frac{2e}{\pi\hbar}\int_{-\infty}^{\infty} \{f(E,\mu_L) - f(E,\mu_R)\}\,T(E)dE, \tag{2-92}$$

this equation is known as the Landauer formula for tunnel current, which describes electronic current in terms of the difference in the population of contacts connected to the device and the probability of transmission through the system [5–8].

Landauer relation

To find this relationship, the expression 2-92 is taken into account, where the net current is presented as a function of the transmission probability, but it also shows the dependence of the difference between the carrier distribution functions of charge of the electrodes f_L and f_R, since, if the electrochemical potentials are equal, there will be no current flow because both contacts are at an equilibrium level $\bar{\mu}$. In the low-temperature limit ($k_BT \to 0$) $\bar{\mu} \to E_F$, with E_F being the Fermi equilibrium energy. When applying a small potential difference V (when considering small potential differences, reference is made to the limit when $eV \to 0$ and therefore $\mu_L - \mu_R \to 0$ of the form $\mu_L - \mu_R = e\Delta V$, remembering that $\mu_{R(L)} = E_F \pm eV/2$), changes are introduced in the transmission function and in the electrochemical potentials of the electrodes, thus the expression 2-92, can be written for small deviations from this equilibrium state, the current is proportional ti the applied bias [9]:

$$\delta I \approx \frac{2e}{h}\int_{-\infty}^{\infty} \{f(E,\mu_L) - f(E,\mu_R)\}\,\delta T(E)dE + \frac{2e}{h}\int_{-\infty}^{\infty} \delta\{f(E,\mu_L) - f(E,\mu_R)\}\,T(E)dE, \tag{2-93}$$

the first term is zero and the second can be expressed by seeing the variations around the electrochemical potentials of each electrode through a Taylor series. Thus the Fermi functions are written in the form:

$$\frac{1}{1+e^{\beta(E-\mu_L)}} \approx f_L(E)|_{\mu_L} + \partial_E f_L(E)|_{\mu_L}(E-\mu_L) + \mathcal{O}(\mu_L^2) + \cdots, \tag{2-94}$$

$$\frac{1}{1+e^{\beta(E-\mu_R)}} \approx f_R(E)|_{\mu_R} + \partial_E f_R(E)|_{\mu_R}(E-\mu_R) + \mathcal{O}(\mu_R^2) + \cdots, \tag{2-95}$$

where $\beta = 1/k_B T$, with k_B the Boltzmann constant. In the equation 2-110 shows how to write $\partial f/\partial\mu = -\partial f/\partial E$.

By evaluating the functions f_R and f_L in the electrochemical potentials it can be seen that they are equal, as are their derivatives, then the net current in the system can be written as the derivative of the Fermi function evaluated in the electrochemical equilibrium potential $\bar{\mu}$. This energy varies throughout the system, since one electrode fills the available states, while the other empties them. By assuming that the difference between μ_R and μ_L is not that great, we are considering that the difference between $\bar{\mu}$ and $\mu_{R(L)}$ is even smaller (see Fig. **2-3**), like this:

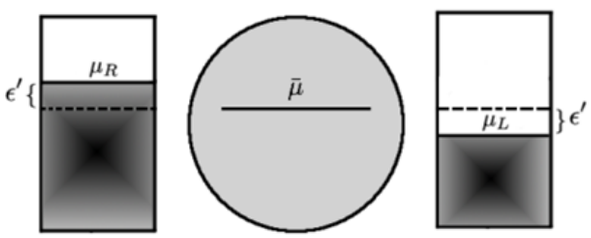

Figure **2-3**: Difference between the electrochemical potentials of the electrodes, compared to the equilibrium energy $\bar{\mu}$.

From Fig. **2-3** it can be deduced that:

$$\mu_L = \bar{\mu} - \varepsilon', \tag{2-96}$$

$$\mu_R = \bar{\mu} + \varepsilon', \tag{2-97}$$

by adding the two previous expressions, we obtain:

$$\bar{\mu} = \frac{\mu_R + \mu_L}{2} \tag{2-98}$$

with the previous expression you can rewrite the equation 2-93 in the following way:

$$I \approx \frac{2e}{h}\int_{-\infty}^{\infty}\left(-\frac{\partial f(E)}{\partial E}\bigg|_{\bar{\mu}}\right)(\mu_R-\mu_L)T(E)dE,$$

$$I \approx \frac{2e^2}{h}\Delta V\int_{-\infty}^{\infty}\left(-\frac{\partial f(E)}{\partial E}\bigg|_{\bar{\mu}}\right)T(E)dE, \tag{2-99}$$

where the term in the parentheses is known as the thermal broadening function (F_T), which when calculated around $E = \bar{\mu}$ has a very pronounced peak, and when calculating the area under the curve gives approximately one, behaving as a delta function, therefore, the result of the integral is the transmission probability evaluated around the equilibrium energy.

Taking the above into account in the equation 2-99 it is possible to determine the electrical conductance ($\mathcal{G}$) as a function of the transmission probability of the system ($T(E)$), thus:

$$\frac{I}{\Delta V} \equiv \mathcal{G} = \frac{2e^2}{h} T(E)|_{\bar{\mu}}. \tag{2-100}$$

The conductance is proportional to the transmission probability evaluated around the equilibrium energy, this is valid for the low-temperature limit ($k_B T \to 0$), in this expression the equilibrium energy $\bar{\mu}$ is the equilibrium energy at the Fermi level E_F. For the general case, for any temperature, the expression for $\mathcal{G}$ is of the following form:

$$\mathcal{G} = \frac{2e^2}{h} \int_{-\infty}^{\infty} \left(-\frac{\partial f(E)}{\partial E} \right) T(E) dE, \tag{2-101}$$

the previous expression is the well-known Landauer formula for the quantification of the conductance [5, 9, 10].

2.1.5 Transport at different temperatures

So far, we have studied the behavior of the electric current that passes through the system of the central region, which is connected to metallic contacts, but due to differences in the temperatures of the contacts, this electric current is always accompanied by a thermal current that constitutes the flow of energy through the system. The only case where thermal effects are not considered is when transport takes place in thermal equilibrium, the value of the thermal current is ignored. The thermal current arises from the temperature gradient induced by the electric current in the system, as described by the following relation, where the resulting voltage is given by:

$$\Delta V = \frac{I}{\mathcal{G}} + S\Delta T, \tag{2-102}$$

the previous expression is the most general way of writing Ohm's law, the first term is due to the electrical part, and the second term is due to the thermal part, where S is the Seebeck coefficient. On the other hand, the heat current I_Q is found from the heat conduction law as:

$$I_Q = k\Delta T, \tag{2-103}$$

where k is the heat conductance or thermal conductance. Similar to Ohm's law, it is possible to write a general form for the law of heat conduction:

$$I_Q = k\Delta T + \Pi I, \tag{2-104}$$

where Π is the Peltier coefficient.

From the expressions 2-102, and 2-104 the following things can be inferred: *i*. a temperature difference can induce currents or voltages, for the special case where the electric current is zero, the Seebeck coefficient induces a potential difference ($\Delta V = -S\Delta T$). *ii*. If there is no temperature difference, there can still be a heat flow ($I_Q = \Pi I$)

Seebeck Effect or Thermopower

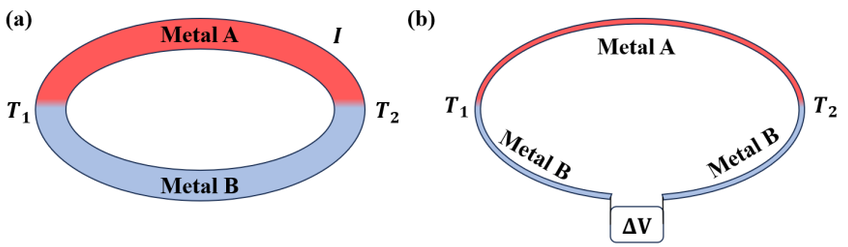

Figure **2-4**: (a) Seebeck effect in a closed circuit where metal A and metal B are different, and T_1 and T_2 are the junctions temperatures, with ($T1 > T2$). When current (I) flows clockwise through metal A, the differential Seebeck coefficient is positive. (b) Seebeck effect in an open circuit, where voltage (ΔV) is obtained between the two open ends of the circuit.

When there is a union between two materials, generally metals, and both are at different temperatures, the temperature gradient induces a potential difference, this is known as the Seebeck effect, it was first reported by Tomas Seebeck in 1821, when he saw that a compass needle reacted when approaching a closed circuit constructed of two different metals with a temperature difference between the junctions. In the closed circuit of figure **2-4** (a), the charge carriers, whether electrons or holes, diffuse from the hot side to the cold side due to a temperature difference, leaving behind their immobile nuclei with an opposite charge on the hot side, giving rise to a thermoelectric voltage.

There are two different methods of causing charge transport by the Seebeck effect, one is by the temperature gradient between the junction of the two metals, and the second is by the potential gradient induced by that same temperature gradient. To understand how the mechanism of the Seebeck effect works, we will study how the transport induced by a short-circuit temperature gradient works: the chemical potential is constant throughout the entire material, or a zero potential difference.

Short circuit condition

Under short circuit conditions (see Fig. **2-4**), having a temperature gradient at a junction of two materials induces a gradient in the charge carrier occupancy statistics; As the difference in temperatures increases, the carrier distribution function broadens around the chemical potential. The material with the highest temperature weighs more electrons occupying states with higher energies, and few in lower states. This causes a force that moves the electrons from the hot end of the material (high energy states) to the cold end (low energy states). This image is confirmed by the expressions derived from Landauer's theory.

In the last section to know the electrical conductance, the difference of the Fermi-Dirac functions was evaluated in the electric current (equation 2-92), around the equilibrium energy ($\bar{\mu} \approx E_F$), but now an equilibrium temperature (T_0) is also considered, knowing that the contact temperatures are T_L and T_R:

$$\partial_{\mu,T}(f_L(E,\mu_L,T_L) - f_R(E,\mu_R,T_R)) \approx \left(\frac{\partial f(E)}{\partial \mu}\right)_{\bar{\mu},T_0} (\Delta\mu) + \left(\frac{\partial f(E)}{\partial T}\right)_{\bar{\mu},T_0} (\Delta T), \quad (2\text{-}105)$$

however, in this case, it is much more convenient to express the derivative of the function f concerning the energy, E, instead of the temperature, T and $\bar{\mu}$, for that rewriting the Fermi-Dirac function as:

$$f(x) = \frac{1}{1+e^x}; \qquad x = \frac{E-\mu}{k_B T}, \quad (2\text{-}106)$$

now we perform the derivatives with respect to E, μ, and T:

$$\frac{\partial f}{\partial \mu} = \frac{\partial f}{\partial x}\frac{\partial x}{\partial \mu} = \frac{\partial f}{\partial x}\left[-\frac{1}{k_B T}\right], \quad (2\text{-}107)$$

$$\frac{\partial f}{\partial E} = \frac{\partial f}{\partial x}\frac{\partial x}{\partial E} = \frac{\partial f}{\partial x}\left[\frac{1}{k_B T}\right], \quad (2\text{-}108)$$

$$\frac{\partial f}{\partial T} = \frac{\partial f}{\partial x}\frac{\partial x}{\partial T} = \frac{\partial f}{\partial x}\left[-\frac{(E-\mu)}{T}\frac{1}{k_B T}\right], \quad (2\text{-}109)$$

from the previous expressions the following conclusions can be reached:

$$\frac{\partial f}{\partial \mu} = -\frac{\partial f}{\partial E}, \quad (2\text{-}110)$$

$$\frac{\partial f}{\partial T} = \left(-\frac{\partial f}{\partial E}\right)\frac{(E-\mu)}{T}. \quad (2\text{-}111)$$

Substituting into the equation 2-105, we have:

$$\partial_{\mu,T}(f_L(E,\mu_L,T_L) - f_R(E,\mu_R,T_R)) \approx \left(-\frac{\partial f(E)}{\partial E}\right)_{\bar{\mu},T_0}(\Delta\mu) + \left(-\frac{\partial f(E)}{\partial E}\right)_{\bar{\mu},T_0}\frac{E-\bar{\mu}}{T_0}(\Delta T),$$

$$\partial_{\mu,T}(f_L(E,\mu_L,T_L) - f_R(E,\mu_R,T_R)) \approx \left(-\frac{\partial f(E)}{\partial E}\right)_{\bar{\mu},T_0}\left[(\Delta\mu) + \frac{E-\bar{\mu}}{T_0}(\Delta T)\right]. \quad (2\text{-}112)$$

Replacing the current, we have the following expression:

$$I \approx \frac{2e}{h}\int_{-\infty}^{\infty}\left(-\frac{\partial f(E)}{\partial E}\bigg|_{\bar{\mu},T_0}\right)\left[(\Delta\mu) + \frac{E-\bar{\mu}}{T_0}(\Delta T)\right]T(E)dE. \quad (2\text{-}113)$$

For low voltages, the current can be written depending on a potential difference and a temperature difference:

$$I = \mathcal{G}\Delta V + \nu\Delta T, \quad (2\text{-}114)$$

Comparing both expressions for the current, the first term is the electrical conductance, and the second term is related to when there is a temperature gradient, and there is an expression analogous to Ohm's Law, but which relates the current to the temperature gradient, and has the following form:

$$I_{\Delta T} = \nu\Delta T, \quad (2\text{-}115)$$

we have that ν is equal to:

$$\nu = \frac{2e}{h}\int_{-\infty}^{\infty}T(E)\left(\frac{E-\bar{\mu}}{T_0}\right)\left(-\frac{\partial f(E)}{\partial E}\right)dE, \quad (2\text{-}116)$$

the parameter ν is an intensive property that determines the response of the current in a temperature gradient.

Open circuit condition

In the case of an open circuit, as represented in Fig. **2-4** (b), the effects suffered by the current caused by a temperature gradient and a potential difference are taken into account (see equation 2-114). These induced current are additive, which are called diffusion and drag currents, respectively. An experimental measure of the Seebeck coefficient is made under open circuit conditions, which means that the net current is zero ($I = 0$), as mentioned earlier, therefore, it is given by the quotient of the voltage difference and the difference of temperature:

$$\Delta V_{OC} = -\frac{I_{\Delta T}}{\mathcal{G}} = -\frac{\nu}{\mathcal{G}}\Delta T = -S\Delta T, \quad (2\text{-}117)$$

when $T_L > T_R$, it says that the V_{OC} is negative, this means that the contact with the highest temperature has a negative electron voltage. By convention, this is defined as a negative Seebeck coefficient.

From the equation 2-117 the Seebeck coefficient can be defined as:

$$S = -\frac{\nu}{\mathcal{G}} = -\left(\frac{1}{eT_0}\right)\frac{\int_{-\infty}^{\infty} T(E)\,(E-\bar{\mu})\left(-\frac{\partial f(E)}{\partial E}\right)dE}{\int_{-\infty}^{\infty}\left(-\frac{\partial f(E)}{\partial E}\right)T(E)dE}, \tag{2-118}$$

Heat Current

Now we will study the currents due to temperature in the system studied. Consider a small energy range located above or below the electrochemical potentials μ_L and μ_R. These two channels will make contributions with opposite signs to the Seebeck effect. Figure **2-5** shows the heat absorbed from the environment for the following conditions. 1 By the time the power is above, the heat absorbed is negative at the source and positive at the drain, indicating that the drain cools and the source heats up. 2 When it is below, the opposite happens. The above is what is known as the Peltier effect, which is the practical principle of thermoelectric refrigerators. Note that the signs of both the Peltier and Seebeck coefficients depend on the sign of $(E-\mu)$ and not to the sign of the charge q.

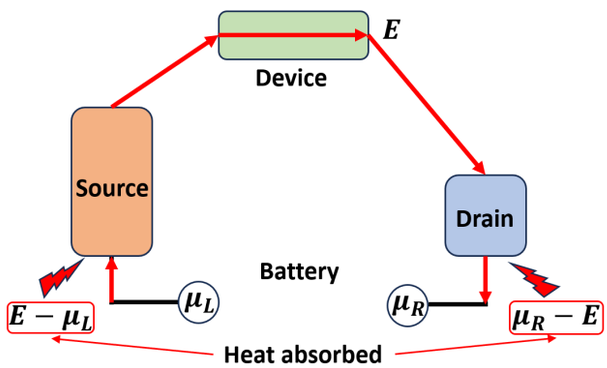

Figure **2-5**: Heat absorbed in each contact.

To write the heat current carried by the electrons in the system shown in Fig. **2-5**, we can extend what was done previously for the current in equation 2-92. Given that an electron with energy E with a charge $-e$ extracts an energy $E-\mu_L$ from the source and pours an energy $E-\mu_R$ into the drain, with this in mind, one can write the heat currents I_{Q_L} (extracted from the source) and I_{Q_R} (extracted from the drain) respectively:

$$I_{Q_L} = \frac{2e}{\pi\hbar}\int_{-\infty}^{\infty}\{f(E,\mu_L) - f(E,\mu_R)\}\left(\frac{E-\mu_L}{e}\right)T(E)dE, \tag{2-119}$$

$$I_{Q_R} = \frac{2e}{\pi\hbar}\int_{-\infty}^{\infty}\{f(E,\mu_L) - f(E,\mu_R)\}\left(\frac{\mu_R - E}{e}\right)T(E)dE. \tag{2-120}$$

The heat current for the source and drain has already been written, but an expression can also be written for the external source (battery) per unit of time, which is given by:

$$I_E = \Delta V I = \frac{2e}{\pi\hbar}\int_{-\infty}^{\infty}\{f(E,\mu_L) - f(E,\mu_R)\}\left(\frac{\mu_L - \mu_L}{e}\right)T(E)dE. \tag{2-121}$$

By general conservation of energy, the sum of the currents found must be equal to zero, therefore:

$$I_{Q_L} + I_{Q_R} + I_E = 0. \tag{2-122}$$

When small voltage conditions are taken into account, that is, $\mu_L \approx \mu_R$, and equilibrium temperature T_0, this causes the electrons flowing from the contact L to the contact R, to take an amount of heat from the source that is $(E-\bar{\mu})/e$ and pour it into the drain. The above assumes that the heat current (I_Q) that flows from the source to the drain is:

$$I_Q \approx \frac{2e}{h}\int_{-\infty}^{\infty}\left(\frac{E-\bar{\mu}}{e}\right)\left(-\frac{\partial f(E)}{\partial E}\bigg|_{\bar{\mu},T_0}\right)\left[(\Delta\mu) + \frac{E-\bar{\mu}}{T_0}(\Delta T)\right]T(E)dE. \tag{2-123}$$

The heat current (I_Q) can also be written in terms of a potential difference and a temperature difference:

$$I_Q = G_P\Delta V + G_Q\Delta T, \tag{2-124}$$

comparing both expressions, we have:

$$G_P = \frac{2e}{h}\int_{-\infty}^{\infty}(E-\bar{\mu})\left(-\frac{\partial f(E)}{\partial E}\right)T(E)dE, \tag{2-125}$$

$$G_Q = \frac{2}{T_0 h}\int_{-\infty}^{\infty}(E-\bar{\mu})^2\left(-\frac{\partial f(E)}{\partial E}\right)T(E)dE. \tag{2-126}$$

These two expressions, along with $\mathcal{G}$ and ν, are standard for thermoelectric coefficients due to electrons. We have that G_Q is the heat conductance under electrical short circuit conditions ($V=0$), and κ is thermal conductance under open electrical circuit conditions ($I=0$):

$$G_Q = \left(\frac{\partial I_Q}{\partial\Delta T}\right)_{V_L=V_R}, \qquad \kappa = \left(\frac{\partial I_Q}{\partial\Delta T}\right)_{I=0},$$

to find an expression for κ, we solve for the voltage difference from the equation 2-114, and substitute it into the equation 2-124:

$$\Delta V = \frac{I}{\mathcal{G}} + \left(-\frac{\nu}{\mathcal{G}}\right)\Delta T,$$

$$I_Q = G_P\left(\frac{I}{\mathcal{G}} - \frac{\nu}{\mathcal{G}}\Delta T\right) + G_Q\Delta T,$$

$$I_Q = \frac{G_P}{\mathcal{G}}I + \left(G_Q - \frac{G_P\nu}{\mathcal{G}}\right)\Delta T, \tag{2-127}$$

the term that multiplies I is the Peltier coefficient, Π, and the term that multiplies ΔT is the thermal conductance, κ:

$$\kappa = G_Q - \frac{G_P\nu}{\mathcal{G}} \tag{2-128}$$

$$\kappa = \frac{2}{T_0 h}\left[\int_{-\infty}^{\infty}(E-\bar{\mu})^2\left(-\frac{\partial f(E)}{\partial E}\right)T(E)dE - \frac{\left(\int_{-\infty}^{\infty}(E-\bar{\mu})\left(-\frac{\partial f(E)}{\partial E}\right)T(E)dE\right)^2}{\int_{-\infty}^{\infty}\left(-\frac{\partial f(E)}{\partial E}\right)T(E)dE}\right]. \tag{2-129}$$

At this point we can define the following quantity:

$$\mathcal{L}_n = -\int_{-\infty}^{\infty}\left(-\frac{\partial f(E)}{\partial E}\right)(E-E_F)^n T(E)dE, \tag{2-130}$$

The above expression is known as the Landauer integral, for when $\bar{\mu} = E_F$. With that in mind, we can rewrite the electrical conductance, the Seebeck coefficient, and the thermal conductance:

$$\mathcal{G} = \frac{2e^2}{h}\mathcal{L}_0, \tag{2-131}$$

$$S = -\frac{1}{eT_0}\frac{\mathcal{L}_1}{\mathcal{L}_0}, \tag{2-132}$$

$$\kappa = \frac{2}{hT_0}\left(\mathcal{L}_2 - \frac{\mathcal{L}_1^2}{\mathcal{L}_0}\right). \tag{2-133}$$

Figures of Merit or ZT

Thermoelectric effects are significant due to their ability to convert waste heat into electricity. From this perspective, what matters is the amount of electrical energy that can be generated from a temperature difference ΔT. This temperature difference is critical in determining the efficiency and performance of thermoelectric devices in converting heat into useful electrical energy. The electrical power is maximized when the internal resistance (R_{int}) of the device is equal to the external resistance R_L, therefore we can write the maximum power in the following way:

$$P_{Max} = \frac{V_{OC}^2}{4R_L} = S^2\mathcal{G}\frac{\Delta T^2}{4}. \tag{2-134}$$

For the systems studied, in addition to having a potential difference, there is also a temperature difference in the contacts, when the contacts are at different temperatures, we expect

a constant flow of heat through the conductor due to its thermal conductance which has to be supplied by the source that maintains the temperature difference ($G_\kappa \Delta T$). Then the maximum power generated can be related to the power supplied by the external source:

$$\frac{P_{Max}}{G_\kappa \Delta T} = \frac{S^2 \mathcal{G} T}{G_\kappa} \frac{\Delta T}{4T}. \tag{2-135}$$

where T is the average temperature $(T_L + T_R)/2$. The figure of merit or ZT for thermoelectric materials is proportional to the relationship between $S^2\mathcal{G}$ to G_κ.

$$ZT = \frac{S^2 \mathcal{G} T}{G_\kappa}, \tag{2-136}$$

where G_κ is the total thermal conductivity, which includes the contributions of charge carriers (electrons or holes) (κ), electron-hole pairs (bipolar) (κ_{bp}) and phonons (κ_{ph}) and is defined as $G_\kappa = \kappa + \kappa_{bp} + \kappa_{ph}$. In this study only the electronic contribution κ will be taken into account, therefore:

$$ZT = \frac{S^2 \mathcal{G} T}{\kappa} = \frac{\mathcal{L}_1^2}{\mathcal{L}_0 \mathcal{L}_2 - \mathcal{L}_1^2}, \tag{2-137}$$

from the previous expression, the higher the figure of merit, the better the efficiency of the device in converting thermal energy to electrical energy. Therefore, there is great interest in improving the ZT in thermoelectric materials [3, 11–16].

The formulation for thermoelectric properties was presented from equations 2-116 and 2-125. The first represents how a temperature gradient generates an electric current; the second represents the thermoelectric coefficient, which relates heat flow to an applied electric potential difference. These two thermoelectric coefficients have a fundamental connection between the irreversible processes of physical phenomena.

It is worth emphasizing that the expressions obtained for the electric current I and the heat current I_Q, given by Eqs. 2-114 and 2-124, are consistent with the linear irreversible thermodynamics framework formulated by Lars Onsager in 1931 [29, 30]. In this formalism, thermodynamic fluxes (e.g., electric or heat currents) are linearly related to their conjugate driving forces (such as gradients of electrochemical potential and temperature) via a matrix of transport coefficients:

$$\begin{pmatrix} I \\ I_Q \end{pmatrix} = \begin{pmatrix} G & \nu \\ G_P & G_Q \end{pmatrix} \begin{pmatrix} \Delta V \\ \Delta T \end{pmatrix} \tag{2-138}$$

This corresponds to Onsager's general form:

$$\begin{pmatrix} J_1 \\ J_2 \end{pmatrix} = \begin{pmatrix} L_{11} & L_{12} \\ L_{21} & L_{22} \end{pmatrix} \begin{pmatrix} X_1 \\ X_2 \end{pmatrix} \tag{2-139}$$

where J_1 and J_2 are generalized fluxes and X_1, X_2 their conjugate thermodynamic forces. The Onsager reciprocity relation, $L_{12} = L_{21}$, follows from the microscopic reversibility of near-equilibrium processes. In the context of thermoelectric transport, this reciprocity leads to the well-known Kelvin relation [31]:

$$\Pi = TS \tag{2-140}$$

This confirms that the Seebeck and Peltier coefficients are not independent but are thermodynamically linked. Therefore, the coefficients ν and G_P derived in this work can be interpreted as Onsager cross-coefficients L_{12} and L_{21}, validating the consistency of the thermoelectric model used.

2.2 Optical properties in semiconductor heterostructures

2.2.1 Effective mass theory

The theory of effective mass is fundamental for studying semiconductor heterostructures, which describes how charge carriers (electrons and holes) interact in a crystalline solid. This technique adequately models the behavior of charge carriers in a crystalline lattice, that is, the electron or hole behaves as if it had a different mass than the one it presents in the free state, and this mass implicitly contains the effects that the system has on the charge carrier. By taking this into account, theoretical calculations to study the electronic and optical properties, among others, of semiconductor heterostructures are simplified. A fundamental method to calculate the effective mass is through the dispersion relationship $E-\vec{k}$ (energy vs wavenumber), and this relationship is constructed, in many cases, through approximations of the dynamics of electrons (or holes) in a crystalline lattice. This theory's strength lies in comparing the theoretical values of the effective mass with values obtained with experimental techniques, where they have been reported for different materials [17–20].

To represent the effective mass, we can describe the electrons as wave packets using Wannier functions:

$$\phi(\vec{r}) = \sum_k a_k e^{i\vec{k}\cdot\vec{r}} u_k(\vec{r}), \tag{2-141}$$

In the above expression, a_k are coefficients, $\vec{k}$ is the wave vector, $\vec{r}$ is the position and $u_k(\vec{r})$ is a periodic Bloch function with the same periodicity as the crystal lattice.

If an external force $\vec{F}$ is applied, which does the following work on the wave packet:

$$dE = \vec{v}_g \cdot \vec{F} dt, \tag{2-142}$$

where $\vec{v}_g$ is the velocity of the group and E is the energy of a particle in the system. Deriving the above equation using the chain rule, it is possible to rewrite it as:

$$\nabla E \cdot \frac{d\vec{k}}{dt} = \vec{v}_g \cdot \vec{F}, \tag{2-143}$$

$$\nabla E \cdot \frac{d\vec{k}}{dt} = \vec{v}_g \cdot \left(\hbar \frac{d\vec{k}}{dt} \right), \tag{2-144}$$

in the above expression we use the quantum mechanical relationship between momentum and wave vector $\vec{F} = d\vec{p}/dt = \hbar d\vec{k}/dt$. Solving for $\vec{v}_g$, we have:

$$\vec{v}_g = \frac{1}{\hbar} \nabla_k E, \tag{2-145}$$

where the energy gradient is calculated with respect to the vector space of the wave vector. Now let's consider the general definition of the acceleration $\vec{a} = d\vec{v}_g/dt$, it can be written:

$$\vec{a} = \frac{1}{\hbar}\frac{\partial}{\partial k_i}\left(\vec{F}\nabla_k E\right)\frac{1}{\hbar}\frac{\partial}{\partial k_i}\sum_j F_j\frac{\partial E}{\partial k_j} = \frac{1}{\hbar^2}\sum_j F_j\frac{\partial^2 E}{\partial k_i \partial k_j}, \tag{2-146}$$

with the previous expression it is possible to write the effective mass in a matrix and can be introduced by the tensor relationship:

$$\begin{bmatrix} a_1 \\ a_2 \\ a_3 \end{bmatrix} = \begin{bmatrix} m_{11}^{*-1} & m_{12}^{*-1} & m_{13}^{*-1} \\ m_{21}^{*-1} & m_{22}^{*-1} & m_{23}^{*-1} \\ m_{31}^{*-1} & m_{32}^{*-1} & m_{33}^{*-1} \end{bmatrix} \begin{bmatrix} F_1 \\ F_2 \\ F_3 \end{bmatrix}, \tag{2-147}$$

we can also represent the equation (2-147) by its component form:

$$a_i = \sum_j m_{ij}^{*-1} F_j, \tag{2-148}$$

now we can compare equations (2-148) and (2-146) therefore, we obtain::

$$m_{ij}^{*-1} = \frac{1}{\hbar^2}\frac{\partial^2 E}{\partial k_i \partial k_j}. \tag{2-149}$$

The objective of this work is to study isotropic systems, which implies that the scalar part can define the effective mass:

$$m^* = \hbar^2\left(\frac{\partial^2 E_k}{\partial k^2}\right)^{-1}. \tag{2-150}$$

Considering the conduction band, the Kane model gives us the parabolic dispersion relation of the form:

$$E \approx E_g + \frac{\hbar^2 k^2}{2m_0} + \frac{\hbar^2 k^2 |P|^2}{E_g}, \tag{2-151}$$

where E_g is the energy gap between the valence and conduction band, m_0 is the mass of the free electron, and $|P|$ is the matrix element of the momentum operator in absolute value. With the equations 2-150 and 2-151 it is possible to find the relationship between the masses of free electrons and the effective mass, which is given by:

$$\frac{m^*}{m_0} = \frac{1}{1 + \frac{2|P|^2 m_0}{E_g}}, \tag{2-152}$$

in the previous expression, $2|P|^2 m_0$ takes a value of approximately 20 meV for many semiconductors. However, for a specific semiconductor, it is possible to calculate it using the nearly free electron model [21, 22].

2.2.2 Electromagnetic field in the effective mass theory

When considering the effect of an external magnetic and electric field on a semiconductor heterostructure under the effective mass approximation, it is necessary to rewrite the Schrödinger equation. For the magnetic field, it is adding the vector potential to the moment operator term, which the Coulomb Gauge gives [23, 24]. The application of an electric field generates changes in the structural potential in which charge carriers are confined in the structure, resulting in the generation of new allowed energy levels due to the Stark effect. For this work, the structure to be studied is formed by a spherical quantum dot, so the electric (F_z) and magnetic field will be applied perpendicular to the xy plane, that is, in the $-z$ direction, so for $\vec{B} = B\hat{k}$, which implies that the vector potential can be defined as $\vec{A}_m = \frac{B}{2}\left(-y\hat{i} + x\hat{j}\right)$, where B is the magnitude of the applied magnetic field. In this case, the Schrödinger equation in Cartesian coordinates for an electron confined in a quantum dot can be written as:

$$\left[\frac{1}{2m^*}\left(\hat{p} + q\hat{A}_m\right)^2 + V(x, y.z) + qF_z z\right]\psi_n(x, y, z) = E_n\psi_n(x, y, z), \tag{2-153}$$

where m^* is the effective mass, q is the absolute value of the electron charge, $V(x, y, z)$ the confining potential, and F_z the magnitude of the external electric field. Solving first the square term, then we have:

$$\left(\hat{p} + q\vec{A}_m\right)^2 = \left(\hat{p} + q\vec{A}_m\right)\cdot\left(\hat{p} + q\vec{A}_m\right) = \left(\hat{p}^2 + q\hat{p}\cdot\vec{A}_m + q\vec{A}_m\cdot\hat{p} + q^2A_m^2\right), \tag{2-154}$$

replacing $\hat{p} = -i\hbar\vec{\nabla}$:

$$\begin{aligned}\left(\hat{p} + q\vec{A}_m\right)^2 &= \left((-i\hbar\nabla)^2 + q\left(-i\hbar\vec{\nabla}\right)\cdot\vec{A}_m + q\vec{A}_m\cdot\left(-i\hbar\vec{\nabla}\right) + q^2A_m^2\right)\\ &= \left(-\hbar^2\nabla^2 - iq\hbar\vec{\nabla}\cdot\vec{A}_m - iq\vec{A}_m\cdot\vec{\nabla} + q^2A_m^2\right),\end{aligned} \tag{2-155}$$

To prove that $\vec{\nabla}\cdot\vec{A}_m = \vec{A}_m\cdot\vec{\nabla}$, we have:

$$\begin{aligned}
\vec{\nabla}\cdot\left(\vec{A}_m\right)\psi(x,y,z) &= \left(\frac{\partial}{\partial x}\hat{i}+\frac{\partial}{\partial y}\hat{j}\right)\cdot\left[\frac{B}{2}\left(-y\hat{i}+x\hat{j}\right)\right]\psi(x,y,z)\\
&= -\frac{B}{2}\,y\,\frac{\partial\psi(x,y,z)}{\partial x}+\frac{B}{2}\,x\,\frac{\partial\psi(x,y,z)}{\partial y}\\
&= \frac{B}{2}\left(-y\,\frac{\partial\psi(x,y,z)}{\partial x}+x\,\frac{\partial\psi(x,y,z)}{\partial y}\right)\\
&= \frac{B}{2}\left(-y\,\hat{i}+x\,\hat{j}\right)\cdot\left(\frac{\partial\psi(x,y,z)}{\partial x}\hat{i}+\frac{\partial\psi(x,y,z)}{\partial y}\right)\\
&= \frac{B}{2}\left(-y\hat{i}+x\hat{j}\right)\cdot\left(\frac{\partial}{\partial x}\hat{i}+\frac{\partial}{\partial y}\hat{j}\right)\psi(x,y,z)\\
&= \vec{A}_m\cdot\vec{\nabla}\psi(x,y,z),
\end{aligned} \tag{2-156}$$

substituting into the previous expression, we have:

$$\left(\hat{p}+q\vec{A}_m\right)^2 = \left(-\hbar^2\nabla^2-2iq\hbar\vec{\nabla}\cdot\vec{A}_m+q^2A_m^2\right), \tag{2-157}$$

replacing the expression 2-157 into the equation 2-155

$$\left[\frac{1}{2m^*}\left(-\hbar^2\nabla^2-2iq\hbar\vec{\nabla}\cdot\vec{A}_m+q^2A_m^2\right)+V(x,y,z)+qF_zz\right]\psi_n(x,y,z)=E_n\psi_n(x,y,z), \tag{2-158}$$

if we preserve the azimuthal symmetry of the system, it is possible to propose in cylindrical coordinates a solution of the type $\psi(x,y,z)=\psi(r,\varphi,z)=R(r,z)\,e^{i\,m\,\varphi}$, where m is the principal quantum number. Consequently, the function $R(r,z)$ satisfies the differential equation, and substituting $\vec{A}_m=\frac{B}{2}\left(-y\hat{i}+x\hat{j}\right)=Br\hat{\varphi}/2$ into (2-158), we find that:

$$\begin{aligned}
&\left[\frac{1}{2m^*}\left(-\hbar^2\left(\frac{1}{r}\frac{\partial}{\partial r}\left(r\frac{\partial}{\partial r}\right)+\frac{1}{r^2}\frac{\partial^2}{\partial\varphi^2}+\frac{\partial^2}{\partial z^2}\right)-2iq\hbar\left(\frac{\partial}{\partial r}\hat{r}+\frac{1}{r}\frac{\partial}{\partial\varphi}\hat{\varphi}+\frac{\partial}{\partial z}\hat{z}\right)\cdot\left(\frac{B}{2}r\hat{\varphi}\right)\right.\right.\\
&\left.\left.+q^2\left(\frac{B^2r^2}{4}\right)\right)+V(r,z)+qF_zz\right]R_n(r,z)e^{i\,m\,\varphi}=E_nR_n(r,z)e^{i\,m\,\varphi},
\end{aligned}$$

$$\begin{aligned}
&\left[\frac{1}{2m^*}\left(-\hbar^2\left(\frac{1}{r}\frac{\partial}{\partial r}\left(r\frac{\partial}{\partial r}\right)+\frac{\partial^2}{\partial z^2}\right)e^{i\,m\,\varphi}-\frac{\hbar^2}{r^2}\frac{\partial^2}{\partial\varphi^2}e^{i\,m\,\varphi}-\frac{2iq\hbar B}{2}\frac{\partial}{\partial\varphi}e^{i\,m\,\varphi}\right.\right.\\
&\left.\left.+\frac{q^2B^2r^2}{4}e^{i\,m\,\varphi}\right)+V(r,z)e^{i\,m\,\varphi}+qF_zze^{i\,m\,\varphi}\right]R_n(r,z)=E_nR_n(r,z)e^{i\,m\,\varphi},
\end{aligned}$$

$$\begin{aligned}
&\left[\frac{1}{2m^*}\left(-\hbar^2\left(\frac{1}{r}\frac{\partial}{\partial r}\left(r\frac{\partial}{\partial r}\right)+\frac{\partial^2}{\partial z^2}\right)+\frac{m^2\hbar^2}{r^2}-\frac{2q\hbar mB}{2}\right.\right.\\
&\left.\left.+\frac{q^2B^2r^2}{4}\right)+V(r,z)+qF_zz\right]R_n(r,z)e^{i\,m\,\varphi}=E_nR_n(r,z)e^{i\,m\,\varphi},
\end{aligned}$$

Finally, the expression to the Schrödinger equation looks like this:

$$\left[-\frac{\hbar^2}{2m^*}\nabla^2_{r,z}+\frac{m^2\hbar^2}{2m^*r^2}-\frac{q\hbar mB}{2m^*}+\frac{q^2B^2r^2}{8m^*}+V(r,z)-qF_zz\right]R_n(r,z)=E_nR_n(r,z), \tag{2-159}$$

2.2.3 Optical absorption theory

To study the optical response (linear and nonlinear) of low-dimensional systems with discrete energy spectrum, and continuous states that are associated with subbands corresponding to free motions with effective mass along one or two dimensions. An example of these systems is quantum heterostructures, where there is a completely discrete energy spectrum. The first to develop this theory were Rosencher and Bois [25] and Ahn and Chuang [26] in the 1960s. In the following section, the development to obtain the absorption coefficients and the change in the refractive index coefficient will be presented in the first and third order for a quantum well. However, the scheme extends directly to wires, rings, and quantum dots.

Density Matrix Equations

To begin studying the optical response, we will first consider the system in the presence of optical radiation with a frequency ω with polarization along the z-axis. The system is characterized by an unperturbed Hamiltonian, $\hat{H}_0$, the density matrix, $\hat{\rho}$, and the electric dipole operator and the electric field intensity of the optical radiation, $\hat{M}$ and $E(t)$ [22,25,26]. Considering the above quantities, the density matrix equation for an electron with intraband relaxation can be written as:

$$\frac{\partial\hat{\rho}}{\partial t}=\frac{1}{i\hbar}\left[\hat{H}_0-\hat{M}\,E(t),\rho\right]-\frac{1}{2}\left[\hat{\gamma}(\hat{\rho}-\hat{\rho}^{(0)})+(\hat{\rho}-\hat{\rho}^{(0)})\hat{\gamma}\right], \tag{2-160}$$

where $\hat{\rho}^{(0)}$ is the unperturbed density matrix and $\hat{\gamma}$ is a phenomenological damping operator due to electron-phonon, electron-electron, and other interactions. To simplify the analysis, only two-level systems ($|1\rangle$, $|2\rangle$) will be analyzed. The incident monochromatic field is defined as:

$$E(t)=\Re(E_0\,e^{-i\omega t})=\frac{1}{2}E_0\,e^{-i\omega t}+\frac{1}{2}E_0\,e^{i\omega t}=\tilde{E}\,e^{-i\omega t}+\tilde{E}\,e^{i\omega t}, \tag{2-161}$$

We assume that $\hat{\gamma}$ is a diagonal matrix and its element $\hat{\gamma}_{mm}$ is the inverse of the relaxation time for the state $|m\rangle$, and the element of the diagonal are given by:

$$\langle 1|\hat{\gamma}|1\rangle=\gamma_{11}=\frac{1}{\tau_1},\qquad\qquad \langle 2|\hat{\gamma}|2\rangle=\gamma_{22}=\frac{1}{\tau_2}. \tag{2-162}$$

The equation 2-160 can be solved by a perturbative series of $\hat{\rho}$ as:

$$\hat{\rho}(t)=\sum_n\hat{\rho}^{(n)}(t), \tag{2-163}$$

Under conditions of thermal equilibrium, $\hat{\rho}^{(}0)$ is a diagonal matrix, and its diagonal elements are the surface thermal population given by: $\hat{\rho}_{11}^{(n)} = \langle 1|\hat{\rho}|1\rangle$, $\hat{\rho}_{12}^{(n)} = \langle 1|\hat{\rho}|2\rangle$, $\hat{\rho}_{21}^{(n)} = \langle 2|\hat{\rho}|1\rangle$, and $\hat{\rho}_{22}^{(n)} = \langle 2|\hat{\rho}|2\rangle$. $\hat{\rho}$ has the property of hermiticity, which implies $\rho_{12}(t) = \rho_{12}^{*}(t)$.

Now replace equation (2-163) into equation (2-160):

$$\begin{aligned}\sum_n \frac{\partial\hat{\rho}}{\partial t} =& \frac{1}{i\hbar}\sum_n \left[(\hat{H}_0 - \hat{M}\,E(t))\hat{\rho}^{(n)} - \hat{\rho}^{(n)}(\hat{H}_0 - \hat{M}\,E(t))\right] \\ &- \frac{1}{2}\sum_n \left[\hat{\gamma}(\hat{\rho}^{(n)} - \hat{\rho}^{(n)}) + (\hat{\rho}^{(n)} - \hat{\rho}^{(n)})\hat{\gamma}\right],\end{aligned} \tag{2-164}$$

From the previous equation of the second term, the sum is distributed, and the expression $\sum_n(\hat{\rho}^{(n)} - \hat{\rho}^{(0)})$ can be rewritten like $\sum_n \hat{\rho}^{(n+1)}$. Substituting into the equation 2-164, we have:

$$\begin{aligned}\sum_n \frac{\partial\hat{\rho}}{\partial t} =& \frac{1}{i\hbar}\sum_n \left[(\hat{H}_0 - \hat{M}\,E(t))\hat{\rho}^{(n)} - \hat{\rho}^{(n)}(\hat{H}_0 - \hat{M}\,E(t))\right] \\ &- \frac{1}{2}\left[\hat{\gamma}\left(\sum_n \hat{\rho}^{(n+1)}\right) + \left(\sum_n \hat{\rho}^{(n+1)}\right)\hat{\gamma}\right],\end{aligned} \tag{2-165}$$

Now $\langle 1|\frac{\partial\hat{\rho}}{\partial t}|2\rangle = \frac{\partial\rho_{21}^{(n)}}{\partial t}$ is calculated

$$\begin{aligned}\sum_n \frac{\partial\rho_{21}^{(n)}}{\partial t} =& \frac{1}{i\hbar}\sum_n \left[\langle 2|\,(\hat{H}_0 - \hat{M}\,E(t))\hat{\rho}^{(n)}\,|1\rangle - \langle 2|\,\hat{\rho}^{(n)}(\hat{H}_0 - \hat{M}\,E(t))\,|1\rangle\right] \\ &- \frac{1}{2}\left[\langle 2|\,\hat{\gamma}\left(\sum_n \hat{\rho}^{(n+1)}\right)|1\rangle + \langle 2|\left(\sum_n \hat{\rho}^{(n+1)}\right)\hat{\gamma}\,|1\rangle\right],\end{aligned} \tag{2-166}$$

$$\begin{aligned}\sum_n \frac{\partial\rho_{21}^{(n)}}{\partial t} =& \frac{1}{i\hbar}\sum_n \left[\langle 2|\,\hat{H}_0\hat{\rho}^{(n)}\,|1\rangle - \langle 2|\,\hat{M}\hat{\rho}^{(n)}\,|1\rangle\;E(t) - \langle 2|\,\hat{\rho}^{(n)}\hat{H}_0\,|1\rangle - \langle 2|\,\hat{\rho}^{(n)}\hat{M}\,|1\rangle\;E(t))\right] \\ &- \frac{1}{2}\left[\langle 2|\,\hat{\gamma}\sum_n \hat{\rho}^{(n+1)}\,|1\rangle + \langle 2|\sum_n \hat{\rho}^{(n+1)}\hat{\gamma}\,|1\rangle\right],\end{aligned} \tag{2-167}$$

we have that $\hat{H}_0\,|m\rangle = E_m\,|m\rangle$, substituting we have:

$$\sum_n \frac{\partial \rho_{21}^{(n)}}{\partial t} = \frac{1}{i\hbar} \sum_n \Big[E_2 \langle 2| \hat{\rho}^{(n)} |1\rangle - \langle 2| \hat{M} \hat{\rho}^{(n)} |1\rangle \; E(t) - E_1 \langle 2| \hat{\rho}^{(n)} |1\rangle - \langle 2| \hat{\rho}^{(n)} \hat{M} |1\rangle \; E(t)) \Big] - \frac{1}{2} \sum_n \left[\langle 2| \hat{\gamma} \hat{\rho}^{(n+1)} |1\rangle + \langle 2| \hat{\rho}^{(n+1)} \hat{\gamma} |1\rangle \right], \tag{2-168}$$

using the completex relation ($|1\rangle \langle 1| + |2\rangle \langle 2| = 1$), we have:

$$\sum_n \frac{\partial \rho_{21}^{(n)}}{\partial t} = \frac{1}{i\hbar} \sum_n \Big[(E_2 - E_1) \rho_{21}^{(n)} - \langle 2| \hat{M} (|1\rangle \langle 1| + |2\rangle \langle 2|) \hat{\rho}^{(n)} |1\rangle \; E(t) - \langle 2| \hat{\rho}^{(n)} (|1\rangle \langle 1| + |2\rangle \langle 2|) \hat{M} |1\rangle \; E(t)) \Big] - \frac{1}{2} \sum_n \Big[\langle 2| \hat{\gamma} (|1\rangle \langle 1| + |2\rangle \langle 2|) \hat{\rho}^{(n+1)} |1\rangle + \langle 2| \hat{\rho}^{(n+1)} (|1\rangle \langle 1| + |2\rangle \langle 2|) \hat{\gamma} |1\rangle \Big], \tag{2-169}$$

$$\begin{aligned} \sum_n \frac{\partial \rho_{21}^{(n)}}{\partial t} = & \frac{1}{i\hbar} \sum_n \Big[(E_2 - E_1) \rho_{21}^{(n)} - (\langle 2| \hat{M} |1\rangle \langle 1| \hat{\rho}^{(n)} |1\rangle + \langle 2| \hat{M} |2\rangle \langle 2| \hat{\rho}^{(n)} |1\rangle) \, E(t) \\ & - (\langle 2| \hat{\rho}^{(n)} |1\rangle \langle 1| \hat{M} |1\rangle + \langle 2| \hat{\rho}^{(n)} |2\rangle \langle 2| \hat{M} |1\rangle) \, E(t)) \Big] \\ & - \frac{1}{2} \sum_n \Big[\langle 2| \hat{\gamma} |1\rangle \langle 1| \hat{\rho}^{(n+1)} |1\rangle + \langle 2| \hat{\gamma} |2\rangle \langle 2| \hat{\rho}^{(n+1)} |1\rangle \\ & + \langle 2| \hat{\rho}^{(n+1)} |1\rangle \langle 1| \hat{\gamma} |1\rangle + \langle 2| \hat{\rho}^{(n+1)} |2\rangle \langle 2| \hat{\gamma} |1\rangle \Big], \end{aligned} \tag{2-170}$$

defining the elements of the matrix $\hat{M}$ as $M_{nm} \equiv \langle n|M|m\rangle$, and $E_{21} = E_2 - E_1$. Furthermore, only the diagonal elements of the $\hat{\gamma}$ matrix will be taken into account:

$$\begin{aligned} \sum_n \frac{\partial \rho_{21}^{(n)}}{\partial t} = & \frac{1}{i\hbar} \sum_n \Big[(E_{21} \rho_{21}^{(n)} - (M_{21} \rho_{11}^{(n)} + M_{22} \rho_{21}^{(n)}) \, E(t) \\ & - (\rho_{21}^{(n)} M_{11} + \rho_{22}^{(n)} M_{21}) \, E(t)) \Big] - \frac{1}{2} \sum_n \Big[\gamma_{22} \rho_{21}^{(n+1)} + \rho_{21}^{(n+1)} \gamma_{11} \Big], \end{aligned} \tag{2-171}$$

$$\begin{aligned} \sum_n \frac{\partial \rho_{21}^{(n)}}{\partial t} = & \frac{1}{i\hbar} \sum_n \Big[E_{21} \rho_{21}^{(n)} - (\rho_{11}^{(n)} - \rho_{22}^{(n)}) M_{21} \, E(t) - (M_{22} - M_{11}) \rho_{21}^{(n)} \, E(t) \Big] \\ & - \frac{1}{2} \sum_n \left[\frac{1}{\tau_2} + \frac{1}{\tau_1} \right] \rho_{21}^{(n+1)}, \end{aligned} \tag{2-172}$$

defining the following expression:

$$\gamma_{12} = \gamma_{21} = \frac{1}{2}\left[\frac{1}{\tau_1} + \frac{1}{\tau_2}\right], \tag{2-173}$$

and using the fact that $\rho_{21}^{(0)} = \rho_{12}^{(0)} = 0$, then:

$$\sum_n \rho_{21}^{(n)} = \sum_n \rho_{21}^{(n+1)}, \tag{2-174}$$

taking into account the equations 2-173 and 2-174 we can rewrite the equation 2-172:

$$\begin{aligned}\sum_n \frac{\partial \rho_{21}^{(n+1)}}{\partial t} =& \frac{1}{i\hbar}\sum_n \left[E_{21}\rho_{21}^{(n+1)} - (\rho_{11}^{(n)} - \rho_{22}^{(n)})M_{21}\,E(t) - (M_{22} - M_{11})\rho_{21}^{(n)}\,E(t)\right] \\ &- \sum_n \gamma_{12}\rho_{21}^{(n+1)},\end{aligned} \tag{2-175}$$

$$\sum_n \frac{\partial \rho_{21}^{(n+1)}}{\partial t} = \sum_n \left[\frac{1}{i\hbar}E_{21} - \gamma_{12}\right]\rho_{21}^{(n+1)} + \frac{1}{i\hbar}\sum_n \left[-(\rho_{11}^{(n)} - \rho_{22}^{(n)})M_{21}\,E(t) - (M_{22} - M_{11})\rho_{21}^{(n)}\,E(t)\right], \tag{2-176}$$

the above expression can be written as a recurrence relation for ρ_{21}^{n+1}.

$$\frac{\partial \rho_{21}^{(n+1)}}{\partial t} = \left[\frac{1}{i\hbar}E_{21} - \gamma_{12}\right]\rho_{21}^{(n+1)} - \frac{1}{i\hbar}\left[\rho_{11}^{(n)} - \rho_{22}^{(n)}\right]M_{21}\,E(t) - \frac{1}{i\hbar}\left[M_{22} - M_{11}\right]\rho_{21}^{(n)}\,E(t). \tag{2-177}$$

Following the same process above for $\partial\rho_{21}^{(n+1)}/\partial t$, the terms for $\partial\rho_{12}^{(n+1)}/\partial t$, $\partial\rho_{22}^{(n+1)}/\partial t$, and $\partial\rho_{11}^{(n+1)}/\partial t$ can be found

$$\frac{\partial \rho_{12}^{(n+1)}}{\partial t} = \left[\frac{1}{i\hbar}E_{12} - \gamma_{21}\right]\rho_{12}^{(n+1)} - \frac{1}{i\hbar}\left[\rho_{22}^{(n)} - \rho_{11}^{(n)}\right]M_{12}\,E(t) - \frac{1}{i\hbar}\left[M_{11} - M_{22}\right]\rho_{12}^{(n)}\,E(t), \tag{2-178}$$

$$\frac{\partial \rho_{22}^{(n+1)}}{\partial t} = -\gamma_{22}\rho_{22}^{(n+1)} - \frac{1}{i\hbar}\left[M_{21}\rho_{12}^{(n)} - M_{12}\rho_{21}^{(n)}\right]E(t), \tag{2-179}$$

$$\frac{\partial \rho_{11}^{(n+1)}}{\partial t} = -\gamma_{11}\rho_{11}^{(n+1)} - \frac{1}{i\hbar}\left[M_{12}\rho_{21}^{(n)} - M_{21}\rho_{12}^{(n)}\right]E(t). \tag{2-180}$$

The previous equations (2-177−2-180) can be solved by expressing the elements of the density matrix in terms of sums proportional to $exp(\pm i\omega t)$ and equating the terms on both sides of the equations with the same time dependence.

In these calculations, we ignore the terms corresponding to higher harmonics that represent successive absorptions and emissions of photons. We focus only on the steady state, therefore, the perturbative term of order, $\rho(n)$, can be written as:

$$\rho^{(n)}(t) = \tilde{\rho}^{(n)}(\omega)e^{-i\omega t} + \tilde{\rho}^{(n)}(-\omega)e^{i\omega t}, \tag{2-181}$$

the above is valid for when n is odd. When n is even, only the DC terms are dominant.

If we take $n = 1$ in equation (2-181), and $n = 0$ in equation (2-177), we have:

$$\rho^{(1)}(t) = \tilde{\rho}^{(1)}(\omega)e^{-i\omega t} + \tilde{\rho}^{(1)}(-\omega)e^{i\omega t}, \tag{2-182}$$

$$\frac{\partial \rho_{21}^{(1)}}{\partial t} = \left[\frac{1}{i\hbar}E_{21} - \gamma_{12}\right]\rho_{21}^{(1)} - \frac{1}{i\hbar}\left[\rho_{11}^{(0)} - \rho_{22}^{(0)}\right]M_{21}\,E(t) - \frac{1}{i\hbar}\left[M_{22} - M_{11}\right]\rho_{21}^{(0)}\,E(t), \tag{2-183}$$

replacing 2-182 and 2-161 into 2-183, and remembering that $\rho_{12}^{(0)} = 0$, we have:

$$\begin{aligned}\frac{\partial}{\partial t}\left(\tilde{\rho}_{21}^{(1)}(\omega)e^{-i\omega t} + \tilde{\rho}_{21}^{(1)}(-\omega)e^{i\omega t}\right) = &\left[\frac{1}{i\hbar}E_{21} - \gamma_{12}\right]\left(\tilde{\rho}_{21}^{(1)}(\omega)e^{-i\omega t} + \tilde{\rho}_{21}^{(1)}(-\omega)e^{i\omega t}\right) \\ &- \frac{1}{i\hbar}\left[\rho_{11}^{(0)} - \rho_{22}^{(0)}\right]M_{21}\left(\tilde{E}e^{-i\omega t} + \tilde{E}e^{i\omega t}\right),\end{aligned} \tag{2-184}$$

now, the derivatives are evaluated and we group the terms with negative and positive power of $\pm i\omega t$. It turns out that

$$\begin{aligned}&-i\omega t\tilde{\rho}_{21}^{(1)}(\omega)e^{-i\omega t} + i\omega t\tilde{\rho}_{21}^{(1)}(-\omega)e^{i\omega t} = \\ &\left[\left(\frac{1}{i\hbar}E_{21} - \gamma_{12}\right)\tilde{\rho}_{21}^{(1)}(\omega) - \frac{1}{i\hbar}\left(\rho_{11}^{(0)} - \rho_{22}^{(0)}\right)M_{21}\tilde{E}\right]e^{-i\omega t} \\ &+\left[\left(\frac{1}{i\hbar}E_{21} - \gamma_{12}\right)\tilde{\rho}_{21}^{(1)}(-\omega) - \frac{1}{i\hbar}\left(\rho_{11}^{(0)} - \rho_{22}^{(0)}\right)M_{21}\tilde{E}\right]e^{i\omega t},\end{aligned} \tag{2-185}$$

equating the terms with the same negative power and solving for $\rho_{21}^{(1)}(\omega)$, we have:

$$\tilde{\rho}_{21}^{(1)}(\omega) = \frac{\left(\rho_{11}^{(0)} - \rho_{22}^{(0)}\right)M_{21}\tilde{E}}{E_{21} - \hbar\omega - i\hbar\gamma_{12}}. \tag{2-186}$$

Now we calculate the term $\tilde{\rho}_{21}^{(3)}(\omega)$. For this $n = 2$ in equation (2-177), and $n = 3$ in equation (2-181), we have:

$$\frac{\partial \rho_{21}^{(3)}}{\partial t} = \left[\frac{1}{i\hbar}E_{21} - \gamma_{12}\right]\rho_{21}^{(3)} - \frac{1}{i\hbar}\left[\rho_{11}^{(2)} - \rho_{22}^{(2)}\right]M_{21}\,E(t) - \frac{1}{i\hbar}\left[M_{22} - M_{11}\right]\rho_{21}^{(2)}\,E(t). \tag{2-187}$$

$$\rho^{(3)}(t) = \tilde{\rho}^{(3)}(\omega)e^{-i\omega t} + \tilde{\rho}^{(3)}(-\omega)e^{i\omega t}, \tag{2-188}$$

substituting equations (2-188) and (2-161) into (2-187) and equating the terms of $\exp(-i\omega t)$, as done previously for $\tilde{\rho}_{21}^{(1)}$. It must be taken into account that the terms $\rho_{11}^{(2)}(t)$, $\rho_{22}^{(2)}(t)$, and $\rho_{21}^{(2)}(t)$, do not change over time, because they are rectification terms, and can be replaced directly by $\tilde{\rho}_{11}^{(2)}(0)$, $\tilde{\rho}_{22}^{(2)}(0)$ and $\tilde{\rho}_{21}^{(2)}(0)$ respectively, therefore

$$\begin{aligned} -i\omega\tilde{\rho}_{21}^{(3)}(\omega) = \left[\frac{1}{i\hbar}E_{21} - \gamma_{12}\right]\rho_{21}^{(3)}(\omega) - \frac{1}{i\hbar}\Big[\Big(\tilde{\rho}_{11}^{(2)}(0) - \tilde{\rho}_{22}^{(2)}(0)\Big)M_{21}\,\tilde{E} \\ + (M_{22} - M_{11})\,\tilde{E}\tilde{\rho}_{21}^{(2)}(0)\Big], \end{aligned} \tag{2-189}$$

from the previous equation, an expression for $\tilde{\rho}_{21}^{(3)}(\omega)$ can be found:

$$\tilde{\rho}_{21}^{(3)}(\omega) = \frac{\tilde{E}}{E_{21} - \hbar\omega - i\hbar\gamma_{12}}\left[\Big(\tilde{\rho}_{11}^{(2)}(0) - \tilde{\rho}_{22}^{(2)}(0)\Big)M_{21} + (M_{22} - M_{11})\,\tilde{\rho}_{21}^{(2)}(0)\right]. \tag{2-190}$$

The goal now is to find the difference between $(\tilde{\rho}_{11}^{(2)}(0) - \tilde{\rho}_{11}^{(2)}(0)\ )$. For this purpose, equations (2-179) and (2-180) must be used. So,

$$\frac{\partial\rho_{22}^{(2)}}{\partial t} = -\gamma_{22}\rho_{22}^{(2)} - \frac{1}{i\hbar}\left[M_{21}\rho_{12}^{(1)} - M_{12}\rho_{21}^{(1)}\right]E(t), \tag{2-191}$$

$$\frac{\partial\rho_{11}^{(2)}}{\partial t} = -\gamma_{11}\rho_{11}^{(2)} - \frac{1}{i\hbar}\left[M_{12}\rho_{21}^{(1)} - M_{21}\rho_{12}^{(1)}\right]E(t). \tag{2-192}$$

We will first focus on equation (2-192), knowing that $\rho_{11}^{(2)}$ is a rectification term, therefore, we have that $\partial\rho_{11}^{(2)}/\partial t = 0$. We also have to replace $\rho_{21}^{(1)}$ and $\rho_{12}^{(1)}$ by their stable components, that is, taking t = 0 in the equation (2-182). Furthermore, we take the DC component of E(t), $\tilde{E}$, so

$$0 = -\gamma_{11}\rho_{11}^{(2)}(0) - \frac{\tilde{E}}{i\hbar}\left[M_{12}\{\tilde{\rho}_{21}^{(1)}(\omega) + \tilde{\rho}_{21}^{(1)}(-\omega)\} - M_{21}\{\tilde{\rho}_{12}^{(1)}(-\omega) + \tilde{\rho}_{12}^{(1)}(\omega)\}\right], \tag{2-193}$$

the terms $\tilde{\rho}_{21}^{(1)}(\omega)$ and $\tilde{\rho}_{21}^{(1)}(-\omega)$ are known as non-resonant and it is possible to calculate them in the same way as equation (2-186), which are given by

$$\tilde{\rho}_{21}^{(3)}(-\omega) = \frac{\left(\rho_{11}^{(0)} - \rho_{22}^{(0)}\right)M_{21}\tilde{E}}{\hbar E_{21} + \hbar\omega - i\hbar\gamma_{12}}, \tag{2-194}$$

$$\tilde{\rho}_{21}^{(3)}(\omega) = \frac{\left(\rho_{11}^{(0)} - \rho_{22}^{(0)}\right)M_{21}\tilde{E}}{\hbar E_{21} + \hbar\omega + i\hbar\gamma_{12}}, \tag{2-195}$$

these last two terms present in their denominators the expression $\hbar E_{21} + \hbar\omega$, which implies that they cannot have the possibility of entering into resonance at any time. Therefore, we ignore them, so:

$$0 = -\gamma_{11}\rho_{11}^{(2)}(0) - \frac{\tilde{E}}{i\hbar}\left[M_{12}\tilde{\rho}_{21}^{(1)}(\omega) - M_{21}\tilde{\rho}_{12}^{(1)}(-\omega)\right], \tag{2-196}$$

solving for $\tilde{\rho}_{11}^{(1)}(0)$, then:

$$\tilde{\rho}_{11}^{(1)}(0) = \frac{i\tilde{E}}{\gamma_{11}\hbar}\left[M_{12}\tilde{\rho}_{21}^{(1)}(\omega) - M_{21}\tilde{\rho}_{12}^{(1)}(-\omega)\right], \tag{2-197}$$

we need to replace $\tilde{\rho}_{21}^{(1)}(\omega)$ (Equation 2-186) and $\tilde{\rho}_{12}^{(1)}(-\omega)$ which can be obtained in the same way as (2-186) or by substituting $\omega \to -\omega$ into equation (2-195). After replacing the mentioned expressions you can obtain the expression for $\tilde{\rho}_{11}^{(2)}(0)$

$$\tilde{\rho}_{11}^{(1)}(0) = -\frac{2\tilde{E}^2|M_{21}|^2(\rho_{11}^{(0)} - \rho_{22}^{(0)})\gamma_{12}}{\gamma_{12}\left[(E_{21} - \hbar\omega)^2 + (\hbar\gamma_{12})^2\right]}, \tag{2-198}$$

To find the expression of $\tilde{\rho}_{22}^{(2)}(0)$ a procedure similar to the previous one must be followed, and knowing that $|M_{21}|^2 = |M_{12}|^2 = M_{21}M_{12}$ and $\gamma_{12} = \gamma_{21}$:

$$\tilde{\rho}_{22}^{(1)}(0) = \frac{2\tilde{E}^2|M_{12}|^2(\rho_{11}^{(0)} - \rho_{22}^{(0)})\gamma_{12}}{\gamma_{22}\left[(E_{21} - \hbar\omega)^2 + (\hbar\gamma_{12})^2\right]}, \tag{2-199}$$

now, using the expressions (2-199) and 2-198, we have:

$$\tilde{\rho}_{11}^{(0)}(0) - \tilde{\rho}_{22}^{(0)}(0) = -2\tilde{E}^2\left(\frac{1}{\gamma_{11}} + \frac{1}{\gamma_{22}}\right)\frac{|M_{12}|^2(\rho_{11}^{(0)} - \rho_{22}^{(0)})\gamma_{12}}{\left[(E_{21} - \hbar\omega)^2 + (\hbar\gamma_{12})^2\right]}, \tag{2-200}$$

with what was done above it is possible to calculate $\tilde{\rho}_{21}^{(2)}$, for this we use the equation (2-177) with $n = 1$ and remembering that we are only interested in the terms stationary. So:

$$\begin{aligned}\frac{\partial\rho_{21}^{(2)}(0)}{\partial t} = &\left[\frac{1}{i\hbar}E_{21} - \gamma_{12}\right]\rho_{21}^{(2)}(0) - \frac{1}{i\hbar}\left(\rho_{11}^{(1)}(0) - \rho_{22}^{(1)}(0)\right)M_{21}\tilde{E} \\ &- \frac{1}{i\hbar}\left(M_{22} - M_{11}\right)\tilde{E}\tilde{\rho}_{21}^{(1)}.\end{aligned} \tag{2-201}$$

Now using equation (2-182), and using the fact that $\partial\rho_{21}^{(2)}(0)/\partial t = 0$ with $t = 0$, we obtain:

$$\begin{aligned}0 = &\left[\frac{1}{i\hbar}E_{21} - \gamma_{12}\right]\rho_{21}^{(2)}(0) - \frac{1}{i\hbar}\left(\rho_{11}^{(1)}(\omega) + \rho_{11}^{(1)}(-\omega) - \rho_{22}^{(1)}(\omega) - \rho_{22}^{(1)}(-\omega)\right)M_{21}\tilde{E} \\ &- \frac{1}{i\hbar}\left(M_{22} - M_{11}\right)\tilde{E}\left(\rho_{21}^{(1)}(\omega) + \rho_{21}^{(1)}(-\omega)\right).\end{aligned} \tag{2-202}$$

Returning to the term $\tilde{\rho}_{11}^{(1)}(\omega)$, using (2-198) with $n = 0$:

$$\frac{\partial \rho_{11}^{(1)}}{\partial t} = -\gamma_{11}\rho_{11}^{(1)} - \frac{1}{i\hbar}\left(M_{12}\rho_{21}^{(0)} - M_{21}\rho_{12}^{(0)}\right)E(t), \tag{2-203}$$

using the fact that $\rho_{21}^{(0)} = \rho_{12}^{(0)} = 0$, then:

$$\frac{\partial \rho_{11}^{(1)}}{\partial t} = -\gamma_{11}\rho_{11}^{(1)}. \tag{2-204}$$

Using once again the equation (2-182) and equating the terms of $\exp(i\omega t)$, it is possible to obtain

$$\tilde{\rho}_{11}^{(1)}(\omega)\left(\gamma_{11} - i\omega\right) = 0, \tag{2-205}$$

The above implies that $\tilde{\rho}_{11}^{(1)}(\omega) = 0$. The same can be said of the terms $\tilde{\rho}_{11}^{(1)}(-\omega) = \tilde{\rho}_{22}^{(1)}(\omega) = \tilde{\rho}_{22}^{(1)}(-\omega) = 0$, and neglecting the non-resonant term $\tilde{\rho}_{21}^{(1)}(-\omega)$ we have:

$$0 = \left[\frac{1}{i\hbar}E_{21} - \gamma_{12}\right]\tilde{\rho}_{21}^{(2)}(0) - \frac{\tilde{E}}{i\hbar}\left(M_{22} - M_{11}\right)\tilde{\rho}_{21}^{(1)}(\omega), \tag{2-206}$$

solving for $\tilde{\rho}_{21}^{(2)}(0)$, and substituting into equation (2-186)

$$\tilde{\rho}_{21}^{(2)} = \frac{\tilde{E}^2 M_{21}\left(M_{22} - M_{11}\right)\left(\rho_{11}^{(0)} - \rho_{22}^{(0)}\right)}{\left(E_{21} - i\hbar\gamma_{12}\right)\left(E_{21} - \hbar\omega - i\hbar\gamma_{12}\right)}. \tag{2-207}$$

Now, let's replace equations (2-200) and (2-207) into equation (2-190), and solve for $\tilde{\rho}_{21}^{(3)}(\omega)$ we have:

$$\begin{aligned}\tilde{\rho}_{21}^{(3)}(\omega) = -\frac{\tilde{E}\tilde{E}^2 M_{21}\left(\rho_{11}^{(0)} - \rho_{22}^{(0)}\right)}{\left(E_{21} - \hbar\omega - i\hbar\gamma_{12}\right)}\left[\frac{2\left(1/\gamma_{11} + 1/\gamma_{22}\right)|M_{12}|^2\gamma_{12}}{\left(E_{21} - \hbar\omega\right)^2 + \left(\hbar\gamma_{12}\right)^2}\right. \\ \left. -\frac{\left(M_{22} - M_{11}\right)^2}{\left(E_{21} - i\hbar\gamma_{12}\right)\left(E_{21} - \hbar\omega - i\hbar\gamma_{12}\right)}\right].\end{aligned} \tag{2-208}$$

The terms $\tilde{\rho}_{22}^{(3)}(\omega)$ and $\tilde{\rho}_{11}^{(3)}(\omega)$ can be obtained also following the previous procedure carried out for $\tilde{\rho}_{21}^{(3)}(\omega)$. However, such terms are insignificant when calculating the third-order absorption coefficient, as mentioned by Ahn and Chuang [2]. These terms are.

$$\tilde{\rho}_{22}^{(3)}(\omega) = \frac{2i\tilde{E}\tilde{E}^2|M_{21}|^2}{\hbar\omega + i\hbar\gamma_{22}}\Im\left[\frac{\left(M_{22} - M_{11}\right)\left(\rho_{11}^{(0)} - \rho_{22}^{(0)}\right)}{\left(E_{21} - i\hbar\gamma_{22}\right)\left(E_{21} - \hbar\omega - i\hbar\gamma_{12}\right)}\right], \tag{2-209}$$

and

$$\tilde{\rho}_{22}^{(3)}(\omega) = -\frac{2i\tilde{E}\tilde{E}^2|M_{21}|^2}{\hbar\omega + i\hbar\gamma_{22}}\Im\left[\frac{(M_{22}-M_{11})\left(\rho_{11}^{(0)}-\rho_{22}^{(0)}\right)}{(E_{21}-i\hbar\gamma_{22})(E_{21}-\hbar\omega-i\hbar\gamma_{12})}\right]. \tag{2-210}$$

Where, $\Im$ is the imaginary part.

Linear and non-linear absorption coefficients

Now we will calculate the Linear and Nonlinear Absorption Coefficients in quantum systems with the results from the last section. When applying an electric field in these systems, we have the electronic polarization $P(t)$ and the optical susceptibility $\chi(t)$. These terms can be expressed by the dipole operator $\hat{M}$ and the density matrix as:

$$P(t) = \varepsilon_0\chi(\omega)\tilde{E}e^{-i\omega t} + \varepsilon_0\chi(-\omega)\tilde{E}e^{i\omega t} = \frac{1}{V}Tr(\tilde{\rho}\tilde{M}), \tag{2-211}$$

in the previous expression, V is the volume of the system to be studied, ε_0 is the permittivity of the vacuum, and Tr denotes the trace of the diagonal elements of the matrix $\tilde{\rho}\tilde{M}$. On the other hand, the susceptibility χ is related to the absorption coefficient $\alpha(\omega)$ as:

$$\alpha(\omega) = \omega\sqrt{\frac{\mu}{\varepsilon_R}}\Im(\varepsilon_0\chi(\omega)), \tag{2-212}$$

where μ is the permeability of the system, ε_R is the real part of the permittivity and $\chi(\omega)$ is the Fourier component of $\chi(t)$ with dependence $\exp(-i\omega t)$. With the above, it is possible to write the polarization as:

$$P(t) = \frac{1}{V}\left[\langle 1|\,\tilde{\rho}\tilde{M}\,|1\rangle + \langle 2|\,\tilde{\rho}\tilde{M}\,|2\rangle\right], \tag{2-213}$$

introducing the complex relation

$$P(t) = \frac{1}{V}\left[\langle 1|\,\tilde{\rho}\,(|1\rangle\langle 1| + |2\rangle\langle 2|)\,\tilde{M}\,|1\rangle + \langle 2|\,\tilde{\rho}\,(|1\rangle\langle 1| + |2\rangle\langle 2|)\,\tilde{M}\,|2\rangle\right], \tag{2-214}$$

$$P(t) = \frac{1}{V}\left[\langle 1|\,\tilde{\rho}\,|1\rangle\langle 1|\,\tilde{M}\,|1\rangle + \langle 1|\,\tilde{\rho}\,|2\rangle\langle 2|\,\tilde{M}\,|1\rangle + \langle 2|\,\tilde{\rho}\,|1\rangle\langle 1|\,\tilde{M}\,|2\rangle + \langle 2|\,\tilde{\rho}\,|2\rangle\langle 2|\,\tilde{M}\,|2\rangle\right], \tag{2-215}$$

replacing the density by its expansion defined in (2-163), and rewriting ρ_{ij} and M_{ij}, we have:

$$P(t) = \frac{1}{V}\left[\rho_{11}^{(n)}M_{11} + \rho_{12}^{(n)}M_{21} + \rho_{21}^{(n)}M_{12} + \rho_{22}^{(n)}M_{22}\right], \tag{2-216}$$

using the relationship (2-181) in the previous expression:

$$\begin{aligned} P(t) = \frac{1}{V}\Big[&\left(\tilde{\rho}_{11}^{(n)}(\omega)M_{11} + \tilde{\rho}_{12}^{(n)}(\omega)M_{21} + \tilde{\rho}_{21}^{(n)}(\omega)M_{12} + \tilde{\rho}_{22}^{(n)}(\omega)M_{22}\right)e^{-i\omega t} \\ &\left(\tilde{\rho}_{11}^{(n)}(-\omega)M_{11} + \tilde{\rho}_{12}^{(n)}(-\omega)M_{21} + \tilde{\rho}_{21}^{(n)}(-\omega)M_{12} + \tilde{\rho}_{22}^{(n)}(-\omega)M_{22}\right)e^{i\omega t}\Big] \end{aligned} \tag{2-217}$$

now we equate the equations (2-211) and (2-217) for $n = 1$, we have:

$$\varepsilon_0\chi^{(1)}(\omega)\tilde{E}e^{-i\omega t}+\varepsilon_0\chi^{(1)}(-\omega)\tilde{E}e^{i\omega t} = \frac{1}{V}\left[\left(\tilde{\rho}_{11}^{(1)}(\omega)M_{11}+\tilde{\rho}_{12}^{(1)}(\omega)M_{21}+\tilde{\rho}_{21}^{(1)}(\omega)M_{12}+\tilde{\rho}_{22}^{(1)}(\omega)M_{22}\right)e^{-i\omega t}\right.$$
$$\left.\left(\tilde{\rho}_{11}^{(1)}(-\omega)M_{11}+\tilde{\rho}_{12}^{(1)}(-\omega)M_{21}+\tilde{\rho}_{21}^{(1)}(-\omega)M_{12}+\tilde{\rho}_{22}^{(1)}(-\omega)M_{22}\right)e^{i\omega t}\right], \tag{2-218}$$

we can neglect the terms outside the resonance and remember that $\tilde{\rho}_{11}^{(1)}(\omega) = \tilde{\rho}_{22}^{(1)}(\omega) = 0$. Then, we equate the negative exponential terms:

$$\varepsilon_0\chi^{(1)}(\omega) = \frac{1}{V\tilde{E}}\left(\tilde{\rho}_{21}^{(1)}(\omega)M_{12}\right), \tag{2-219}$$

replacing equation (2-186) into (2-219):

$$\varepsilon_0\chi^{(1)}(\omega) = \frac{1}{V\tilde{E}}\left[\frac{\left(\rho_{11}^{(0)}-\rho_{22}^{(0)}\right)M_{21}\tilde{E}}{E_{21}-\hbar\omega-i\hbar\gamma_{12}}M_{12}\right], \tag{2-220}$$

$$\varepsilon_0\chi^{(1)}(\omega) = \frac{|M_{12}|^2\left(\rho_{11}^{(0)}-\rho_{22}^{(0)}\right)}{V}\left[\frac{E_{21}-\hbar\omega+i\hbar\gamma_{12}}{(E_{21}-\hbar\omega)^2+(\hbar\gamma_{12})^2}\right], \tag{2-221}$$

$$\varepsilon_0\chi^{(1)}(\omega) = \frac{|M_{12}|^2\left(\rho_{11}^{(0)}-\rho_{22}^{(0)}\right)}{V}\left[\frac{E_{21}-\hbar\omega}{(E_{21}-\hbar\omega)^2+(\hbar\gamma_{12})^2}+i\frac{\hbar\gamma_{12}}{(E_{21}-\hbar\omega)^2+(\hbar\gamma_{12})^2}\right], \tag{2-222}$$

Taking only the imaginary part:

$$\Im(\varepsilon_0\chi^{(1)}(\omega)) = \frac{|M_{12}|^2\left(\rho_{11}^{(0)}-\rho_{22}^{(0)}\right)\hbar\gamma_{12}}{V\left((E_{21}-\hbar\omega)^2+(\hbar\gamma_{12})^2\right)}, \tag{2-223}$$

replacing equation (2-223) into equation (2-212), then:

$$\alpha^{(1)}(\omega) = \omega\sqrt{\frac{\mu}{\varepsilon_R}}\frac{|M_{12}|^2\left(\rho_{11}^{(0)}-\rho_{22}^{(0)}\right)\hbar\gamma_{12}}{V\left((E_{21}-\hbar\omega)^2+(\hbar\gamma_{12})^2\right)}, \tag{2-224}$$

defining that $\sigma_v = (\rho_{11}^{(0)}-\rho_{22}^{(0)})/V$ as the three-dimensional concentration of electrons in the system, therefore, we have:

$$\alpha^{(1)}(\omega) = \omega\sqrt{\frac{\mu}{\varepsilon_R}}\frac{|M_{12}|^2\sigma_v\hbar\gamma_{12}}{\left((E_{21}-\hbar\omega)^2+(\hbar\gamma_{12})^2\right)}, \tag{2-225}$$

this expression is to calculate the first-order absorption coefficient.

Following a procedure similar to the previous one, finding an expression for the third-order absorption coefficient is possible. To achieve this, we take $n = 3$ in equation (2-218), we

neglect the term that is outside the resonance $\tilde{\rho}_{12}^{(3)}(\omega)$, and remembering that the terms $\tilde{\rho}_{11}^{(3)}(\omega)$ and $\tilde{\rho}_{22}^{(3)}(\omega)$ induce a small contribution to the absorption, therefore, we can neglect them in this calculation. Equating the terms with negative exponentials, we have:

$$\varepsilon_0\chi^{(3)}(\omega)\tilde{E} = \frac{1}{V}\left(\tilde{\rho}_{11}^{(3)}(\omega)M_{11} + \tilde{\rho}_{12}^{(3)}(\omega)M_{21} + \tilde{\rho}_{21}^{(3)}(\omega)M_{12} + \tilde{\rho}_{22}^{(3)}(\omega)M_{22}\right), \tag{2-226}$$

$$\varepsilon_0\chi^{(3)}(\omega) = \frac{1}{V\tilde{E}}\left(\tilde{\rho}_{21}^{(3)}(\omega)M_{12}\right), \tag{2-227}$$

replacing equation 2-208 into equation 2-227

$$\begin{aligned}\varepsilon_0\chi^{(3)}(\omega) = &-\frac{1}{V\tilde{E}}\frac{\tilde{E}\tilde{E}^2M_{21}\left(\rho_{11}^{(0)}-\rho_{22}^{(0)}\right)}{(E_{21}-\hbar\omega-i\hbar\gamma_{12})}\left[\frac{2\left(1/\gamma_{11}+1/\gamma_{22}\right)|M_{12}|^2\gamma_{12}}{\left(E_{21}-\hbar\omega\right)^2+\left(\hbar\gamma_{12}\right)^2}\right.\\ &\left.-\frac{\left(M_{22}-M_{11}\right)^2}{\left(E_{21}-i\hbar\gamma_{12}\right)\left(E_{21}-\hbar\omega-i\hbar\gamma_{12}\right)}\right]M_{12},\end{aligned} \tag{2-228}$$

$$\begin{aligned}\varepsilon_0\chi^{(3)}(\omega) = &-\frac{1}{V}\tilde{E}^2|M_{21}|^2\left(\rho_{11}^{(0)}-\rho_{22}^{(0)}\right)\left\{\frac{1}{E_{21}-\hbar\omega-i\hbar\gamma_{12}}\left[\frac{2\left(1/\gamma_{11}+1/\gamma_{22}\right)|M_{12}|^2\gamma_{12}}{\left(E_{21}-\hbar\omega\right)^2+\left(\hbar\gamma_{12}\right)^2}\right.\right.\\ &\left.\left.-\frac{\left(M_{22}-M_{11}\right)^2}{\left(E_{21}-i\hbar\gamma_{12}\right)\left(E_{21}-\hbar\omega-i\hbar\gamma_{12}\right)}\right]\right\},\end{aligned} \tag{2-229}$$

taking the imaginary part of the equation (2-229) and substituting into the equation (2-212)

$$\begin{aligned}\alpha^{(3)}(\omega,I) = &-\omega\sqrt{\frac{\mu}{\varepsilon_R}}\frac{\tilde{E}^2|M_{21}|^2\left(\rho_{11}^{(0)}-\rho_{22}^{(0)}\right)}{V}\Im\left\{\frac{1}{E_{21}-\hbar\omega-i\hbar\gamma_{12}}\left[\frac{2\left(1/\gamma_{11}+1/\gamma_{22}\right)|M_{12}|^2\gamma_{12}}{\left(E_{21}-\hbar\omega\right)^2+\left(\hbar\gamma_{12}\right)^2}\right.\right.\\ &\left.\left.-\frac{\left(M_{22}-M_{11}\right)^2}{\left(E_{21}-i\hbar\gamma_{12}\right)\left(E_{21}-\hbar\omega-i\hbar\gamma_{12}\right)}\right]\right\}.\end{aligned} \tag{2-230}$$

The following change of expression will be made for simplicity, let's choose $\gamma_{11} = \gamma_{22}$, which implies that $\gamma_{12} = \gamma_{11} = \gamma_{22}$, then:

$$\frac{\gamma_{12}(\gamma_{11}+\gamma_{22})}{\gamma_{11}\gamma_{22}} = 2 \tag{2-231}$$

Defining the intensity of the external electromagnetic field as:

$$\tilde{E}^2 = \frac{I}{2\varepsilon_0 n_r c}, \tag{2-232}$$

where c is the speed of light in a vacuum and n_r is the refractive index of the medium. Now, we replace the definition of σ_v, shown above, and equation (2-232) into equation (2-230), we have:

$$\alpha^{(3)}(\omega, I) = -\omega\sqrt{\frac{\mu}{\varepsilon_R}}\frac{I}{2\varepsilon_0 n_r c}|M_{21}|^2\sigma_v \Im\left\{\frac{1}{E_{21}-\hbar\omega-i\hbar\gamma_{12}}\left[\frac{4|M_{12}|^2}{(E_{21}-\hbar\omega)^2+(\hbar\gamma_{12})^2}\right.\right.$$
$$\left.\left.-\frac{(M_{22}-M_{11})^2}{(E_{21}-i\hbar\gamma_{12})(E_{21}-\hbar\omega-i\hbar\gamma_{12})}\right]\right\}, \tag{2-233}$$

solving the imaginary part of the previous equation, we have:

$$\alpha^{(3)}(\omega, I) = -\omega\sqrt{\frac{\mu}{\varepsilon_R}}\frac{I}{2\varepsilon_0 n_r c}\frac{|M_{21}|^2\sigma_v\hbar\gamma_{12}}{\left[(E_{21}-\hbar\omega)^2+(\hbar\gamma_{12})^2\right]^2}$$
$$\times\left[4|M_{12}|^2-\frac{(M_{22}-M_{11})^2\left(3E_{21}^2-4\hbar\omega E_{21}+\hbar^2(\omega^2-\gamma_{12}^2)\right)}{E_{21}^2+(\hbar\gamma_{12})^2}\right]. \tag{2-234}$$

Finally we can write the total optical absorption coefficient in terms of the linear and non-linear part as:

$$\alpha(\omega, I) = \alpha^{(1)}(\omega) + \alpha^{(3)}(\omega, I). \tag{2-235}$$

Linear and non-linear changes in the refractive index

This section will show a procedure analogous to the previous one, to calculate changes in the refractive index. First, it is assumed that the change in the refractive index is related to the optical susceptibility through the following equation:

$$\frac{\Delta n(\omega)}{n_r} = \Re\left(\frac{\chi(\omega)}{2n_r^2}\right), \tag{2-236}$$

To find the first-order term, we use the equation (2-219), replace the previous definitions of each term, and taking the real part, the above allows us to find the following expression:

$$\frac{\Delta n^{(1)}(\omega)}{n_r} = \frac{\sigma_v|M_{12}|^2}{2n_r^2\varepsilon_0}\frac{E_{21}-\hbar\omega}{(E_{21}-\hbar\omega)^2+(\hbar\gamma_{12})^2}. \tag{2-237}$$

Now we are going to calculate the third order correction to the change in the refractive index from equation (2-229), where we will take the real part of the expression, therefore, we have:

$$\frac{\Delta n^{(3)}(\omega, I)}{n_r} = -\frac{I|M_{12}|^2\sigma_v}{4n_r^3\varepsilon_0 c}\Re\left\{\frac{E_{21}-\hbar\omega-i\hbar\gamma_{12}}{\left[(E_{21}-\hbar\omega)^2+(\hbar\gamma_{12})^2\right]^2}\times\right.$$
$$\left.\left[4|M_{12}|^2-\frac{(M_{22}-M_{11})^2\left(E_{21}^2+i\hbar\gamma_{12}\right)\left(E_{21}-\hbar\omega+i\hbar\gamma_{12}\right)}{E_{21}^2+(\hbar\gamma_{12})^2}\right]\right\}, \tag{2-238}$$

we use the relationship $c^2 = 1/\varepsilon_0\mu$ and solve the real part, we can arrive at:

$$\frac{\Delta n^{(3)}(\omega, I)}{n_r} = -\frac{|M_{12}|^2 \sigma_v}{4 n_r^3 \varepsilon_0 c} \frac{\mu c I}{\left[(E_{21} - \hbar\omega)^2 + (\hbar\gamma_{12})^2\right]^2} \left\{ 4(E_{21} - \hbar\omega)|M_{12}|^2 - \frac{(M_{22} - M_{11})^2}{E_{21}^2 + (\hbar\gamma_{12})^2} \times \left[(E_{21} - \hbar\omega)\left(E_{21}(E_{21} - \hbar\omega) - (\hbar\gamma_{12})^2\right) - (\hbar\gamma_{12})^2[2E_{21} - \hbar\omega]\right] \right\}, \tag{2-239}$$

the total change in refractive index is given by the sum of the first and third order terms, therefore:

$$\frac{\Delta n(\omega, I)}{n_r} = \frac{\Delta n^{(1)}(\omega)}{n_r} + \frac{\Delta n^{(3)}(\omega, I)}{n_r}. \tag{2-240}$$

With what was done above we have that to the first order no variations in the absorption or the change in the refractive index with the intensity of the field are observed due to the independence of these with the $\tilde{E}$. In order not to ignore this dependence on the intensity of the external field, it is necessary to consider in the calculations at least the third-order term that has an explicit dependence on both the frequency of the external field and its intensity [25–27].

2.2.4 The Finite Element Method

The finite element method (FEM) is a numerical technique for finding approximate solutions to boundary value problems for partial differential equations (PDE). A weak formulation is used together with the discretization of the PDE. The method consists of transforming the PDE from its differential operational form to an integral form, and in terms of discretization, the integrals are replaced by sums. Discretization involves a finite number of points and subdomains in the mesh problem domain, as shown in **2-6**. In this section, we will show the steps to transform the Schrödinger equation to its weak formulation. In systems comprising two or more materials, the effective mass is not constant throughout the structure. Considering the above, a more general form of the Schrödinger equation for a potential V is:

$$\vec{\nabla} \cdot \left[\left(\frac{-\hbar^2}{2m^*} \right) \vec{\nabla} \right] \psi + V\psi = E\psi \tag{2-241}$$

where $\hbar$ is the reduced Planck constant, m^* is the effective mass, ψ the wave function, and E the energy. Multiplying this equation by some test function ϕ, integrating into the volume Ω:

$$\int_\Omega \nabla \cdot \left[\left(-\frac{\hbar^2}{2m^*} \nabla\psi \right) \right] \phi \, d\Omega + \int_\Omega (V - E)\, \psi\phi \, d\Omega = 0, \tag{2-242}$$

using the divergence property

$$\vec{\nabla} \cdot \left(\vec{F} v \right) = \vec{F} \cdot \vec{\nabla} v + \left(\vec{\nabla} \cdot \vec{F} \right) v, \tag{2-243}$$

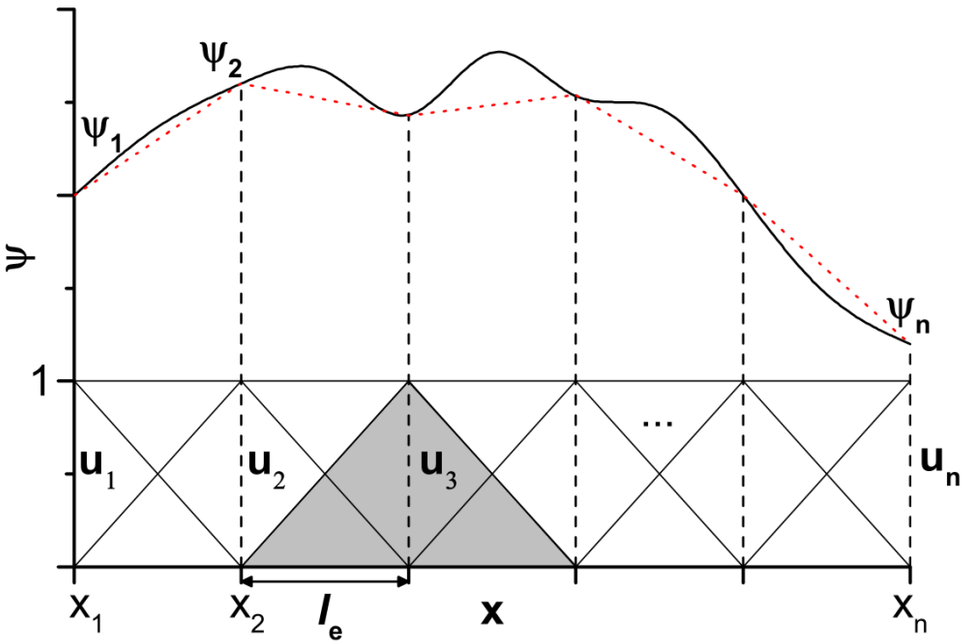

Figure **2-6**: Illustration of FEM discretization. The U_n are linear base functions and ψ_n are the coefficients that adjust the numerical solution to the exact solution.

where $\vec{F} = \frac{-\hbar^2}{2m^*}\vec{\nabla}\psi$, taking into account the property shown in equation 2-243 in equation 2-242, we have:

$$\int_\Omega \frac{\hbar^2}{2m^*}\vec{\nabla}\psi\cdot\vec{\nabla}\phi d\Omega + \int_\Omega \vec{\nabla}\cdot\left[\left(\frac{-\hbar^2}{2m^*}\vec{\nabla}\psi\right)\phi\right]d\Omega + \int_\Omega (V-E)\,\psi\phi d\Omega = 0, \tag{2-244}$$

Using Green's first identity theorem:

$$\int_\Omega \nabla\cdot(u\nabla v)d\Omega = \oint_{\partial\Omega} u\nabla v\cdot\hat{n}d(\partial\Omega), \tag{2-245}$$

where $\partial\Omega$ is the boundary of the system and $\hat{n}$ is the unit vector pointing outward and perpendicular to the surface. Applying the identity of the equation 2-245 to the equation 2-244, we can obtain the following expression:

$$\int_\Omega \frac{\hbar^2}{2m^*}\vec{\nabla}\psi\cdot\vec{\nabla}\phi d\Omega - \oint_\Omega \frac{\hbar^2}{2m^*}\vec{\nabla}\psi\cdot\hat{n}\phi d(\partial\Omega) + \int_\Omega (V-E)\,\psi\,\phi\,d\Omega = 0, \tag{2-246}$$

when stationary problems are considered, the zero-flow condition of the system is considered at the boundaries, therefore, the second term is zero [14]. The final simplified version of the weak formulation is of the form:

$$\int_\Omega \left(\frac{\hbar^2}{2m^*}\vec{\nabla}\psi\cdot\vec{\nabla}\phi d\Omega\right) + \int_\Omega (V-E)\,\psi\phi d\Omega. \tag{2-247}$$

Equation (2-247) includes the superposition of the functions or their gradient, which simplifies the calculations for small regions where the superposition is not zero. The great advantage of the weak form is that no second-order derivative is involved and the functions ψ and ϕ have to be continuous and differentiable only in the subdomains.

To understand how the method operates, Figure **2-6** illustrates how a domain is discretized with the FEM. First, the function ψ is divided into $n-1$ elements, or subdomains, with the same length l_e, corresponding to the n nodes. In the figure, the black solid line is the exact values, and the red dotted line is the FEM approximation. Something to remember is that within a subdomain (contained between x_i and x_{i+1}) only two base functions contribute, the others being zero. Vertical black dotted lines delimit the subdomain.

The example illustrated in Figure **2-6** uses linear functions based on u_i with $i = 1, 2, 3 \cdots, n$. With the above, it is possible to write the real solution to the problem by making an approximation through the linear combination of the functions $\psi = \sum_i u_i \psi_i$, where the coefficients ψ_i are exact solutions of the problem in each node x_i since the function is 1 there. The coefficients ψ_i can be obtained from the equation that governs the problem under study, which are simplified as a set of algebraic equations due to discretization.

In Figure **2-6**, the shaded part represents the basis function and the periodic behavior that it presents in a regular partition. Considering that the weak form of PDE contains the multiplication of the solution and the basic functions or their gradients, integral overlap only occurs between two neighboring functions, which facilitates the calculations. So, to solve a given problem, the first step is to take the initial differential equation to its weak form, then the integrals are solved in each of the subdomains and the sum of all these contributions corresponds to the complete solution. What finally sums up in a system of n algebraic equations that correspond to the n nodes in the discretization.

There are two common ways of choosing functions to do the discretization, the Rayleigh-Ritz and Galerkin methods. The main difference between the two methods is that Galerkin uses the same set of basis and test functions, while Rayleigh-Ritz does not. The Galerkin method is very precise for solving differential equations in systems with complex geometries since it allows the generation of adaptive meshes as well as a refinement or increase of nodes at points that are difficult to solve [7, 22, 28].

References

[1] Economou, E. N. Green's functions in quantum physics. *Springer Science & Business Media.* **2006**, *7*.

[2] Cuevas, J. C.; Scheer, E. Molecular electronics: an introduction to theory and experiment. *World Scientific.* **2010**, *1*.

[3] Ferry, D.; Goodnick, S. M. Transport in nanostructures. *Cambridge university press.* **1999**, *6*.

[4] Slater, J. C.; Koster, G. F. Simplified LCAO method for the periodic potential problem. *Phys. Rev.* **1954**, *6*, 1498-1524.

[5] Medina-Cuy, F. Propiedades térmicas y de transporte de la molécula de Bifenilo. [Universidad Pedagógica y Tecnológica de Colombia] *repositorio.uptc.edu.co.* **2014**.

[6] Di Ventra, M. Electrical transport in nanoscale systems. *Cambridge university press.* **2008**, *1*.

[7] Gil Corrales, J. A. Electronic properties in heterostructures under external fields. [Universidad de Antioquia] *bibliotecadigital.udea.edu.co.* **2022**.

[8] Paulsson, M. Non equilibrium green's functions for dummies: Introduction to the one particle NEGF equations. *cond-mat.mes-hall.* **2008**, 1-9.

[9] Datta, S. Electronic transport in mesoscopic systems. *Cambridge university press.* **1997**.

[10] Datta, S. Quantum transport: atom to transistor. *Cambridge university press.* **2005**.

[11] Gainza, J. Thermoelectric materials, chalcogenides and pnictides, with new phenomenologies: synthesis and characterization. [Universidad Complutense de Madrid] *hdl.handle.net/10261/274663.* **2022**.

[12] Yelgel, O. C. Thermoelectric Properties of V-VI Semiconductor Alloys and Nanocomposites. *University of Exeter (United Kingdom).* **2013**.

[13] Musland, L. Theory and calculations of thermoelectric transport in heterostructures. [University of Oslo.] *arXiv:1910.11303 cond-mat.mes-hall.* **2019**.

[14] Ziman, J. M. Electrons and phonons: the theory of transport phenomena in solids. *Oxford university press.* **2001**.

[15] Supriyo, D. Lessons From Nanoelectronics: A New Perspective On Transport-Part A: Basic Concepts. *World Scientific.* **2017**.

[16] Karamitaheri, H. Thermal and thermoelectric properties of nanostructures. *iue.tuwien.ac.at/phd/karamitaheri/DissHTML.html.* **2013**.

[17] Kulbachinskii, V. A.; Oveshnikov, L. N.; Lunin, R. A.; Yuzeeva, N. A.; Galiev, G. B.; Klimov, E. A.; Maltsev, P. P. Experimental determination of the electron effective masses and mobilities in each dimensionally-quantized subband in an In x Ga 1- x As quantum well with InAs inserts. *Semiconductors* **2015**, *49*, 199–208.

[18] Liu, C. T.; Lin, S. Y.; Tsui, D. C.; Lee, H.; Ackley, D. Cyclotron resonance measurements of electron effective mass in strained AlGaAs/InGaAs/GaAs pseudomorphic structures. *Applied physics letters* **1988**, *53*, 2510–2512.

[19] Herrmann, R.; Krüger, H. Determination of the Effective Masses of the Electron Jack, Hole Octahedron, and Ellipsoids of Molybdenum by Cyclotron Resonance Measurements. *physica status solidi (b)* **1970**, *41*, 99–106.

[20] Everett, G. E. Cyclotron Resonance Measurements in Bismuth. *Physical Review* **1962**, *128*, 2564.

[21] Peter, Y. U.; Cardona, M. Fundamentals of semiconductors: physics and materials properties. *Springer Science & Business Media* **2010**.

[22] Vinasco, J. Electronic and optical properties of GaAS/AlGaAs quantumrings: effects of geometry, impurities, electric, magnetic, and intense laser fields. Doctoral thesis. Universidad de Antiquia, Medellín, Colombia. **2019**.

[23] Planelles, J.; Climente, J.; Rajadell, F. Quantum rings in tilted magnetic fields. *Physica E* **2006**, *33*, 370-375.

[24] Pourmand, S.; Rezaei, G.; Vaseghi, B. Impacts of external fields and Rashba and Dresselhaus spin-orbit interactions on the optical rectification, second and third harmonic generations of a quantum ring. *The European Physical Journal B* **2019**, *92:96*, 2-7.

[25] Rosencher, E.; Bois, P.; Model system for optical nonlinearities: Asymmetric quantum wells. *Phys. Rev. B* **1991**, *14*, 11315.

[26] Ahn, D.; Chuang, S.-L. Calculation of linear and nonlinear intersubband optical absorptions in a quantum well model with an applied electric field. *IEEE J. Quantum Elect* **1987**. *23*, 2196.

[27] Akimov, V.; Tiutiunnyk, A.; Demediuk, R.; Tulupenko, V.; Soto. E.; Peñaranda, J.; Orellana, P.; Ojeda, J.; Gil-Corrales, J.; León-González, J.; Toscano-Negrette, R.; Caicedo, D.; Mora, J.; Restrepo, R.; Morales, A.; Duque, C.M.; Duque, C.A. Study of delta-doped quantum wells, energy levels and applications in the terahertz region. *Editorial Instituto Antioqueño de Investigación*. **2022**.

[28] Ern, A.; Guermond, J.-L. Theory and practice of finite elements. *Springer 159*. **2004**.

[29] Onsager, Lars. Reciprocal relations in irreversible processes I. *Physical review*, **1931**, *37*, 4, 405-426.

[30] Onsager, Lars. Reciprocal relations in irreversible processes II. *Physical review*, **1931**, *38*, 12, 2265-2279.

[31] Callen, H. B. Thermodynamics and an introduction to thermostatistics. *Wiley*, **1960**.

3 Optical Properties in a ZnS/CdS/ZnS Core/Shell/Shell Spherical Quantum Dot: Electric and Magnetic Field and Donor Impurity Effects

3.1 Abstract

A theoretical analysis of optical properties in a ZnS/CdS/ZnS core/shell/shell spherical quantum dot was carried out within the effective mass approximation. The corresponding Schrödinger equation was solved using the finite element method via the 2D axis-symmetric module of COMSOL-Multiphysics software. Calculations included variations of internal dot radius, the application of electric and magnetic fields (both oriented along z-direction), as well as the presence of on-center donor impurity. Reported optical properties are the absorption and relative refractive index change coefficients. These quantities are related to transitions between the ground and first excited states, with linearly polarized incident radiation along the z-axis. It is found that transition energy decreases with the growth of internal radius, thus causing the red-shift of resonant peaks. The same happens when the external magnetic field increases. When the strength of applied electric field is increased, the opposite effect is observed, since there is a blue-shift of resonances. However, dipole matrix moments decrease drastically with the increase of the electric field, leading to a reduction in amplitude of optical responses. At the moment impurity effects are activated, a decrease in the value of the energies is noted, significantly affecting the ground state, which is more evident for small internal radius. This is reflected in an increase in transition energies.

Keywords: core/shell/shell quantum dot; donor impurity; external electric and magnetic field; absorption coefficients.

3.2 Introduction

The study of low-dimensional semiconductor heterostructures (LDSH) has gained relevance due to their high-efficient optoelectronic properties. In accordance, numerous theoretical and experimental studies have been performed [1–5]. Among these structures it is possible to mention the quantum wells (with charge carrier confinement along one dimension), quantum wires (confinement in two dimensions), and quantum dots (QDs). In the latter, electrons (holes) are confined in all spatial directions, allowing for electronic properties of great scientific and technological interest. Such features can be controlled by modifying the size and/or the geometry of the system through the application of external electromagnetic probes, hydrostatic pressure, and temperature; and also by suitable doping with impurity atoms [6–15]. These LDSH have found practical realization in nanophotonics and nanoelectronics thanks to controlled fabrication using techniques such as molecular beam epitaxy (MBE), ultrasonic sol-gel, and hydrothermal method, among others; with nanostructure sizes below 10 nm [16–21].

Among the most studied QDs, different geometrical shapes are present: cylindrical, pyramidal, conical, and spherical [22–25]. In this work, we focus on studying a kind of core/shell/shell

spherical QD, which consists of a semiconductor material surrounded by another one which exhibits a different value of the energy band gap. In a QD, discrete energies depend on size, external fields, band gaps, etc., with which physical and optical properties can be controlled and used for applications in fields such as electronics, medicine, chemistry, and biology [26]. The most used semiconductor compounds to fabricate QDs are those formed by atoms of II–VI, III–V, and IV–VI groups of the periodic table. Lately, researchers have become of significant interest in studying core-shell QDs based on ZnS/CdS semiconductors, which find a number of applications in photovoltaics, optoelectronics, medicine, and so on [27–30]. For example, Linkov et al. demonstrated that multicomponent core/shell CdSe/ZnS/CdS/ZnS QDs can be used as optimal fluorescent probes for the development of systems for cancer diagnosis and treatment using anticancer compounds based on acridine derivatives [31]. In 2019, Zeiri et al. conducted a study on the third-order nonlinear optical susceptibility for CdS/ZnS/CdS/ZnS core/shell/well/shell spherical QDs, reporting that both the position and the intensity of the peaks can be controlled by varying the thickness of the shell. Furthermore, as the width of the inner or outer layer increases, the susceptibility peaks are shifted towards the red with increasing intensities [32]. In 2022, Kuzyk et al. studied the possible applications in nanomedicine of deformation effects in CdSe-core/ZnS/CdS/ZnS-shell QDs, and how they interact with human serum albumin, finding that QDs with three layers are more sensitive to deformation and, at the same time, the strain is almost independent of the radius of the core. In the proposed system, significant strains arise in the CdSe/ZnS/CdS/ZnS/Qd-human serum albumin bionanocomplexes, which can lead to an energy shift of the conduction band edge by 40 meV. Lastly, they state that their results can be used to develop bionanosensors for the determination of albumin concentration [33].

Here, we shall use the effective mass approximation to conduct a theoretical analysis of ZnS/CdS/ZnS core-shell-shell QD optical properties. The electronic states in the system are numerically determined using finite element method (FEM) as implemented in COMSOL-Multiphysics package in the axis-symmetric module. The calculations include the variation of the internal radius (R_1), as well as changes in the intensities of the external magnetic and electric fields, both with and without the presence of an on-center donor impurity. The analysis of optical response goes through the evaluation of linear and nonlinear coefficients of both light absorption and relative refractive index change from the corresponding expressions derived within the density matrix formalism. The article's organization is as follows: Section 3.3 presents the theoretical framework, in Section 3.4, we discuss the results, and Section 3.5 is devoted to the main conclusions of the work.

3.3 Theoretical Model

Figure **3-1** shows the investigated system, a ZnS/CdS/ZnS spherical QD of the core/shell/shell type (a). The dimensions of the core, inner shell, and outer shell are R_1, R_2,

and R_3, respectively (b). In (b), the lowest part of the figure shows a schematic view of the radial-dependent confinement potential. This function is set as zero within the CdS material, V_0 in the ZnS material, and infinite in the vacuum-external region. Effects of an on-center donor impurity, an axially applied magnetic ($\vec{B}$), and an electric ($\vec{F}_z$) field, have been taken into account. In Figure 3-1c, the projection on the plane $\varphi = 0$ of the structure is presented. The rotation of the region shown around the z-axis gives rise to the structure shown in Figure 3-1a. In addition, the particular mesh used in FEM calculations is schematically presented. It is readily apparent that in the region of the first shell layer, much greater refinement of the mesh has been considered compared to that chosen for the other two regions. Dirichlet boundary conditions are assumed on the semicircle of radius $r = R_3$ (the outer one).

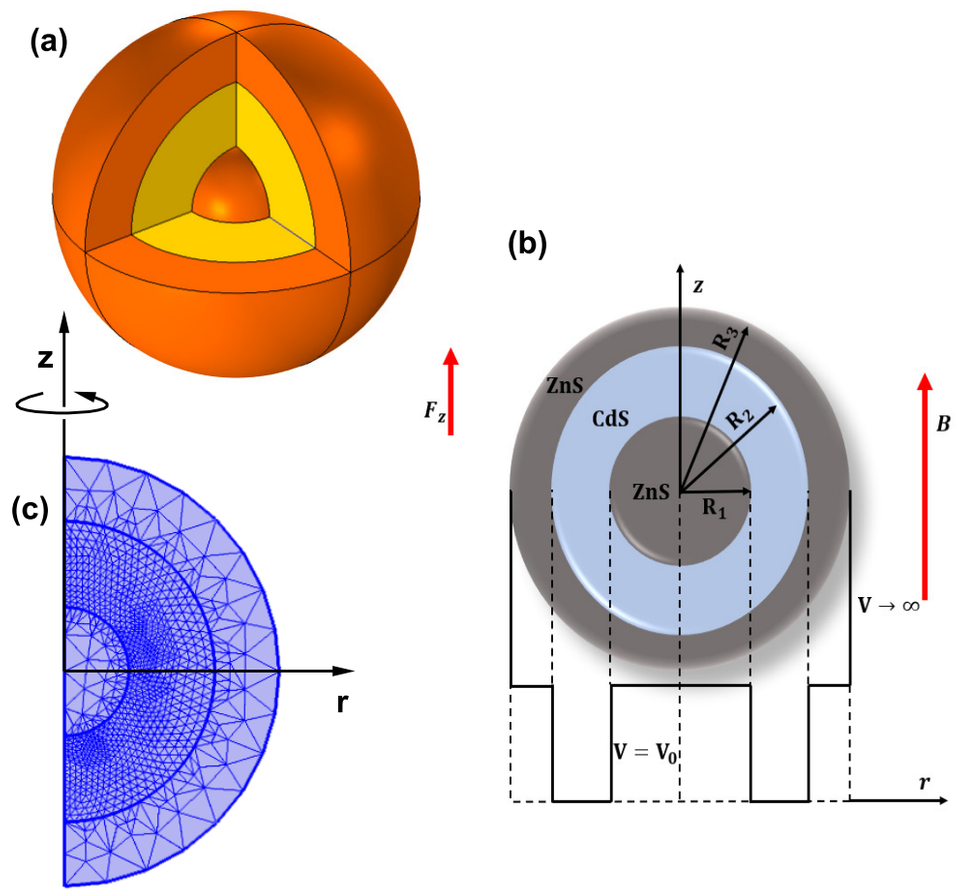

Figure **3-1**: (**a**) ZnS/CdS/ZnS spherical quantum dot heterostructure considered in this work. In (**b**), the dimensions of the quantum dot and the applied axial electric and magnetic field are indicated together with the radial dependent confinement potential. In (**c**) is depicted the $\varphi = 0$-projection of the heterostructure (where cylindrical coordinates are considered) together with the refined mesh used in the finite element method calculations.

In Cartesian coordinates, the parabolic band effective-mass Schrödinger equation for a conduction electron confined in the structure, with all the contributions mentioned above, is written in the form:

$$\left[\frac{1}{2\,m^{*c}}\left(\vec{p}+e\,\vec{A}\right)^2+e\,F_z\,z+V(x,y,z)-\frac{\kappa\,e^2}{4\,\pi\,\varepsilon_0\,\varepsilon_r^c\,R}\right]\psi(x,y,z)=E\,\psi(x,y,z)\,, \tag{3-1}$$

where m^{*c} is the electron effective mass, ε_r^c is the static dielectric constant (the index c indicates the core or shell materials), $R=\sqrt{x^2+y^2+z^2}$ is the electron-impurity distance (with the shallow-donor impurity placed at the center of the structure), $\vec{p}=-i\,\hbar\,\vec{\nabla}$, e is the absolute value of the electron charge, and $V(x,y,z)=V(r)$ (with $V(r)$ expressed in cylindrical coordinates) is the radially symmetric confinement potential. Here, κ is a parameter that controls the presence or absence of the shallow donor impurity ($\kappa=0$ removes the impurity effects whereas $\kappa=1$ turns them on). Besides, $\vec{A}=-\frac{B}{2}\,(y\,\widehat{i}-x\,\widehat{j})$ represents the potential vector associated to the applied magnetic field, where $\vec{B}=\vec{\nabla}\times\vec{A}$ comes from the symmetric gauge. As mentioned, we impose Dirichlet boundary conditions at the outer edges of the barrier matrix. The process also assumes BenDaniel-Duke conditions at the inner QD interfaces (see Figure **3-1**b,c).

The m^{*c} and $V(r)$ terms in Equation (3-1) depend on the radial position in the heterostructure and they are expressed as:

$$m^{*c}=\begin{cases}m^{*\mathrm{ZnS}}\,, & \text{if } 0\le r\le R_1\,,\\ m^{*\mathrm{CdS}}\,, & \text{if } R_1<r\le R_2\,,\\ m^{*\mathrm{ZnS}}\,, & \text{if } R_2<r\le R_3\,,\end{cases} \tag{3-2}$$

and

$$V(r)=\begin{cases}V_0\,, & \text{if } 0<r\le R_1\,,\\ 0\,, & \text{if } R_1<r\le R_2\,,\\ V_0\,, & \text{if } R_2<r\le R_3\,,\\ \infty\,, & \text{if } r>R_3\,.\end{cases} \tag{3-3}$$

Expanding Equation (3-1), and using the azimuthal symmetry condition of the system, it is possible to propose in cylindrical coordinates a solution of the type $\psi(x,y,z)=\psi(r,\varphi,z)=R(r,z)\,e^{i\,m\,\varphi}$, where the m is the principal quantum number. Consequently, the $R(r,z)$ function satisfies the differential equation

$$\begin{aligned}&\left[-\frac{\hbar^2}{2\,m^{*c}}\nabla_{r,z}^2+\frac{m^2\,\hbar^2}{2\,m^{*c}\,r^2}+\frac{\hbar\,e\,B\,m}{2\,m^{*c}}+\frac{e^2\,B^2\,r^2}{8\,m^{*c}}+e\,F_z\,z\right.\\ &\left.-\frac{k\,e^2}{4\,\pi\,\varepsilon_0\,\varepsilon_r^c\,R}+V(r)\right]R(r,z)=E_m\,R(r,z),\end{aligned} \tag{3-4}$$

where $\nabla^2_{r,z}$ is the r- and z-dependent two-dimensional Laplacian operator and $\rho = \sqrt{r^2 + z^2}$ is the electron-impurity distance.

The study is focused on electron confinement effects related to QD dimensions and on the influence of externally applied electric and magnetic fields, with and without on-center donor impurity effects. The Equation (3-4), is solved via the FEM [34–36], using the COMSOL-Multiphysics licensed software [37–39], with which it is possible to obtain the wave functions and the energies of the different states. The settings used to build an extra fine, user-controlled mesh are: 6185 mesh vertices, 12,104 triangles, 460 edge elements, 10 vertex elements, 0.6179 minimum element quality, 0.8964 medium element quality, 0.2051 element area ratio, and 226.2 nm^2 mesh area. Employed hardware contains a single 11th-generation i7 processor. Obtained electron states are then used to evaluate the optical properties (absorption and the relative refractive index change coefficients) associated with transitions between the lowest two energy levels (the ground state and the first excited state). Keeping in mind the characteristic spherical symmetry of the system, the expression to evaluate the first-order absorption coefficients is:

$$\alpha^{(1)}(\omega) = \sqrt{\frac{\mu_0}{\varepsilon_r\,\varepsilon_0}}\;\frac{\omega\, e^2\,\sigma\,\hbar\,\Gamma_{12}\,|M_{12}|^2}{(E_{12}-\hbar\,\omega)^2 + (\hbar\,\Gamma_{12})^2}\,. \tag{3-5}$$

The expression to evaluate the third-order absorption coefficients is given by

$$\alpha^{(3)}(\omega, I) = -\sqrt{\frac{\mu_0}{\varepsilon_r\,\varepsilon_0}}\;\frac{2\,I}{n\,\varepsilon_0\,c}\;\frac{\omega\, e^4\,\sigma\,\hbar\,\Gamma_{12}\,|M_{12}|^4}{[(E_{12}-\hbar\,\omega)^2 + (\hbar\,\Gamma_{12})^2]^2}\,. \tag{3-6}$$

The total absorption coefficient is the sum of the linear and the third order:

$$\alpha(\omega, I) = \alpha^{(1)}(\omega) + \alpha^{(3)}(\omega, I)\,. \tag{3-7}$$

The corresponding expressions to evaluate the relative refractive index change are, respectively:

$$\frac{\Delta n^{(1)}(\omega)}{n} = \frac{\sigma\, e^2\,|M_{12}|^2}{2\,\varepsilon_0\,\varepsilon_r}\;\frac{E_{12}-\hbar\,\omega}{(E_{12}-\hbar\,\omega)^2 + (\hbar\,\Gamma_{12})^2}\,, \tag{3-8}$$

$$\frac{\Delta n^{(3)}(\omega)}{n} = \frac{-\sigma\,\mu_0\,c\,I}{n^3\,\varepsilon_0}\;\frac{e^4\,|M_{12}|^4\,(E_{12}-\hbar\,\omega)}{[(E_{12}-\hbar\,\omega)^2 + (\hbar\,\Gamma_{12})^2]^2}\,, \tag{3-9}$$

and

$$\frac{\Delta n(\omega, I)}{n} = \frac{\Delta n^{(1)}(\omega)}{n} + \frac{\Delta n^{(3)}(\omega, I)}{n}\,. \tag{3-10}$$

The above expressions arise from the density matrix formalism as developed in Ref. [40], where $E_{12} = E_2 - E_1$ is the transition energy between the initial ("1") and final ("2") state. In addition, M_{12} represents the reduced off-diagonal dipole matrix element between the two electronic states (divided by the charge of the electron). For z-polarized incident radiation,

this quantity can be written as $M_{12} = \langle\psi_1(r,\varphi,z)|z|\psi_2(r,\varphi,z)\rangle$. Additionally, $\hbar\Gamma_{12}$ is a damping term associated with the electron lifetime due to the dispersion between subbands (which, here, has a value of 0.7 meV). Besides, $n = \sqrt{\varepsilon_r}$ is the relative refractive index, μ_0 is the vacuum magnetic permeability ($4\,\pi \times 10^{-7}\,\mathrm{T\,m\,A^{-1}}$), σ is the charge carrier density, set at 3.0×10^{22} m^{-3}. Finally, I represents the intensity of the optical radiation in the system, whose value has been chosen equal to 30 MW/m^2.

The interaction energy between the electron and the impurity is known as the binding energy. It is calculated from the following expression:

$$E_b = E_{\kappa=0} - E_{\kappa=1}, \tag{3-11}$$

where $E_{\kappa=0}$ and $E_{\kappa=1}$ are the ground state energies without ($\kappa = 0$) and with impurity ($\kappa = 1$), respectively.

3.4 Results and Discussion

Besides values above commented for some input parameters, the remaining ones used in this work are: $m^{*\mathrm{CdS}} = 0.19\,m_0$, $m^{*\mathrm{ZnS}} = 0.25\,m_0$, $\varepsilon^{\mathrm{CdS}} = 8.3$, $\varepsilon^{\mathrm{ZnS}} = 8.9$, and $V_0 = 0.8$ eV. Here, m_0 is the free electron mass [41]. In Equations (3-5)–(3-10), the parameters n and ε_r are those corresponding to CdS.

In Figure **3-2**, the lowest electronic states of a ZnS/CdS/ZnS spherical core/shell/shell QD, for $F_z = 0$ and $B = 0$, are depicted as functions of the R_1 radius, with and without shallow-donor impurity effects. Figure **3-2**a,b show that the energy of the three lowest levels increases as R_1 augments. This effect is associated with the Heisenberg uncertainty principle since as the inner radius becomes larger, the thickness of the CdS shell, where the electron is confined, decreases. Greater confinement produces an increase in energy. Figure **3-2**b shows the effect of a shallow donor impurity placed at the QD center. In this case, the energy levels shift toward lower energies, below the conduction band, due to attractive electron-impurity interaction. The minimum value of the electron-impurity distance is for the ground state ($m = 0$). This explains why this state is the one that undergoes a greater displacement towards lower energies. The inset in Figure **3-2**a shows the electron-impurity binding energy as a function of the internal radius. One may notice a decrease in the binding energy as the internal radius grows. For example, for $R_1 = 1$ nm, it has a value of 39.195 meV, while for $R_1 = 4$ nm is 24.392 meV. In fact, as the radius R_1 increases, the electron moves further away from the impurity, and this causes the impurity-electron Coulomb interaction to decrease. Due to the spherical symmetry of the QD, in the absence and presence of impurities at the center of the quantum dot, the energies shown in Figure **3-2**a,b must have the same degeneracies of a bulk hydrogen atom. For example, the first excited state must be triply

degenerate, with the three solutions $m = 0, \pm 1$. Then, the second excited state has a five-fold degeneracy: $m = 0, \pm 1, \pm 2$.

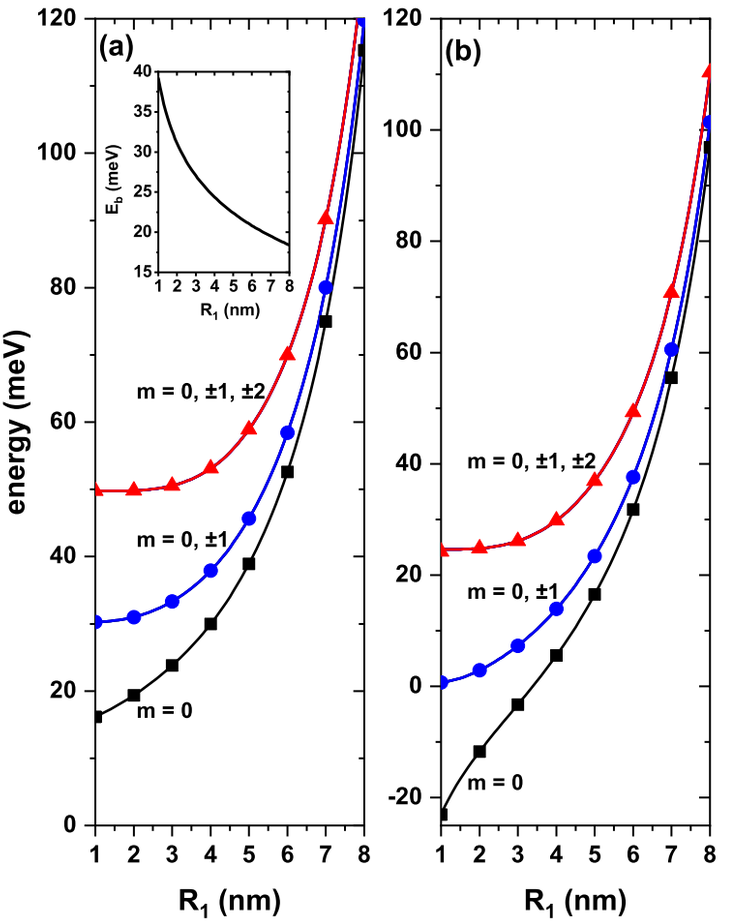

Figure **3-2**: The first three lowest electronic states of a ZnS/CdS/ZnS spherical core/shell/shell quantum dot as functions of the R_1 radius. Figure (**a**) presents the results without, and (**b**) those with effects of an on-center donor impurity, with $R_2 = 11\,\text{nm}$ and $R_3 = 12\,\text{nm}$, for different values of the m-quantum number and without effects of external electric and magnetic fields. Labels near the curves indicate the values of the m-quantum number. The inset in Figure (**a**) corresponds to the ground state (lowest state with $m = 0$) binding energy between the impurity and the electron as a function of the internal dot radius. In both panels, solid symbols correspond to the energies obtained by solving the three-dimensional problem using Equation (3-1).

With the aim of confirming the results obtained, we have proceeded to derive the solution directly from Equation (3-1), which corresponds to a three-dimensional problem. The corresponding outcome appears plotted in Figure **3-2** using solid symbols. As can be seen,

the results exactly coincide for both the 3D solution, Equation (3-1), and the 2D solution, Equation (3-6), which uses the axial symmetry of the problem. Likewise, in the case of the configuration without impurity, in the absence of applied fields, the problem of an electron confined in a multilayer QD with spherical symmetry has a quasi-exact solution. Accordingly, the wave function in the different regions of the QD can be written as a linear combination of radial Bessel functions. Applying the Ben Daniel-Duke boundary conditions, we arrive at a transcendental equation whose numerical solution leads to obtaining the energies of the confined particle. The full symbols have also been obtained by solving this quasi-exact problem, again showing an excellent agreement for the three calculation procedures used. One of the differences between obtaining the solution of Equations (3-1) and (3-6) lies in the computation time. Using a 2.8 GHz Intel i7-processor, obtaining the ground state energy [using Equation (3-6)], for a single value of R_1 in Figure **3-2**a, takes 3 s of computing time, a situation that increases by a factor of 4 when calculating the same energy in the 3D-module that corresponds to the solution of Equation (3-1).

Figure **3-3** contains plots of the lowest three electronic states in a ZnS/CdS/ZnS spherical core/shell/shell QD as functions of the applied magnetic field with and without on-center shallow donor impurity effects for several values of the m-quantum number. From Figure **3-3**a, it is possible to observe that the magnetic field breaks the first excited state triple degeneracy and the second excited state degeneracy. States with a positive value of m always increase in energy with the strengthening of the applied magnetic field. For states with a negative m-value, energies initially show a decreasing character with the magnetic field. They evolve to reach a minimum value, becoming the actual ground state of the system and, then, start to augment. Consequently, as a result of the modification of the energy spectrum due to the increment in magnetic field intensity, the ground state does not preserve the s-like symmetry. From this figure, it is also noticed that, with a zero magnetic field, the first and second excited states have degeneracies of order three and five, respectively, as indicated in the discussions of Figure **3-2**a,b. On the other hand, Figure **3-3**b shows the energies as functions of the external magnetic field, taking into account the effects of the donor impurity at the center of the QD. As commented, energy levels shift towards lower values due to the attractive nature of the Coulombic coupling with the ionized impurity. It is seen that in Figure **3-3**a,b, the energy behavior shows the same trend. Actually, the impurity effect under the magnetic field is not very noticeable compared to the system without the impurity since it changes from about 3.723 meV to 3.874 meV. This is reflected in the binding energy (see inset in Figure **3-3**b), where it increases as the magnetic field increases.

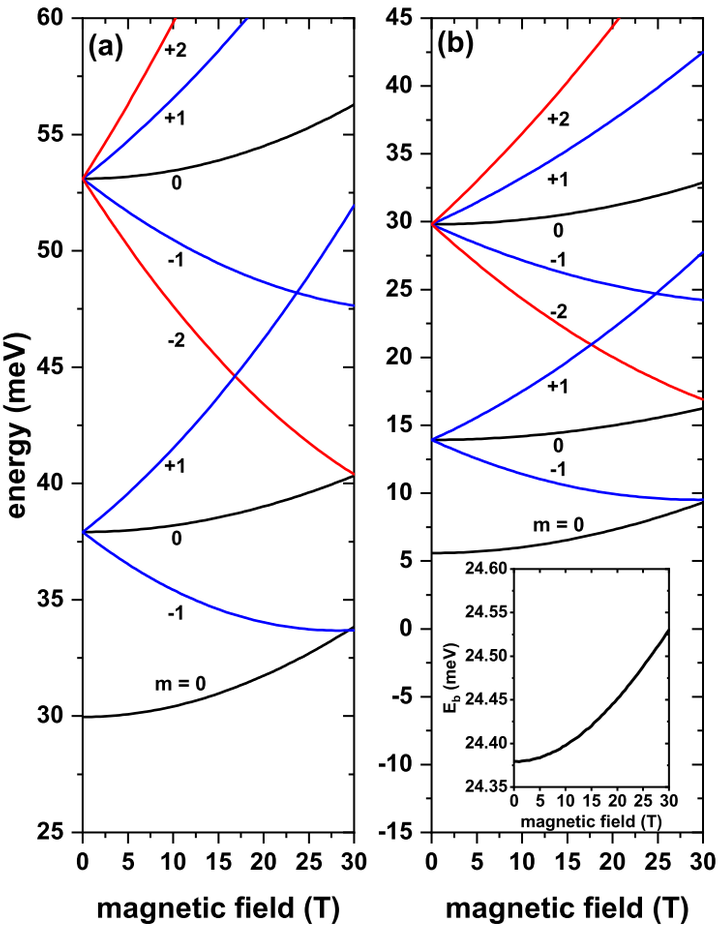

Figure **3-3**: The lowest three electronic states in a ZnS/CdS/ZnS spherical core/shell/shell quantum dot as functions of the applied magnetic field. Plot (**a**) contains results without, and (**b**) includes on-center donor impurity effect, for $R_1 = 4\,\text{nm}$, $R_2 = 11\,\text{nm}$, and $R_3 = 12\,\text{nm}$. Different values of the m-quantum number and without external electric field effects have been considered. Labels close to the curves give the values of the m-quantum number. The inset in (**b**) corresponds to the ground state (lowest state with $m = 0$) binding energy as a function of the applied magnetic field.

Results for allowed electron energies as functions of an externally applied static electric field appear plotted in Figure **3-4**, without and with on-center donor impurity effects for $B = 0$. Figure **3-4**a shows that energy drops as the intensity of the applied electric field increases. Due to the spherical symmetry of the system, the same behavior for negative values of the electric field occurs, so the plot only shows positive values of field intensity. In the high electric field regime, the wave function is compressed towards the regions with $z = -R_2$, the region at which the confining potential becomes deeper due to the negative potential contribution. As observed, the electric field breaks the triple degeneracy of the first excited

state, giving rise to a doubly degenerate energy state that comes from the solutions with $m = \pm 1$ and to a non-degenerate state for $m = 0$; for which the two antinodes are located along the z-axis. This state responds differently to the electric field than the states with $m = \pm 1$, since it initially shows a growing behavior, after which there begins a descent when the field becomes strong enough.

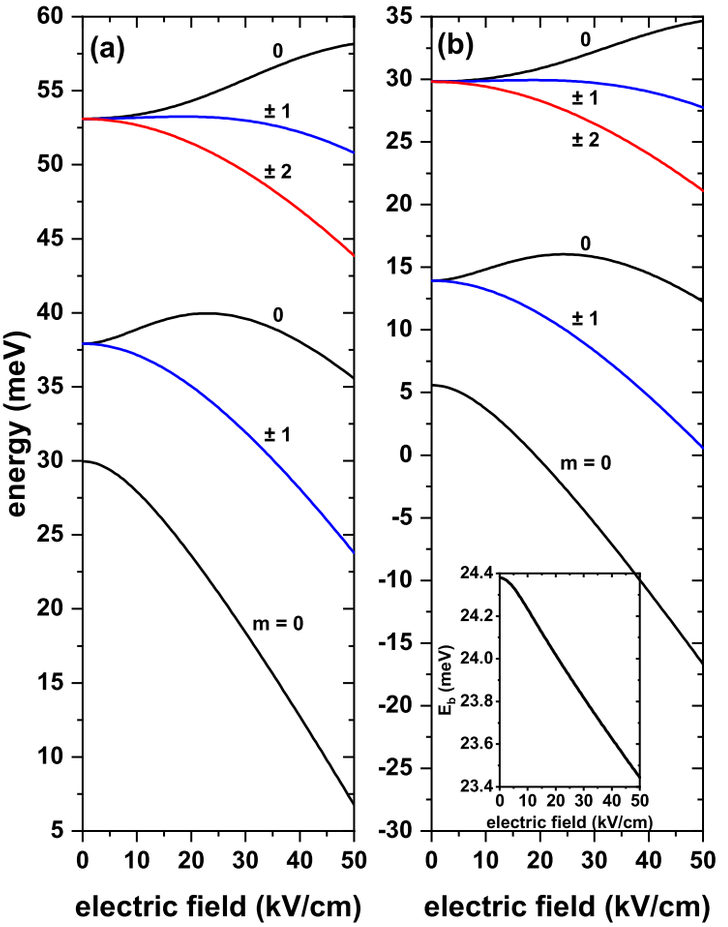

Figure **3-4**: The lowest electronic states in a ZnS/CdS/ZnS spherical core/shell/shell quantum dot as functions of the applied electric field. In (**a**), results are presented without, and in (**b**) with on-center donor impurity effects, with $R_1 = 4$ nm, $R_2 = 11$ nm, and $R_3 = 12$ nm. Different values of the m-quantum number and without external magnetic field effects have been considered. Labels above each of the curves give the values of the m-quantum number. The inset in (**b**) corresponds to the ground state (the lowest state with $m = 0$) binding energy as a function of the applied electric field.

Figure 3-4b presents the effects of the donor impurity combined with the electric field. The first thing to highlight is that there is a drop in the energy values compared to the situation

depicted in Figure 3-4a. The second aspect to note is the systematic decrease of the energies as the electric field increases—opposite to the trend reported in Figure 3-3b—and the presence of the same kind of degeneracies discussed above. This has to do with the impurity position at the center in the QD, which preserves the spherical symmetry. When analyzing the behavior of binding energy as the electric field increases (see inset in Figure 3-4b), it is noticed a reduction in its value; for example, for a zero electric field, we have a binding energy of 24.392 meV, and for an electric field of 50 kV/cm is 23.443 meV. The electric field confines the electron to the inner edge of the region $z = -R_2$, which implies a drop in the Coulomb interaction between the impurity and the electron since the effective electron-impurity distance augments.

Now, we report on the behavior of squared reduced dipole moment matrix element ($|M_{12}|^2$) for electron transitions from the ground state ($|1\rangle$) to the first excited state ($|2\rangle$) in a ZnS/CdS/ZnS spherical core/shell/shell QD, with $m = 0$. Results will be presented taking into account the influence of external fields—electric and magnetic—oriented along the z-direction, as well as the changes in the QD dimensions, controlled through R_1. Analysis of Figures 3-5–3-7 requires an understanding of wave functions symmetries. Transitions studied are those involving states with $m = 0$ since the used incident radiation is linearly polarized in the z-direction, thus making the transitions to states with $m \neq 0$ to be forbidden.

Variation of $|M_{12}|^2$ and transition energy, E_{12}, as functions of the internal radius for a confined electron in a ZnS/CdS/ZnS spherical QD with and without the effects of on-center donor impurity is shown in Figure 3-5. According to Figure 3-5a, by increasing the QD internal radius, the size of the shell -where the electron is confined- decreases, causing a linear increase of $|M_{12}|^2$. This behavior is shown in the inset, from which one may conclude that the spatial overlap between wave functions increases when moving from 1 nm to 8 nm in the internal radius. In Figure 3-5b, with the inclusion of donor impurity influence, a similar behavior is observed for $|M_{12}|^2$. From the inset in Figure 3-5b, it is seen that the ground state wave function is attracted to the impurity while the first excited wave function remains almost unchanged. Hence, the overlap between both states decreases concerning the case without impurity. For example, $|M_{12}|^2$ has a value of 13.330 nm^2 for $R_1 = 1$ nm without impurity. With impurity effects, the value falls to 8.380 nm^2, with a difference of 4.950 nm^2, which becomes smaller as the radius increases, weakening the Coulombic interaction. Figure 3-5c,d show the corresponding variation of the transition energy from the ground state to the first excited state, with and without impurity, from which it is seen that as the R_1 increases, this energy decreases. As the internal radius increases, the shell decreases, causing the energies of the ground state and the first excited state to increase, becoming closer to each other for large radii (see Figure 3-2). From these two plots, Figure 3-5c,d, one may conclude that the transition energy is higher for small internal radii with donor impurity effects. This happens because, at a small internal radius, the interaction between the impurity and the

electron is greater, causing the electron energies to fall below the conduction band (see Figure 3-2b). But, when the inner radius gets larger, the impurity-electron interaction becomes weaker, making the transition energy similar to the case without impurity. For example, when $R_1 = 6$ nm, without impurity, the transition energy is 5.820 meV, and with impurity, it is 5.876 meV, having a difference of 0.056 meV.

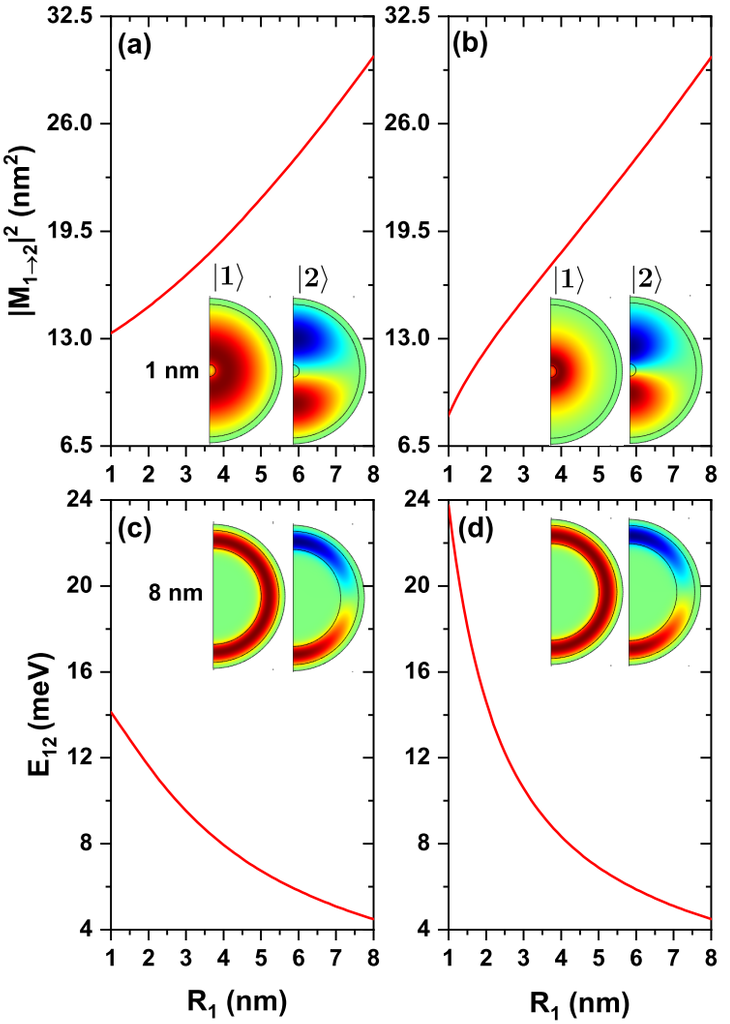

Figure **3-5**: The variation of the $|M_{12}|^2$ (**a**,**b**), and the transition energy (**c**,**d**), as functions of the internal radius R_1, for transitions from the ground state ($|1\rangle$) to the first excited state ($|2\rangle$) with $m = 0$, for an electron confined in a ZnS/CdS/ZnS spherical QD. (**a**,**c**), present the results without, and (**b**,**d**) with the effects of a donor impurity located at the center of the dot system. Calculations are with $R_2 = 11\,\text{nm}$ and $R_3 = 12\,\text{nm}$, without effects of external electric and magnetic fields.

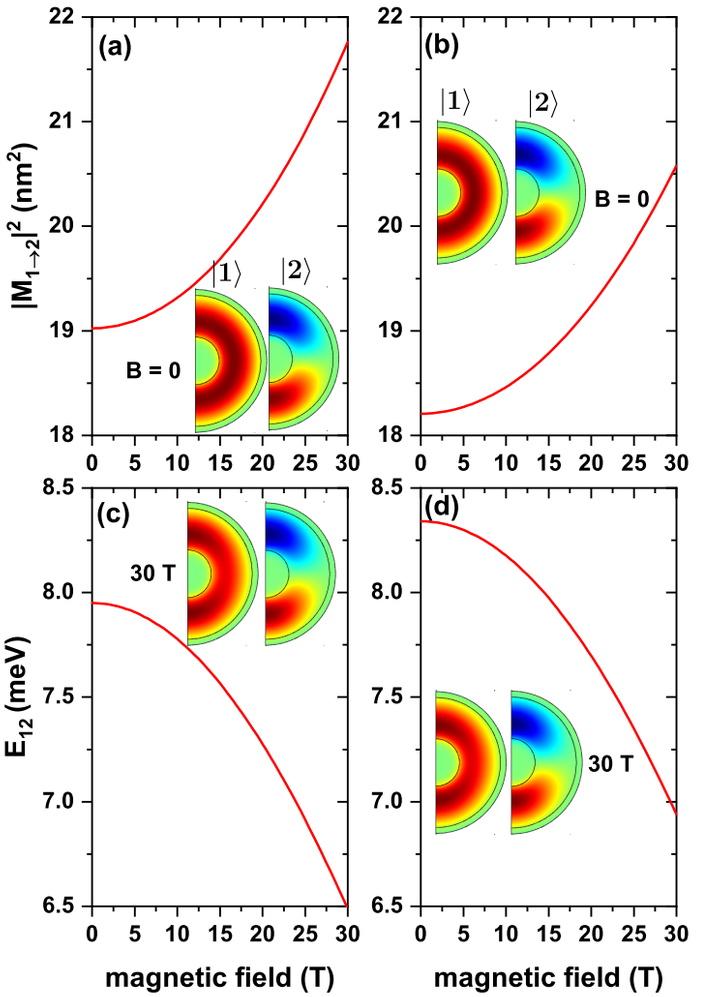

Figure **3-6**: The variation of $|M_{12}|^2$ (**a**,**b**), and the transition energy (**c**,**d**), as a function of the magnetic field, for transitions from the ground state ($|1\rangle$) to the first excited state ($|2\rangle$) with $m = 0$, for an electron confined in a ZnS/CdS/ZnS spherical QD. (**a**,**c**) are without, and (**b**,**d**) are with the effects of a donor impurity located at the QD center. Calculations are with $R_1 = 4$ nm, $R_2 = 11$ nm, and $R_3 = 12$ nm, without electric field effects.

Plots in Figure **3-6**, represent results for the same quantities as in Figure **3-5** but considering the variation of the intensity of the applied static magnetic field. From Figure **3-6**a, it is noticed an increase in $|M_{12}|^2$ as the strength of the applied magnetic field increases. This happens because the ground state gradually changes from a uniformly distributed probability density at $B = 0$ to a concentrated probability density at the upper and lower regions of the QD for $B = 30\,\mathrm{T}$. At these regions, the first excited state presents its maximum probability density, so the overlap between wavefunctions becomes larger. Effects associated with an on-center donor impurity appear in Figure **3-6**b, showing the same behavior as in

Figure 3-6a. That is, when comparing the values of $|M_{12}|^2$ for the system with and without impurity, a lower value is seen when there are impurity effects. For example, when $B = 0$, in the absence of any impurity, $|M_{12}|^2$ has a value of 19.024 nm^2. In the case that considers the presence of an ionized impurity, it has a value of 18.208 nm^2. Switching on the magnetic field to $B = 30$ T leads to a similar behavior. In the case without impurities, it has a value of 21.760 nm^2, and for the case with an on-center donor, it has a value of 20.581 nm^2. This is because, at zero applied magnetic field, the ground state wave function has its probability density concentrated around the impurity. The first excited state presents a more significant probability density localization at the upper and lower QD regions, thus producing a smaller overlap between the involved states. In the 30 T case, the ground state wave function probability density is concentrated at the upper and lower areas of the QD. Consequently, the overlap with the first excited state wave function grows since its probability density largely locates within the same regions. At the same time, Figure 3-6c,d show the transition energy from the ground state to the first excited state, with and without a donor impurity. It can be observed that as the magnetic field increases, this quantity diminishes. This happens because the action of the magnetic field is to bring together the energies of the ground state and the first excited state for $m = 0$ (see Figure 3-3). So, the higher the magnetic field, the smaller the difference between these energies. From both plots, it can be seen that the transition energy is higher for small magnetic fields with donor impurity effects than when the impurity is not considered. This is due to the impurity-induced energy shift towards lower values, making the difference in E_b greater. This shift has an average magnitude of 0.412 meV.

Figure 3-7 concerns to the same kind of study reported in previous Figures 3-5 and 3-6, considering the applied electric field as the external probe. Results plotted in Figure 3-7a show that as the applied electric field strengthens, there is a magnitude decay of $|M_{12}|^2$. Initially. it reaches a maximum value for $F_z = 0$, and then, it decreases. This maximum appears because the ground state wave function is uniformly distributed over the QD confinement region. In contrast, the first excited state has its lobes concentrated at $z = \pm R_2$, thus producing the largest wave function overlap. The decreasing nature of $|M_{12}|^2$ is because the electric field pushes $|1\rangle$ and $|2\rangle$ toward $z = -R_2$; for example, at $F_z = 50$ kV/cm the state $|1\rangle$ is concentrated at $z = -R_2$, and the lower lobes of state $|2\rangle$ are also concentrated there, giving the lowest overlap (see inset in Figure 3-7). In Figure 3-7b, the results presented include the effects of the donor impurity. A behavior very similar to the system without impurity is noted, with the difference that, for small values of the electric field, $|M_{12}|^2$ has a smaller magnitude. For example, for $F_z = 0$, without impurities, $|M_{12}|^2$ has a value of 19.024 nm^2, and 18.208 nm^2 with impurity, although this difference begins to disappear as the electric field increases. This situation has to do with the electron-impurity interaction. For low electric fields, it is the dominant one -since the electron is closer to the impurity-. In contrast, it loses strength in large fields due to the more significant electron-

impurity separation. In this case, the ground state wave function gets closer to the impurity, so the overlap is smaller than in Figure 3-7a.

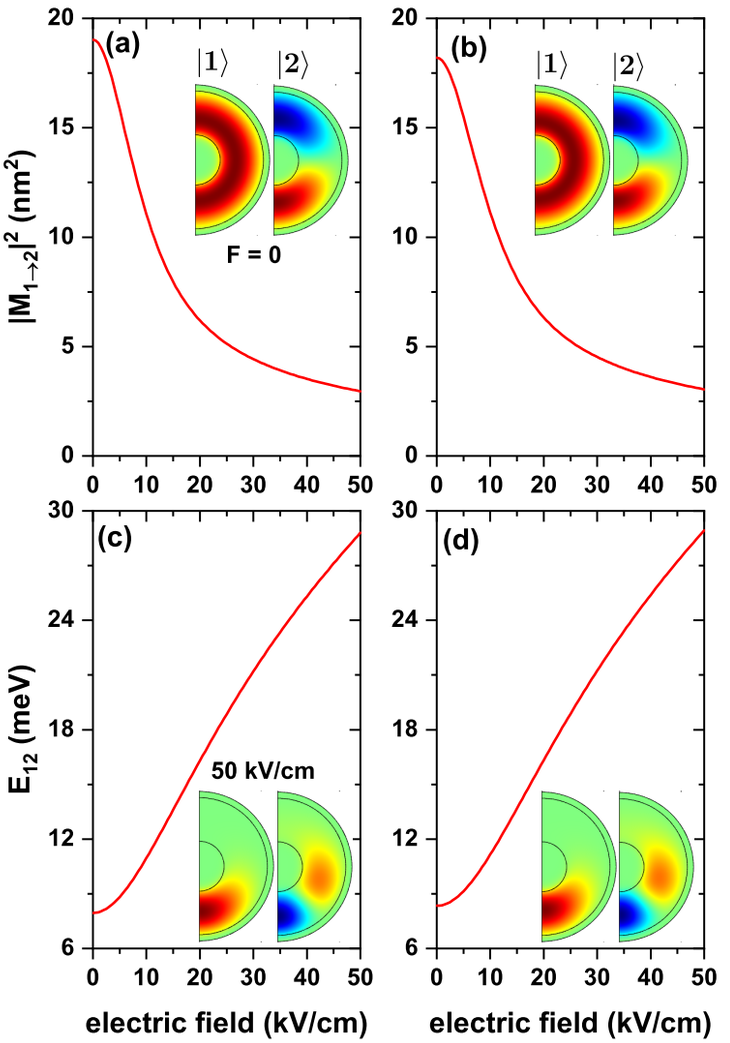

Figure **3-7**: The variation of the $|M_{12}|^2$ (**a**,**b**), and the transition energy (**c**,**d**), as a function of the electric field F_z, for transitions from the ground state ($|1\rangle$) to the first excited state ($|2\rangle$) with $m = 0$, for an electron confined in a ZnS/CdS/ZnS spherical QD. (**a**,**c**) results without, and (**b**,**d**) with the effects of a donor impurity, located at the QD center, with $R_1 = 4$ nm, $R_2 = 11$ nm and $R_3 = 12$ nm, without external magnetic field effect.

Finally, Figure 3-7c,d show the transition energy from the ground state to the first excited state, with and without impurity in the structure. In this plot, E_{12} increases as the electric field strengthens. The reason for this variation is that an increase in the electric field implies greater electron confinement. As plotted in Figure 3-4, all energies exhibit a decreasing

trend, but the ground level decreases at a faster rate compared to the first excited one. When evaluating E_{12}, a more significant difference is obtained. On the other hand, by comparing Figure **3-7**c,d, it is observed that for zero electric fields, the transition energy is greater for the case with impurity, but as the electric field increases, this difference disappears, which indicates that the action of electric field predominates in the system.

The results reported in Figures **3-5**–**3-7** for the transition energies and $|M_{12}|^2$ factor are the key elements to analyze the features of the optical responses of interest in this work. That is, total optical absorption coefficient (α) and relative changes in the total refractive index coefficient (Δn), both as functions of the incident photon energy through Equations (3-7) and (3-10). Accordingly, the incoming electromagnetic wave is assumed to be polarized along the z-direction. Results will be presented considering both the absence and presence of the donor impurity at the center of the QD. In Figure **3-8**, three values of the internal radius (R_1) are considered, taking into account the results of Figure **3-5**. In Figure **3-9**, three values of the applied magnetic field will be shown, taking into account the results of Figure **3-6**. In Figure **3-10**, three values of the applied electric field will be shown, taking into account the results of Figure **3-7**. The light intensity value used for the calculations shown below is $30\,\mathrm{MW/cm^2}$.

In Figure **3-8** the reported results correspond to the optical absorption coefficient and the relative refractive index change coefficient, both as functions of the incident photon energy in a ZnS/CdS/ZnS spherical core/shell/shell QD for several values of the internal dot radius. Figure **3-8**a,b show that there is a drop in the resonant peak magnitude for the linear absorption coefficient ($\alpha^{(1)}$) as the inner radius increases. From Equation (3-5) it is seen that the $\alpha^{(1)}$ maximum amplitude is related to the quantity $E_{12}|M_{12}|^2$. According to our results, $|M_{12}|^2$ increases (see Figure **3-5**a,b) and (E_{12}) decreases (see Figure **3-5**c,d) due to the greater degree of confinement. In both cases, as a result, the $\alpha^{(1)}$ amplitude decreases as the radius increases. This occurs because the E_{12} value decays in greater proportion than the increase of $|M_{12}|^2$. Accordingly, the decrease in amplitude, and the peak shift of $\alpha^{(1)}$ to the red, are directly related to the E_{12} behavior. The opposite effect occurs for the third-order absorption coefficient ($\alpha^{(3)}$) since it shows an increase in amplitude as the radius increases. This behavior is explained by Equation (3-6), in which it is observed that the $\alpha^{(3)}$ maximum amplitude is related to $E_{12}|M_{12}|^4$. So, the fourth power dominates the increase in the product. With Equation (3-7) and the above in mind, the behavior of the total absorption coefficient (α) is explained. This quantity decreases both in its amplitude and in the position of the peaks (redshift) due to the increase of the inner radius. The fall in the amplitude of the total absorption coefficient is further enhanced by the increase in the magnitude of $\alpha^{(3)}$. Analyzing α in the presence of the on-center donor impurity allows observing that, for a small radius, α exhibits a greater amplitude and a shift to higher energy as compared to the no-impurity case; this is because E_{12} has a higher value for this case (see

Figure 3-5c,d).

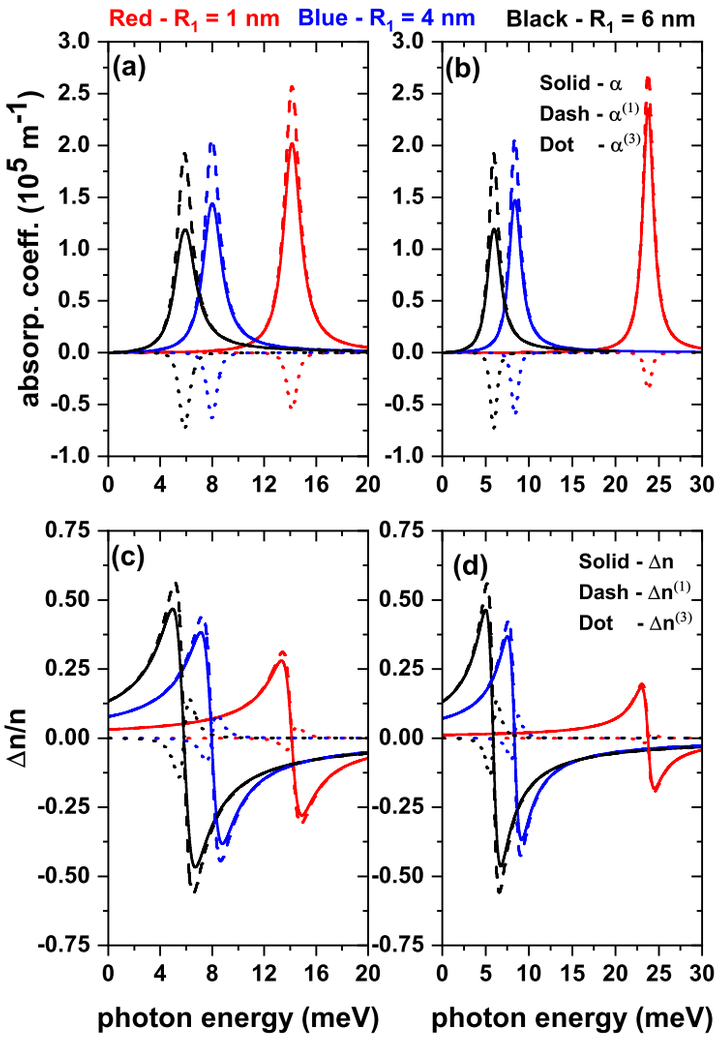

Figure **3-8**: The total (solid line), linear (dashed line), and nonlinear (dotted line) optical absorption coefficient (**a**,**b**), and the total (solid line), linear (dashed line), and nonlinear (dotted line) relative changes in the refractive index coefficient (**c**,**d**) as functions of the incident photon energy in a ZnS/CdS/ZnS spherical core/shell/shell quantum dot, for three values of the internal radius: 1 nm (red line), 4 nm (blue line), and 6 nm (black line). Results are without (**a**,**c**) and with (**b**,**d**) donor impurity at the center of the dot. Calculations are with $R_2 = 11\,\text{nm}$ and $R_3 = 12\,\text{nm}$. The optical transition is between the states $|1\rangle \rightarrow |2\rangle$, with $m = 0$ and without external electric and magnetic field effects.

Besides, Figure 3-8c,d show the linear and third-order contributions to the relative change in the total refractive index coefficient. It is observed that both $\Delta n^{(1)}$ and $\Delta n^{(3)}$ increase

in amplitude and shift to the red part of the spectrum as the internal radius increases, with or without impurities. This behavior is driven by the increase of $|M_{12}|^2$ and the decrease of (E_{12}), Equations (3-8) and (3-9), producing very similar results in both cases with and without impurity.

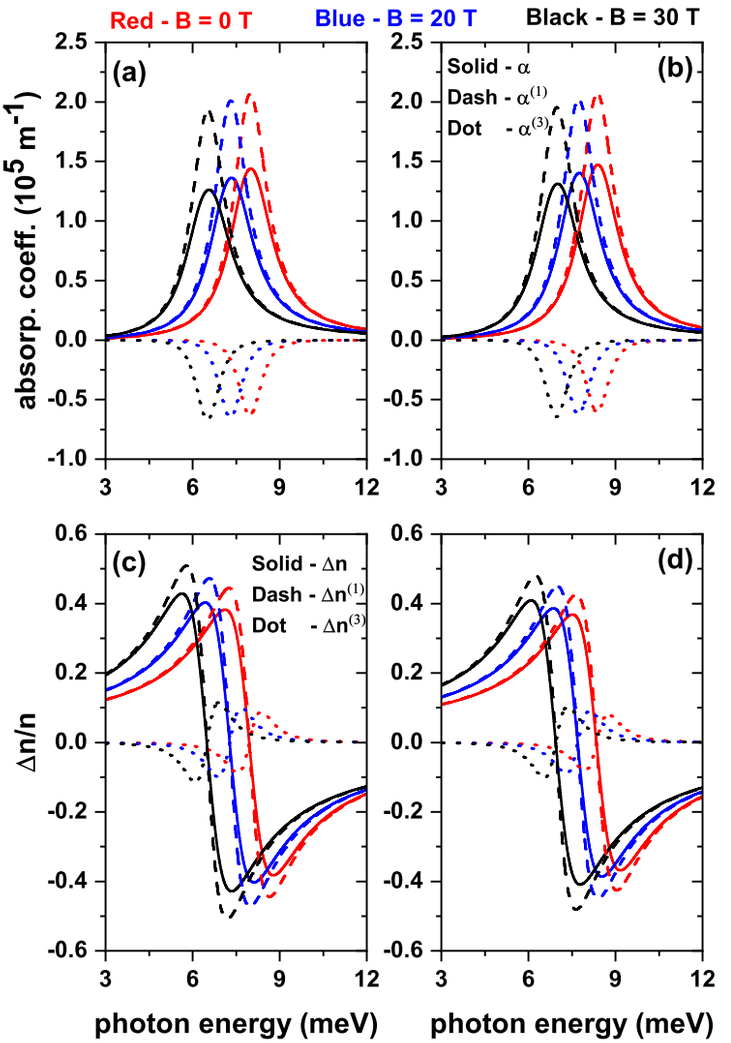

Figure **3-9**: The total (solid line), linear (dashed line), and nonlinear (dotted line) optical absorption coefficient (**a**,**b**), and the total (solid line), linear (dashed line), and nonlinear (dotted line) relative changes in the refractive index coefficient (**c**,**d**) as functions of the incident photon energy in a ZnS/CdS/ZnS spherical core/shell/shell quantum dot, for three values of the magnetic field: zero (red line), 20 T (blue line), and 30 T (black line). The results are without (**a**,**c**) and with (**b**,**d**) donor impurity at the center in the QD. Calculations are with $R_1 = 4\,\text{nm}$, $R_2 = 11\,\text{nm}$, and $R_3 = 12\,\text{nm}$. The optical transition is between the states $|1\rangle \rightarrow |2\rangle$, with $m = 0$ and without external electric field effects.

The results depicted in Figure 3-9 are as those appearing in Figure 3-8, but with the consideration of the influence of an applied magnetic field with increasing strength. Figure 3-9a,b present the peak magnitude and energy of the total, linear, and non-linear optical absorption coefficients. It is possible to notice that these coefficients decrease in magnitude and energy position as long as the magnetic field increases. This diminishing trend relates to the reduction in the value of the $E_{12}|M_{12}|^2$ term as the magnetic field increases (see Figure 3-6a,b). The energy shift towards the red results from the decreasing behavior of E_{12} as the magnetic field intensity augments. A reflection of the rise in $|M_{12}|^2$ (see Figure 3-9c,d) are the changes suffered by Δn, $\Delta n^{(1)}$, and $\Delta n^{(3)}$ with the increase of the magnetic field. Their peaks increase in amplitude, in all cases, with and without the effect of impurity. Again, the energy shift to lower energies is due to the decreasing character of E_{12}. When comparing the results with and without impurity, there are no very appreciable changes in the magnitude and position on the energy scale, which reaffirms what is shown in Figure 3-6, that the impurity effect on the electron is small.

The calculated optical coefficients shown in Figure 3-10 follow the same structure as in Figures 3-8 and 3-9 but were evaluated for several values of an applied electric field. Figure 3-10a,b show a clear decrease in the magnitude of both the absorption coefficient peak and the relative refraction index change coefficient as the intensity of the applied electric field increases. This occurs because, unlike the previous results in Figures 3-8 and 3-9, $|M_{12}|^2$ strongly decreases whilst E_{12} strongly increases with the field [see Figure 3-7]. The product $E_{12}|M_{12}|^2$ decreases as the electric field intensifies. A shift in the energy values towards the blue appears because E_{12} increases as the electric field increases [see Figure 3-7c,d]. Finally, in Figure 3-10c,d, it is shown that Δn decreases as the electric field increases and shifts to higher values of the incident photon energy due to the same reasons discussed above. An important result to keep in mind is that the impurity interacts more with the electron for zero electric fields, but as the field increases, the influence of the impurity becomes almost null. It is worth mentioning that $\alpha^{(3)}$, and $\Delta n^{(3)}$ are not shown in the graphs because depending on $|M_{12}|^4$, their amplitudes are very small, and their contribution to the total values of α, and Δn, is unimportant.

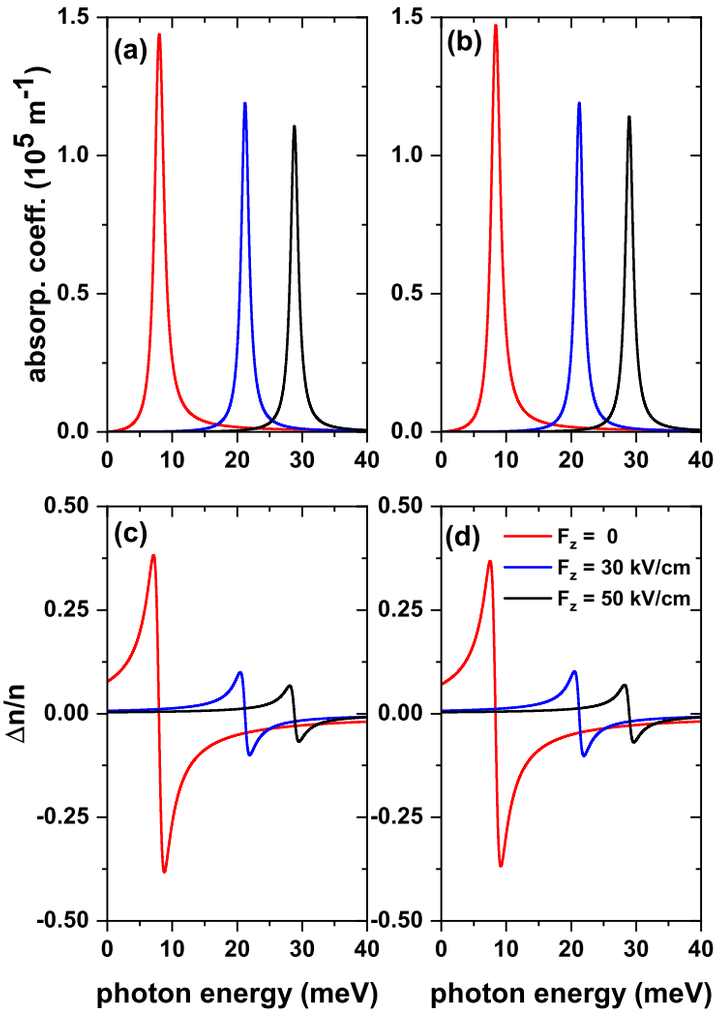

Figure **3-10**: The total optical absorption coefficient (**a**,**b**) and relative changes in the total refractive index coefficient (**c**,**d**) as a function of the energy of the incident photon in a ZnS/CdS/ZnS spherical QD, for three values of the electric field: zero, 30 kV/cm, and 50 kV/cm. The results are without (**a**,**c**) and with (**b**,**d**) donor impurity at the QD center. Calculations are for $R_1 = 4$ nm, $R_2 = 11$ nm, and $R_3 = 12$ nm. The optical transition is between the states $|1\rangle \rightarrow |2\rangle$, with $m = 0$ and without external magnetic field effects.

Finally, it is worth commenting that the so-called colloidal quantum dots correspond to the type of multilayer structures reported in this study. In general, their sizes are in the range of 4 nm and 10 nm in diameter, and their optical properties for technological uses are modifiable with electric fields in the range of several tens of kV/cm and magnetic fields in the range from 0–50 T [42–44]. We hope that this study will serve as motivation for researchers in the experimental field to undertake the task of synthesizing the type of multilayer structures such as the one reported in this article and to consider the possibility of technological applications.

3.5 Conclusions

We have investigated the nonlinear optical response of ZnS/CdS/ZnS core/shell/shell spherical quantum dots related to energy transitions between the ground state ($|1\rangle$) and the first excited state ($|2\rangle$) in the system. For that purpose, the electronic states were determined from the solution of the effective mass equation -with and without the presence of a donor impurity (which was assumed to be placed at the center of the spherical complex)- using the finite element method as implemented in COMSOL-Multiphysics software. The study considers the influence of changes in dot size and the presence of static electric and magnetic fields externally applied to the system. It is determined that geometrical modifications, as well as the increment in applied field intensities, have a noticeable impact on the amplitude and the position of total -linear plus third-order nonlinear- light absorption and relative refractive index change coefficients. Besides, the inclusion of impurity effects reveals significant modifications in the electronic spectrum, which also reflect on the investigated optical properties.

Results obtained for peak energies and amplitudes in the optical coefficients could be used in the designing of optoelectronic devices, which would be tuned to different energies and amplitudes by changing the external probes and electric and magnetic fields. For instance, in this case, transition energies fall within the range 1.5–20 meV, which corresponds to the terahertz region.

References

[1] Mommadi, O.; El Moussaouy, A.; Chnafi, M.; El Hadi, M.; Nougaoui, A.; Magrez, H. Exciton phonon properties in cylindrical quantum dot with parabolic confinement potential under electric field. *Physica E* **2020**, *118*, 113903. [CrossRef]

[2] Heyn, C.; Radu, A.; Vinasco, J.A.; Laroze, D.; Restrepo, R.L.; Tulupenko, V.; Hieu, N.N.; Phuc, H.V.; Mora-Ramos, M.E.; Ojeda, J.H.; et al. Exciton states in conical quantum dots under applied electric and magnetic fields. *Opt. Laser Technol.* **2021**, *139*, 106953. [CrossRef]

[3] Mora-Ramos, M.E.; Vinasco, J.A.; Laroze, D.; Radu, A.; Restrepo, R.L.; Heyn, C.; Tulupenko, V.; Hieu, N.N.; Phuc, H.V.; Ojeda, J.H.; et al. Electronic structure of vertically coupled quantum dot-ring heterostructures under applied electromagnetic probes. A finite-element approach. *Sci. Rep.* **2021**, *11*, 4015. [CrossRef]

[4] Elborg, M.; Noda, T.; Mano, T.; Kuroda, T.; Yao, Y.; Sakuma, Y.; Sakoda, K. Self-assembly of vertically aligned quantum ring-dot structure by multiple droplet epitaxy. *J. Cryst. Growth* **2017**, *477*, 239–242. [CrossRef]

[5] Babin, H.G.; Ritzmann, J.; Bart, N.; Schmidt, M.; Kruck, T.; Zhai, L.; Löbl, M.C.; Nguyen, G.N.; Spinnler, C.; Ranasinghe, L.; et al. Charge tunable GaAs quantum dots in a photonic n-i-p diode. *Nanomaterials* **2021**, *11*, 2703. [CrossRef] [PubMed]

[6] Portacio, A.A.; Jiménez, A.F.; Urango, M.P. Theoretical study on the change of index of refraction and the optical absorption in a quantum dot in the presence of a uniform magnetic field. *Rev. Mex. Fis.* **2016**, *62*, 330–335.

[7] Holovatsky, V.; Chubrey, M.; Voitsekhivska, O. Effect of electric field on photoionisation cross-section of impurity in multilayered quantum dot. *Superlattices Microstruct. 2020*, *145*, 106642. [CrossRef]

[8] Kuzyk, O.; Dan'kiv, O.; Peleshchak, R.; Stolyarchuk, I. Baric properties of CdSe-core/ZnS/CdS/ZnS-multilayer shell quantum dots. *Physica E* **2022**, *143*, 115381. [CrossRef]

[9] Niculescu, E.C.; Cristea, M. Impurity states and photoionization cross section in CdSe/ZnS core–shell nanodots with dielectric confinement. *J. Lumin.* **2013**, *135*, 120–127. [CrossRef]

[10] Holovatsky, V.A.; Voitsekhivska, O.M.; Yakhnevych, M.Y. The effect of magnetic field and donor impurity on electron spectrum in spherical core-shell quantum dot. *Superlattices Microstruct.* **2018**, *116*, 9–16. [CrossRef]

[11] Cristea, M. Simultaneous effects of electric field, shallow donor impurity and geometric shape on the electronic states in ellipsoidal ZnS/CdSe core-shell quantum dots. *Physica E* **2018**, *103*, 300–306. [CrossRef]

[12] Chnafi, M.; Belamkadem, L.; Mommadi, O.; Boussetta, R.; Hadi, M.E.; Moussaouy, A.E.; Falyouni, F.; Vinasco, J.A.; Laroze, D.; Mora-Rey, F.; et al. Hydrostatic pressure and temperature effects on spectrum of an off-center single dopant in a conical quantum dot with spherical edge. *Superlattices Microstruct.* **2021**, *159*, 107052. [CrossRef]

[13] Duque, C.A.; Porras-Montenegro, N.; Barticevic, Z.; Pacheco, M.; Oliveira, L.E. Electron-hole transitions in self-assembled InAs/GaAs quantum dots: Effects of applied magnetic fields and hydrostatic pressure. *Microelectron. J.* **2005**, *36*, 231–233. [CrossRef]

[14] Hien, N.D.; Duque, C.A.; Feddi, E.; Hieu, N.N.; Phuc, H.V. Magneto-optical effect in GaAs/GaAlAs semi-parabolic quantum well. *Thin Solid Films* **2019**, *682*, 10–17. [CrossRef]

[15] Montes, A.; Duque, C.A.; Porras-Montenegro, N. Density of shallow-donor impurity states in rectangular cross section GaAs quantum-well wires under applied electric field. *J. Phys. Condens. Matter* **1998**, *10*, 5351–5358. [CrossRef]

[16] Heyn, C. Kinetic model of local droplet etching. *Phys. Rev. B Condens. Matter* **2011**, *83*, 165302. [CrossRef]

[17] Heyn, C.; Zocher, M.; Küster, A.; Hansen, W. Droplet etching during semiconductor epitaxy for single and coupled quantum structures. *Quantum Dots Nanostructures Growth, Charact. Model. XV* **2018**, *10543*, 38–47.

[18] Xiao, X.; Fischer, A.J.; Wang, G.T.; Lu, P.; Koleske, D.D.; Coltrin, M.E.; Wright, J.B.; Liu, S.; Brener, I.; Subramania, G.S.; et al. Quantum-size-controlled photoelectrochemical fabrication of epitaxial InGaN quantum dots. *Nano Lett.* **2014**, *14*, 5616–5620. [CrossRef]

[19] Wang, J.; Zhou, G.; He, R.; Huang, W.; Zhu, J.; Mao, C.; Wu, C.; Lu, G. Experimental preparation and optical properties of CeO_2/TiO_2 heterostructure. *J. Mater. Res. Technol.* **2020**, *9*, 9920–9928. [CrossRef]

[20] Yang, W.; Zhang, B.; Ding, N.; Ding, W.; Wang, L.; Yu, M.; Zhang, Q. Fast synthesize ZnO quantum dots via ultrasonic method. *Ultrason. Sonochem.* **2016**, *30*, 103–112. [CrossRef]

[21] Valizadeh, A.; Mikaeili, H.; Samiei, M.; Farkhani, S.M.; Zarghami, N.; kouhi, M.; Akbarzadeh, A.; Davaran, S. Quantum dots: Synthesis, bioapplications, and toxicity. *Nanoscale Res. Lett.* **2012**, *7*, 1–14. [CrossRef] [PubMed]

[22] Aouami, A.E.; Feddi, E.; El-Yadri, M.; Aghoutane, N.; Dujardin, F.; Duque, C.A.; Phuc, H.V. Electronic states and optical properties of single donor in GaN conical quantum dot with spherical edge. *Superlattices Microstruct.* **2018**, *114*, 214–224. [CrossRef]

[23] Heyn, C.; Duque, C.A. Donor impurity related optical and electronic properties of cylindrical $GaAs-Al_xGa_{1-x}$ As quantum dots under tilted electric and magnetic fields. *Sci. Rep.* **2020**, *10*, 9155. [CrossRef] [PubMed]

[24] Pulgar-Velásquez, L.; Sierra-Ortega, J.; Vinasco, J.A.; Laroze, D.; Radu, A.; Kasapoglu, E.; Restrepo, R.L.; Gil-Corrales, J.A.; Morales, A.L.; Duque, C.A. Shallow donor impurity states with excitonic contribution in GaAs/AlGaAs and CdTe/CdSe truncated conical quantum dots under applied magnetic field. *Nanomaterials* **2021**, *11*, 2832. [CrossRef]

[25] Rodríguez-Magdaleno, K.A.; Pérez-Álvarez, R.; Ungan, F.; Martínez-Orozco, J.C. Strain effect on the intraband absorption coefficient for spherical CdSe/CdS/ZnSe core–shell–shell quantum dots. *Mater. Sci. Semicond. Process.* **2022**, *141*, 106400. [CrossRef]

[26] Divsar, F. *Introductory Chapter: Quantum Dots, in Quantum Dots—Fundamental and Applications*; IntechOpen: London, UK, 2020.

[27] Selopal, G.S.; Zhao, H.; Wang, Z.M.; Rosei, F. Core/shell quantum dots solar cells. *Adv. Funct. Mater.* **2020**, *30*, 1908762. [CrossRef]

[28] Sahu, A.; Kumar, D. Core-shell quantum dots: A review on classification, materials, application, and theoretical modeling. *J. Alloys Compd.* **2022**, *924*, 166508. [CrossRef]

[29] Huang, X.; Tong, X.; Wang, Z. Rational design of colloidal core/shell quantum dots for optoelectronic applications. *J. Electron. Sci. Technol.* **2020**, *18*, 100018. [CrossRef]

[30] Zeiri, N.; Naifar, A.; Nasrallah, S.A.B.; Said, M. Third nonlinear optical susceptibility of CdS/ZnS core-shell spherical quantum dots for optoelectronic devices. *Optik* **2019**, *176*, 162–167. [CrossRef]

[31] Linkov, P.A.; Vokhmintcev, K.V.; Samokhvalov, P.S.; Laronze-Cochard, M.; Sapi, J.; Nabiev, I.R. Effect of the semiconductor quantum dot shell structure on fluorescence quenching by acridine ligand. *JETP Lett.* **2018**, *107*, 233–237. [CrossRef]

[32] Zeiri, N.; Naifar, A.; Nasrallah, S.A.B.; Said, M. Theoretical investigation on the third order nonlinear optical susceptibility in CdS/ZnS/CdS/ZnS core/shell/well/shell quantum dots for optoelectronic applications. *Phys. Scr.* **2020**, *95*, 017001. [CrossRef]

[33] Kuzyk, O.; Stolyarchuk, I.; Dan'kiv, O.; Peleshchak, R. Baric properties of quantum dots of the type of core (CdSe)-multilayer shell (ZnS/CdS/ZnS) for biomedical applications. *Appl. Nanosci.* **2022**, 1–10. [CrossRef]

[34] Vinasco, J.A.; Radu, A.; Niculescu, E.; Mora-Ramos, M.E.; Feddi, E.; Tulupenko, V.; Restrepo, R.L.; Kasapoglu, E.; Morales, A.L.; Duque, C.A. Electronic states in GaAs-(Al,Ga)As eccentric quantum rings under nonresonant intense laser and magnetic fields. *Sci. Rep.* **2019**, *9*, 1427. [CrossRef] [PubMed]

[35] Vinasco, J.A.; Londoño, M.A.; Restrepo, R.L.; Mora-Ramos, M.E.; Feddi, E.M.; Radu, A.; Kasapoglu, E.; Morales, A.L.; Duque, C.A. Optical absorption and electroabsorption related to electronic and single dopant transitions in holey elliptical GaAs quantum dots. *Phys. Status Solidi B* **2018**, *255*, 1700470. [CrossRef]

[36] Popescu, I.; Hristache, M.; Ciobanu, S.S.; Barseghyan, M.G.; Vinasco, J.A.; Morales, A.L.; Radu, A.; Duque, C.A. Size or shape—What matters most at the nanoscale? *Comput. Mater. Sci.* **2019**, *165*, 13–22. [CrossRef]

[37] COMSOL. *Multiphysics*; v. 5.4; COMSOL AB: Stockholm, Sweden, 2018.

[38] COMSOL. *Multiphysics Reference Guide*; COMSOL AB: Stockholm, Sweden, 2012.

[39] COMSOL. *Multiphysics Users Guide*; COMSOL AB: Stockholm, Sweden, 2012.

[40] Ahn, D.; Chuang, S.-L. Calculation of linear and nonlinear intersubband optical absorptions in a quantum well model with an applied electric field. *IEEE J. Quantum Electron.* **1987**, *23*, 2196–2204.

[41] Hasanirokh, K.; Radu, A.; Duque, C. Donor impurity in CdS/ZnS spherical quantum dots under applied electric and magnetic fields. *Nanomaterials* **2022**, *12*, 4014. [CrossRef]

[42] Liu, M.; Yazdani, N.; Yarema, M.; Jansen, M.; Wood, V.; Sargent, E.H. Colloidal quantum dot electronics. *Nat. Electron.* **2021**, *4*, 548–558. [CrossRef]

[43] Furis, M.; Hollingsworth, J.A.; Klimov, V.I.; Crooker, S.A. Time-and polarization-resolved optical spectroscopy of colloidal CdSe nanocrystal quantum dots in high magnetic fields. *J. Phys. Chem. B* **2005**, *109*, 15332–15338. [CrossRef]

[44] Yu, J.; Shendre, S.; Koh, W.K.; Liu, B.; Li, M.; Hou, S.; Hettiarachchi, C.; Delikali, S.; Hernández-Martínez, P.; Birowosuto, M.; et al. Electrically control amplified spontaneous emission in colloidal quantum dots. *Sci. Adv.* **2019**, *5*, eaav3140. [CrossRef]

4 Effect of External Fields on the Electronic and Optical Properties in ZnTe/CdSe and CdSe/ZnTe Spherical Quantum Dots

4.1 Abstract

A theoretical analysis was carried out to investigate the electronic and optical properties of a confined electron–hole pair in type-II core–shell spherical quantum dots based on CdSe/ZnTe and ZnTe/CdSe heterostructures. The Schrödinger equations for the electron and the hole were numerically solved using the 2D axisymmetric module of COMSOL Multiphysics, which employs the finite element method under the effective mass approximation. Additionally, a custom Fortran code was used to compute the excitonic energy by solving the Coulomb integral. The calculations encompassed variations in the inner radius (R_1), as well as variations in the electric (F_z) and magnetic (B) fields along the z-axis. The absorption coefficients were determined for transitions between the hole and electron ground states, considering z-polarized incident radiation. Including a magnetic field increases the transition energy, consequently causing the absorption peaks to shift toward the blue region of the spectrum. On the other hand, the electric field decreased the overlap of the electron and hole wavefunctions. As a result, the amplitude of the absorption peaks decreased with an increase in the electric field.

Keywords: type-II quantum dot; absorption coefficient; ZnTe/CdSe; CdSe/ZnTe; magnetic field; electric field.

4.2 Introduction

There is an increasing demand for electronic devices based on semiconductor heterostructures at the nanometer scale. This demand has led to a rise in theoretical and experimental studies to discover new properties (such as electronic, optical, and optoelectronic) or improve existing ones in these devices.

When two semiconductor materials with different forbidden energy gaps are brought together, one acts as the potential well region while the other acts as the barrier region for electrons and holes. A quantum well is formed when the motion of electrons and holes is confined in one dimension. Similarly, confinement in two spatial dimensions results in a quantum wire, and confinement in all three dimensions leads to quantum dots (QDs), where the whole energy spectrum of particles becomes discrete. These systems are highly sensitive to geometry, size, and external probes, such as magnetic and electric fields [1–4]. They are also influenced by the shallow-donor and -acceptor impurities [5–7], neutral and charged excitons [8–10], intense resonant and non-resonant lasers [11], hydrostatic pressure, temperature [12], and the inclusion of spin–orbit and Zeeman effects, represented by the Rashba and Dresselhaus terms [13,14]. All these effects significantly modify the electronic, optical, thermal, and mechanical properties of semiconductor nanostructures. It is worth recalling that when considering most of the external effects mentioned earlier, analytical solutions for the

problem of finding energy eigenstates are not available. Therefore, various numerical methods are employed, such as the finite element method (FEM) and the finite difference method.

Moreover, QDs can be fabricated in the experimental domain using molecular beam epitaxy (MBE), hydrothermal method, and ultrasonic sol-gel. These techniques allow for precise control over the dimensions and composition of the QDs [15–20]. The semiconductor properties of QDs are highly influenced by their shapes and sizes compared to the constituent materials [21]. Among the various 2D geometries studied, we have disks and rings, while in the 3D realm, there are structures like cylinders, cones, pyramids, and spherical shapes [22–26]. The primary focus of this work is to investigate type-II core-shell QDs with a spherical shape. These QDs are characterized by having the conduction band minimum (electron confinement) spatially separated from the valence band maximum (hole confinement). This implies that when electrons are confined in the core, the holes are confined in the shell, or vice versa.

An example of a type-II QD is formed by combining two semiconductor materials, CdSe and ZnTe. In this case, CdSe acts as the hole barrier and electron well, while ZnTe is the hole well and electron barrier. The literature contains numerous reports emphasizing the excellent electronic and optical properties of type-II QDs based on ZnTe and CdSe [27–29]. One notable study was conducted by Chen et al. where they synthesized and characterized CdSe/CdTe/ZnTe type-II core-shell-shell QDs. They discovered an extraordinarily long radiative lifetime of 10 ms for interband emission due to the spatial separation of electrons and holes between CdSe and ZnTe facilitated by the CdTe intermediate layer [30]. In 2023, Jaouane et al. performed a theoretical analysis of the optical properties of spherical core-shell QDs with a modified Kratzer potential. Their investigation focused on transitions between the ground and the first excited states. They observed that the absorption coefficients were redshifted by varying the parameter r_e, representing the potential bond length. Additionally, they found that these quantities were blue-shifted when shielding and control parameters of the Kratzer potential were varied [31]. Another study in 2023 by Koç et al. explored the electronic and optical properties of excitons and biexcitons in multi-shell CdS/ZnSe/ZnTe/CdSe QDs as a function of the core size. The researchers reported that the size of the ZnSe shell could be manipulated to control the overlap between electron and hole wavefunctions while keeping the exciton and biexciton transition energy nearly unchanged. This ability to engineer the wavefunctions in type-II multilayers allowed for a wide range of tunability in radiation lifetime without significant changes in transition energies [**?**]. Restrepo and co-authors developed a theoretical model to describe excitonic states in colloidal spherical QDs with quasi-infinite confinement potential [33]. Using a two-band model, they found an excellent match between their theoretical findings and the experimentally reported photoluminescence energy, obviously, with minor differences.

Type II quantum dots (QDs) undergo significant changes in their electronic and optical

properties when exposed to external fields. In a study conducted by Holovatsky et al. in 2023 [34], they theoretically explored the effects of a magnetic field on the electronic properties and optical quantum interband transitions in type II ZnTe/CdSe and CdSe/ZnTe QDs. Their findings revealed that the magnetic field breaks the spherical symmetry of the system, resulting in energy spectrum degeneracy concerning the magnetic quantum number. Moreover, they observed a dependence of the oscillator strength on the magnetic field, as the field affects the overlap of electron and hole wavefunctions. In 2007, Kuskovsky et al. [35] presented experimental and theoretical studies on magnetoexcitons in type II QDs formed in Zn-Se-Te multilayers. Their primary objective was to investigate the impact of an intense magnetic field (31 T) on the optical properties. The results demonstrated that the magneto-photoluminescence exhibited a non-monotonic behavior of the exciton emission intensity concerning the magnetic field, indicating the manifestation of the Aharonov–Bohm effect. These findings were further supported by the performed numerical calculations. Additionally, Roy et al. in 2012 [36] conducted an experimental study on the influence of magnetic and electric fields on type II ZnTe/ZnSe QDs. The authors reported observing robust and narrow Aharonov–Bohm oscillations in the magneto photoluminescence intensity of the stacked QDs due to an embedded electric field. Furthermore, they noticed a decrease in Aharonov–Bohm oscillations, which they attributed to the electric field's presence.

Building upon the previously reported works mentioned above, this study aims to investigate the effects induced by changes in the core size and the inclusion of external electric and magnetic fields on the electronic and optical properties of type-II quantum dots (QDs) made of ZnTe/CdSe and CdSe/ZnTe. To achieve this, we will conduct numerical calculations using the Finite Element Method (FEM) within COMSOL-Multiphysics software, employing the 2D axis-symmetric module while considering the effective mass approximation. The theoretical calculations will focus on determining the energies and wavefunctions of spherical core-shell type-II QDs composed of ZnTe/CdSe and CdSe/ZnTe. These calculations will take into account variations in the internal radius (R_1) as well as changes in the external electric (F_z) and magnetic (B) field strengths, both aligned along the z-axis. To account for the Coulomb interaction between the electron and the hole, a Fortran code will be utilized. Subsequently, using the energies and wavefunctions obtained for the electron-hole system, we will examine the optical response of the QDs to light absorption by analyzing the absorption coefficient at the quantum interband transitions between the hole's ground state and the electron's ground state. The structure of the article is organized as follows: Section 4.3 presents the theoretical framework used in the calculations, Section 4.4 discusses the results obtained from the simulations, and Section 4.5 provides a summary of the main conclusions drawn from this study.

4.3 Theoretical Model

Figure 4-1 shows the pictorial views of the two investigated systems, which are type-II spherical ZnTe/CdSe and CdSe/ZnTe core/shell QDs. The inner and outer radius dimensions are R_1 and R_2, respectively. In the lowest part of the figure, we have represented a schematic view of the r-dependent confinement potential for valence and conduction bands. This function is set for electrons as zero within the CdSe material, V_e in the ZnTe material, and infinite in the vacuum external region. This function is set for holes as zero within the ZnTe material, V_h in the CdSe material, and infinite in the vacuum external region. An axially applied magnetic ($B\,\widehat{k}$) and electric ($F_z\,\widehat{k}$) field have been taken into account.

In Cartesian coordinates, the effective mass Schrödinger equation for an electron (hole) confined in the structure, with all the above-mentioned contributions, is written in the form:

$$\left\{\left(\vec{p}_i - q_i\,\vec{A}_i\right)\cdot\left[\frac{1}{2\,m_i^*(\vec{r}_i)}\left(\vec{p}_i - q_i\,\vec{A}_i\right)\right] - q_i\,\vec{F}\cdot\vec{r}_i + V_i(\vec{r}_i)\right\}\psi_i(\vec{r}_i) = E_i\,\psi_i(\vec{r}_i)\,, \tag{4-1}$$

where $i = e, h$ corresponds to electron (hole), $m_i^*(\vec{r}_i)$ is the position-dependent electron (hole) effective mass, $\vec{p}_i = -i\,\hbar\,\vec{\nabla}_i$, $\vec{r}_i = x_i\,\widehat{i} + y_i\,\widehat{j} + z_i\,\widehat{k}$, $q_e = -e$ is the electron charge, $q_h = +e$ is the hole charge, and e is the absolute value of the elementary charge. Additionally, $\vec{A}_i = -\frac{B}{2}\,(y_i\,\widehat{i} - x_i\,\widehat{j})$ is the vector potential associated with the applied magnetic field, where $\vec{B} = \vec{\nabla}_i \times \vec{A}_i$ and $\vec{\nabla}_i \cdot \vec{A}_i = 0$.

Expanding Equation (1), and considering that the electric field is applied along the z-direction, we obtain:

$$\begin{aligned}\Bigg\{-\frac{\hbar^2}{2}\vec{\nabla}_i\cdot\left(\frac{1}{m_i^*(\vec{r}_i)}\vec{\nabla}_i\right) - \frac{i\,\hbar\,q_i\,B}{2\,m_i^*(\vec{r}_i)}\left(y\frac{\partial}{\partial x} - x\frac{\partial}{\partial y}\right) - \frac{i\,\hbar\,q_i\,B}{4}\vec{\nabla}\left(\frac{1}{m_i^*(\vec{r}_i)}\right)\cdot(y_i\,\widehat{i} - x_i\,\widehat{j}) \\ + \frac{q_i^2\,B^2(x_i^2+y_i^2)}{8\,m_i^*(\vec{r}_i)} - q_i F_z z_i + V_i(\vec{r}_i)\Bigg\}\psi_i(\vec{r}_i) = E_i\,\psi_i(\vec{r}_i)\,.\end{aligned} \tag{4-2}$$

In the absence of electric and magnetic fields, our problem has spherical symmetry, and the 3D wavefunction can be written as the product of a one-dimensional function for the coordinate r and a two-dimensional function depending on the angular coordinates, θ and φ, known as spherical harmonics. By turning on either or both electric or magnetic fields applied along the z-direction, the system loses spherical symmetry but preserves cylindrical symmetry about the z-axis. This situation is also valid when both fields are zero. In that sense, it is useful to work in cylindrical coordinates to use such symmetry. Using the azimuthal symmetry condition, it is possible to propose, in cylindrical coordinates, a solution of the type

$$\psi_i(\vec{r}_i) = \psi_i(\rho_i, \varphi_i, z_i) = R_i(\rho_i, z_i)\, e^{i\, m_i\, \varphi_i}\,, \tag{4-3}$$

where the m_i-integer is the magnetic quantum number ($m_i = 0, \pm 1, \pm 2, \dots$). Consequently, the $R_i(\rho_i, z_i)$ function satisfies the differential equation

$$\begin{aligned}\Bigg[-\vec{\nabla}_{2D,i} \cdot \left(\frac{\hbar^2}{2\, m_i^*(\rho_i, z_i)} \vec{\nabla}_{2D,i}\right) + \frac{m_i^2\, \hbar^2}{2\, m_i^*(\rho_i, z_i)\, \rho_i^2} - \frac{\hbar\, q_i\, B\, m_i}{2\, m_i^*(\rho_i, z_i)} \\ + \frac{q_i^2\, B^2\, \rho_i^2}{8\, m_i^*(\rho_i, z_i)} - q_i\, F_z\, z_i + V_i(\rho_i, z_i)\Bigg]\, R_i(\rho_i, z_i) = E_i\, R_i(\rho_i, z_i),\end{aligned} \tag{4-4}$$

where $\vec{\nabla}_{2D,i}$ is the ρ_i- and z_i-dependent two-dimensional gradient operator.

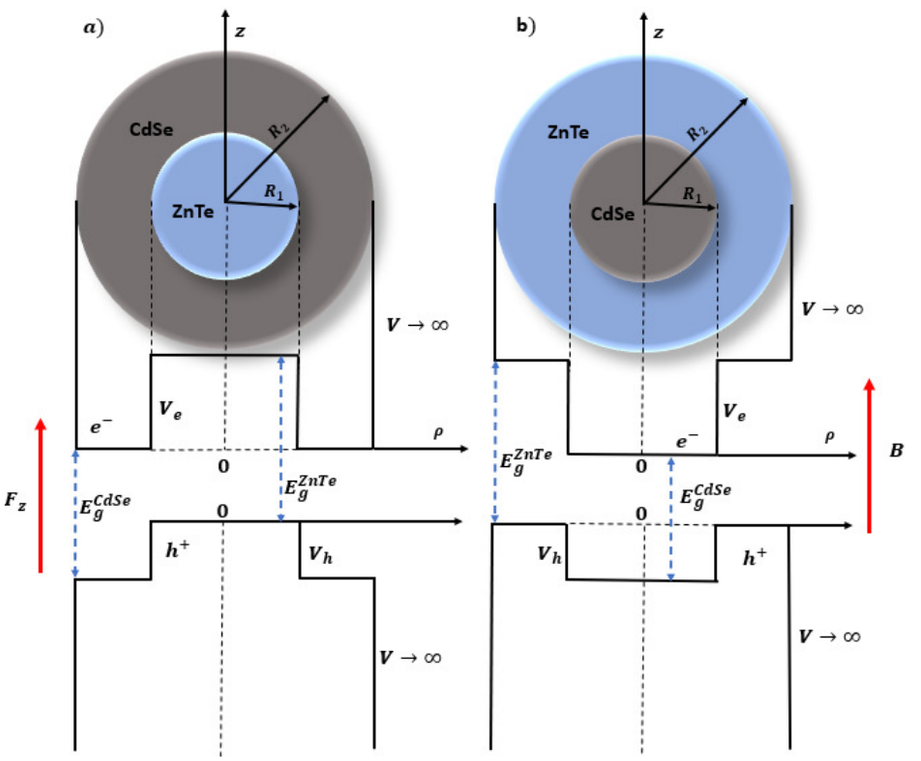

Figure **4-1**: ZnTe/CdSe (**a**) and CdSe/ZnTe (**b**) spherical quantum dot cross-section. The dimensions of the QD and the axially applied electric and magnetic field are indicated together with the r-dependent confinement potentials.

We consider the parabolic band approximation, together with Dirichlet boundary conditions at the outer edges of the barrier matrix and the BenDaniel–Duke conditions at the inner QD interfaces (see Figure 4-1). Accordingly, m_i^* and $V_i(\rho_i, z_i)$ both depend on the position in the heterostructure, and they are expressed for ZnTe/CdSe as

$$m_i^{*c}(\rho_i, z_i) = \begin{cases} m_h^{*\mathrm{ZnTe}} & \text{if } 0 \leq r_i \leq R_1 \\ m_e^{*\mathrm{CdSe}} & \text{if } R_1 < r_i \leq R_2 \end{cases} \tag{4-5}$$

and

$$V_e(\rho_e, z_e) = \begin{cases} V_e & \text{if } 0 < r_e \leq R_1 \\ 0 & \text{if } R_1 < r_e \leq R_2 \\ \infty & \text{if } r_e > R_2 \end{cases} \qquad V_h(\rho_h, z_h) = \begin{cases} 0 & \text{if } 0 < r_h \leq R_1 \\ V_h & \text{if } R_1 < r_h \leq R_2 \\ \infty & \text{if } r_h > R_2\,. \end{cases} \tag{4-6}$$

In the case of CdSe/ZnTe, the expressions are:

$$m_i^{*c}(\rho_i, z_i) = \begin{cases} m_e^{*\mathrm{CdSe}} & \text{if } 0 \leq r_i \leq R_1 \\ m_h^{*\mathrm{ZnTe}} & \text{if } R_1 < r_i \leq R_2 \end{cases} \tag{4-7}$$

and

$$V_e(\rho_e, z_e) = \begin{cases} 0 & \text{if } 0 < r_e \leq R_1 \\ V_e & \text{if } R_1 < r_e \leq R_2 \\ \infty & \text{if } r_e > R_2 \end{cases} \qquad V_h(\rho_h, z_h) = \begin{cases} V_h & \text{if } 0 < r_h \leq R_1 \\ 0 & \text{if } R_1 < r_h \leq R_2 \\ \infty & \text{if } r_h > R_2\,. \end{cases} \tag{4-8}$$

In Equations (4-5)–(4-8), $r_i = \sqrt{\rho_i^2 + z_i^2}$.

By solving Equation (4-4), the ground state wavefunctions of the electron ($\psi_e^1(\vec{r_e})$) and the hole ($\psi_h^1(\vec{r_h})$) are obtained. With them, it is possible to use a first-order perturbative approximation to evaluate the excitonic interaction by means of the following Coulomb integral [37,38]

$$E_{exc} = \frac{e^2}{4\,\pi\,\epsilon_0\,\epsilon_r} \int_{\Omega_h} \int_{\Omega_e} \frac{|\psi_e^1(\vec{r_e})|^2 |\psi_h^1(\vec{r_h})|^2}{|\vec{r_e} - \vec{r_h}|} dV_e\, dV_h\,, \tag{4-9}$$

where ϵ_0 and ϵ_r are the vacuum permittivity and dielectric constant, respectively, and $|\vec{r_e} - \vec{r_h}|$ is the $e - h$ distance. Moreover, dV_e and dV_h represent the differential volume for electron and hole. Since the interest is focused on the magnitude of the Coulomb interaction, the negative sign of the electrostatic energy has been omitted. We want to highlight that Heyn and co-workers have used this perturbative approach in multiple studies where excitonic states in heterostructures with axial symmetry have been described and found very good agreement with experimental results for the photoluminescence peak energy transition [37,38].

Taking advantage of the azimuthal symmetry of the problem, it is possible to calculate the angular integration of Equation (4-9) analytically with a first-order elliptic integral ($K(x)$). This will reduce the dimensions of the integral, going from six variables, three for the electron and three for the hole ($\rho_{e(h)}$, $\varphi_{e(h)}$, $z_{e(h)}$), to four variables ($\rho_{e(h)}$, $z_{e(h)}$):

$$E_{exc} = \frac{q^2}{4\pi\epsilon_0\epsilon_r} \int_{\Omega'_h} \int_{\Omega'_e} |R^1_e(\rho_e, z_e)|^2 |\, R^1_h(\rho_h, z_h)|^2 \left[\frac{8\,\pi\, K\left(\frac{r_p}{1+r_p}\right)}{r\,\sqrt{1+r_p}} \right] dV'_e d\,V'_h\,, \tag{4-10}$$

where $dV'_{e(h)} = 2\,\pi\,\rho_{e(h)}\,d\rho_{eh}\,dz_{e(h)}$, $r_p = 4\,\rho_e\,\rho_h/r$, and $r = \sqrt{(\rho_e - \rho_h)^2 + (z_e - z_h)^2}$. In the above expression, the terms inside the square brackets come from the double angular integral of the inverse electron-hole distance, and Ω'_h and Ω'_e correspond to the area. Note that due to the system azimuthal symmetry in Fig. **4-1**, the electron and the heavy hole ground state wavefunctions do not depend on angular coordinates ($\varphi_{e(h)}$) [42].

This study focuses on investigating the effects of external magnetic and electric fields as well as variations in the core size (represented by the parameter R_1), on type-II spherical QDs composed of ZnTe/CdSe and CdSe/ZnTe. The study specifically examines the confinement of holes, electrons, and excitons within these QDs. Notably, despite utilizing an external magnetic field, the Zeeman effect has been disregarded to facilitate a more detailed analysis of the energy levels of the particles under investigation because for 30 T the Zeeman effect is of the order of 0.5 meV (not shown here); this is very small compared to the orbital splitting in our results.

Equation (4-4) is solved using the FEM within the axis-symmetric module of the COMSOL-Multiphysics licensed software [39–41]. This solution provides the electron and hole wavefunctions and their corresponding energies. The computational settings employed in this work include a user-controlled extra fine mesh with 15,520 vertices, 30,586 triangles, 664 edge elements, and seven vertex elements. The minimum element quality is set at 0.4766, while the mean element quality is 0.9235. The area ratio element size is 0.0442, with a total mesh area of 353.4 nm^2. The hardware utilized consists of a single 11th-generation i7 processor with 16 GB of RAM. To numerically calculate Equation (4-10), a Fortran 77 code is employed. The ground state wavefunctions (R^1_e and R^1_h), obtained from COMSOL-Multiphysics regarding the coordinates (ρ, z), are exported and used as input. By discretizing the electron and hole coordinates over the same set of mesh points, the wavefunctions are represented at these specific locations. Consequently, the integral in Equation (4-10) can be approximated using a Riemann sum [42].

The obtained electronic states for the electron and the hole are then utilized to evaluate the absorption coefficient, which is dependent on the transitions occurring between the ground

state of the electron and the hole. The following relationship provides the expression for evaluating the absorption coefficients:

$$\alpha(\hbar\,\omega) = \frac{e^2\,\omega\,\pi}{n_r\,\epsilon_0\,c\,L}\sum_k f_k\,\delta_k(E_{e-h} - \hbar\,\omega), \tag{4-11}$$

where E_{e-h} is the transition energy of the exciton, $\hbar\,\omega$ is the energy of the incident photon, δ_k is the line shape function, f_k is the oscillator strength, and L is the diameter of QD [11, 26, 43]. The sum is performed over all possible transitions in the system. Only the transition $1s-1s$ of the electron and hole is considered for the absorption edge. The following relationship calculates the oscillator strength for these optical transitions:

$$f_{1-1} = \frac{2\,\pi^2\,E_p}{E_{e-h}}\left|\int_{-R_2}^{+R_2}\int_0^{+R_2} R_e^1(\rho,z)\,R_h^1(\rho,z)\,\rho\,d\rho\,dz\right|^2, \tag{4-12}$$

where the squared term, within the absolute value, is the overlap between the electron and hole wavefunctions [44], and E_p is the Kane energy (19.1 eV for ZnTe [45] and 21 eV for CdSe [44]). A homogeneous line broadening was considered; for that purpose, a hyperbolic secant type function is selected to represent the δ-function in Equation (4-11), i.e.,

$$\delta_{1-1}(E_{e-h} - \hbar\,\omega) \cong \frac{1}{\pi\,\hbar\,\Gamma}\,\mathrm{sech}\left(\frac{\hbar\omega - E_{e-h}}{\hbar\,\Gamma}\right). \tag{4-13}$$

Here, $\hbar\,\Gamma$ is the linear factor of the broadening, which is related to the lifetime, and is taken to be 30 meV [26, 44]. Note that Equation (4-13) represents a δ-function shifted so that its maximum position coincides with the $e-h$ energy transition. Finally, the transition energy is given by

$$E_{e-h} = E_g + E_e^1 + E_h^1 - E_{exc}^1\,. \tag{4-14}$$

Additionally, E_g is the effective energy gap between the lower part of the CdSe conducting band and the upper part of the ZnTe valence band. For ZnTe/CdSe, $E_g = E_g^{ZnTe} - V_e$, whereas for CdSe/ZnTe, $E_g = E_g^{CdSe} - V_h$ [29].

4.4 Results and Discussion

The parameters used in this work are: $m_e^{*\mathrm{CdSe}} = 0.13\,m_0$, $m_h^{*\mathrm{CdSe}} = 0.45\,m_0$, $\varepsilon^{\mathrm{CdSe}} = 10.6$, $E_g^{\mathrm{CdSe}} = 1.75\,\mathrm{eV}$, $m_e^{*\mathrm{ZnTe}} = 0.15\,m_0$, $m_h^{*\mathrm{ZnTe}} = 0.2\,m_0$, $\varepsilon^{\mathrm{ZnTe}} = 9.7$, $E_g^{\mathrm{ZnTe}} = 2.2\,\mathrm{eV}$, $V_e = 1.27\,\mathrm{eV}$, and $V_h = 0.84\,\mathrm{eV}$ [35]. Here, m_0 is the free electron mass.

Figure 4-2 illustrates the energy variation concerning the inner radius for the ZnTe/CdSe (Figure 4-2a,c) and CdSe/ZnTe (Figure 4-2b,d) QDs. In Figure 4-2a–d, the electron/hole energies are depicted. Figure 4-2a,d demonstrate the confinement of both electrons and

holes within the shell, where an increment in the inner radius leads to a reduction in the size of the shell, with the subsequent increase in energies. Conversely, Figure 4-2b,c display the case of confinement within the core, with energy levels decreasing as R_1 becomes larger. The observed behavior can be explained by considering the Heisenberg uncertainty principle. As the shell size decreases, the confinement volume for the particles diminishes, leading to an increase in energy. On the other hand, when the particle localizes within the core, the confinement volume increases with the growth of R_1, resulting in a decrease in energy.

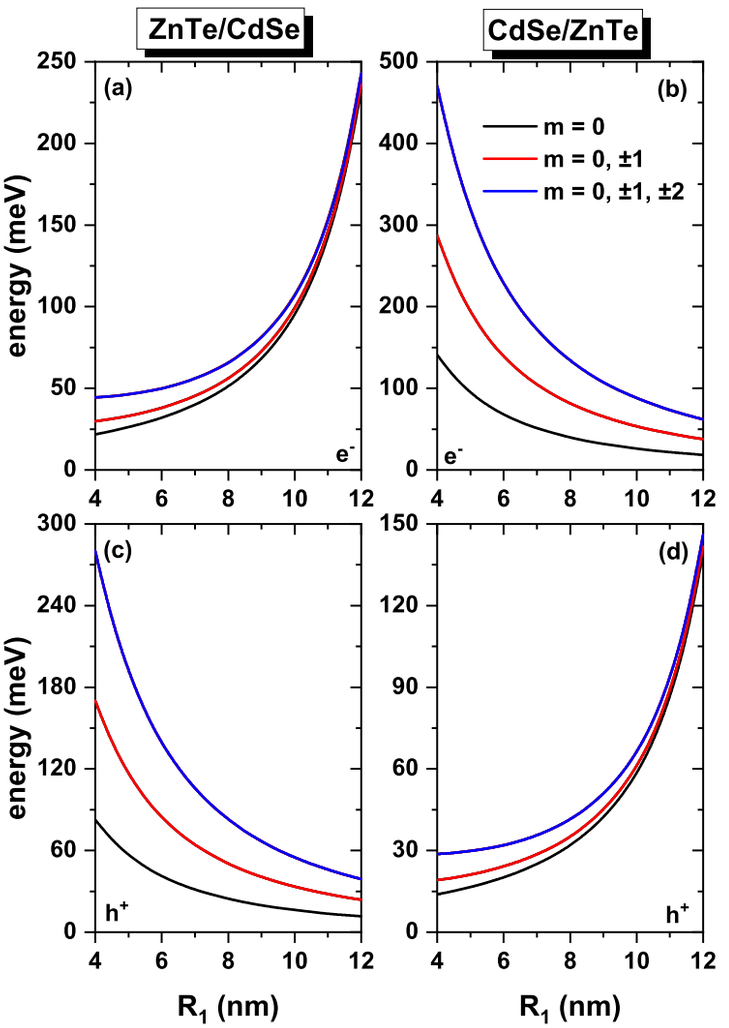

Figure **4-2**: Electronic states of a spherical core/shell quantum dot of ZnTe/CdSe (**a**,**c**) and CdSe/ZnTe (**b**,**d**) as functions of the inner radius, R_1. Panels (**a**–**d**) present the results for electrons/holes, with $R_2 = 15\,\text{nm}$, for different values of the m-quantum number, and without external electric and magnetic field effects.

The results presented in Figure 4-2 correspond to different values of the m-quantum number. The first state, with $m = 0$, exhibits no degeneracy. The first excited state is triply degen-

erate, characterized by $m = 0, \pm 1$, while the second excited state is five-fold degenerate, represented by $m = 0, \pm 1, \pm 2$. These trends align with the well-known behavior observed in a bulk hydrogen atom.

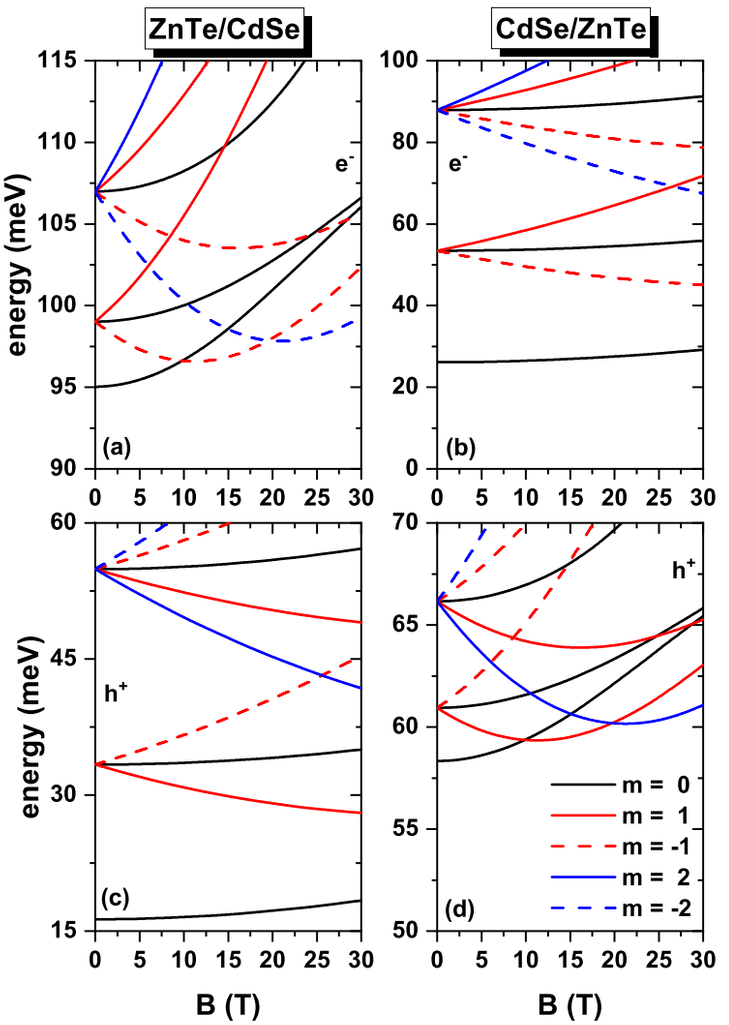

Figure **4-3**: Electronic states of a spherical core/shell quantum dot of ZnTe/CdSe (**a**,**c**) and CdSe/ZnTe (**b**,**d**) as functions of the applied magnetic field, B. Panels (**a**–**d**) present the results for electrons/holes with $R_1 = 10\,\text{nm}$ and $R_2 = 15\,\text{nm}$, for different values of the m-quantum number, and without electric field effects.

Figure 4-3 demonstrates the impact of introducing a magnetic field, which leads to the breaking of degeneracy among the excited states. For instance, in the absence of a magnetic field, the initially triply degenerate first excited state now splits into three distinct states with $m = 0, \pm 1$ as the magnetic field strength (B) increases. A similar behavior is observed for the second excited state, where introducing a magnetic field gives rise to five states. associated with $m = 0, \pm 1, \pm 2$. It is important to note that, for electrons, the energies corresponding

to positive values of m consistently increase with the magnetic field, while the energies for negative values of m initially exhibit a decreasing trend until reaching a minimum value, after which they begin to rise. Conversely, for holes, the energies display an increasing trend for negative values of m, whereas they demonstrate a decreasing and subsequently increasing pattern for positive values of m. This behavior arises from the interplay between the linear and quadratic terms associated with the applied magnetic field in Equation (4-4). Specifically in Figure **4-3**a,d, when the magnetic field is below 10 T, the linear term dominates, while for fields exceeding 10 T, the quadratic term becomes predominant. This behavior gives rise to oscillations in the ground state. For $B \leq 10$ T the ground state corresponds to $m = 0$ (s-like symmetry). Within the magnetic field range of 10 T to 20 T, the ground state corresponds to $m = -1$. Subsequently, the ground state transitions to that with $m = -2$, within the range of 20 T to 30 T. This behavior holds for electrons, Figure **4-3**a. A similar behavior is observed for holes but for positive values of m within roughly the same magnetic field range, Figure **4-3**d. These effects are more pronounced when the electron or hole is confined to the shell region, Figure **4-3**a,d. Notably, when the electron or hole is confined to the core, the ground state with $m = 0$ retains the symmetry of an s-type state within the reported range of magnetic fields.

Figure **4-4** illustrates the energy dependence on the electric field without considering the effects of an external magnetic field. The plots reveal that the electric field also disrupts the degeneracy of the excited states, resulting in two energy levels for the first excited state: one for $m = 0$ and another doubly degenerate for $m = \pm 1$. Additionally, the energy values decrease as the electric field intensity increases. This behavior is particularly pronounced when the electron or hole is confined within the shell (Figure **4-4**a,d). Conversely, when confinement occurs in the core (Figure **4-4**b,c), the energies do not exhibit such a significant variation in the presence of the electric field. This observation can be attributed to the fact that, with a greater spatial localization of electron and hole wavefunctions inside the core, there will be a higher resistance to the electric field effect. In contrast, when the particles are confined to the shell, they exhibit less localization, reducing resistance to wavefunction polarization. The decrease in energies with increasing electric field can be attributed to the strong localization of the wavefunctions of the studied particles associated with the newly added z-dependent linear term in the potential energy. For instance, in the case of an electron confined in the ZnTe/CdSe QD, the wavefunction predominantly resides in the lower region of the quantum dot ($z = -R_2$), while the hole wavefunction is localized at $z = R_1$. Similarly, for the CdSe/ZnTe QD, the electron wavefunction is located at $z = -R_1$, while the hole wavefunction is situated in the upper portion of the quantum dot at $z = R_2$.

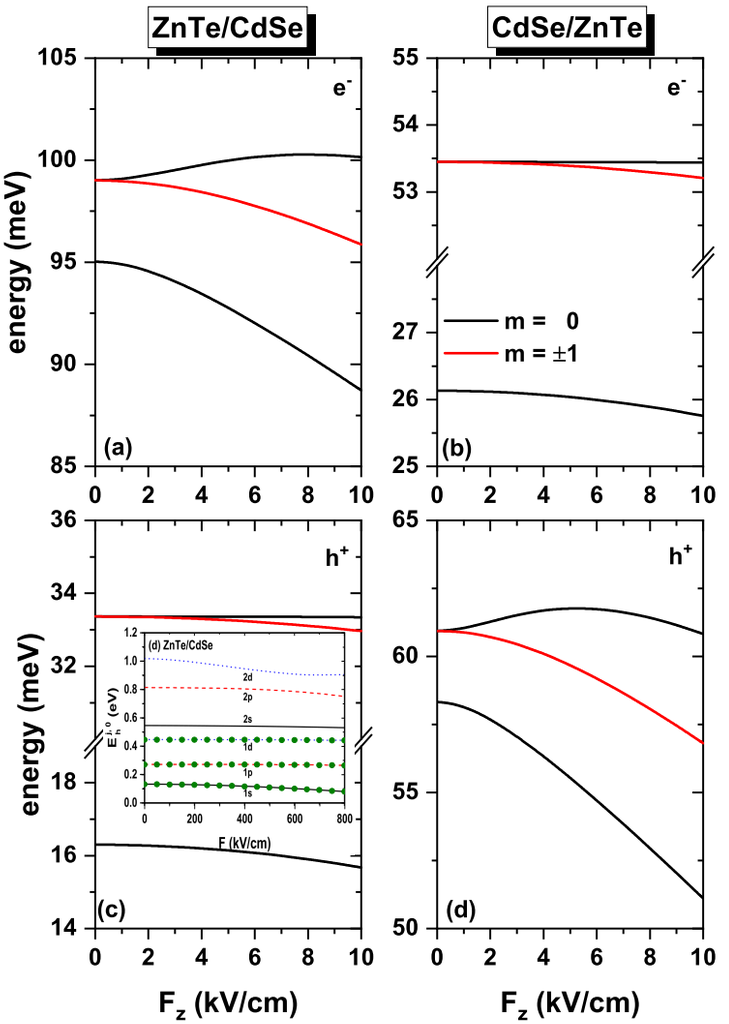

Figure **4-4**: Electronic states of a spherical core/shell quantum dot of ZnTe/CdSe (**a**,**c**) and CdSe/ZnTe (**b**,**d**) as functions of the applied electric field, F_z. Panels (**a**–**d**) present the results for electrons/holes with $R_1 = 10\,\text{nm}$ and $R_2 = 15\,\text{nm}$, for different values of the m-quantum number, and without magnetic field effects. The inset in panel (**c**) corresponds to the comparison made with the theoretical work of Holovastky et al. [29].

In the inset of Figure 4-4c, a comparison is shown between the method here used and the theoretical results obtained in 2022 by Holovatsky et al. Their study uses the diagonalization method to solve for a spherical type II core-shell QD of ZnTe/CdSe and CdSe/ZnTe under the influence of an electric field. The same internal radius (3 nm) and external radius (5 nm) parameters used by the authors were employed, and the electric field was varied from 0 to 800 kV/cm. In the inset, the states 1s, 1p, 1d, 2s, 2p, and 2d correspond to the results reported by Holovatsky et al., while the green dots on the 1s, 1p, and 1d curves represent

our results. Based on this comparison, it can be stated that an excellent agreement was achieved between both data sets.

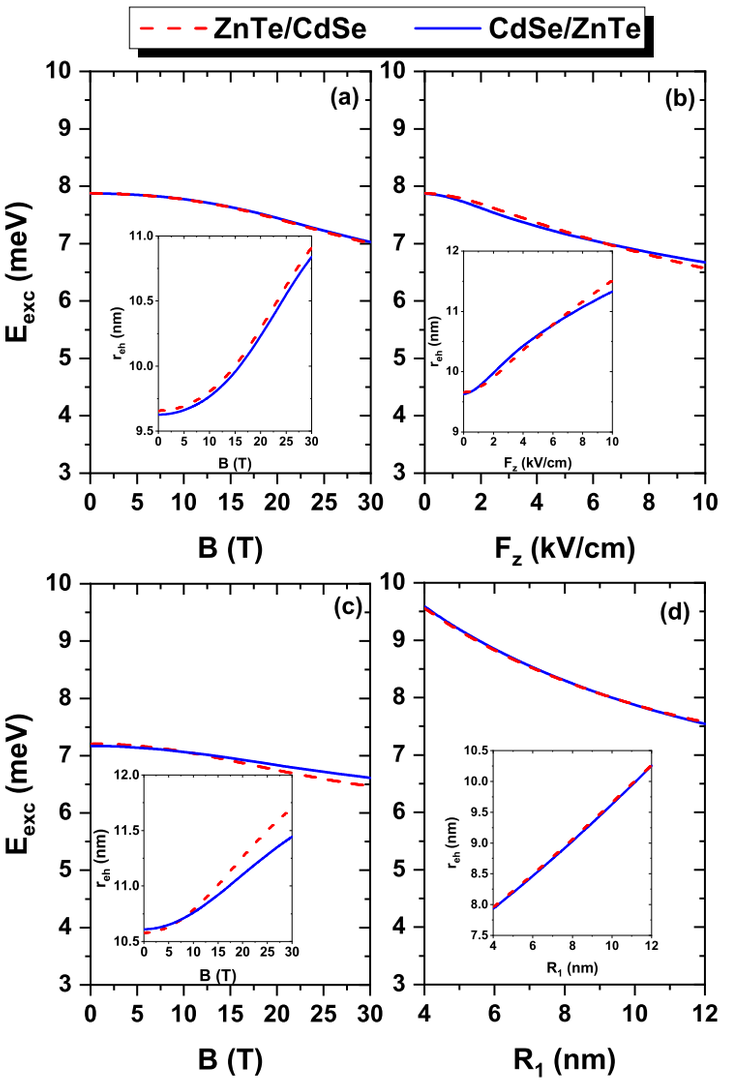

Figure **4-5**: Exciton energy as a function of the applied magnetic field (**a**), applied electric field (**b**), (**c**) applied magnetic field with $F_z = 5\,\mathrm{kV/cm}$ (with $R_1 = 10\,\mathrm{nm}$, and $R_2 = 15\,\mathrm{nm}$), and (**d**) internal radius size (with $R_2 = 15\,\mathrm{nm}$). Results are for $m = 0$. The solid-blue (dashed-red) line corresponds to CdSe/ZnTe (ZnTe/CdSe) QD. The inset in each panel shows the corresponding dependence of the expectation value of the electron-hole separation (r_{eh}). Panel (**a**) is without an external electric field, panel (**b**) is without an external magnetic field, and panel (**d**) does not present any external field.

Figure 4-5 presents the results for exciton energy, calculated using the Coulomb integral described by Equation (4-10), for the ground state ($m = 0$) of an electron–hole pair in

CdSe/ZnTe and ZnTe/CdSe spherical core/shell QDs. In Figure **6-5**a, the exciton energy is plotted as a function of the magnetic field, B, while in Figure **4-5**b, it is shown as a function of the electric field, F_z. Moreover, Figure **4-5**c displays the exciton energy as a function of the inner radius, R_1. In Figure **4-5**a, a slight decrease in exciton energies can be observed as the magnetic field increases. For instance, at zero field, the exciton energy is 7.87 meV, while at 30 T, it is 7.02 meV for the CdSe/ZnTe system and 7.00 meV for the ZnTe/CdSe system. So, there is a variation of approximately 0.87 meV. The decrease in energy values is attributed to the influence of the magnetic field, causing an increase in the expectation value of the electron-hole separation distance, which goes from 9.60 nm at $B = 0$ to 10.84 nm at $B = 30$ T (see inset in Figure **4-5**a). This reflects in a weakening of electron-hole Coulomb interaction. On the other hand, Figure **4-5**b illustrates the exciton energy as a function of the external electric field, applied along the z-direction (F_z). The figure shows a decrease in exciton energies with the presence of the electric field, ranging from 7.87 meV (at $F_z = 0$) to 6.67 meV (CdSe/ZnTe) and 6.56 meV (ZnTe/CdSe) for an electric field of 10 kV/cm. This decrease in exciton energy arises because the electric field confines the electron and hole wavefunctions to opposite regions, while the electron wavefunction is redistributed in the lower region of the QD, the hole wavefunction occupies the upper region. This separation of the probability densities leads to an increase in the expectation value of the electron-hole distance, from 9.65 nm ($F_z = 0$) to 11.32 nm (CdSe/ZnTe) and 11.51 nm (ZnTe/CdSe) at $F_z = 10$ kV/cm (see inset in Figure **4-5**b), resulting in a reduction in exciton energy. Figure **4-5**b also indicates that the ZnTe/CdSe system is more affected by the electric field compared to the CdSe/ZnTe system. This behavior is expected since, in the ZnTe/CdSe system, the electron is confined to the shell, where it has a lower effective mass than the hole. Consequently, the electron experiences stronger effects from the electric field than the hole confined in the shell (CdSe/ZnTe system). Figure **4-5**c illustrates the energy of the exciton as a function of the magnetic field with an applied electric field of 5 kV/cm to the system. As expected, the presence of the electric field affects the exciton energy compared to results that solely considers the magnetic field (Figure **4-5**a). Specifically, the exciton energy is reduced by approximately 0.71 meV, as also evident in the graph showing exciton energies as a function of the electric field (Figure **4-5**b). Apart from this difference, the behavior of the exciton energy with respect to the magnetic field remains the same, displaying a decreasing trend as the magnetic field increases. This energy decay is attributed to the increase in the electron-hole distance, which corresponds to the elevated magnetic field (see inset in Figure **4-5**c). In Figure **4-5**d, a decrease in exciton energy can be observed as the inner radius, R_1, increases. This reduction is attributed to the increase in the core size with the expansion of R_1, leading to a larger distance between the electron and the hole (see inset in Figure **4-5**d). Consequently, the strength of the Coulombic interaction between the electron and hole diminishes. It is worth noting that this phenomenon is similar for both systems, regardless of whether the electron is confined in the core and the hole in the shell (CdSe/ZnTe, represented by the blue curve), or when the electron is confined in the

shell and the hole in the core (ZnTe/CdSe, represented by the red curve). This similarity indicates that the decrease in exciton energy, resulting from changes in the internal radius, is not dependent on the type of confining material but rather on the geometry of the system.

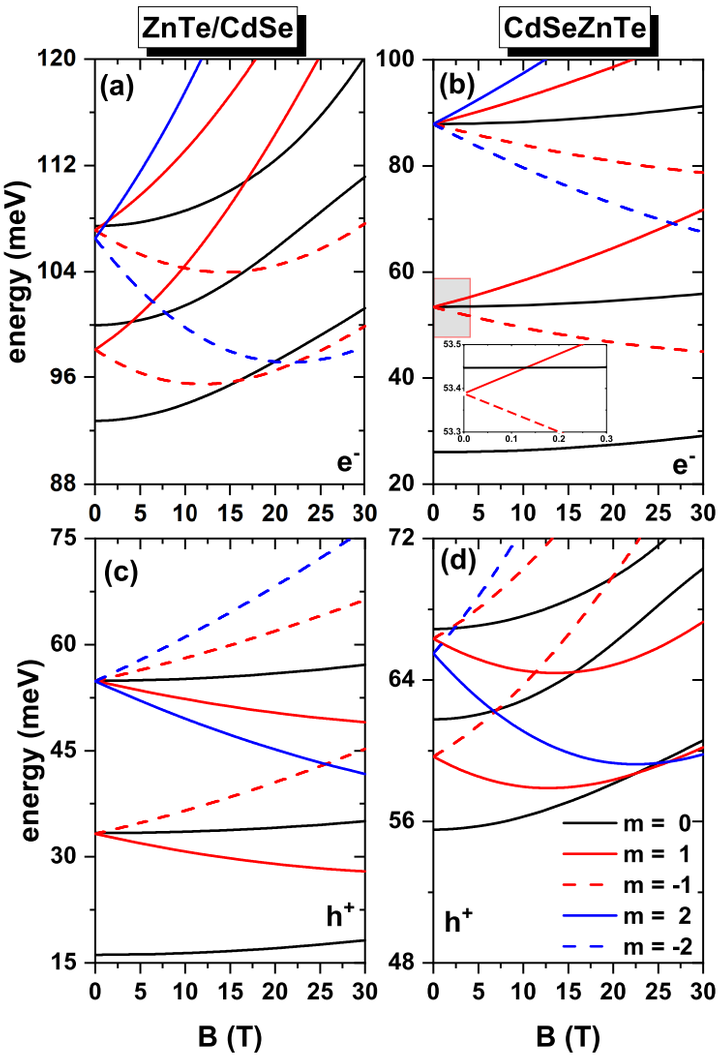

Figure **4-6**: Electronic states of a spherical core/shell quantum dot of ZnTe/CdSe (**a**,**c**) and CdSe/ZnTe (**b**,**d**) as functions of the applied magnetic field, B, with $F_z = 5\,\mathrm{kV/cm}$. Panels (**a**–**d**) present the results for electrons/holes with $R_1 = 10\,\mathrm{nm}$ and $R_2 = 15\,\mathrm{nm}$, for different values of the m-quantum number.

Figure 4-6 shows the energy levels as functions of the magnetic field in the presence of an electric field of 5 kV/cm. The energy curves exhibit similar behavior when only the magnetic field is active, as shown in Figure 4-3. However, when the magnetic field is set to zero, the excited states display a splitting phenomenon induced by the electric field. For instance, at $B = 0$, the first excited state manifests two distinct energy levels, while the second ex-

cited state exhibits three of them, as depicted in the figures with an electric field only (see Figure 4-4). Notably, these effects are more pronounced when the electron and hole are confined in the shell region (Figure 4-6a,d), but they are also present when the particle is confined in the core (Figure 4-6b,c). This distinction is particularly evident for the first excited state, as shown in the inset of Figure 4-6b, where the energy difference at $B = 0$ is approximately 0.1 meV, compared to around 2 meV in Figure 4-6a,d.

We present in Figure 4-7a the intensity of oscillator strength related to interband transitions as a function of the applied magnetic field for CdSe/ZnTe QDs (solid blue curve) and ZnTe/CdSe QDs (red dashed curve). It is observed from the figure that, for both systems, the magnitude of this quantity decreases as the magnetic field strengthens. This is expected since band transitions' oscillator strength is directly proportional to the superposition of electron and hole wavefunctions, which diminishes with the increasing magnetic field. Specifically, when the electron or hole is confined to the shell, their distribution shifts towards the upper and lower regions of the quantum dot as long as the magnetic field intensity augments (compare the first and second column in panel (d) and in the inset in panel (a)), thus resulting in a reduced overlap. In Figure 4-7b, it is observed that the amplitude of the oscillator strength for interband transitions diminishes as the electric field intensifies. This decrease is evident for CdSe/ZnTe and ZnTe/CdSe systems. The diminishing amplitude of the oscillator strength is attributed to the decreased overlap between the wavefunctions of particles confined to the shell and core. At zero electric field, the wavefunctions of the shell and core particles are confined throughout the spherical region. However, with a non-zero electric field, the hole wavefunction shifts towards the upper region of the quantum dot, while the electron wavefunction shifts towards the lower region (compare the first and third column in panel (d) and in the inset in panel (a)), leading to a reduction in the overlap. Furthermore, in Figure 4-7c, a decrease in the magnitude of the oscillator strength is observed in the range from 4.0 nm to 7.6 nm, where its value goes down from 4.69 (at $R_1 = 4$ nm) to 2.64 for the CdSe/ZnTe system and 2.93 for ZnTe/CdSe at $R_1 = 7.6$ nm. However, the opposite trend is observed in the range from 7.6 nm to 12 nm, as the magnitude value of the oscillator strength increases, reaching a maximum value of 5.97 for CdSe/ZnTe and 8.35 for ZnTe/CdSe at $R_1 = 12$ nm. The behavior of the oscillator strength described above can be attributed to the superposition of the electron and hole wavefunctions. The inset of Figure 4-7c provides insight into this phenomenon by showing the overlap volume of the revolution solid formed by the two wavefunctions at different radii (4 nm, 7.6 nm, and 12 nm). It is clear that, for an internal radius of 4 nm, the revolution solid representing the superposition of the two wavefunctions has a larger volume compared to the case of 7.6 nm. Conversely, the overlap volume is more significant for a radius of 12 nm than in the previous two cases.

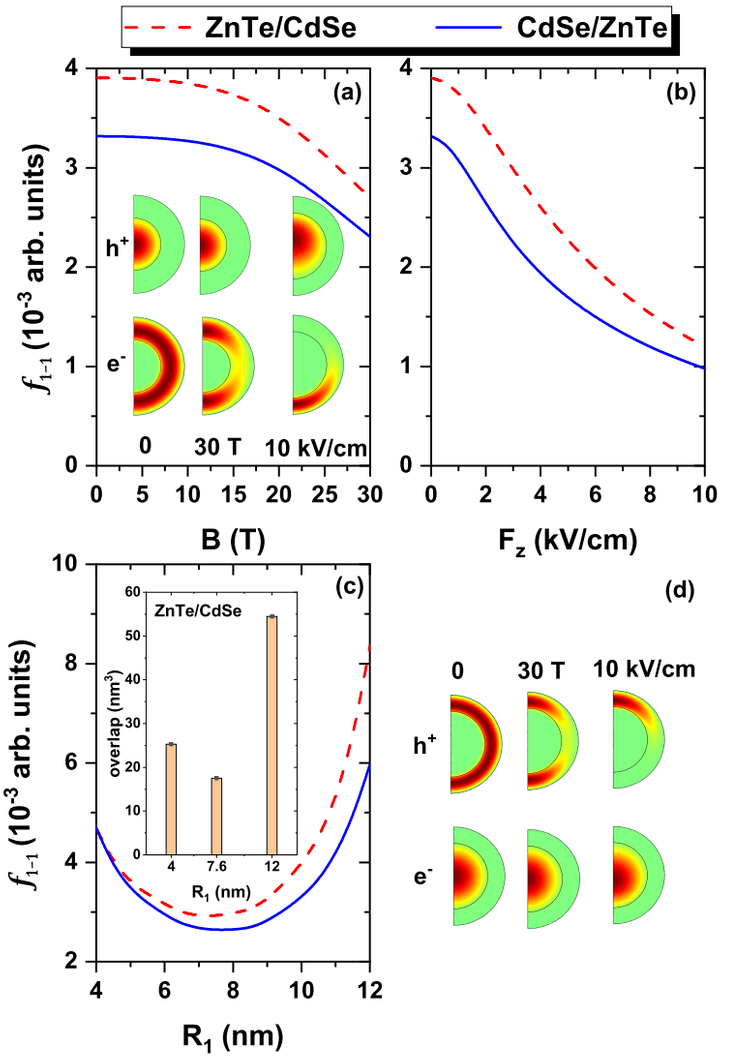

Figure **4-7**: Oscillator strength for interband transitions as a function of the applied magnetic field (**a**), applied electric field (**b**) (with $R_1 = 10\,\text{nm}$, and $R_2 = 15\,\text{nm}$), and (**c**) the internal radius (with $R_2 = 15\,\text{nm}$). The solid-blue (dashed-red) curve represents the CdSe/ZnTe (ZnTe/CdSe) QD results. In panel (**d**) are shown the distributions of the ground state wavefunctions for the CdSe/ZnTe QD considering several setups of the applied magnetic and electric field: zero fields (first column), $B = 30\,\text{T}$ with $F_z = 0$ (second column), and $B = 0$ with $F_z = 10\,\text{kV/cm}$ (third column). The identical wavefunction distributions but for ZnTe/CdSe QDS are shown in the inset of panel (**a**). The inset in (**c**) is the value of the volume overlap of the wavefunctions for different R_1-radius: 4 nm, 7.6 nm, and 12 nm. Panel (**a**) is without an external electric field, panel (**b**) is without an external magnetic field, and panel (**c**) does not present any external field.

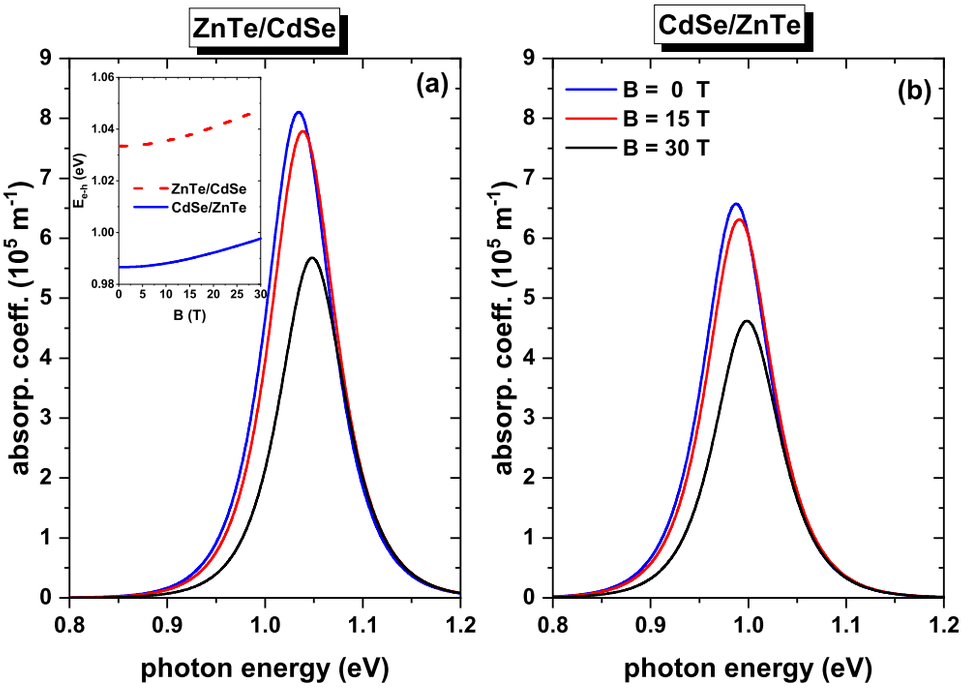

Figure **4-8**: Light absorption coefficient as a function of the energy of the incident photon for three different magnetic fields and zero electric fields: $B = 0$ (blue), 15 T (red), and 30 T (black). In (**a**), the results are for ZnTe/CdSe QDs, whereas in (**b**) are for CdSe/ZnTe QDs. The inset in panel (**a**) corresponds to the transition energy as a function of B: red-dashed line for ZnTe/CdSe QDs and blue-solid one for CdSe/ZnTe. Calculations are for $R_1 = 10$ nm, $R_2 = 15$ nm, and without an external electric field.

Figure 4-8 contains the plots of the optical absorption coefficient as a function of the incident photon energy for three different magnetic field values. Figure 4-8a presents the results for ZnTe/CdSe QDs, while Figure 4-8b displays the corresponding ones for CdSe/ZnTe QDs. The figures demonstrate that the absorption peaks undergo a blueshift as the magnetic field increases. Additionally, a decrease in the amplitude of the resonant peak can be observed. The displacement of the absorption peaks to higher energies can be attributed to the increase in transition energy as the magnetic field strength rises (see the inset in Figure 4-8a). The oscillator strength influences the amplitude of the absorption peaks (see Figure 4-7a), which decreases with the magnetic field, thus impacting the overall magnitude of absorption. As noticed from Equation (4-11), the magnitude of absorption response is directly proportional to the oscillator strength. Furthermore, a distinction can be noted in the peaks and amplitudes between the two studied systems. For instance, in the ZnTe/CdSe system, at a magnetic field intensity of 30 T, the absorption peak is observed at an energy of 1.04 eV, whereas in the CdSe/ZnTe system, the peak appears at 0.99 eV. This difference in energy and magnitude, with ZnTe/CdSe exhibiting a higher amplitude than CdSe/ZnTe,

can be attributed to the difference in the dependence of transition energy and oscillator strength between the two systems (see the inset in Figure 4-8a and the overall behavior in Figure 4-7a).

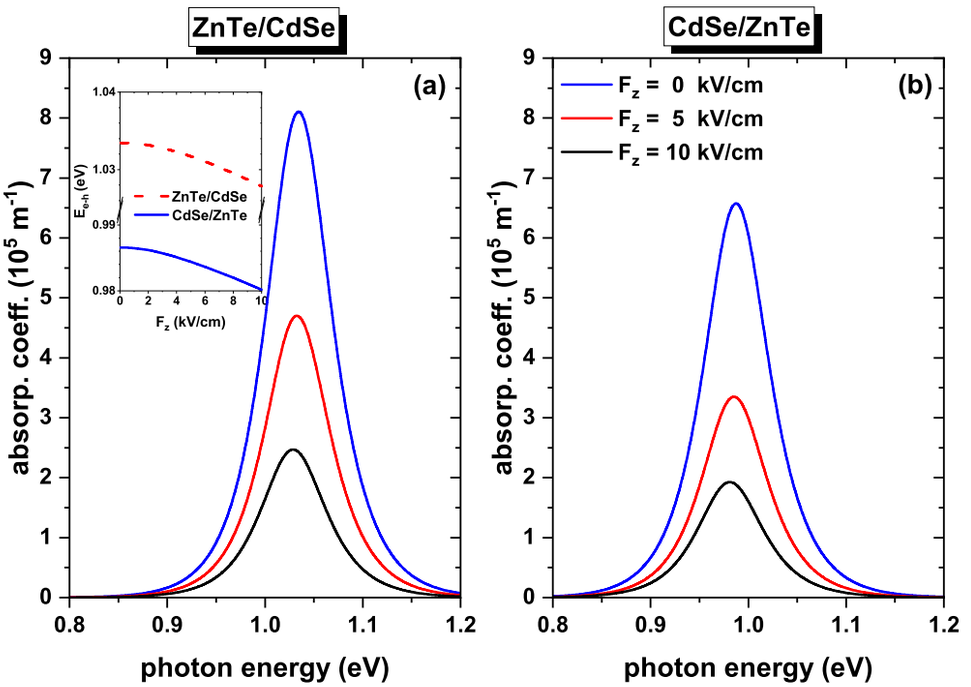

Figure **4-9**: Light absorption coefficient as a function of the energy of the incident photon for three different electric fields and zero magnetic fields: $F_z = 0$ (blue), 5 kV/cm (red) , and 10 kV/cm (black). In (**a**), the results are for ZnTe/CdSe QDs, whereas in (**b**) are for CdSe/ZnTe QDs. The inset in panel (**a**) corresponds to the transition energy as a function of F_z: red-dashed line for ZnTe/CdSe QDs and blue-solid one for CdSe/ZnTe. Calculations are for $R_1 = 10$ nm, $R_2 = 15$ nm, and without external magnetic field.

Figure 4-9 depicts the absorption coefficient as a function of the incident photon energy for three different electric field values in the absence of an external magnetic field. Figure 4-9a presents the results for ZnTe/CdSe QDs, while Figure 4-9b displays the results for CdSe/ZnTe QDs. From both figures, a notable change observed upon introducing the electric field is the decrease in the amplitude of the absorption coefficients. This decrease is directly related to the oscillator strength (see Figure 4-7b), as it diminishes rapidly with an increasing electric field. Furthermore, the figures show that the absorption peaks undergo a slight shift towards lower energies for both systems. This shift is associated with the transition energy (see the inset in Figure 4-9a), which decreases with the electric field. However, the decrease is approximately 6 meV for both systems. It is important to mention that in the case of the ZnTe/CdSe system, the absorption peaks are located at higher energies of

the incident photon and exhibit a greater amplitude compared to the CdSe/ZnTe system. This disparity arises from the fact that the ZnTe/CdSe QDs have higher transition energy and oscillator strength amplitudes (see Figure 4-7b).

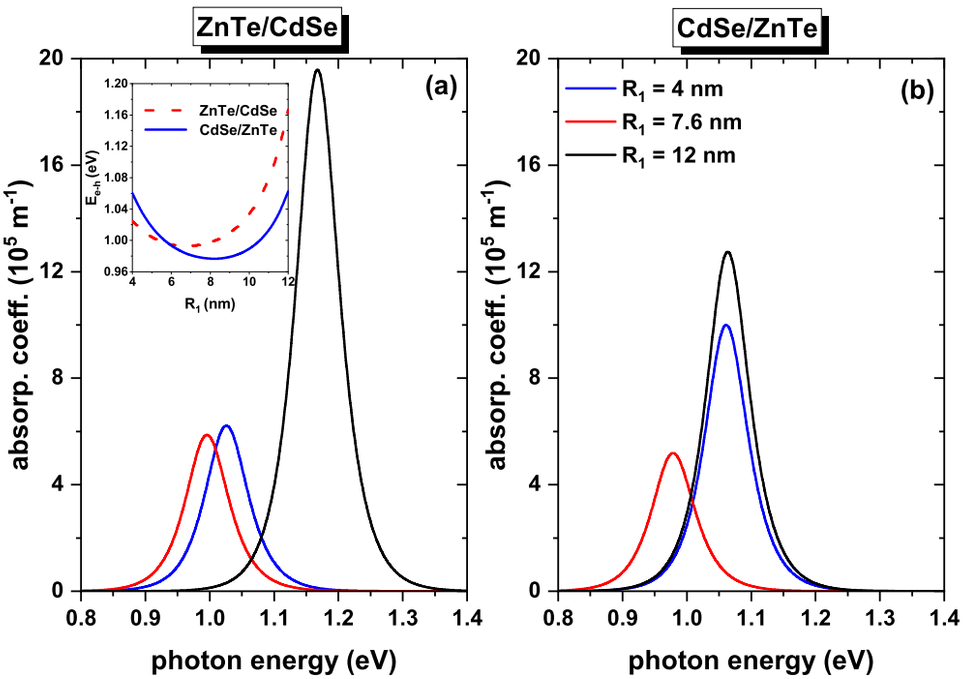

Figure **4-10**: Light absorption coefficient as a function of the energy of the incident photon for three different internal radii for zero electric and magnetic fields: $R_1 = 4\,\text{nm}$ (blue), $7.6\,\text{nm}$ (red), and $12\,\text{nm}$ (black). In (**a**), the results are for ZnTe/CdSe QDs, whereas in (**b**) are for CdSe/ZnTe QDs. The inset in panel (**a**) corresponds to the transition energy as a function of R_1: red-dashed line for ZnTe/CdSe QDs and blue-solid one for CdSe/ZnTe. Calculations are for $R_2 = 15\,\text{nm}$, and without external field.

Figure 4-10 illustrates the absorption coefficient as a function of the incident photon energy for three different values of the internal radius in the absence of external fields. Figure 4-10a displays the ZnTe/CdSe QDs results. It can be observed that the peaks at 4 nm and 7.6 nm exhibit similar amplitudes but at different incident photon energies. Specifically, one peak is located at 0.99 eV (7.6 nm), while the other is slightly shifted to the right at 1.03 eV (4 nm). In the case of the internal radius of 12 nm, the peak displays a greater amplitude than the previous cases, and its energy is blueshifted to 1.17 eV. The observed behavior in the energy position of the absorption peaks is directly related to that of the transition energies (see the inset in Figure 4-10a). The transition energies show a minimum value at 7.6 nm, an intermediate value at 4 nm, and a maximum value at 12 nm. This variation occurs because the energy of the hole ground state (see Figure 4-2a) and the energy of the exciton

(see Figure 4-5c) decrease more rapidly in the smaller radius values than the energy of the electron increases. However, above 8 nm, the energy of the electron increases at a faster rate. Regarding the difference in amplitude, it can be related to the oscillator strength (see Figure 4-7c), which exhibits a maximum value for $R_1 = 12$ nm. In Figure 4-10b, the results for CdSe/ZnTe QDs are presented. The absorption coefficient peaks for the 12 nm and 4 nm values of radius occur at similar incident photon energies, specifically at 1.06 eV. However, they differ in amplitude, with the peak at 12 nm displaying a greater amplitude. In the case of $R_1 = 7.6$ nm, the peak is shifted to the left (towards the red region) at 0.97 eV, and it has a smaller amplitude compared to the previous cases. As discussed previously, the positions of the resonant absorption peaks and their amplitudes can be attributed to the corresponding values of transition energy and oscillator strength. For the 12 nm and 4 nm radii, they possess the same transition energy (see the inset in Figure 4-10a). Regarding the amplitude, the oscillator strength is higher for the 12 nm case, resulting in a greater amplitude for the 4 nm and 7.6 nm cases (see Figure 4-7c).

Finally, we wish to emphasize that our results represent a phenomenological study of the electron, hole, and electron–hole interacting pair confined in type-II spherical core-shell heterostructures. We primarily focus on presenting the basic aspects of the problem and do not claim to provide a direct comparison with experimental results. It is important to note that certain additional effects have not been taken into account, such as: *(i)* The image charge effect, which arises from the significant differences in the dielectric constants between the core and shell regions. *(ii)* The influence of radial and tangential stresses and strains associated with the values of lattice constants of the core and shell. When approaching our results, it must be also borne in mind that we have not considered variations in the electron and hole effective masses as the quantum dot (QD) size changes. In a comprehensive and detailed study of confined excitons in spherical QDs with infinite confinement, S. Pokutnyi [46, 47] has presented a modified effective mass approximation. He demonstrated that as the size of the QD approaches the dimensions of the effective Bohr radius, an accurate description of the excitonic states necessitates considering the dependence of the effective mass on the QD's radius. These effects could be relevant in providing a more comprehensive understanding of the system's behavior.

To validate our findings against experimental results, we conducted a comparison with the photoluminescence peak obtained by Jiang and Kelley for ZnTe/CdSe core/shell nanocrystals, where the shell was grown using the Stranski–Krastanov technique [48]. According to the authors' report, the ZnTe core has a radius of 1.3 nm, and the CdSe shell has a thickness of 0.9 nm. After an annealing time of 80 min, they achieved a stable structure with an emission peak at 1.669 eV. Jiang and Kelley's work involved comparing their experimental results with a theory that combines the effective mass approximation, interdiffusion at the core/shell interface, and radial and tangential stresses and strains.

In our study, we considered that for ZnTe/CdSe QDs, the electron and hole are located in the shell/core region, with effective Bohr radius and Rydberg energy values of $a_B = 5.57$ nm and $Ry = 15.56$ meV, respectively. Combining the core and shell dimensions from Jiang and Kelley's work, we concluded that the system's dimensions are of the order of $\sim$0.39, a_B, indicating a highly confined system. So, Coulomb interaction, calculated via a perturbative approach using Equation (4-9), proved to be a good approximation.

To account for high quantum confinement, we implemented the modified effective mass theory suggested by S. Pokutnyi [46, 47]. Our calculations for the system described in Ref. [48] yielded a photoluminescence peak energy located at 1.6875 eV, with corresponding electron, hole, and electron-hole interaction energies of 0.653 eV, 0.2023 eV, and 0.099 eV, respectively. Based on these results, we can confidently state that our findings are in good phenomenological agreement with the experimental results, and the predictive numerical experiments presented in this research are physically accurate.

4.5 Conclusions

In conclusion, this study investigated the optical transitions between the hole and electron ground states in type-II spherical QDs, specifically ZnTe/CdSe and CdSe/ZnTe core/shell ones. The effects of changes in the internal radius and the application of external electric and magnetic fields were examined. The calculations revealed several key findings. Firstly, the transition energy rises as the magnetic field increases, while the overlap between the electron and hole wavefunctions decreases. Consequently, the absorption coefficient peaks experience a blue shift, accompanied by a decrease in their amplitude. Secondly, variations in the electric field cause a decrease in the transition energy and the overlap of the electron and hole wavefunctions. This results in a slight red shift of the absorption coefficient peaks and a significant reduction in their magnitude. Furthermore, the exciton energy and the oscillator strength decreased with increasing magnetic and electric fields. The former is linked to the expectation value of the electron–hole distance, which increases under the influence of magnetic and electric fields. The latter is associated with decreased electron and hole wavefunctions overlap. Moreover, changes in the internal radius affected the transition energy and oscillator strength. In the ZnTe/CdSe QD, the transition energy and oscillator strength exhibited a minimum value at 7.6 nm, an intermediate value at 4 nm, and a maximum value at 12 nm. A similar trend was observed for the CdSe/ZnTe QD, where the transition energy and oscillator strength reached a minimum at 7.6 nm. However, for the 4 nm and 12 nm radii, they had similar values of transition energy. The behavior of the transition energy was linked to the electron and hole energies as the internal radius changed, while the overlap of the wavefunctions directly influenced the oscillator strength. As a result of the transition energy and oscillator strength behavior, the absorption coefficients exhibited their highest

amplitude and energy of incident photons at an internal radius of 12 nm for the ZnTe/CdSe system. Conversely, at an internal radius of 7.6 nm, the absorption coefficients displayed the lowest amplitude and energy of incident photons. In the CdSe/ZnTe system, the absorption coefficient reached its maximum amplitude at 12 nm, shared the same energy of incident photons with 4 nm, and had the lowest amplitude and energy of incident photons at 7.6 nm.

Our study has been validated with experimental results reported in the literature. Considering the simple model we report here, we believe that we have obtained a good agreement between theory and experiment, which generates confidence in our predictive findings.

References

[1] Portacio, A.A.; Jiménez, A.F.; Urango, M.P. Theoretical study on the change of index of refraction and the optical absorption in a quantum dot in the presence of a uniform magnetic field. *Rev. Mex. Fis.* **2016**, *62*, 330–335.

[2] Holovatsky, V.; Chubrey, M.; Voitsekhivska, O. Effect of electric field on photoionisation cross-section of impurity in multilayered quantum dot. *Superlattices Microstruct* **2020**, *145*, 106642. [CrossRef]

[3] Holovatsky, V.A.; Voitsekhivska, O.M.; Yakhnevych, M.Y. The effect of magnetic field and donor impurity on electron spectrum in spherical core-shell quantum dot. *Superlattices Microstruct* **2018**, *116*, 9–16. [CrossRef]

[4] Hasanirokh, K.; Radu, A.; Duque, C.A. Donor impurity in CdS/ZnS spherical quantum dots under applied electric and magnetic fields. *Nanomaterials* **2022**, *12*, 4014. [CrossRef]

[5] Niculescu, E.C.; Cristea, M. Impurity states and photoionization cross section in CdSe/ZnS core–shell nanodots with dielectric confinement. *J. Lumin.* **2013**, *135*, 120–127. [CrossRef]

[6] Toscano-Negrette, R.G.; León-González, J.C.; Vinazco, J.A.; Moreles, A.L.; Koc, F.; Kavruk, A.E.; Sahin, M.; Mora-Ramos, M.E.; Sierra-Oretega, J.; Martínez-Orozco, J.C.; et al. Optical properties in a ZnS/CdS/ZnS core/shell/shell spherical quantum dot: Electric and magnetic field and donor impurity effects. *Nanomaterials* **2023**, *13*, 550. [CrossRef]

[7] Cristea, M. Simultaneous effects of electric field, shallow donor impurity and geometric shape on the electronic states in ellipsoidal ZnS/CdSe core-shell quantum dots. *Phys. E* **2018**, *103*, 300–306. [CrossRef]

[8] Niculescu, E.C.; Cristea, M.; Spandonide, A. Exciton states in CdSe/ZnS core–shell quantum dots under applied electric fields. *Superlattices Microstruct* **2013**, *63*, 1–9. [CrossRef]

[9] Wu, S.; Cheng, L. Exciton diamagnetic shift and optical properties in CdSe nanocrystal quantum dots in magnetic fields. *Phys. B* **2018**, *534*, 98–104. [CrossRef]

[10] Mathan Kumar, K.; John Peter, A.; Lee, C.W. Optical absorption and refraction index change of a confined exciton in a spherical quantum dot nanostructure. *Eur. Phys. J. B* **2011**, *84*, 431–438. [CrossRef]

[11] Yücel, M.B.; Sari, H.; Duque, C.M.; Duque, C.A.; Kasapoglu, E. Theoretical study ofthe exciton binding energy and exciton absorption in differentHyperbolic-type quantum wellsunder applied electric, magnetic, and intense laser fields. *Int. J. Mol. Sci.* **2022**, *23*, 11429. [CrossRef] [PubMed]

[12] Duque, C.M.; Mora-Ramos, M.E.; Duque, C.A. Hydrostatic pressure and electric field effects and nonlinear optical rectification of confined excitons in spherical quantum dots. *Superlattices Microstruct* **2011**, *49*, 264–268. [CrossRef]

[13] León-González, J.C.; Toscano-Negrette, R.G.; Morales, A.L.; Vinasco, J.A.; Yücel, M.B.; Sari, H.; Kasapoglu, E.; Sakiroglu, S.; Mora-Ramos, M.E.; Restrepo, R.L.; et al. Spin–orbit and zeeman effects on the electronic properties of single quantum rings: Applied magnetic field and topological defects. *Nanomaterials* **2023**, *13*, 1461. [CrossRef]

[14] Zamani, A.; Azargoshasb, T.; Niknam, E. Second and third harmonic generations of a quantum ring with Rashba and Dresselhaus spin-orbit couplings: Temperature and Zeeman effects. *Phys. B* **2017**, *523*, 85–91.

[15] Heyn, C. Kinetic model of local droplet etching. *Phys. Rev. B Condens. Matter* **2011**, *83*, 165302. [CrossRef]

[16] Heyn, C.; Zocher, M.; Küster, A.; Hansen, W. Droplet etching during semiconductor epitaxy for single and coupled quantum structures. *Quantum Dots Nanostructures Growth Charact. Model XV* **2018**, *10543*, 38–47.

[17] Xiao, X.; Fischer, A.J.; Wang, G.T.; Lu, P.; Koleske, D.D.; Coltrin, M.E.; Wright, J.B.; Liu, S.; Brener, I.; Subramania, G.S.; et al. Quantum-Size-Controlled Photoelectrochemical Fabrication of Epitaxial InGaN Quantum Dots. *Nano Lett.* **2014**, *14*, 5616–5620. [CrossRef]

[18] Wang, J.; Zhou, G.; He, R.; Huang, W.; Zhu, J.; Mao, C.; Wu, C.; Lu, G. Experimental preparation and optical properties of CeO_2/TiO_2 heterostructure. *J. Mater. Res. Technol.* **2020**, *9*, 9920–9928. [CrossRef]

[19] Yang, W.; Zhang, B.; Ding, N.; Ding, W.; Wang, L.; Yu, M.; Zhang, Q. Fast synthesize ZnO quantum dots via ultrasonic method. *Ultrason. Sonochem.* **2016**, *30*, 103–112. [CrossRef]

[20] Valizadeh, A.; Mikaeili, H.; Samiei, M.; Farkhani, S.M.; Zarghami, N.; kouhi, M.; Akbarzadeh, A.; Davaran, S. Quantum dots: Synthesis, bioapplications, and toxicity. *Nanoscale Res. Lett.* **2012**, *7*, 1–14.

[21] Xu, G.; Zeng, S.; Zhang, B.; Swihart, M.T.; Yong, K.T.; Prasad, P.N. New generation cadmium-free quantum dots for biophotonics and nanomedicine. *Chem. Rev.* **2016**, *116*, 12234–12327. [CrossRef] [PubMed]

[22] Vinasco, J.A.; Londoño, M.A.; Restrepo, R.L.; Mora-Ramos, M.E.; Feddi, E.M.; Radu, A.; Kasapoglu, E.; Morales, A.L.; Duque, C.A. Optical absorption and electroabsorption related to rlectronic and single dopant transitions in holey elliptical GaAs quantum dots. *Phys. Status Solidi B* **2018**, *255*, 1700470. [CrossRef]

[23] Popescu, I.; Hristache, M.; Ciobanu, S.S.; Barseghyan, M.G.; Vinasco, J.A.; Morales, A.L.; Radu, A.; Duque, C.A. Size or shape—What matters most at the nanoscale? *Comput. Mater. Sci.* **2019**, *165*, 13–22. [CrossRef]

[24] Aouami, A.E.; Feddi, E.; El-Yadri, M.; Aghoutane, N.; Dujardin, F.; Duque, C.A.; Phuc, H.V. Electronic states and optical properties of single donor in GaN conical quantum dot with spherical edge. *Superlattices Microstruct* **2018**, *114*, 214–224. [CrossRef]

[25] Heyn, C.; Duque, C.A. Donor impurity related optical and electronic properties of cylindrical $GaAs-Al_xGa_{1-x}$ As quantum dots under tilted electric and magnetic fields. *Sci. Rep.* **2020**, *10*, 1–18. [CrossRef]

[26] Rodríguez-Magdaleno, K.A.; Pérez-Álvarez, R.; Ungan, F.; Martínez-Orozco, J.C. Strain effect on the intraband absorption coefficient for spherical CdSe/CdS/ZnSe core–shell–shell quantum dots. *Mater. Sci. Semicond. Process.* **2022**, *141*, 106400. [CrossRef]

[27] Long, T.; Cao, J.; Jiang, Z.J. Predictable spectroscopic properties of type-II ZnTe/CdSe nanocrystals and electron/hole quenching. *PCCP* **2019**, *21*, 5824–5833. [CrossRef]

[28] Naifar, A.; Zeiri, N.; Nasrallah, S.A.B.; Said, M. Optical properties of CdSe/ZnTe type II core shell nanostructures. *Optik* **2017**, *146*, 90–97. [CrossRef]

[29] Holovatsky, V.A.; Chubrei, M.V.; Duque, C.A. Core-shell type-II spherical quantum dot under externally applied electric field. *Thin Solid Film.* **2022**, *747*, 139142. [CrossRef]

[30] Chen, C.Y.; Cheng, C.T.; Lai, C.W.; Hu, Y.H.; Chou, P.T.; Chou, Y.H.; Chiu, H.T. Type-II CdSe/CdTe/ZnTe (core–shell–shell) quantum dots with cascade band edges: The separation of electron (at CdSe) and hole (at ZnTe) by the CdTe layer. *Small* **2005**, *1*, 1215–1220.

[31] Jaouane, M.; El-Bakkari, M.; Al, E.B.; Sali, A.; Ungan, F. Linear and nonlinear optical properties of CdSe/ZnTe core/shell nanostructures with screened modified Kratzer potential. *Eur. Phys. J. Plus* **2023**, *138*, 319. [CrossRef]

[32] Koc, F.; Kavruk, A.E.; Sahin, M. Advanced tunability of optical properties of CdS/ZnSe/ZnTe/CdSe multi-shell quantum dot by the band edge engineering. *Phys. E* **2023**, *145*, 115479. [CrossRef]

[33] Restrepo, R.L.; Ospina, W.; Feddi, E.; Mora-Ramos, M.E.; Vinasco, J.A.; Morales, A.L.; Duque, C.A. Excitons in spherical quantum dots revisited: Analysis of colloidal nanocrystals. *Eur. Phys. J. B* **2020**, *93*, 109. [CrossRef]

[34] Holovatsky, V.A.; Holovatskyi, I.; Chubrei, M.; Duque, C.A. Theoretical modeling of magnetic field effects on the optical properties of type-II core–shell quantum dot. *Appl. Nanosci.* **2023**, 1–9. [CrossRef]

[35] Kuskovsky, I.L.; MacDonald, W.; Govorov, A.O.; Mourokh, L.; Wei, X.; Tamargo, M.C.; Tadic, M.; Peeters, F.M. Optical Aharonov-Bohm effect in stacked type-II quantum dots. *Phys. Rev. B* **2007**, *76*, 035342. [CrossRef]

[36] Roy, B.; Ji, H.; Dhomkar, S.; Cadieu, F.J.; Peng, L.; Moug, R.; Tamargo, M.C.; Kim, Y.; Smirnov, D.; Kuskovsky, I.L. Enhancement and narrowing of the Aharonov-Bohm oscillations due to built-in electric field in stacked type-II ZnTe/ZnSe quantum dots: Spectral analysis. *Phys. Rev. B* **2007**, *86*, 165310.

[37] Heyn, C.; Küster, A.; Zocher, M.; Hansen, W. Field-controlled quantum dot to ring transformation in wave-function tunable cone-shell quantum structures. *Phys. Status Solidi RRL* **2018**, *2018*, 1800245. [CrossRef]

[38] Heyn, C.; Radu, A.; Vinasco, J.A.; Laroze, D.; Restrepo, R.L.; Tulupenko, V.; Hieu, N.H.; Phuc, H.V.; Mora-Ramos, M.E.; Ojeda, J.H.; et al. Exciton states in conical quantum dots under applied electric and magnetic fields. *Opt. Laser Technol.* **2021**, *139*, 106953. [CrossRef]

[39] COMSOL. *Multiphysics*, v. 6.1; COMSOL AB: Stockholm, Sweden, 2023.

[40] COMSOL. *Multiphysics Reference Guide*; COMSOL AB: Stockholm, Sweden, 2012.

[41] COMSOL. *Multiphysics Users Guide*; COMSOL AB: Stockholm, Sweden, 2012.

[42] Pulgar-Velásquez, L.; Sierra-Ortega, J.; Vinasco, J.A.; Laroze, D.; Radu, A.; Kasapoglu, E.; Restrepo, R.L.; Gil-Corrales, J.A.; Morales, A.L.; Duque, C.A. Shallow donor impurity states with excitonic contribution in GaAs/AlGaAs and CdTe/CdSe truncated conical quantum dots under applied magnetic field. *Nanomaterials* **2021**, *11*, 2832. [CrossRef]

[43] Davies, J.H. *The Physics of Low-Dimensional Semiconductors: An Introduction*; Cambridge University Press: Cambridge, UK, 1996.

[44] Şahin, M.; Nizamoglu, S.; Kavruk, A.E.; Demir, H.V. Self-consistent computation of electronic and optical properties of a single exciton in a spherical quantum dot via matrix diagonalization method. *J. Appl. Phys.* **2009**, *106*, 043704. [CrossRef]

[45] Cheche, T.O.; Barna, V.; Chang, Y.C. Analytical approach for type-II semiconductor spherical core–Shell quantum dots heterostructures with wide band gaps. *Superlattices Microstruct* **2013**, *60*, 475–486. [CrossRef]

[46] Pokutnyi, S.I. Exciton states in semiconductor quantum dots in the modified effective mass approximation. *Semiconductors* **2007**, *41*, 1323–1328. [CrossRef]

[47] Pokutnyi, S.I. Exciton States in quasi-zero-dimensional semiconductor nanosystems. *Semiconductors* **2012**, *46*, 165–170. [CrossRef]

[48] Jiang, Z.-J.; Kelly, F. Stranski-Krastanov shell growth in ZnTe/CdSe core/shell Nanocrystals. *J. Phys. Chem. C* **2013**, *117*, 6826–6834. [CrossRef]

5 Theoretical Study of Thermoelectric Properties of a Single Molecule of Diphenyl-Ether

5.1 Abstract

Considering the extensive research on the optical and electrical properties of molecular systems—particularly their efficient thermoelectric energy conversion at the nanoscale—we propose a new alternative by employing a specific Diphenyl-ether molecule as a functional device Such a molecular system is modeled as a planar segment coupled to two electrodes in the first-neighbor approximation within a tight-binding Hamiltonian. We study the electrical and thermal properties of Diphenyl-ether molecules such as the electric current, electrical and thermal conductance, Seebeck coefficient, and figure of merit, in the strong and weak coupling regimes, considering different structural configurations and variations with temperature. Our results could be valuable for laboratory applications and/or verification, since, in addition to characterizing in this work the Diphenyl-ether molecule as a semiconductor device for different structural models.

Keywords: Diphenil-ether, Tight-Binding, Seebeck coefficient, Figure of merit ZT

5.2 Introduction

The foundations of molecular electronics began to be established in the 1970s when Aviram and Ratner prepared and characterized a molecular system with a donor-acceptor species by performing electron transfer tests, in order to find devices with rectifying properties when the system was submitted to a potential difference [1]. In the last decades, the interest in the study of low dimensional molecular systems has increased in search of their possible use and application, in particular, systems such as organic molecules have been analyzed by coupling them to electrodes, obtaining conductive, semiconducting, and/or insulating behaviors, making them worthy of being considered for electronic connectors, rectifiers, amplifiers, and/or storage devices [2–5].

Molecular systems have sparked great interest in the field of optoelectronic devices due to their unique properties when interacting with light. These systems, which can consist of individual molecules or molecular assemblies, exhibit exceptional capabilities to absorb, emit, or scatter photons. This light-interacting characteristic of molecular systems has driven their application in the field of renewable energy, particularly in the development of solar cells. Solar cells based on molecular systems offer a sustainable solution to the growing energy demand by harnessing solar light, an unlimited and environmentally friendly energy source. The efficient conversion of sunlight and waste heat into usable electricity presents a fundamental challenge for researchers in this field. The goal is to fully replace the use of fossil fuels, thereby avoiding environmental pollution and promoting a cleaner and more sustainable means of energy generation [6–9].

Molecular systems can exhibit nonlinear optical properties, which can be utilized in applications such as optical information processing, integrated optics, and telecommunications. Compounds with large delocalized electron systems show exceptionally large nonlinear responses and higher laser damage thresholds compared to inorganic materials. Furthermore, these properties can be modified to optimize additional properties, such as mechanical and thermal stability. An example of such molecular compounds with a significantly large first-order nonlinear optical response is Diphenyl-ether [10].

According to the above, in the literature, we can find very interesting analyses of thermoelectric and magnetic properties in molecular systems such as DNA chains, benzene molecules, biphenyl molecules [11–14], and especially theoretical-experimental studies of these properties through the molecular system Diphenyl-ether. Motivated by the particular characteristics of this last Diphenyl-ether molecular system, especially those reported by Tali Dadosh et al. (2005), where they characterized it as a conducting molecular device, we analyze through this work its thermoelectric properties taking into account different structural configurations.

To complement the above, it is important to emphasize that Tali Dadosh et al. studied a system of three short organic molecules: 4,4-biphenyldithiol (BPD) conjugated molecule; a bis-(4-mercaptophenyl)-ether (BPE) molecule, in which the conjugate is broken in the center by an oxygen atom; and the 1,4-benzenedimethanethiol (BDMT) molecule, in which the conjugate is broken near the contacts by a methylene group, concluding that the oxygen in BPE and the methylene groups in BDMT suppress electrical conduction relative to BPD [15]. Now to make our study of the Diphenyl-ether properties even more interesting, we highlight the work done by S. K. Maiti, who performed a theoretical study of the electron transport properties through single conjugated molecules (BPD, BPE, and BDMT) sandwiched between two non-superconducting electrodes, using the Green's function technique, within a tight-binding model, finding that the electron transport properties are significantly influenced by the existence of localized groups in these conjugated molecules and the coupling strength between the molecule and the electrode [16].

On the other hand, we know that to analyze any system of low dimensionality that leads to characterize it through its electrical, thermal, spintronic, structural properties, among others, there are many methods that are being used both theoretically and experimentally, for example, at the experimental level, we find the Mechanically Controlled Breakage Joints (MCBJ), which search to find the relationship of the electrical conductance as a function of the electrode separation, the Scanning Tunneling Microscope (STM), which seeks to characterize the tunneling current with the application of a voltage [17–25], among others, and on the side of theoretical methods we can find among many, two important ways; one (strictly numerical) that includes the application of the quantum correlation functional theory through effective equations of a single particle, also known as the density functional theory (DFT), and an-

other (numerical and/or analytical) that includes a process of renormalization of the real space by using Green's functions, where the degrees of freedom of the system are reduced to obtain a one-dimensional system that contains all the structural information of the quantum system [26–30].

It is important to remark that with the two theoretical methods mentioned above, it is possible to determine both the electrical and thermal properties, as well as the spintronic properties of different molecular systems, however, in this work we have used the second one (renormalization process) due to its low computational cost compared to the first one (DFT), facilitating even more numerical or analytical calculations [31–36].

Returning to the purpose of this work, it should be noted that we focus on determine the thermoelectric properties of the planar Diphenyl-ether molecule taking into account different structural forms, which can provide interesting behaviors such as obtaining a high figure of merit (ZT), which depends on the electrical conductance ($\mathcal{G}$), the Seebeck coefficient (S), and the thermal conductance (κ). Now, to obtain a more extensive knowledge of the ZT behavior, these thermoelectric quantities are explored using the already known and standard method of tight binding, calculating the transmission probability (T) by Green's functions through the Fisher-Lee relation [37–39], while the thermoelectric quantities are evaluated by Landauer's theory [38, 39].

Our paper is organized as follows. In Section 2, we present the model of the Diphenyl-ether molecule based on a TB Hamiltonian. In Section 3, we describe the method used for the calculations of different thermoelectric quantities. Finally, we report our essential discoveries as conclusions in Section 5. In addition to this, an appendix is presented as a complement to explain in detail the renormalization method or process of the system under study.

5.3 Model

To study the transport properties of the Diphenyl ether molecule ($C_{12}H_{10}O$), it is connected between two metal electrodes (Left-L and Right-R) through the atomic sites i, resulting different structural configurations depending on the connections between ($i-L/R$), as shown in Figure **5-1**. In the tight-binding approximation, the total system can be represented by the Hamiltonian given by:

$$H = H_M + H_L + H_I, \tag{5-1}$$

where H_M corresponds to the Hamiltonian of the molecule, which has the following form:

$$H_M = \sum_i t_i \left(c_i^\dagger c_{(i+1)} + c_{(i+1)}^\dagger c_i \right) + \sum_i E_i c_i^\dagger c_i, \tag{5-2}$$

where $c_i^\dagger$ and c_i are the operators for creating and destroying an electron at the site i. E_i is the site energy for the carbon (E_c) or oxygen (E_o) atoms, t_i is the hopping between the atoms, which can be t_v for $C-C$ coupling into the benzene molecule, and t_w, when the coupling is between the benzene molecules and the oxygen atom. The terms H_L and H_I of equation 5-1 represent the Hamiltonian of the leads and the molecule-leads interaction, respectively and are given by:

$$H_L = \sum_{k_L} \varepsilon_{k_L} d_{k_L}^\dagger d_{k_L} + \sum_{k_R} \varepsilon_{k_R} d_{k_R}^\dagger d_{k_R}, \tag{5-3}$$

$$H_I = \sum_{k_L} \Gamma_L d_{k_L}^\dagger c_1 + \sum_{k_R} \Gamma_R d_{k_R}^\dagger c_N + h.c., \tag{5-4}$$

here the operator $d_{k_{L(R)}}^\dagger$ is the creation operator of an electron in a state $k_{L(R)}$ with energy ε_{k_L}; $\Gamma_{L(R)}$ is the coupling between each lead with the molecule, and h.c. is the complex conjugate of the Hamiltonian.

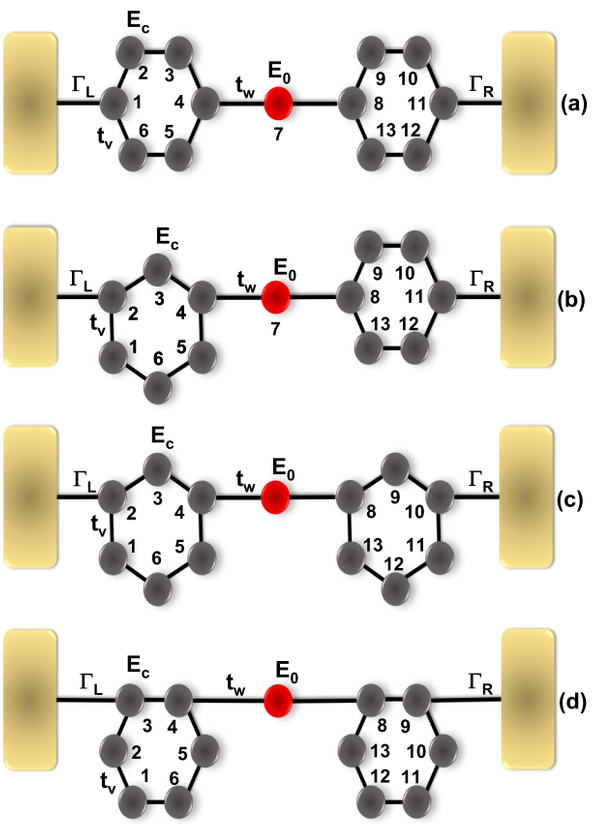

Figure **5-1**: Diphenyl-ether molecule connected from different atomic sites to Left and Right leads. Model (a) Connections $1-L$ and $11-R$, Model (b) Connections $2-L$ and $11-R$, Model (c) Connections $2-L$ and $10-R$ and Model (d) Connections $3-L$ and $9-R$.

5.4 Method

To determine the thermoelectric properties of the Diphenyl-ether molecule, we first focus on calculating the fundamental property that we need to determine the others, which is defined as the transmission probability $T(E)$ as a function of the energy with which the electron enters through the molecular system. This property is calculated using Green's function techniques, through the Fisher-Lee relation [37–39] and is given by:

$$T(E) = Tr[\Gamma_L G^r \Gamma_R G^a], \tag{5-5}$$

where $G^{a(r)}$ represent the advanced(retarded) Green's functions and $\Gamma_{L(R)}$ represent the spectral density matrices of the Left(Right) electrodes respectively, which are given by $\Gamma_{L(R)} = i\left(\Sigma_{L(R)} - \Sigma^{\dagger}_{L(R)}\right)$[1]. Now, to calculate the total Green functions given in the expression 5-5 for each model[2], the Dyson equation is used taking into account that $G = G^0 + G^0(\Sigma_L + \Sigma_R)G$, where G^0 is the Green function of the molecular system without being coupled to the contacts. It is important to note that, as soon as the decimation process is performed for all the models, and the systems are reduced to one-dimensional models, the Fisher-Lee relation to be taken into account for our calculations becomes:

$$T(E) = \Gamma_R \Gamma_L |G_{1N}|^2, \tag{5-6}$$

where N is the number of sites in the new linear system.

Then, once the transmission probability is determined by the relationship 5-6, we can analyze the antiresonances in the $T(E)$ profile for all models, where both the Green's function and transmission function are equal to zero indicating that the cofactor is also zero. However, not all zeros of the cofactor result in an antiresonance in the transmission, therefore, we calculate the cofactor where there is no antiresonance and be able to calculate the Green's function as a function of the cofactor using the expression:

$$G_{ij} = \frac{C_{ji}(E - H)}{det(E - H)}, \tag{5-7}$$

where C_{ij} is the cofactor of the hamiltonian matrix H, and is given by:

$$C_{ij}(H) = (-1)^{j+i} det(h_{ji}), \tag{5-8}$$

being h_{ji} a submatrix of H obtained by removing the jth row and the ith column [40].
In particular, when there is a cyclic molecular system, such as a benzene ring, it is possible to convert the $6-site$ system to two effective sites, with a 2×2 effective Hamiltonian matrix

[1] For our calculations we take $\Sigma_L = \Sigma_R = -i\Gamma/2$.

[2] See the appendix for details on the calculation of Green's functions for each model using the renormalization scheme.

having the following form:

$$H_{eff} = \begin{pmatrix} \tilde{E}_a & V_{ab} \\ V_{ab} & \tilde{E}_b \end{pmatrix}, \tag{5-9}$$

where the diagonal terms (E_a and E_b) are the effective energies of sites a and b respectively, which result from renormalizing the $n - sites$ with energy E_i to an effective site, and off-diagonal terms are the effective couplings between the two effective sites mentioned, and with this Hamiltonian we calculate the Green's function from site a to b with the equation 5-7, given the expression:

$$G_{ab} = \frac{V_{ab}}{(E - \tilde{E}_a)(E - \tilde{E}_b) - V_{ab}^2}. \tag{5-10}$$

From the equation 5-10, we can observe that when V_{ab} is zero, the Green's function is zero and therefore the profile in the transmission probability results in an anti-resonance [41].

Likewise, having the transmission calculated, the current flowing through the molecular system (which is considered as a process of dispersion of an electron between the contacts), is calculated using the Landauer formalism by means of the expression:

$$I(V) = I_0 \int_{-\infty}^{\infty} (f_L - f_R) T(E) dE, \tag{5-11}$$

where $I_0 = 2e/h$, e is the electronic charge, h represents the Plank's constant and $f_{L(R)} = [1 + \exp(\beta(E - \mu_{L(R)}))]^{-1}$ is the Fermi-Dirac distribution function with $\beta = 1/k_B\Theta$ is the Botzmann's factor, and $\mu_{L(R)} = E_f \pm eV/2$ is the chemical potential [41].

Additionally we use the Landauer's integrals $\mathcal{L}_n$, which has the following expression:

$$\mathcal{L}_n = -\int T(E)(E - E_f)^n \left(\frac{\partial f(E)}{\partial E}\right) dE, \tag{5-12}$$

where E_f describes the equilibrium Fermi energy of the system under zero bias condition. With this expression (equation 5-12) we calculate the thermoelectric properties (object of this work) such as the electrical conductance $\mathcal{G}$, the Seebeck coefficient S, the thermal conductance κ and the figure of merit ZT defined as:

$$\mathcal{G} = \frac{2e^2}{h}\mathcal{L}_0, \tag{5-13}$$

$$S = -\frac{1}{e\Theta}\frac{\mathcal{L}_1}{\mathcal{L}_0}, \tag{5-14}$$

$$\kappa = \frac{2}{h\Theta}\left(\mathcal{L}_2 - \frac{\mathcal{L}_1^2}{\mathcal{L}_0}\right), \tag{5-15}$$

$$ZT = \frac{\mathcal{G}S^2\Theta}{\kappa} = \frac{\mathcal{L}_1^2}{\mathcal{L}_0\mathcal{L}_2 - \mathcal{L}_1^2}, \tag{5-16}$$

here, Θ is the equilibrium temperature [25].

5.5 Results and Discussion

In this section, we analyze the quantum transport properties ($T(E)$, $I(V)$, $\mathcal{G}$, S, κ and ZT) through a single Diphenyl-ether molecule, considering 4 different structural models (see figure **5-1**).

In the first instance, and in order to validate the real space renormalization method used in this work, a comparison of the calculation of the transmission probability determined for two molecular systems similar to that of Diphenyl-ether is performed (see Figure **5-2**). The first system taken into account is a 4,4'-Diaminodiethyl Diphenyl-ether molecule ($C_{12}H_{12}N_2O$), through which Wang Y.H et. et. al. calculated the transmission using the DFT method, such molecule contains two benzene rings linked by an oxygen atom and two NH_2 groups that couple the molecule to the electrodes, and a second system that is also characterized by two benzene rings, but this one contains two H atoms, which serve as a bridge to couple the molecule to the electrodes and is called bis-(4-mercaptophenyl)-ether ($C_{12}H_{10}S_2O$). For this last molecular system, the transmission is calculated analytically with the method used in this work, where the site energy used for the Sulfur atom $E_s = -0.98\,\text{eV}$, the site energy of the Carbon atom $E_c = 0\,\text{eV}$, the site energy for the Oxygen atom $E_o = -2.2\,\text{eV}$. For the hopping values, we have: between $S-C$ it is $t_s = -0.83\,\text{eV}$, between $C-C$ it is $t_c = -2\,\text{eV}$, and between $O-C$ it is $t_o = -1\,\text{eV}$.

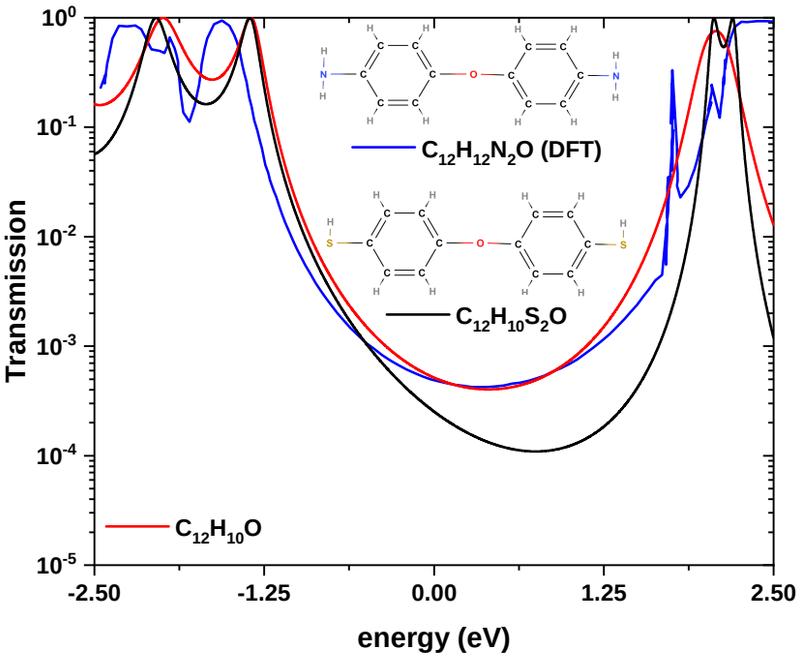

Figure **5-2**: Transmission probability as a function of incident electron's energy for the molecular systems: 4,4'-Diaminodiphenyl-ether (blue curve), bis-(4-mercaptophenyl)-ether (black curve), and Dyphenyl-ether Model (a) (red curve). For the bis-(4-mercaptophenyl)-ether molecule a $\Gamma = 4\,eV$ was used, and for the Dyphenyl-ether molecule a $\Gamma = 0.5\,eV$ was used.

Figure **5-2** shows the probability of transmission as a function of the energy of the incident electron, for the 4,4'-diaminodiphenyl-ether systems calculated by DFT (blue cur- ve), and the bis-(4-mercaptophenyl)-ether molecule by analytical method (black curve), which is compared with the data obtained for the Diphenyl-ether Model (a) system (red curve). It is observed that around the Fermi level ($E_F = 0$) the same behavior occurs, which is a destructive quantum interference in the transmission, caused by the Oxygen site, which breaks the delocalization of the system, this agrees with results from previous works [15]. The other hand the figure **5-2** shows that for the three systems, the energy of the HOMO and the LUMO are very similar, which are around -1.25 and 2.00 eV, presenting a gap of approximately the same width. In order to find a good comparison with the system reported by DFT, a $\Gamma = 4\,eV$ was used for the bis-(4-mercaptophenyl)-ether system, and a $\Gamma = 0.5\,eV$ for the Dyphenyl-ether system, which tells us that the additional radicals cause a stronger coupling with the electrodes, compared to the Dyphenyl-ether molecule alone. It is important to note that the Γ-parameter for the three molecules is different, $\Gamma = 4\,eV$ corresponds to a strong coupling to the electrodes where the electrode molecular orbitals hybridize strongly with the molecule orbitals, while $\Gamma = 0.5\,eV$ corresponds to a weaker hybridization. In the DFT calculation no report of Γ was expel out. Also, the magnitude difference around the Fermi level for the three curves is irrelevant since this accounts for very

small transmission values. In the models shown in Figure **5-1**, the site energies $Ec = 0\,eV$, and $E_o = -2.2\,eV$ have been taken, as the potential between the $C-C$ sites is $t_v = 1\,eV$, and $C-O$ is $t_w = -1\,eV$.

Figure **5-3** presents the transmission profile as a function of the incident electron energy, for a value of $\Gamma = 0.2\,eV$ (weak coupling).

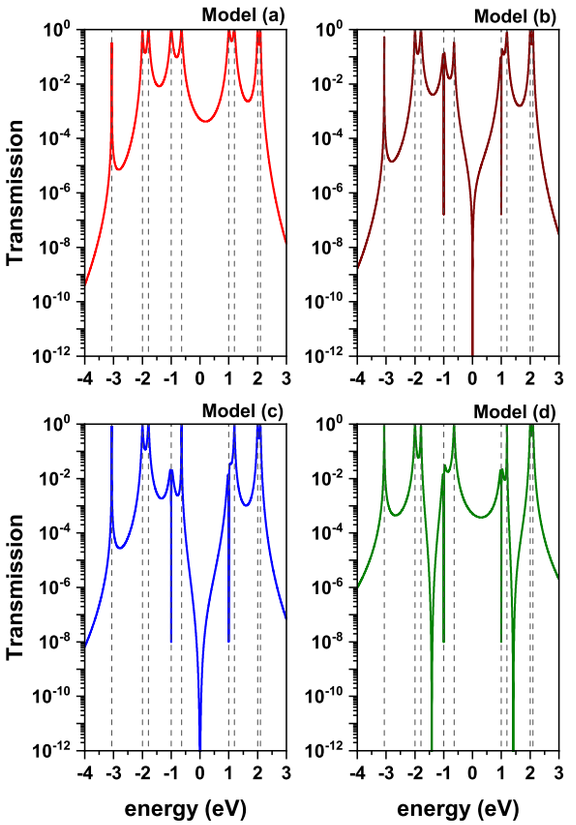

Figure **5-3**: Transmission probability for the molecule Diphenyl-ether, as a function of the energy of the incident electron, for models (a), (b), (c) and (d), which have different coupling sites with the electrodes. The calculations are in a weak coupling regime ($\Gamma = 0.2\,eV$).

The resonant peaks observed in the transmission plot are associated with the eigen values of the diphenyl ether molecule, on the other hand 9 resonances are seen (degenerate and non-degenerate) in model (a), which are related to the 13 eigenvalues of the molecule $(-3.06, -2.00, -1.78, -1.00, -0.63, 1.00, 1.19, 2.00, 2.09\,eV)$, eigenvalues $(1.00, -1.00\,eV)$ are triple degenerate. When considering weak coupling, $\Gamma = 0.2\,eV$, it implies that the electronic states of the electrodes have not mixed with those of the molecule, for this reason there are quite defined peaks, while that for all models there are antiresonances with the some eigenvalues of the molecule, these are associated with destructive quantum interference. This fact

can be explained by means of Feynman integrals, where the electron can traverse all possible paths within the molecule and, depending on the paths chosen, it can arrive at the drain electrode in phase (constructive interference) or out of phase (destructive interference). For model (a) the antiresonance is at $E_F = 0\,eV$, for model (b) at at $E_F = 0$, $\pm 1\,eV$, for model (c) at at $E_F = 0$, $\pm 1\,eV$, and for model (d) at $E_F = 0$, $\pm 1\,eV$, $\pm 1.4\,eV$. Furthermore, if these paths cancel in pairs, it leads to a node at the transmission probability at $E = E_F$ [42], as in the case of model (b) and (c).

Cofactor

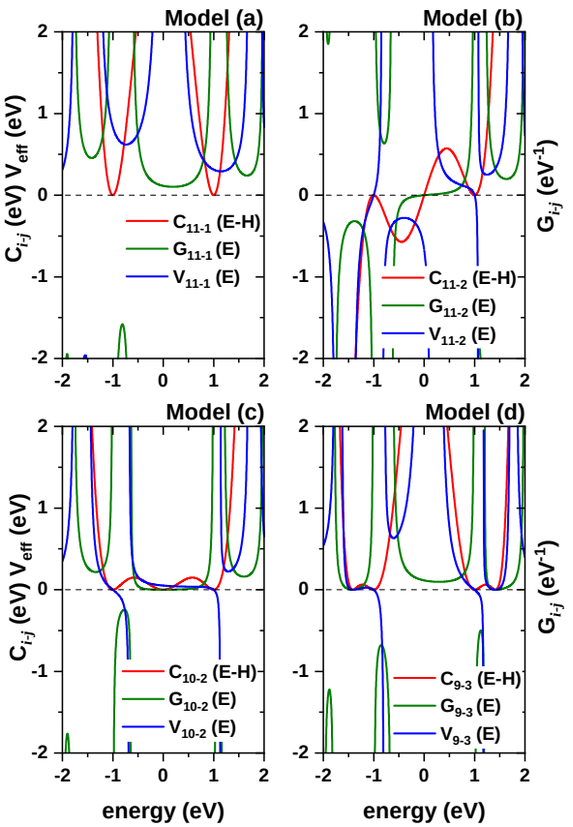

Figure **5-4**: Comparison of the cofactor, with the Green's function of the different contact sites, and the effective potential at two sites of the models (a), (b), (c) and (d). In the weak coupling regime with the electrodes ($\Gamma = 0.2$) eV. Where G_{i-j} and C_{i-j}, is the Green's function, and the cofactor of the system coupled to site i and site j, respectively.

Figure 5-4 shows the graphs of the cofactor comparison with the Green functions, as well as the effective coupling to the two sites of all the models (a, b, c, and d), in the weak coupling regime ($\Gamma = 0.2\,eV$). In the model figure (a) there are two roots for the cofactor

(C_{11-1}), but there are no crossings with the Green's function (G_{11-1}), nor with the effective coupling (V_{11-1}) on the cofactor zeros. This agrees with what is shown in the transmission plot of Figure **5-3** for model (a), in which we do not have destructive quantum interference. For models (b) and (c), there are three roots for C_{11-2}, and there are three crossings at these energy values, one for zero energy with G_{11-2} (model (b)), and G_{10-2} (model (c)), and two with energy - 1 eV and 1 eV, with the V_{11-2} and V_{10-2}. Comparing these results with the graph of the transmission of Figure **5-3** for the model (b) and (c), it is expected that it presents the 3 destructive quantum interferences at 0, 1 and -1 eV. For model (d), we have a similar analysis, but this model presents 4 cofactor crossings, two with G_{9-3}, at energies of -1.4 and 1.4 eV, and two with V_{9-3} at -1 and 1 eV, and this agrees with what is shown in Figure **5-3**, where for the d model, there are 4 destructive quantum interferences. This analysis allows us to verify the results obtained for the probability of transmission. The Green's function G_{11-1} and the effective coupling V_{11-1} represent model (a), where the molecule is connected to sites 1 and 11. On the other hand, G_{11-2} and V_{11-2} correspond to model (b), in which the molecule is connected to the electrodes of sites 2 and 11. Regarding model (c), G_{10-2} and V_{10-2} are used when the molecule is connected to the electrodes of sites 2 and 10. Finally, for the system connected through sites 9 and 3 (model (d)), G_{9-3} and V_{9-3} are employed.

Transmission by varying Γ

Figure **5-5** shows a sweep in both Γ and the energy of the incident electron for the diphenyl-ether molecular system, for different coupling sites of the molecule and the metal electrodes.

At the bottom of the plots is a contour plot of the transmission probability logarithm, on the vertical axis is the sweep in Γ, and on the horizontal axis is the sweep in the energy of the incident electron. In the upper part is the probability of transmission logarithm as a function of the incident electron energy, for two different values of Γ, one of weak coupling (0.2 eV), and another for strong coupling (1 eV). For the strong coupling, in all the models the loss of some peaks is observed in thetransmission probability graph (upper graph). This is due to the peaks overlaping since the Γ parameter is related to the peak with at half maximum. This is due to the hybridization that exists between the delocalized states of the electrode and the localized states of the molecular system. For example, in the model (a), for weak coupling (red graph) for energies of $-2\,eV$ we have two close peaks, something similar happens for energies of -1, 1 and $2\,eV$, but when there is strong coupling, these two peaks combine, forming one. This same analysis can be done for models (b), (c), and (d).

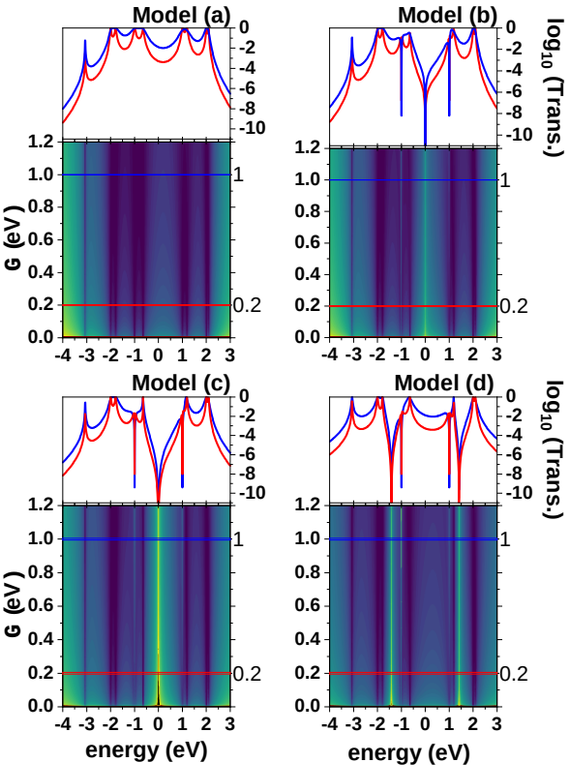

Figure **5-5**: Transmission probability of the Diphenyl-ether molecule, as a function of the energy of the incident electron and the coupling potential with the lead (Γ), for models (a), (b), (c) and (d). In the upper part, the red line corresponds to the logarithm of the transmission for a value of $\Gamma = 0.2\,\text{eV}$ (weak coupling), and the blue curve corresponds to the logarithm of the transmission for a value of $\Gamma = 1\,\text{eV}$ (strong coupling).

Current-voltage characteristics

The Figure **5-5** shows the plot of current versus voltage, the Fermi equilibrium energy E_F is set at $0\,eV$, and for a temperature of $300\,K$.

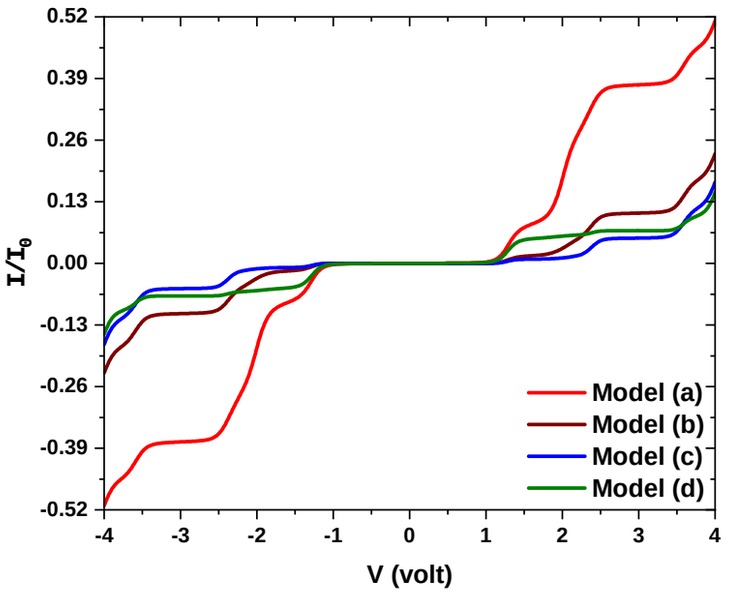

Figure **5-6**: Current-voltage curve, for a single Diphenyl-ether molecule connected to two electrodes. Model (a) (red line), Model (b) (wine line), Model (c) (blue line) and Model (d) (green line).

Figure **5-6** shows the plot of current versus voltage, the Fermi equilibrium energy E_F is set at 0 eV, and for a temperature of 300 K. It is noticed regions of constant current, where the system is far from the transmission resonances (see Figure **5-3**), and steep current regions where the transmission resonances are located. Also, the current curves are antisymmetric with respect to zero volts. From Figure **5-6**, it can be seen that as the voltage increases, the gap between the electrodynamic potentials of the electrodes (left and right) becomes larger, and when the value of the electrodynamic potential coincides with a value characteristic of the molecule, there is a jump in the injection energy of the electron, until reaching a saturation value, which is when the molecule cannot store more electrons, the injection energy becomes constant, and there will be no more energy jumps, no matter how much the voltage is increased. This saturation value is reached for a voltage of approximately 4 *volts*, at this point a maximum current amplitude is obtained. Model (a) is the one with the greatest amplitude in the current, and it is to be expected, since it presents the greatest area under the curve in the transmission graph, followed by model (b), model (c), and finally the model (d). In the systems shown in the I vs. V graph, all present a value of 0 current in the voltage range of $-1\,volt$ and $1\,volt$, which indicates that the systems are not conductive, but it can be considered a semiconductor behavior, since they present this gap, which is due to the small transmission value seen in figure **5-3**. This feature can be useful for designing an electronic switch.

Electrical conductance

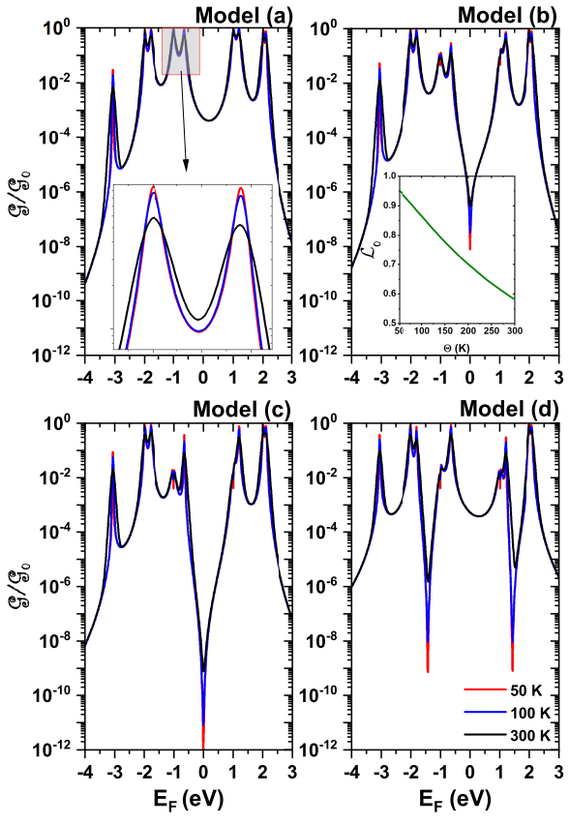

Figure **5-7**: Electrical conductance in a single Diphenyl-ether molecule, as a function of the Fermi energy, for models (a), (b), (c) and (d), which have different coupling sites with the electrodes. The graph shows calculations for 3 different temperatures 50 K (red), 100 K (blue) and 300 K (black). The calculations are in a weak coupling regime ($\Gamma = 0.2\,\text{eV}$). The inset in the figure corresponding to model (a), is an enlargement of the shadow region at the upper part of the figure.The insert in the figure corresponding to model (b) is the graph of the integral $\mathcal{L}_0$ as a function of temperature.

Figure **5-7** shows the electrical conductance of a single Diphenyl ether molecule, as a function of the Fermi energy, for models (a), (b), (c) and (d), for 3 different temperatures 50 K (red), 100 K (blue) and 300 K (black). The calculations are in the weak coupling regime ($\Gamma = 0.2\,\text{eV}$), that is, the behavior of the molecule will be studied when the electrons pass through it. For all the models shown in the electrical conductance graph, it can be seen that it is proportional to the transmission probability (see Figure **5-3** and eq. 13), that is, they share the same number of resonant peaks, and in the same energy positions. In all models, it can be noted that a forbidden band is generated, which is between -0.63 eV and 1 eV, due to destructive quantum interference between the localized states of the molecule and the

delocalized states of the electrodes. At first glance, not many changes in conductance are noticeable for the different temperatures, but in the inset image of the model (a), it can be seen that the conductance decreases as the temperature increases. This decrease is a consequence of the derivative decrease, with respect to the energy, of the Fermi-Dirac distribution function in the integrand of the conductance eq. 13, as the temperature increases (see the insert of Figure **5-7** corresponding to model (b).).

The decrease in conductance is also related to scattering by molecular vibrations which mecanism is not included in the present work, this occurs due to the fact that when the temperature increases there is an increase in the electron's kinetic energy, since they move faster, thus increasing the amplitude of vibration of the atoms of the molecular system, thus behaving as a harmonic oscillator. This phenomenon causes the resistance to the passage of free electrons to increase since it is difficult to pass from one electrode to the other, since the interference of the atoms with the trajectories of the valence electrons throughout the molecule increases.

Seebeck coefficient

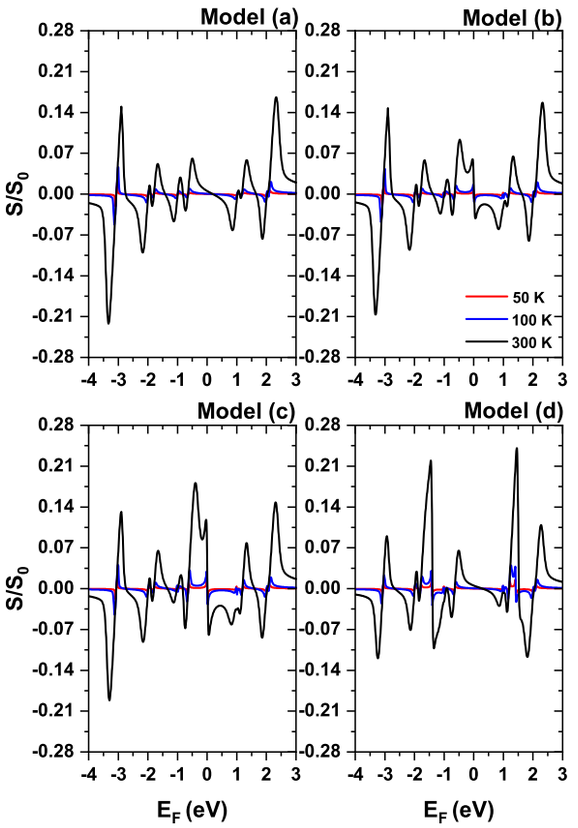

Figure **5-8**: Seebeck coefficient for a single Diphenyl-ether molecule as a function of Fermi energy for models (a), (b), (c), and (d), which differ in their electrode anchoring sites. The graph displays results for three temperatures: 50 K (red), 100 K (blue), and 300 K (black). Calculations were performed in the weak coupling regime ($\Gamma = 0.2\,\mathrm{eV}$).

The thermoelectric properties are now shown, starting with the Seebeck coefficient, next the thermal conductance, and finally, the ZT or figure of merit, taking into account the calculations of the previous physical quantities, in order to know the efficiency of the models to convert thermal energy into electricity.

Figure 5-8 shows the Seebeck coefficient (S) in a single molecule of Diphenyl-ether, as a function of the Fermi energy, for models (a), (b), (c), and (d). The graph shows calculations for 3 different temperatures $50\,K$ (red), $100\,K$ (blue), and $300\,K$ (black). The calculations are in a weak coupling regime ($\Gamma = 0.2\,eV$). The S is extracted from the results close to the $HOMO - LUMO$ gap. Table 1 shows parameters taken from figures 5-3, 5-7, and 5-8, for $300\,K$. It is observed that the Fermi energy is closer to the $HOMO$ level indicating a

positive S value for all models considered. Also, it is verified that high S values are coupled with low conductance values. The most notable result is that the S is higher for models (b) and (c) where an antiresonance occurs at the Fermi energy which coincides with the low $HOMO$ conductance. It is important to note that the low temperature Seebeck coefficient results are very small due to the $\mathcal{L}_0$, *eq*.12, increasing magnitud as the temperature decreases (see the insert of figure **5-7** corresponding to model (b).).

Model	**H**	**L**	**Conductance**	S/S_0	ZT
a	-0.63	1.00	h-H, h-L	0.06	1.59
b	-0.63	1.00	l-H, h-L	0.09	3.85
c	-0.63	1.00	l-H, h-L	0.18	25.78
d	-0.63	1.00	h-H, l-L	0.06	2.09

Table **5-1**: Seebeck coefficients. h = high, l = low, H = HOMO, L = LUMO

Thermal conductance

Now show the thermal conductance as a function of the Fermi energy, for a weak coupling of $0.2\,eV$, for different temperatures.

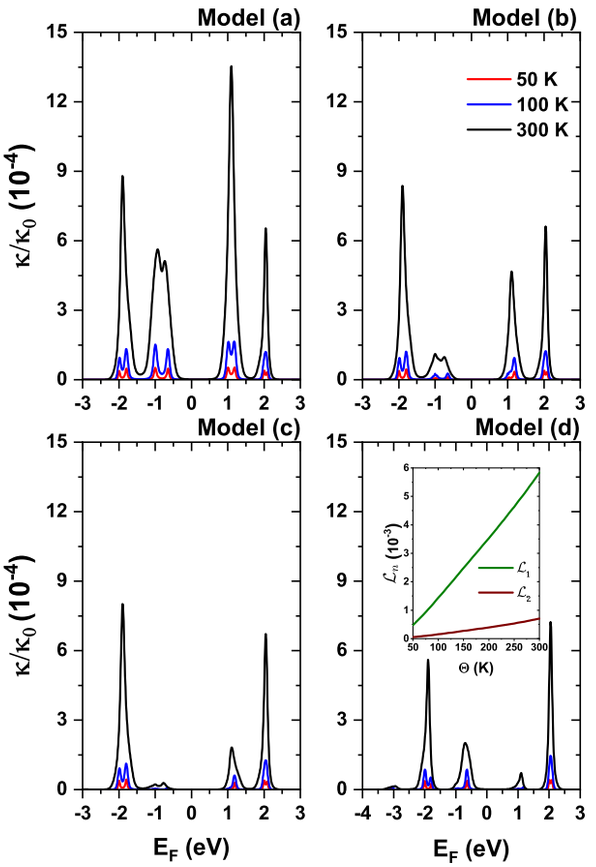

Figure **5-9**: Thermal conductance in a single Diphenyl-ether molecule, as a function of Fermi energy, for models (a), (b), (c) and (d), which have different coupling sites with the electrodes. The graph shows calculations for 3 different temperatures 50 K (red), 100 K (blue) and 300 K (black). The calculations are in a weak coupling regime ($\Gamma = 0.2\,\text{eV}$). The insert in the figure corresponding to model (d) is the graph of the integral $\mathcal{L}_1$, and $\mathcal{L}_2$ as a function of temperature.

Figure 5-9 shows that thermal conductance increases as temperature increases, unlike electrical conductance. This is due to the fact that the increase in temperature, the integral of $\mathcal{L}_2$ and $\mathcal{L}_1$, increases in value (see inset in the Figure 5-9 corresponding to the model (d)), from the *eq*.15, the electrical conductance of depends on the sum of $\mathcal{L}_2$ and the division of $\mathcal{L}_1^2$ by $\mathcal{L}_0$, although the latter decreases with temperature, gain $\mathcal{L}_1^2$. Another way of looking at thermal conductance is directly related to the increase in vibration of the atoms in the molecule, and these vibrations increase the average speed of the particles and therefore increase heat transfer, which is related to thermal conductance of the proposed models, the one with the greatest amplitude in thermal conductance is (a), this is related to the symmetry that this model presents, since the electrons when leaving one electrode to another, since when dividing in the molecule, like the molecule travels, they recombine through the same

number of sites, arriving in phase (see Figure **5-3**).

Figure of merit ZT

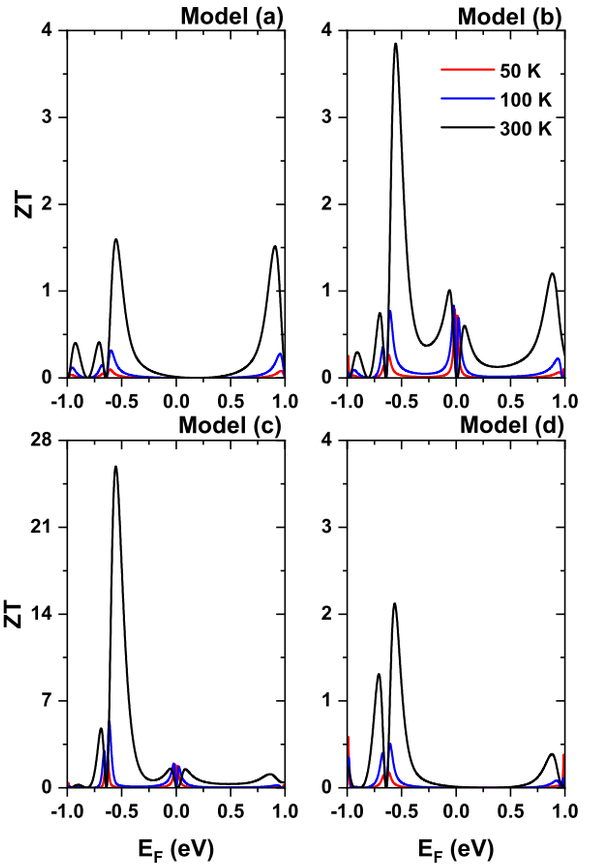

Figure **5-10**: ZT figure of merit in a single Diphenyl-ether molecule, as a function of the Fermi energy, for models (a), (b), (c), and (d), which have different binding sites. coupling with the electrodes. The graph shows calculations for 3 different temperatures 50 K (red), 100 K (blue) and 300 K (black). The calculations are in a weak coupling regime $\Gamma = 0.2\,\text{eV}$.

Finally we have in the Figure **5-10** the ZT, or figure of merit, is shown as a function of the Fermi energy (E_F), to carry out the calculations of the ZT the results obtained for G, S and κ. Of the figures for the ZT, the model that presents the highest value is (c), which is consistent with the calculations obtained for the Seebeck Coefficient (see Table 1), since it is the model that presents the highest S, and the higher S, the higher the value of ZT. This is due to the fact that model (c) presents an interference in the graph of the transmission probability around the Fermi level, and this is more pronounced than in model (b), which

is the model with the second highest ZT.

The model with the smallest ZT is presented by (a), therefore it is with the smallest S, which is the most symmetrical model, and does not present interference in its transmission. For all the models shown, the $ZT \geq 1$, these values indicate that the systems studied can present a good efficiency in the conversion of thermoelectric energy, which is slightly higher than the ZT value of the commercially available inorganic semiconductor, bismuth telluride (Bi_2Te_3) that has a ZT of 1. [43] Lastly, it is important to mention that the higher the temperature, the higher the efficiency.

5.6 Conclusion

The electrical and thermoelectric properties of a single molecule of Diphenyl ether, connected to two metal electrodes, were studied for different atomic sites of the molecule with the electrodes. Using the technique of Green's functions out of equilibrium to renormalize the molecule to 5 effective sites, and with the Landauer-Büttiker formalism, the electrical and thermoelectric properties were calculated, finding very appreciable changes in the thermoelectric properties when taking into account different coupling sites between the molecular system and leads. For example, that the transmission graph for Model (a) does not present quantum antiresonances, as the other models do, this behavior makes this model present greater amplitude in the current graph. The model that presents the best behavior in thermoelectric properties is (c), since it presents the highest value in the Seebeck coefficient, and therefore presents the highest ZT, or figure of merit. Lastly, it is worth mentioning that all the models studied would be great candidates for thermoelectric devices, since the value of ZT is greater than or equal to 1.

5.7 Appendix

Decimation Procedure

We are going to study the quantum transport through the Diphenyl-ether molecule, changing the coupling site of the molecule with the electrodes, in total 4 models will be studied, see Figure **5-1**, we will also show generalities of the decimation process of all the models.

Decimation Model (a)

To perform the decimation of model (a), first the renormalization for the benzene rings to two effective sites is performed:

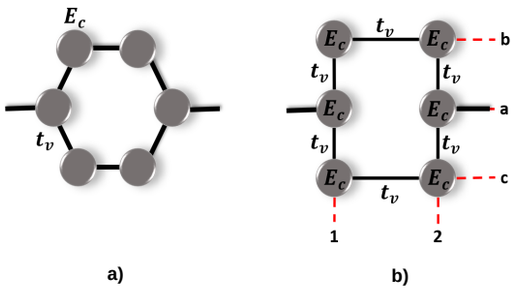

Figure **5-11**: First benzene ring of the model (a), a) isolated molecule, b) reorganization of the molecule to carry out the renormalization.

Figure 5-11 a) shows the isolated benzene ring, and Fig. 5-11 b) shows a reorganization of the ring in order to perform the renormalization, where the information enters the ring through site $1a$ and exits through site $2a$, applying the Dyson equation to first neighbors, the following equations are obtained.

$$G^a_{11} = g_c + g_c t_v G^b_{11} + g_c t_v G^c_{11}, \tag{5-17}$$

$$G^b_{11} = g_c t_v G^a_{11} + g_c t_v G^b_{12}, \tag{5-18}$$

$$G^c_{11} = g_c t_v G^a_{11} + g_c t_v G^c_{12}, \tag{5-19}$$

$$G^c_{12} = g_c t_v G^c_{11} + g_c t_v G^a_{12}, \tag{5-20}$$

$$G^b_{12} = g_c t_v G^b_{11} + g_c t_v G^a_{12}, \tag{5-21}$$

Solving the system of equations gives an expression for G^a_{11} in terms of G^a_{12}.

$$G^a_{11} = \frac{g_c(1 - g_c^2 t_v^2)}{1 - 3g_c^2 t_v^2} + \frac{2g_c^2 t_v^3}{1 - g_c^2 t_v^2} G^a_{12}, \tag{5-22}$$

The above expression has the form of a Dyson equation, where the first term is the effective Green's function of a site 1 connected to a site 2, the second term, which multiplies G^a_{12}, is the effective coupling with the effective site 2.

$$g_1 = \frac{g_c(1 - g_c^2 t_v^2)}{1 - 3g_c^2 t_v^2}, \tag{5-23}$$

and

$$v_1 = \frac{2g_c^2 t_v^3}{1 - g_c^2 t_v^2}, \tag{5-24}$$

The above process works for both benzene rings, therefore, model (a) is decimated to a system with 5 sites, of which 4 are effective (see Figure 5-14 a)).

Decimation Model (b)

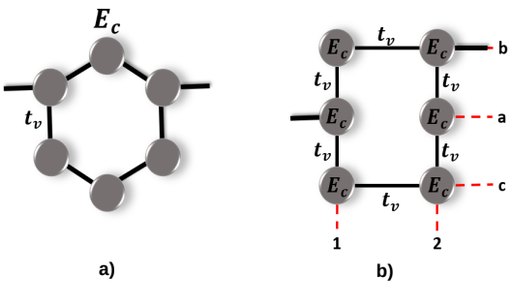

Figure **5-12**: First benzene ring of the model (b), a) isolated molecule, b) reorganization of the molecule to carry out the renormalization.

Figure 5-12 a) shows the isolated benzene ring, and Figure 5-12 b) shows a reorganization of the ring in order to perform the renormalization, where the information enters the ring through site $1a$ and exits through site $2b$, applying the Dyson equation to first neighbors, the following equations are obtained.

$$G^a_{11} = g_c + g_c t_v G^b_{11} + g_c t_v G^c_{11}, \tag{5-25}$$

$$G^b_{11} = g_c t_v G^a_{11} + g_c t_v G^b_{12}, \tag{5-26}$$

$$G^c_{11} = g_c t_v G^a_{11} + g_c t_v G^c_{12}, \tag{5-27}$$

$$G^c_{12} = g_c t_v G^c_{11} + g_c t_v G^a_{12}, \tag{5-28}$$

$$G^a_{12} = g_c t_v G^c_{12} + g_c t_v G^b_{12}, \tag{5-29}$$

Solving the system of equations gives an expression for G^a_{11} in terms of G^b_{12}.

$$G^a_{11} = \frac{g_c(1-2g_c^2t_v^2)}{1-4g_c^2t_v^2+3g_c^4t_v^4} + \frac{g_c t_v^2(1-g_c^2t_v^2)}{1-2g_c^2t_v^2} G^b_{12}, \tag{5-30}$$

The above expression has the form of a Dyson equation, where the first term is the effective Green's function of a site 1 connected to a site 2, the second term, which multiplies G^b_{12}, is the effective coupling with the effective site 2.

$$g_2 = \frac{g_c(1-2g_c^2t_v^2)}{1-4g_c^2t_v^2+3g_c^4t_v^4}, \tag{5-31}$$

and

$$v_2 = \frac{g_c t_v^2(1-g_c^2t_v^2)}{1-2g_c^2t_v^2}, \tag{5-32}$$

The process carried out for the first ring of the model (a) serves for the second ring of the model (b), therefore, the model (b) is decimated to a system with 5 sites, of which 4 are effective, two with effective Green's functions g_1 and effective coupling v_1, and two with effective Green's functions g_2 and effective coupling v_2 (see Figure **5-14** b))

Decimation Model (c)

For model (c), the two rings have the same configuration as the first ring of model (b), therefore, when performing the decimation process, the effective Green's function g_2 is obtained, and the effective coupling v_2, after the renormalization process, the model (c) is decimated to a linear system of 5 sites, where 4 are effective (see Figure **5-14** a))

Decimation Model (d)

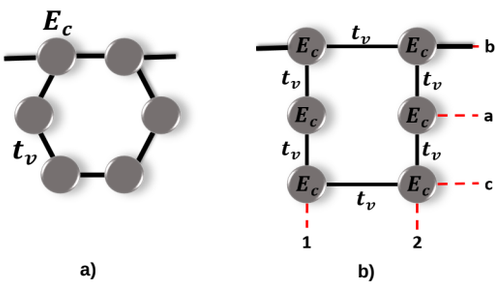

Figure **5-13**: First benzene ring of the model (d), a) isolated molecule, b) reorganization of the molecule to carry out the renormalization.

Figure **5-13** a) shows the isolated benzene ring, and Figure **5-13** b) shows a reorganization of the ring in order to perform the renormalization, where the information enters the ring through site $1b$ and exits through site $2b$, applying the Dyson equation to first neighbors, the following equations are obtained.

$$G^b_{11} = g_c + g_c t_v G^a_{11} + g_c t_v G^b_{12}, \tag{5-33}$$

$$G^a_{11} = g_c t_v G^b_{11} + g_c t_v G^c_{11}, \tag{5-34}$$

$$G^c_{11} = g_c t_v G^a_{11} + g_c t_v G^c_{12}, \tag{5-35}$$

$$G^c_{12} = g_c t_v G^c_{11} + g_c t_v G^a_{12}, \tag{5-36}$$

$$G^a_{12} = g_c t_v G^c_{12} + g_c t_v G^b_{12}, \tag{5-37}$$

Solving the system of equations gives an expression for G^b_{11} in terms of G^b_{12}.

$$G^b_{11} = \frac{g_c(1 - 3g_c^2 t_v^2 + g_c^4 t_v^4)}{1 - 4g_c^2 t_v^2 + 3g_c^4 t_v^4} + \frac{t_v(1 - 3g_c^2 t_v^2 + 2g_c^4 t_v^4)}{1 - 3g_c^2 t_v^2 + g_c^4 t_v^4}, \tag{5-38}$$

The above expression has the form of a Dyson equation, where the first term is the effective Green's function of a site 1 connected to a site 2, the second term, which multiplies G^b_{12}, is the effective coupling with the effective site 2.

$$g_3 = \frac{g_c(1 - 3g_c^2t_v^2 + g_c^4t_v^4)}{1 - 4g_c^2t_v^2 + 3g_c^4t_v^4}, \tag{5-39}$$

and

$$v_3 = \frac{t_v(1 - 3g_c^2t_v^2 + 2g_c^4t_v^4)}{1 - 3g_c^2t_v^2 + g_c^4t_v^4}. \tag{5-40}$$

The above process works for both benzene rings, therefore, model (d) is decimated to a system with 5 sites, of which 4 are effective (see Figure 5-14 a).

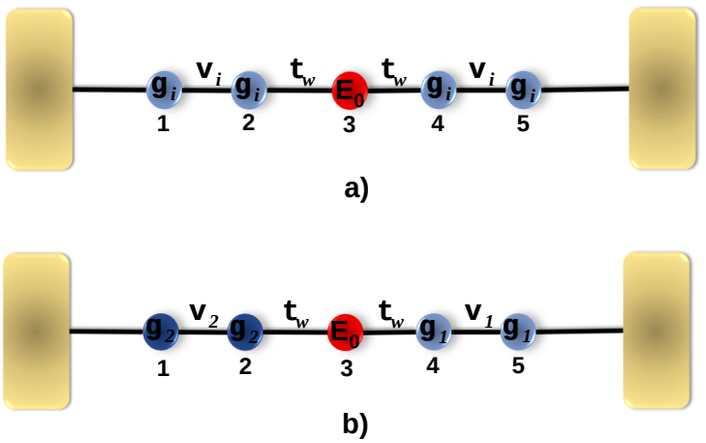

Figure **5-14**: The models in Figure 1 were decimated to 5 sites, **a)** models (a), (c) and (d), **b)** model (b). i can take the values 1, 2 and 3, corresponding to models (a), (c), and (d), respectively.

All the models in Figure 5-1 are decimated to 5 sites, where we have 4 effective sites and the central oxygen site. For models (a), (c) and (d) they are symmetrical systems (see Figure 5-14 (a)), where g_i is the effective local Green's function and v_i is the effective potential between sites, where i can be 1 (model (a)), 2 (model (c)) and 3 (model (d)). For model (b), we have an asymmetric system (see Figure 5-14 (b)), which is a combination of the decimation made for the benzene rings of model a and the rings of model (c).

To obtain the Green's functions of sites 1 and 5 of the linear system, shown in Figure 5-14 (a), the Dyson equation is applied to first neighbors, we have:

$$G^{a,c,d}_{11} = g_i + g_iv_iG^{a,c,d}_{12}, \tag{5-41}$$

$$G^{a,c,d}_{12} = g_iv_iG^{a,c,d}_{11} + g_it_wG^{a,c,d}_{13}, \tag{5-42}$$

$$G_{13}^{a,c,d} = g_o t_w G_{12}^{a,c,d} + g_o t_w G_{14}^{a,c,d}, \tag{5-43}$$

$$G_{14}^{a,c,d} = g_i t_w G_{13}^{a,c,d} + g_i v_i G_{15}^{a,c,d}, \tag{5-44}$$

$$G_{15}^{a,c,d} = g_i v_i G_{14}^{a,c,d}, \tag{5-45}$$

Solving the system of equations gives the expression of the Green's functions $G_{11}^{a,c,d}$, and $G_{15}^{a,c,d}$. Due to the symmetry that the system in the Figure **5-14** (a) presents, it can be affirmed that the functions of the sites $G_{11}^{a,c,d}$ and $G_{55}^{a,c,d}$ are equal and have the following form:

$$G_{11}^{a,c,d} = \frac{g_i(1 - g_i^2 v_i^2 - 2g_i g_o t_w^2 + g_i^3 g_o v_i^2 t_w^2)}{(1 - g_i^2 v_i^2)(1 - g_i^2 v_i^2 - 2g_i g_o t_w^2)}, \tag{5-46}$$

we can also say the same about Green's functions $G_{15}^{a,c,d}$ and $G_{51}^{a,c,d}$, which are the same, which is:

$$G_{15}^{a,c,d} = \frac{g_i^4 g_o v_i^2 t_w^2}{(1 - g_i^2 v_i^2)(1 - g_i^2 v_i^2 - 2g_i g_o t_w^2)}. \tag{5-47}$$

To obtain the Green's functions of the linear system shown in Figure **5-14** (b), the Dyson equation is applied to first neighbors, this system does not have a symmetrical shape, like the one shown in Figure **5-14** (a), for which the analysis is made in the direction 1 to 5, and from 5 to 1. Analyzing from site 1 to 5, we have:

$$G_{11}^{b} = g_2 + g_2 v_2 G_{12}^{b}, \tag{5-48}$$

$$G_{12}^{b} = g_2 v_2 G_{11}^{b} + g_2 t_w G_{13}^{b}, \tag{5-49}$$

$$G_{13}^{b} = g_o t_w G_{12}^{b} + g_o t_w G_{14}^{b}, \tag{5-50}$$

$$G_{14}^{b} = g_1 t_w G_{13}^{b} + g_1 v_1 G_{15}^{b}, \tag{5-51}$$

$$G_{15}^{b} = g_1 v_1 G_{14}^{b}. \tag{5-52}$$

Analyzing from site 5 to 1, we have:

$$G_{55}^{b} = g_1 + g_1 v_1 G_{54}^{b}, \tag{5-53}$$

$$G_{54}^{b} = g_1 v_1 G_{55}^{b} + g_1 t_w G_{53}^{b}, \tag{5-54}$$

$$G_{53}^{b} = g_o t_w G_{54}^{b} + g_o t_w G_{52}^{b}, \tag{5-55}$$

$$G_{52}^{b} = g_2 t_w G_{53}^{b} + g_2 v_2 G_{51}^{b}, \tag{5-56}$$

5

$$G_{51}^{b} = g_2 v_2 G_{52}^{b}, \tag{5-57}$$

Solving the system of equations gives the expressions of the Green's functions G_{11}^{b}, G_{55}^{b}, and G_{15}^{b}, and have the following form:

$$G_{11}^{b} = \frac{g_2(1 - g_1^2 v_1^2 - g_o g_1 t_w^2 - g_o g_2 t_w^2 (1 - g_1^2 v_1^2))}{(1 - g_1^2 v_1^2)(1 - g_2^2 v_2^2) - g_o t_w^2 (g_2 + g_1 (1 - g_1 g_2 v_1^2 - g_2^2 v_2^2))}, \tag{5-58}$$

$$G_{55}^{b} = \frac{g_1(1 - g_2^2 v_2^2 - g_o g_2 t_w^2 - g_o g_1 t_w^2 (1 - g_2^2 v_2^2))}{(1 - g_1^2 v_1^2)(1 - g_2^2 v_2^2) - g_o t_w^2 (g_2 + g_1 (1 - g_1 g_2 v_1^2 - g_2^2 v_2^2))}, \tag{5-59}$$

and

$$G_{15}^{b} = \frac{g_o g_1^2 g_2^2 v_1 v_2 t_w^2}{(1 - g_1^2 v_1^2)(1 - g_2^2 v_2^2) - g_o t_w^2 (g_2 + g_1 (1 - g_1 g_2 v_1^2 - g_2^2 v_2^2))}. \tag{5-60}$$

With the effective Green's functions calculated $G_{11}^{a,b,c,d}$, $G_{15}^{a,b,c,d}$, and G_{55}^{b} , the total Green function of the system can be represented, given by the following expression:

$$G_{15} = \frac{G_{15}^{a,b,c,d}}{(1 - \Sigma_L G_{11}^{a,b,c,d})(1 - \Sigma_R G_{55}^{a,b,c,d}) - \Sigma_L \Sigma_R (G_{15}^{a,b,c,d})^2}. \tag{5-61}$$

The new transmission probability for the effective molecular system in one dimension, as shown in Figure **5-14**, can be written as:

$$T(E) = \Gamma_R \Gamma_L |G_{15}|^2. \tag{5-62}$$

References

[1] Aviram, A.; Ratner, M. Molecular rectifiers. *Chemical Physics Letters* **1974**, *29*, 277–283.

[2] Mendoza-Uribe, G.; Rodriguez-Lopez, J. Nanoscience and nanotechnology: a revolution in progress. *Perf. latinoam.* **2007**, *14*, 161–186.

[3] Charles, P.; Frank, O. *Introduction to nanotechnology*; John Wiley & Sons, 2003.

[4] Joachim, C.; Gimzewski, J.; Aviram, A. Electronics using hybrid-molecular and mono-molecular devices. *Nature* **2000**, *408*, 541–548.

[5] Aviram, A. Molecules for memory, logic, and amplification. *J.A.C.S.* **1988**, *110*, 5687–5692.

[6] Khireddine, A.; Bouhemadou, A.; Maabed, S.; Bin-Omran, S.; Khenata, R.; Al-Douri, Y. Elastic, electronic, optical and thermoelectric properties of the novel Zintl-phase Ba_2ZnP_2. *Solid State Sci.* **2022**, *128*, 106893.

[7] Liu, G.; Chen, T.; Xu, J.; Li, G.; Wang, K. Solar evaporation for simultaneous steam and power generation. *J. Mater. Chem. A* **2020**, *8*, 513–531.

[8] Gholikhani, M.; Roshani, H.; Dessouky, S.; Papagiannakis, A.T. A critical review of roadway energy harvesting technologies. *J. Mater. Chem. A* **2020**, *261*, 114388.

[9] Zheng, Y.; Goh, T.; Fan, P.; Shi, W.; Yu, J.; Taylor, A.D. Toward efficient thick active PTB7 photovoltaic layers using diphenyl ether as a solvent additive. *ACS Appl. Mater. Interfaces* **2016**, *8*, 15724–15731.

[10] Zhao, B.; Chen, C.; Zhou, Z.; Cao, Y.; Li, M. A comparative study on the nonlinear optical properties of diphenyl ether and diphenyl sulfide compounds. *J. Mater. Chem.* **2000**, *10*, 1581–1584.

[11] Ojeda, J.; Pacheco, M.; Rosales, L.; Orellana, P. Current and Shot noise in DNA chains. *Organic Electronics* **2012**, *13*, 1420–1429.

[12] Ojeda, J.; Maiti, S. Thermal properties of ordered and disordered DNA chains: Efficient energy conversion. *ChemPhysChem* **2019**, *20*, 3346–3353.

[13] Abbas, M.; Hanoon, F.; Al-Badry, L. Theoretical study of electron transport throughout some molecular structures. *Superlattices and Microstructures* **2017**, *111*, 273–285.

[14] Markussen, T.; Stadler, R.; Thygesen, K. The relation between structure and quantum interference in single molecule junctions. *Nano letters* **2010**, *10*, 4260–4265.

[15] Dadosh, T.; Gordin, Y.; Krahne, R.; Khivrich, I.; Mahalu, D.; Frydman, V.; Sperling, J.; Yacoby, A.; Bar-Joseph, I. Measurement of the conductance of single conjugated molecules. *Nature* **2005**, *436*, 677–680.

[16] Maiti, S. Effect of localizing groups on quantum transport through single conjugated molecules. *Physica B: Condensed Matter* **2007**, *394*, 33–38.

[17] Xiang, D.; Jeong, H.; Lee, T.; Mayer, D. Mechanically controllable break junctions for molecular electronics. *Advanced Materials* **2013**, *25*, 4845–4867.

[18] Tian, J.H.; Yang, Y.; Zhou, X.S.; Schöllhorn, B.; Maisonhaute, E.; Chen, Z.B.; Yang, F.Z.; Chen, Y.; Amatore, C.; Mao, B.W.; et al. Electrochemically assisted fabrication of metal atomic wires and molecular junctions by MCBJ and STM-BJ methods. *ChemPhysChem* **2010**, *11*, 2745–2755.

[19] Wang, L.; Wang, L.; Zhang, L.; Xiang, D. Advance of mechanically controllable break junction for molecular electronics. *Molecular-Scale Electronics* **2019**, pp. 45–86.

[20] Perrin, M.; Burzurí, E.; van der Zant, H. Single-molecule transistors. *Chemical Society Reviews* **2015**, *44*, 902–919.

[21] Perrin, M.; Martin, C.; Prins, F.; Shaikh, A.; Eelkema, R.; van Esch, J.; van Ruitenbeek, J.; van der Zant, H.; Dulić, D. Charge transport in a zinc–porphyrin single-molecule junction. *Beilstein journal of nanotechnology* **2011**, *2*, 714–719.

[22] Han, W.; Durantini, E.; Moore, T.; Moore, A.; Gust, D.; Rez, P.; Leatherman, G.; Seely, G.; Tao, N.; Lindsay, S. STM contrast, electron-transfer chemistry, and conduction in molecules. *The Journal of Physical Chemistry B* **1997**, *101*, 10719–10725.

[23] Pomerantz, M.; Aviram, A.; McCorkle, R.; Li, L.; Schrott, A. Rectification of STM current to graphite covered with phthalocyanine molecules. *Science* **1992**, *255*, 1115–1118.

[24] Xue, Y.; Datta, S.; Hong, S.; Reifenberger, R.; Henderson, J.; Kubiak, C. Negative differential resistance in the scanning-tunneling spectroscopy of organic molecules. *Physical Review B* **1999**, *59*, R7852.

[25] Fujii, S.; Montes, E.; Cho, H.; Yue, Y.; Koike, M.; Nishino, T.; Vázquez, H.; Kiguchi, M. Mechanically Tuned Thermopower of Single-Molecule Junctions. *Advanced Electronic Materials* **2022**, p. 2200700.

[26] Souza, A.; Rungger, I.; Schwingenschlögl, U.; Sanvito, S. The image charge effect and vibron-assisted processes in Coulomb blockade transport: a first principles approach. *Nanoscale* **2015**, *7*, 19231–19240.

[27] Sadeghi, H.; Sangtarash, S.; Lambert, C. Electron and heat transport in porphyrin-based single-molecule transistors with electro-burnt graphene electrodes. *Beilstein journal of nanotechnology* **2015**, *6*, 1413–1420.

[28] Xu, K.; Yi, G.; Wang, W.; Wang, J.; Wang, C.; Li, Q. Theoretical insights into the diverse and tunable charge transport behavior of stilbene-based single-molecule junctions. *Chemical Physics* **2022**, *556*, 111478.

[29] Ojeda, J.; Duque, C.; Laroze, D. Electron–phonon interaction in quantum transport through quantum dots and molecular systems. *Physica B: Condensed Matter* **2016**, *502*, 73–81.

[30] Ojeda, J.; Cortés, J.; Gómez, J.; Duque, C. Current's fluctuations through molecular wires composed of thiophene rings. *Molecules* **2018**, *23*, 881.

[31] Ojeda, J.; Duque, C.; Laroze, D. Shot noise and thermopower in aromatic molecules. *Physica E: Low-dimensional Systems and Nanostructures* **2014**, *62*, 15–20.

[32] Ojeda, J.; Paez, J.; Duque, C. Thermo-Electrical Conduction of the 2,7-Di([1,1'-Biphenyl]-4-yl)-9H-Fluorene Molecular System: Coupling between Benzene Rings and Stereoelectronic Effects. *Molecules* **2020**, *25*, 3215.

[33] Rivera, M.; Ojeda, J.; Gallego, D. Thermoelectric properties through a wire composed of isoprene molecules. *AIP Advances* **2020**, *10*, 065021.

[34] Sanvito, S.; Rocha, R. Molecular-spintronics: The art of driving spin through molecules. *Journal of Computational and Theoretical Nanoscience* **2006**, *3*, 624–642.

[35] Ojeda, J.; Orellana, P.; Laroze, D. Aromatic molecules as spintronic devices. *The Journal of chemical physics* **2014**, *140*, 104308.

[36] Ojeda, J.; Pacheco, M.; Orellana, P. An array of quantum dots as a spin filter device by using Dicke and Fano effects. *Nanotechnology* **2009**, *20*, 434013.

[37] Fisher, D.S.; Lee, P.A. Relation between conductivity and transmission matrix. *Physical Review B* **1981**, *23*, 6851.

[38] Datta, S. *Electronic Transport in Mesoscopic Systems*; Cambridge Studies in Semiconductor Physics and Microelectronic Engineering, Cambridge University Press, **1995**. https://doi.org/10.1017/CBO9780511805776.

[39] Di Ventra, M. *Electrical Transport in Nanoscale Systems*; **2008**.

[40] Hansen, T.; Solomon, G.; Andrews, D.; Ratner, M. Interfering pathways in benzene: An analytical treatment. *The Journal of chemical physics* **2009**, *131*, 194704.

[41] Ojeda, J.; Rey-González, R.; Laroze, D. Quantum transport through aromatic molecules. *Journal of Applied Physics* **2013**, *114*, 213702.

[42] Stafford, C.; Cardamone, D.; Mazumdar, S. The quantum interference effect transistor. *Nanotechnology* **2007**, *18*, 424014.

[43] Bubnova, O.; Khan, Z.U.; Malti, A.; Braun, S.; Fahlman, M.; Berggren, M.; Crispin, X. Optimization of the thermoelectric figure of merit in the conducting polymer poly (3, 4-ethylenedioxythiophene). *Nat. Mater.* **2011**, *10*, 429-433.

6 Theoretical study of the thermoelectric properties through a single-molecule junction of Zinc Porphyrin

6.1 Abstract

A theoretical analysis was performed to investigate the transport properties of Zinc Porphyrin molecule and its response to thermal fluctuations. The renormalization method was used for this analysis, using the Green's functions technique through the Dyson equation, focusing on first-neighbor interactions. This study produced various results, including energy-dependent transmission probability, voltage-current characteristic curves, electrical and thermal conductance assessments, Seebeck coefficient, and figure of merit (ZT). In order to validate the method used, both the profile results in the transmission probability and the I-V curves were compared with theoretical (DFT) and experimental results, respectively, obtaining significant agreements in the HOMO and LUMO of the molecule, as well as a characteristic behavior of a rectifying device. Complementing the above by calculating the ZT through the molecular system Zn(5,15-di(p-thiolphenyl)-10,20-di(p-tolyl)porphyrin) (ZnTPPdT), it was demonstrated that said molecule could be used as an efficient thermoelectric device that allows thermal energy to be converted into electrical energy.

Keywords: Zinc Porphyrin, renormalization, voltage-current characteristic curves, ZT

6.2 Introduction

In recent decades, there has been increasing interest in the study of molecular electronics, which focuses on studying the behavior of charge carriers when they pass through systems that are between two or more electrodes, which, depending on their structure, may have properties of known electronic devices, such as rectifiers, transistors, diodes, among others.

Since current semiconductor-based devices are reaching a miniaturization threshold (Moore's law), where the density of transistors on a microchip has increased over the years [1, 2], the idea is to be able to replace current electronic components with monomolecular devices of a few nanometers. Nowadays, many theoretical and experimental studies can be found on electronic devices based on a single molecule, such as wires, switches, storage, amplification, and logic devices, to mention a few [4–7].

Within experimental studies, currently, there are many techniques to measure the response of the passage of electrons through molecular junctions (MJs), such as Scanning Tunneling Microscopy (STM), which uses individual molecular junctions on surfaces to manipulate and characterize molecules at the nanometric scale; in this process, the charge carriers generated by a potential difference feel the mechanism of the tunnel effect [8–11]. Methods for the study of MJs, such as scanning tunneling spectroscopy (STS), are complementary to STM, allowing the study of the electronic properties of a single MJs [12]. On the other hand, there

are experimental techniques for manufacturing individual molecules and studying their transport properties, such as scanning probe microscopy (SPM), which consists of breaking joints of a sharp-tipped probe, facilitating the surface of a sample to be scanned and measure its topography, conductivity, magnetic field, etc. [13].

Other important experimental techniques to mention here are electromigration breakdown junctions (EBJ) [14] and mechanically controlled breakdown junctions (MCBJ), which are characterized by having two metal electrodes separated by a small distance (from the order of nanometers), which can be moved mechanically, and a molecule can be placed between them to act as a bridge. By varying the distance between the metal tips, the conductance of the molecule can be studied as a function of the separation of the electrodes. The difference between the two methods is that MCBJ has high mechanical stability, and the electrode spacing can be finely tuned [15–19].

At a theoretical level, the first to report on the rectifying properties of a molecule based on tetrathia-fulvalene (donor) and tetracyanoquinodimethane (acceptor), linked by a saturated methylene bridge, were Aviram and Ratner in 1974 [3].

There is also a range of theoretical methods for the study of molecular systems, such as density functional theory (DFT), with the non-equilibrium Green's functions (NEGF) formalism [20–22], Monte Carlo [23], renormalization method by Green's functions out of equilibrium, applying the Dyson equation to first neighbors, under the tight-binding approximation [24–29]. With the methods mentioned above (DFT and renormalization), a study can be made on the electronic and optical properties of molecular systems, such as transmission probability, current vs. voltage, electrical and thermal conductance, Seebeck coefficient, the figure of merit (ZT), and absorption, among others, all the above, taking into account variations in temperatures, external fields, etc.

Many authors have studied electronic coherence in molecular systems with the Tight Binding approximation method, using the Landauer formalism due to certain interactions such as electron-phonon, adjusting the energies of sites and couplings between sites, among others [30–32]. Where it has been reported that the inclusion of this interaction creates new electronic states near the Fermi level [33]. There are also many studies in the literature that seek to improve the photothermal conversion of these thermoelectric materials, where they seek to improve the efficiency in the absorption of solar energy in a wide range of the energy spectrum of the incident photon [34–36], such as the control of mid-infrared thermal emitter [37].

The method used in this work is renormalization, which consists of decimating the molecular system using the Dyson equation and Green's functions, which translates into going from a

2D system with many atomic sites to a linear system with effective sites but maintaining the information of the original system.

The molecular system to be studied is Zinc porphyrin, more specifically Zn(5,15-di(p-thiol phenyl)-10,20-di(p-tolyl)porphyrin) (ZnTPPdT). The Zn-Porphyrin molecular system is widely studied because of its optical properties, which are used to incorporate them into solar cells to improve efficiency, as optical sensors for the detection of heavy metals in aqueous media, to improve the detection of electrochemiluminescent and electrochemical sensors of drugs [38–42].

Systems based on Zn-Porphyrin are also widely studied for their electronic properties, such as the study reported by Perrin *et al.* in 2013 [43], where they studied the current curve as a function of voltage in a ZnTPPdT molecule, for different electrode distances, using the MCBJ method. By increasing the electrode separation, they observed a substantial increase in the transport gap with level changes of several hundred meV for displacements of a few angstroms [43].

In 2015, Souza *et al.* [44], studied the electronic properties in a single molecule of ZnTPPdT by DFT, where they obtained the transmission probability and current-voltage characteristic curve with good results when comparing the results reported by Perrin in 2013. As of mid-2016, Galiby *et al.* [45] studied the thermoelectric properties in metalloporphyrins by DFT, finding that the resulting thermopowers of a single molecule at room temperature vary from almost zero for the Co and Cu centers, up to $+80\,\mu V\,K^{-1}$ and $+230\,\mu V\,K^{-1}$ for Ni and Zn respectively.

In this work, the thermoelectric properties of a ZnTPPdT molecule will be studied by the renormalization method, applying the Dyson equation to the first nearest neighbors and finding the total Green function of a linear system with effective sites. The transmission probability will be calculated by the Fisher-Lee relationship, the calculation of the current-voltage characteristic curve will be done via the Landauer-Büttiker formalism, and finally, the electrical and thermal conductance, Seebeck coefficient, and figure of merit, ZT, will be calculated using Landauer integrals.

The article is organized as follows. In Section 2, the model of the ZnTPPdT molecule based on a tight-binding Hamiltonian is presented. In Section 3, the method used for calculations of electrical and thermal quantities is described. Section 4 is devoted to results and corresponding discussions. Finally, the conclusions are summarized in Section 5. The appendix presents, in detail, the renormalization process of the system under study.

6.3 Model

To study the transport properties, in the tight-binding approximation, of the Zn(5,15-di(p-thiolphenyl)-10,20-di(p-tolyl) porphyrin) (ZnTPPdT) molecule, it is connected between two metal electrodes (Left, Right), see Fig. **6-1**. The total system is represented by the Hamiltonian with the form:

$$H = H_M + H_L + H_I \ , \tag{6-1}$$

where H_M corresponds to the Hamiltonian of the molecule of ZnTPPdT, which has the following form:

$$H_M = \sum_i t_i \left(c_i^\dagger c_{(i+1)} + c_{(i+1)}^\dagger c_i \right) + \sum_i E_i c_i^\dagger c_i \ , \tag{6-2}$$

here, $c_i^\dagger$ and c_i are the operators for creating and destroying an electron at the site i. E_i is the site energy for the carbon, sulfur, nitrogen, or zinc atoms, t_i is the hopping between the atoms, which can be t_C for the coupling between C−C, t_S for the coupling between S−C, t_N for the coupling between N−C, and t_{Zn} for the coupling between Zn−N.

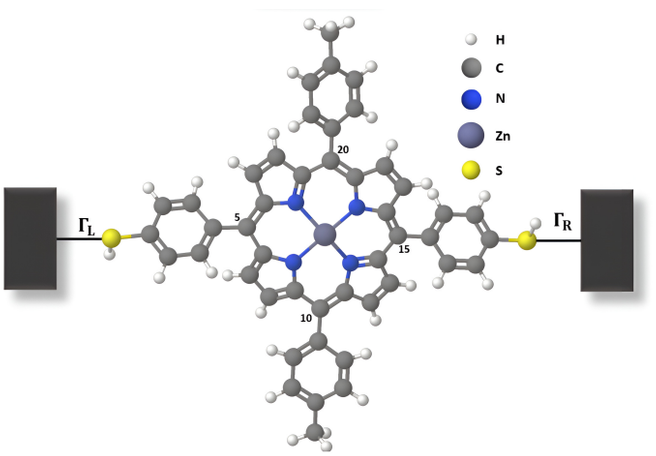

Figure **6-1**: Zn(5,15-di(p-thiolphenyl)-10,20-di(p-tolyl)porphyrin) (ZnTPPdT) molecule connected to leads Γ_L and Γ_R (Left and Right respectively). Each color represents a different type of atom.

The terms H_L and H_I of Eq. 6-1 represent the Hamiltonian of the leads and the molecule-leads interaction, respectively, and are given by:

$$H_L = \sum_{k_L} \varepsilon_{k_L} d_{k_L}^\dagger d_{k_L} + \sum_{k_R} \varepsilon_{k_R} d_{k_R}^\dagger d_{k_R} + h.c. \, , \tag{6-3}$$

and

$$H_I = \sum_{k_L} \Gamma_L d^\dagger_{k_L} c_1 + \sum_{k_R} \Gamma_R d^\dagger_{k_R} c_N + h.c. \ . \tag{6-4}$$

The operator $d^\dagger_{k_{L(R)}}$ is the creation operator of an electron in a state $k_{L(R)}$ with energy ε_{k_L}; $\Gamma_{L(R)}$ is the coupling between each lead with the molecule, and $h.c.$ is the complex conjugate of the Hamiltonian [46, 47].

6.4 Method

To calculate the thermoelectric properties in the ZnTPPdT molecular system, the renormalization process is carried out, which is detailed in Appendix A, using the Dyson equation to first neighbors given by:

$$G = G^0 + G^0(\Sigma_L + \Sigma_R)G \ , \tag{6-5}$$

where Σ_L and Σ_R are the self-energies of the left and right leads, respectively, and G^0 is the Green function of the molecular system.

After doing the entire decimation process to a linear system with effective sites, the total Green function is obtained, which will be in terms of the Green functions $G^0_{11}, G^0_{1N}, G^0_{NN}$, and G^0_{N1}, with

$$G_{1N} = \frac{G^0_{1N}}{(1 - G^0_{11}\Sigma_L)(1 - G^0_{NN}\Sigma_R) - G^0_{N1}G^0_{1N}\Sigma_L\Sigma_R} \ , \tag{6-6}$$

where G^0_{11} is the Green function of site 1, G^0_{NN} is the Green function of size N, G^0_{1N} is the Green function of site N seen from site 1, and G^0_{N1} is the Green function of site 1 seen from site N.

The calculation of the transmission probability will be done using the Fisher-Lee relation, which is the trace of a matrix that depends on the total delayed and advanced Green functions calculated above and on the functions of the electrodes spectral density matrix Γ_L and Γ_R, i.e.,

$$T(E) = Tr\left[\Gamma_L \, G^r \, \Gamma_R \, G^a\right] \ , \tag{6-7}$$

here the spectral density matrix for the left (right) electrode is given by

$$\Gamma_{L(R)} = i\left(\Sigma_{L(R)} - \Sigma^\dagger_{L(R)}\right) \ , \tag{6-8}$$

with $\Sigma_L = \Sigma_R = -i\,\Gamma/2$.

The current-voltage characteristic curve is calculated to determine the quantum transport properties, which describe the flow of charge carriers through the molecule from one electrode to the other. The obtained expression for the transmission probability is then multiplied by the difference of the electrode Fermi functions and integrated in terms of energy. All of this is done under the framework of the Landauer-Büttiker formalism and is shown in the following relationship:

$$I(V) = I_0 \int_{-\infty}^{\infty} \left[f_L(E,V) - f_R(E,V) \right] T(E) dE \ , \tag{6-9}$$

where $I_0 = 2e/h$, e is the electronic charge, E is the electron energy, V is the bias voltage, and h represents the Plank constant. $f_{L(R)}(E,V)$ is the Fermi-Dirac distribution function for the left (right) electrode and has the following form:

$$f_{L(R)}(E,V) = \frac{1}{1 + \exp[\beta(E - \mu_{L(R)}(V))]} \ , \tag{6-10}$$

where $\beta = 1/k_B T$ is the Botzmann factor, $\mu_{L(R)}(V) = E_f \pm eV/2$ is the chemical potential, and E_f is the equilibrium Fermi energy under zero biased condition.

To calculate the thermal transport properties, the n-order Landauer integrals will be used,

$$\mathcal{L}_n = -\int T(E)(E - E_f)^n \left(\frac{\partial f(E)}{\partial E} \right) dE \ , \tag{6-11}$$

Using Eq. 6-11, the electrical conductance ($\mathcal{G}$), the Seebeck coefficient S, the thermal conductance κ, and the figure of merit ZT can be obtained via the following relationships

$$\mathcal{G} = \frac{2\,e^2}{h} \mathcal{L}_0 \ , \tag{6-12}$$

$$S = -\frac{1}{e\,T} \frac{\mathcal{L}_1}{\mathcal{L}_0} \ , \tag{6-13}$$

$$\kappa = \frac{2}{h\,T} \left(\mathcal{L}_2 - \frac{\mathcal{L}_1^2}{\mathcal{L}_0} \right) \ , \tag{6-14}$$

$$ZT = \frac{\mathcal{G}\,S^2\,T}{\kappa} = \frac{\mathcal{L}_1^2}{\mathcal{L}_0\,\mathcal{L}_2 - \mathcal{L}_1^2} \ , \tag{6-15}$$

where T is the equilibrium temperature [48, 49].

It is worth mentioning that the thermal conductance is the sum of the electronic and phonon contributions, but when comparing both contributions, the electronic is usually much higher than the phonon thermal conductance, which is true in these molecular systems [52, 53], for that reason in this work, only the thermal conductance due to the electronic part will be taken into account.

6.5 Results and discussion

In this section, an analysis will be made of the numerical results obtained from the electrical properties of a ZnPTPPdT molecule, such as transmission probability graph as a function of the energy of the incident electron, current characteristic curve as a function of voltage, and the variation of electrical conductance as a function of the Fermi energy for different temperatures. A study will also be carried out on the variation that the following physical quantities present with changes in temperature, thermal conductance, Seebeck coefficient, and, finally, the figure of merit or ZT.

To validate the method used in this work, the transmission probability plot has been made as a function of the energy of the incident electron (see Fig. **6-2**), for all site energies equal to 0 eV, and hopping of 1 eV, and will be compared with the eigenvalues of the molecular system shown in Fig. **6-1**.

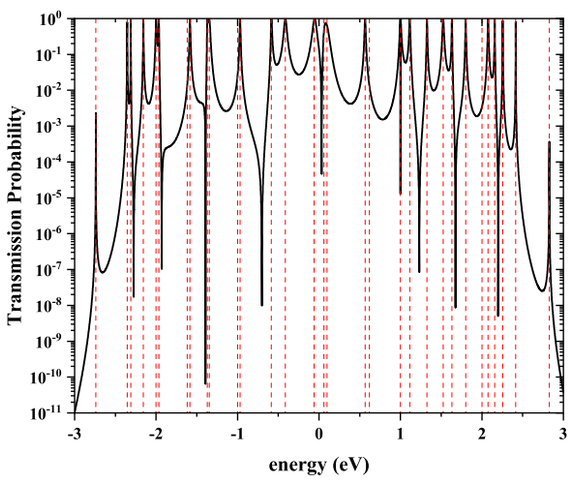

Figure **6-2**: Transmission probability as a function of the energy of the incident electron (black curve), and eigenvalues for a ZnPTPPdT molecule (red dash lines), with site energy of 0 eV, hopping of 1 eV, and $\Gamma_I = \Gamma_D = 0.2$ eV.

Fig. **6-2** shows the plot of the transmission probability (black curve) and the eigenvalues of a ZnPTPPdT molecule (red dash lines) connected to two metal electrodes for the system shown in Fig. **6-1**. The purpose of the previous graph is to show that the eigenvalues of the molecule largely coincide with resonant peaks (26) and zeros (5) of the transmission, which tells us that the method used for the decimation carried out gives very good results with the test parameters. The graph shows 31 eigenvalues in eV, which are presented below (and in parentheses how many times it appears degenerate) 2.8267, -2.7401, 2.4142 (2), -2.3546 (2), -2.3102, 2.2554, 2.1576, - 2.1565, 2.0759 (2), -2.0000 (2), 2.0000, -1.9650, 1.8009, 1.6322, -1.6180 (4), -1.5843, 1.5247 (2), -1.3721, -1.3457 (2), 1.3255, 1.1147, - 1.0000 (4), 1.0000 (6), -0.9688, 0.6180 (4), -0.5844, 0.5666, -0.4142 (2), 0.0996 (2), 0.0606, -0.0589, in total there

Table **6-1**: Comparison with results reported in the literature

	HOMO	LUMO	I(μA)	
			V= −0.8 volt	V = 0.8 volt
This work	−0.51	1.32	−0.050	0.050
Souza *et al.* [44]	−0.50	1.31	———	———
Perrin *et al.* [43]	———	———	−0.040	0.052

are 53 eigenvalues, which are related to the 53 atomic sites shown in Fig. **6-1**.

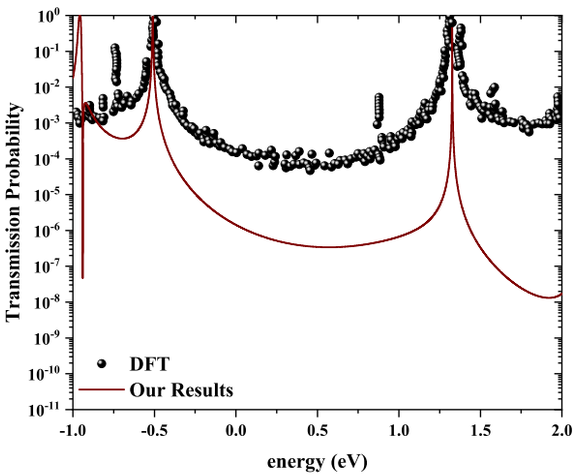

Figure **6-3**: Transmission probability as a function of incident electron energy obtained via the procedure described in this work (solid line). A comparison is made with DFT calculations (solid symbols) [44]. The results are for a ZnPTPPdT molecule.

Fig. **6-3** shows the comparison of the transmission probability obtained for a ZnPTPPdT molecule by using the analytical method described here and theoretical results obtained by Souza *et al.* using DFT [44]. For comparison effects, the reference site energy and hopping parameters are from the works of Sadeghi *et al.* [50] and Ojeda *et al.* [51]. From Fig. **6-3**, the same energies of the HOMO and LUMO reported by DFT are obtained (see table **6-1**), which are around −0.51 eV and 1.32 eV, presenting an energy gap of approximately the same order (Which is reflected in the graph of current vs. voltage in Fig. **6-4**), which shows us a very good agreement. To carry out the comparison, the following parameters were used: $E_C = -6.03\,\text{eV}$ (Carbon site energy), $E_N = -4.66\,\text{eV}$ (Nitrogen site energy), $E_{Zn} = -20.7$ eV (Zinc site energy), $E_S = 0.98\,\text{eV}$ (Sulfur site energy), $t_C = -2.40\,\text{eV}$ (Carbon−Carbon hopping), $t_N = -4.13\,\text{eV}$ (Nitrogen−Carbon hopping), $t_{Zn} = -2.50\,\text{eV}$ (Zinc−Nitrogen hopping), and $t_S = -0.83$ eV(Sulfur−Carbon hopping). For the coupling of the molecule with the electrodes, we use $\Gamma_I = 1\,\text{eV}$ and $\Gamma_D = 2\,\text{eV}$.

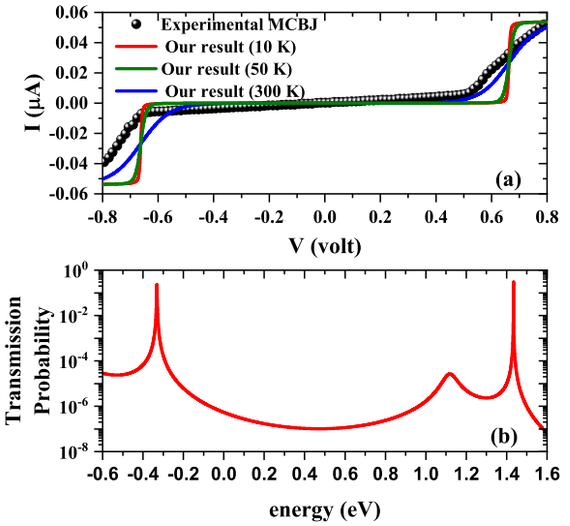

Figure **6-4**: (a) Current-voltage characteristic curve for the ZnP system, compared with experimental results by the MCBJ method, at a temperature of 6 K (black dots), reported by Perrin *et al.* [43], with the obtained analytical results, at a temperature of 10 K (red curve), 50 K (green curve), and 300 K (blue curve). (b) Transmission probability as a function of the energy of the incident electron, for the new parameters $\Gamma_I = 0.07\,\text{eV}$, $\Gamma_D = 1.12\,\text{eV}$, and $E_C = -5.85\,\text{eV}$.

In Fig. **6-4**(a), an additional comparison is made, but in this case with experimental results of the current-voltage characteristic curve by the MCBJ method at a temperature of 6 K for a ZnPTPPdT molecule (see table **6-1**), reported by Perrin *et al.* [43]. Solid symbols are from Ref. [43], whereas solid lines are our findings for several temperature values. From the experimental results, it can be seen that the value of the current increases as the voltage increases, up to a voltage value of approximately -0.7 volt, then it presents a gap, that is, the magnitude of the current is practically zero, up to a voltage value of $+0.5$ volt, from that value onwards the current amplitude begins to grow. Our findings (solid lines) show the same behavior since for voltage values of approximately -0.7 volt to $+0.5$ volt, the graphs present that approximate gap. When the temperature is 300 K, it presents the same behavior as the experimental curve. The gap can be observed in the transmission probability graph, Fig. **6-4**(b), which presents values different from zero for HOMO and LUMO energies. It is worth mentioning that the difference in the values of our model's current amplitudes compared to the experimental one at low temperatures maybe because it only considers transport by electronic factors, ignoring the vibrational aspects of the system. Furthermore, the model used is not the best to describe the system at low temperatures due to the behavior suffered by the Fermi functions. To carry out the comparison, the following parameters were used: Couplings between the molecule and the electrodes, $\Gamma_I = 0.07\,\text{eV}$, and $\Gamma_D = 1.12\,\text{eV}$, an

adjustment is also made in the energy value of the Carbon site, which is at $E_C = -5.85\,\text{eV}$. From now on, the other physical quantities will be made considering these parameters.

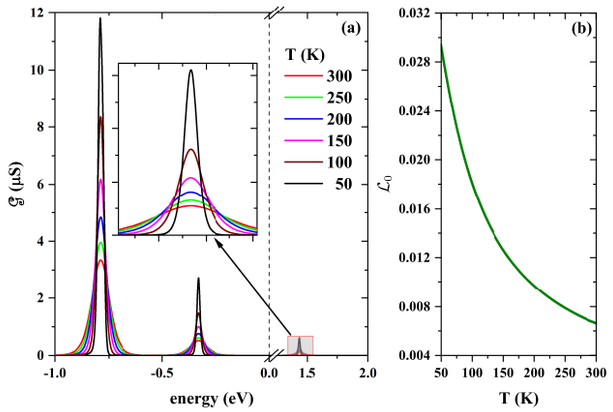

Figure **6-5**: (a) Electrical conductance in the ZnPTPPdT molecular system, as a function of the Fermi energy for different temperature values. The vertical dashed line represents the Fermi level. In (b), the $\mathcal{L}_0$-Landauer integral is shown as a temperature function.

Fig. **6-5**(a) shows the graph of the electrical conductance in the ZnPTPPdT molecular system as a function of the Fermi energy for different temperatures. Note that as the temperature increases, there is a decrease in the value of the electrical conductance, which cannot be seen with the naked eye for energy = 1.5 eV. It is worth mentioning that the conductance is proportional to the transmission of the molecular system (see Fig. **6-4**b), in which it is noticeable to see the HOMO and LUMO characteristic of the ZnTPPdT molecular system at the same energies of the incident electron. The decrease in the amplitude of the conductance is related to the electronic properties of the system, which is reflected in the variation that $\mathcal{L}_0$ undergoes with the increase in temperature; remember that this depends on the subtraction of the Fermi functions of the electrodes (Eq. 6-11), which means that when the temperature increases, the contribution to the amplitude of the electrical conductance decreases (see Fig. **6-5**(b)). Something to keep in mind is that when the properties due to the vibrations present in these systems are considered, these also contribute greatly to the decrease in the amplitude of the electrical conductance. This is because increasing the vibrations due to the increase in temperature makes it difficult for electrons to pass through the molecular system, causing the electrical conductance to decrease.

Figure **6-6**(a) shows the graph of thermal conductance as a function of Fermi energy for various temperatures with $\kappa_0 = 2/h\,\text{T}$. In this figure, it is observed that as the temperature increases, there is an increase in the magnitude of the thermal conductance, which is more evident in the vicinity of the Fermi energy (0 eV), i.e., in the vicinity of the HOMO of the molecule. Such a situation is opposite to that of the electrical conductance (see Fig. **6-**

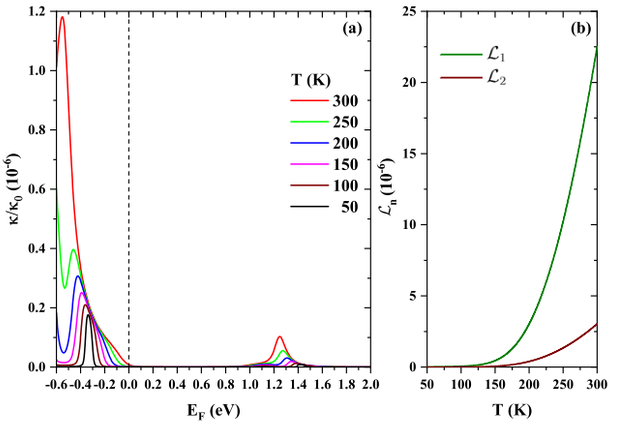

Figure **6-6**: (a) Thermal conductance in the ZnPTPPdT molecular system as a function of the Fermi energy for different temperatures with $\kappa_0 = 2/hT$. The vertical dashed line represents the Fermi level. In (b) are shown the Landauer integrals $\mathcal{L}_1$ and $\mathcal{L}_2$ concerning the temperature.

5). This behavior is associated with the variation that the Landauer integrals ($\mathcal{L}_1$ and $\mathcal{L}_2$) present with increasing temperature (see Fig. **6-6**(b)). They increase with the increase in temperature, but this growth does not present a linear behavior, which would explain why for an energy close to the HOMO, the change in the magnitude of the conductance is significant for a temperature of 300 K, compared to lower temperatures. It is worth mentioning that this behavior would also be seen by the vibrations that the system would present when the temperature increases, something interesting to study.

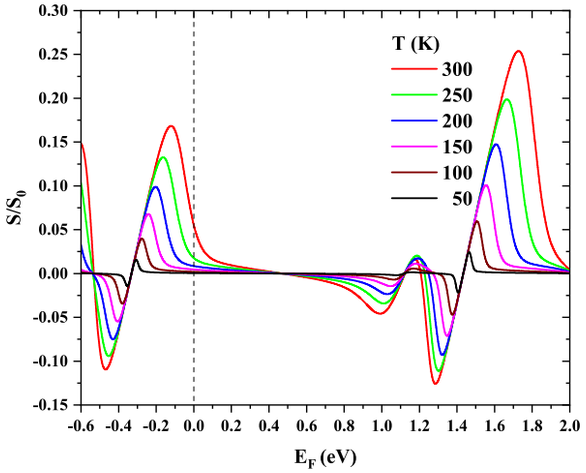

Figure **6-7**: Seebeck coefficient in the ZnPTPPdT molecular system as a function of the Fermi energy for different temperatures with $S_0 = 1/eT$. The vertical dashed black line represents the Fermi level.

Fig. **6-7** shows the graph of the Seebeck coefficient as a function of the Fermi energy for

different values of temperatures with $S_0 = 1/e\,\mathrm{T}$. From the graph, a higher value of the Seebeck coefficient is observed at high temperatures, which indicates a greater conversion of thermal energy to electrical energy. It is noted that around the Fermi energy, it goes from a positive to a negative value, which indicates that the predominant charge carriers (electrons) respond positively to the temperature gradient. The electrons tend to move towards a hotter region, thus causing an electric current in the direction of the temperature gradient, which generates the potential difference. It should be noted that when the transmission probability is at a resonant peak (at an eigenvalue of the molecule), the Seebeck coefficient is zero; this is because, as the electrons for that specific energy, they can move freely from an electrode to another through the molecule, which means that when there is a high electrical conductivity, a potential difference does not occur due to the difference in temperature of the electrodes. Around the Fermi energy, close to the HOMO and LUMO, it can be seen that the Seebeck coefficient has a positive value close to the HOMO (0.168), and the LUMO the maximum positive value is 0.253. This behavior illustrates how the alignment of the HOMO and LUMO levels concerning the electrodes influences the redistribution of electronic states under a temperature gradient. As a result, thermally excited electrons tend to flow from the hotter electrode toward the colder one, giving rise to a thermoelectric potential difference.

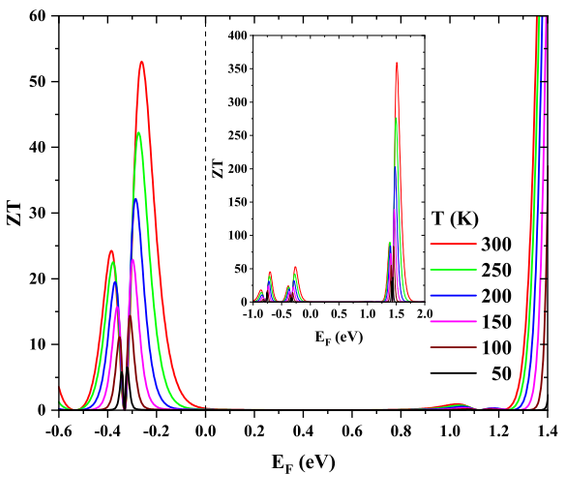

Figure **6-8**: The figure of merit (ZT) in the ZnPTPPdT molecular system as a function of the Fermi energy for different temperatures. The vertical dashed line represents the Fermi level. The inset represents the same graph of the ZT, but in a larger range of E_F.

Figure **6-8** shows the ZT, or figure of merit, of the ZnPTPPdT molecule as a function of the Fermi energy for different temperatures. In this graph, it can be seen that as the temperature increases, the ZT value increases, reaching a value close to 55, for $T = 300\,\mathrm{K}$ and energies close to the Fermi energy ($E_F = 0\,\mathrm{eV}$), which can give us indications that the molecular system behaves as a good thermoelectric material and that its efficiency increases with temperature. The above makes sense with what is observed in the graphs of the

thermal conductance κ (Fig. 6-6), and the Seebeck coefficient S (Fig.6-7), since at higher temperatures, the greater the magnitude of κ and S, which means that more thermal energy will be converted into electrical energy, due to the potential difference generated by the temperature gradient of the electrodes. These ZT values can give us a perspective that the molecular system studied would present a very good efficiency when converting thermal energy into electrical energy, which would postulate it as a good candidate to be used in molecular electronic circuits.

6.6 Conclusions

The electrical and thermoelectric properties of a single ZnPTPPdT molecule connected to two metal electrodes were investigated. The Dyson equations were employed for nearest neighbors, and the non-equilibrium Green functions were used to renormalize the molecular system into a linear system with eight effective sites, following the tight-binding approach. The thermoelectric properties were computed by applying the Landauer–Büttiker formalism. Our results indicate a favorable match between the calculated transmission probability and the HOMO and LUMO levels as predicted by DFT. Additionally, the experimentally reported current-voltage characteristic curve using the MCBJ method closely aligns with the gap and amplitude values. Regarding the thermoelectric properties, notably high Seebeck coefficient values and thermal conductance values were observed, leading to significantly high ZT values. These findings suggest that the molecular system holds promise as an electronic device capable of efficiently converting thermal energy into electrical energy.

6.7 Appendix

Decimation Procedure

This section shows in detail the process carried out to decimate the ZnTPPdT molecule (Fig. 6-1). We will begin by making a new distribution in the molecule to start the renormalization process (Fig. 6-9).

First, the benzene rings on the left and right (Fig. 6-10a) will be decimated to two effective sites (Fig. 6-10c).

To carry out the decimation process of the benzene molecule, using the system of Fig. 6-10 b, where the information enters the ring through the site $1a$ and leaves through the site $2a$, following the process carried out by Toscano-Negrette *et al.* [47] takes the system to two effective sites (see Fig. 6-10 c), and the effective functions of the two sites have the following form:

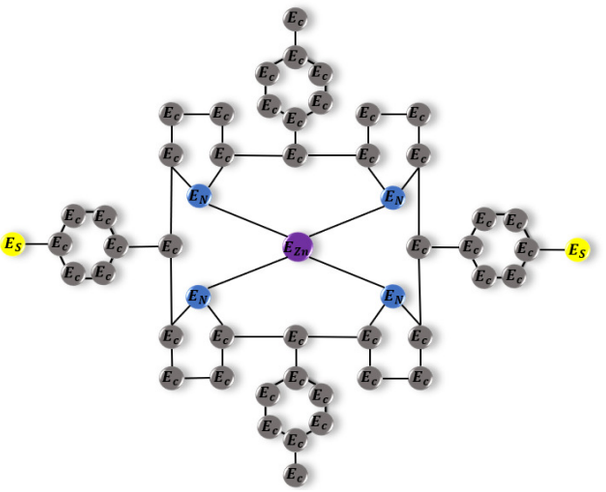

Figure **6-9**: Reorganization of the molecule shown in Fig. **6-1**, in order to carry out the decimation process.

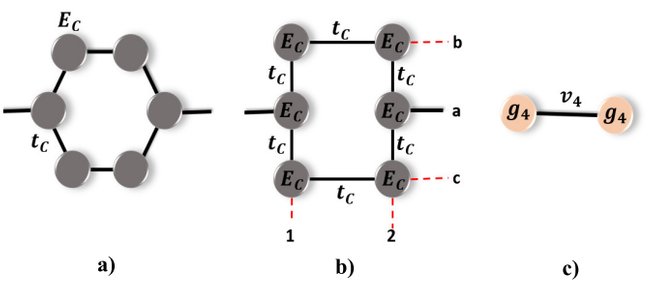

Figure **6-10**: a) Benzene molecule, b) benzene molecule rearranged for decimation, and c) system decimated to two effective sites.

$$g_4 = \frac{g_C(1 - g_C^2 t_C^2)}{1 - 3g_C^2 t_C^2}, \tag{6-16}$$

and

$$v_4 = \frac{2g_C^2 t_C^3}{1 - g_C^2 t_C^2}\,. \tag{6-17}$$

Now we proceed to decimate two benzene rings, up and down, which are connected to two Carbon atoms (see Fig. **6-11**a).

To begin the decimation, we proceed to a reorganization of the molecule (see Fig. **6-11**b), where we already have the decimation of the benzene molecule, and there are two effective sites connected to two carbon atoms, as shown in Fig. **6-11**c. We want to send all the

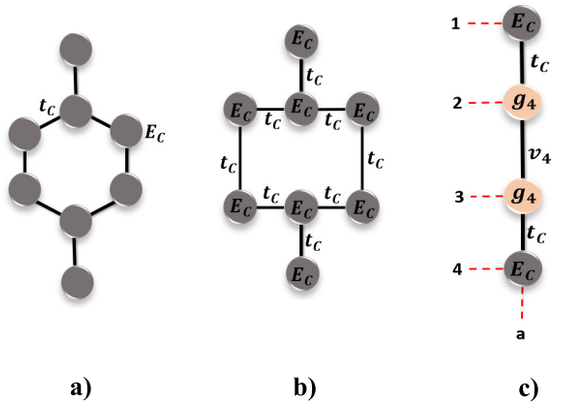

Figure **6-11**: a) Benzene molecule with two carbon atoms, b) molecule rearranged to decimate, and c) system decimated to two effective sites and two carbon atoms.

information to site $1a$; for that, we apply the Dyson equation to the first neighbors, obtaining the following system of equations:

$$G^a_{11} = g_C + g_C t_C G^a_{12}\,, \tag{6-18}$$

$$G^a_{12} = g_4 t_C G^a_{11} + g_4 v_4 G^a_{13}\,, \tag{6-19}$$

$$G^a_{13} = g_4 v_4 G^a_{12} + g_4 t_C G^a_{14}\,, \tag{6-20}$$

$$G^a_{14} = g_C t_C G^a_{13}. \tag{6-21}$$

Solving the system of equations for the function G^a_{11}, which is the effective Green function for an effective site g_3:

$$G^a_{11} = \frac{g_C(1 - g_4 g_C t_C^2 - g_4^2 v_4^2)}{1 - 2g_4 g_C t_C^2 + g_4^2 g_C^2 t_C^4 - g_4^2 v_4^2} = g_3\,. \tag{6-22}$$

The decimation of the Pyrrole rings (Fig. **6-12**a) will be done at three sites, where two will be effective and the Nitrogen atom (Fig. **6-12**c). For decimation, the system is reorganized by placing the Carbon atoms linearly (Fig. **6-12**b); the idea is to leave the information in place $1a$ and $4a$. Applying the Dyson equation, we have:

$$G^a_{11} = g_C + g_C t_C G^a_{12}\,, \tag{6-23}$$

$$G^a_{12} = g_C t_C G^a_{11} + g_C t_C G^a_{13}\,, \tag{6-24}$$

$$G^a_{11} = g_C t_C G^a_{12} + g_C t_C G^a_{14}\,. \tag{6-25}$$

Solving the previous system of equations for G^a_{11} in terms of G^a_{14}, we can obtain

$$G^a_{11} = \frac{g_C(1 - g_C^2 t_C^2)}{1 - 2g_C^2 t_C^2} + \frac{g_C^3 t_C^3}{1 - 2g_C^2 t_C^2} G^a_{14}\,, \tag{6-26}$$

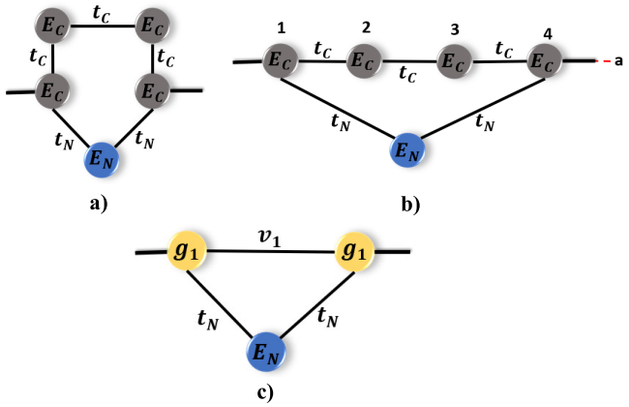

Figure **6-12**: a) Pyrrole molecule, b) rearranged system for decimation, and c) system decimated to two effective sites and one Nitrogen atom.

where the previous equation represents two effective sites, with effective Green equation g_1 and effective coupling v_1; they have the following expressions

$$g_1 = \frac{g_C(1 - g_C^2 t_C^2)}{1 - 2g_C^2 t_C^2}, \tag{6-27}$$

and

$$v_1 = \frac{g_C^2 t_C^3}{1 - g_C^2 t_C^2}\,. \tag{6-28}$$

Fig. **6-13** shows how the system looks with the decimations already made previously.

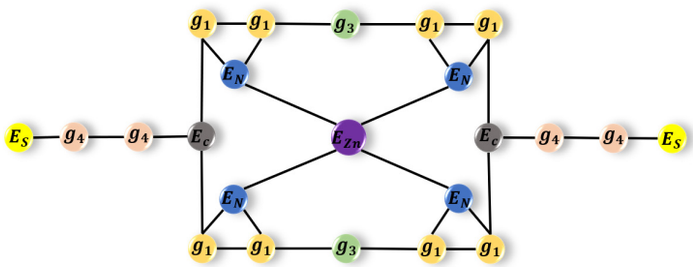

Figure **6-13**: Partially decimated ZnTPPdT system.

Now we are going to decimate the central system of Fig. **6-13**; for that it is reorganized according to Fig. **6-14**, where the information enters the system through site $1a$ and leaves through site $5a$. Applying the Dyson equation, the following system of equations is obtained:

$$G_{11}^a = g_C + g_C t_C G_{11}^e + g_C t_C G_{11}^d\,, \tag{6-29}$$

$$G_{11}^e = g_1 t_C G_{11}^a + g_1 v_1 G_{12}^e + g_1 t_N G_{12}^b\,, \tag{6-30}$$

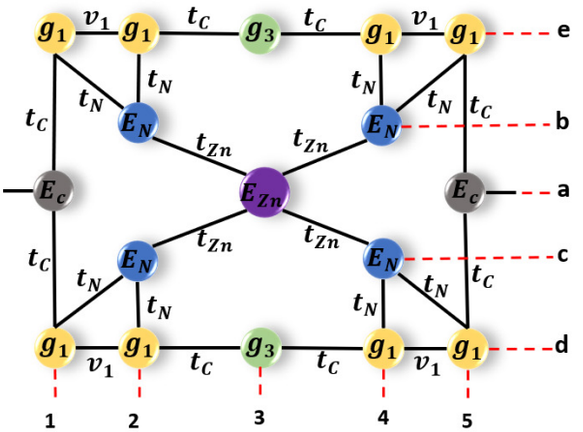

Figure **6-14**: Reorganization of the central system of Fig. **6-13** to be able to perform the decimation.

$$G^e_{12} = g_1 v_1 G^e_{11} + g_1 t_N G^b_{12} + g_1 t_C G^e_{13}\,, \tag{6-31}$$

$$G^b_{12} = g_N t_N G^e_{11} + g_N t_N G^e_{12} + g_N t_{Zn} G^a_{13}\,, \tag{6-32}$$

$$G^e_{13} = g_3 t_C G^e_{12} + g_3 t_C G^e_{14}\,, \tag{6-33}$$

$$G^e_{14} = g_1 t_C G^e_{13} + g_1 v_1 G^e_{15} + g_1 t_N G^b_{14}\,, \tag{6-34}$$

$$G^e_{15} = g_1 v_1 G^e_{14} + g_1 t_C G^a_{15} + g_1 t_N G^b_{14}\,, \tag{6-35}$$

$$G^b_{14} = g_N t_N G^e_{14} + g_N t_N G^e_{15} + g_N t_{Zn} G^a_{13}\,, \tag{6-36}$$

$$G^d_{15} = g_1 t_C G^a_{15} + g_1 v_1 G^d_{14} + g_1 t_N G^c_{14}\,, \tag{6-37}$$

$$G^d_{14} = g_1 v_1 G^d_{15} + g_1 t_C G^d_{13} + g_1 t_N G^c_{14}\,, \tag{6-38}$$

$$G^c_{14} = g_N t_N G^d_{15} + g_N t_N G^d_{14} + g_N t_{Zn} G^a_{13}\,, \tag{6-39}$$

$$G^d_{13} = g_3 t_C G^d_{14} + g_3 t_C G^d_{12}\,, \tag{6-40}$$

$$G^d_{12} = g_1 t_C G^d_{13} + g_1 v_1 G^d_{11} + g_1 t_N G^c_{12}\,, \tag{6-41}$$

$$G^d_{11} = g_1 t_C G^a_{11} + g_1 v_1 G^d_{12} + g_1 t_N G^c_{12}\,, \tag{6-42}$$

$$G^c_{12} = g_N t_N G^d_{12} + g_N t_N G^d_{11} + g_N t_{Zn} G^a_{13}\,, \tag{6-43}$$

$$G^a_{13} = g_{Zn} t_{Zn} G^b_{12} + g_{Zn} t_{Zn} G^b_{14} + g_{Zn} t_{Zn} G^c_{14} + g_{Zn} t_{Zn} G^c_{12}\,. \tag{6-44}$$

By solving the system of equations for G^a_{11} in terms of the function of G^a_{15}, we have:

$$G^a_{11} = g_2 + g_2 v_2 G^a_{15}, \tag{6-45}$$

were

$$
\begin{aligned}
g_2 = &-((g_C(1+R)(-1+2FP+R)(2BM(-1+FP)-(1+R)(-1+2FP+R)+4HL(-1+2BM+R^2)))/\\
&(-(1+R)(-1+2FP+R)(2BM(-1+FP)-(1+R)(-1+2FP+R)+4HL(-1+2BM+R^2))\\
&+2AB(-(-1+FP)(1+R)(-1+2FP+R)+BM(2+FP(-4+FP)-2FPR-R^2)\\
&+2HL((2+FP(-3+R)-2R)(1+R)+2BM(-2+R^2+FP(3+2R))))),
\end{aligned}
\tag{6-46}
$$

and

$$
v_2 = \frac{2AB(BF^2MP^2+B(1-4HL)MR^2+2FP(BMR+HL((1+R)^2-2B(M+2MR))))}{g_C(1+R)(-1+2FP+R)(2BM(-1+FP)-(1+R)(-1+2FP+R)+4HL(-1+2BM+R^2))}\,. \tag{6-47}
$$

In the above expressions of g_2 and v_2, $A = g_C t_C$, $B = g_1 t_C$, $R = g_1 v_1$, $P = g_1 t_N$, $F = g_N t_N$, $H = g_N t_{Zn}$, $L = g_{Zn} t_{Zn}$, and $M = g_3 t_C$.

With what was done previously, the system of Fig. **6-14** is decimated to two effective sites, and the entire molecular system is decimated to a linear system, with six effective sites and the two sulfur atoms, as shown. shown in Fig. **6-15**.

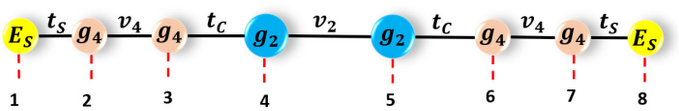

Figure **6-15**: Decimation to a linear chain with effective sites for the ZnTPPdT molecule.

To find the Green function of site 1 and that of site 8, we must apply the Dyson equation again.

$$G^0_{11} = g_S + g_S t_S G^0_{12}\,, \tag{6-48}$$

$$G^0_{12} = g_4 t_S G^0_{11} + g_4 v_4 G^0_{13}\,, \tag{6-49}$$

$$G^0_{13} = g_4 v_4 G^0_{12} + g_4 t_C G^0_{14}\,, \tag{6-50}$$

$$G^0_{14} = g_2 t_C G^0_{13} + g_2 v_2 G^0_{15}\,, \tag{6-51}$$

$$G^0_{15} = g_2 v_2 G^0_{14} + g_2 t_C G^0_{16}\,, \tag{6-52}$$

$$G^0_{16} = g_4 t_C G^0_{15} + g_4 v_4 G^0_{17}\,, \tag{6-53}$$

$$G^0_{17} = g_4 v_4 G^0_{16} + g_4 t_S G^0_{18}\,, \tag{6-54}$$

$$G^0_{18} = g_S t_S G^0_{17}\,. \tag{6-55}$$

When solving the system of equations, the expressions for G^0_{11}, and G^0_{18} are:

$$\begin{aligned} G^0_{11} =&(g_S(-1+2Q^2-Q^4+UV-Q^2UV+W^2-2Q^2W^2+Q^4W^2-UVW^2+Q^2UVW^2+2JX \\ &-2JQ^2X-2JUVX+JQ^2UVX-J^2X^2+J^2UVX^2))/(-1+2Q^2-Q^4+2UV-2Q^2UV \\ &-U^2V^2+W^2-2Q^2W^2+Q^4W^2-2UVW^2+2Q^2UVW^2+U^2V^2W^2+2JX-2JQ^2X \\ &-4JUVX+2JQ^2UVX+2JU^2V^2X-J^2X^2+2J^2UVX^2-J^2U^2V^2X^2)\,, \end{aligned} \tag{6-56}$$

and

$$\begin{aligned} G^0_{18} =&(-g_SJQ^2UVWX)/(-1+2Q^2-Q^4+2UV-2Q^2UV-U^2V^2+W^2 \\ &-2Q^2W^2+Q^4W^2-2UVW^2+2Q^2UVW^2+U^2V^2W^2+2JX-2JQ^2X \\ &-4JUVX+2JQ^2UVX+2JU^2V^2X-J^2X^2+2J^2UVX^2-J^2U^2V^2X^2)\,. \end{aligned} \tag{6-57}$$

In the above expressions of G^0_{11} and G^0_{18}, $V = g_St_S$, $U = g_4t_S$, $Q = g_4v_4$, $J = g_2t_C$, $W = g_2v_2$, and $X = g_4t_C$. It should be noted that the system in Fig. **6-15**, presents a symmetry if looked from left to right; therefore, if the system from 1 to 8 is studied, it would give us the same functions if studied from 8 to 1, in other words, $G^0_{11} = G^0_{88}$ and $G^0_{18} = G^0_{81}$.

References

[1] Marqués-González, S.; Low, P.J. Molecular electronics: history and fundamentals. *Aust. J. Chem.* **2016**, *69*, 244–253.

[2] Xin, N.; Guo, X. Catalyst: the renaissance of molecular electronics. *Chem.* **2017**, *3*, 373–376

[3] Aviram, A.; Ratner, M. Molecular rectifiers. *Chem. Phys. Lett.* **1974**, *29*, 277–283.

[4] Joachim, C.; Gimzewski, J.; Aviram, A. Electronics using hybrid-molecular and mono-molecular devices. *Nature.* **2000**, *408*, 541–548.

[5] Aviram, A. Molecules for memory, logic, and amplification. *J.A.C.S.* **1988**, *110*, 5687–5692.

[6] Mendoza-Uribe, G.; Rodriguez-Lopez, J. Nanoscience and nanotechnology: a revolution in progress. *Perf. latinoam.* **2007**, *14*, 161–186.

[7] Charles, P.; Frank, O. *Introduction to nanotechnology*; John Wiley & Sons, 2003.

[8] Fujii, A.; Cho, H.; Yue, Y.; Koike, M.; Nishino, T.; Kiguchi, K. Mechanically tuned thermopower of single-molecule junctions. *Adv. Electron. Mater.* **2022**, *8*,2200700.

[9] Han, W.; Durantini, E.; Moore, T.; Moore, A.; Gust, D.; Rez, P.; Leatherman, G.; Seely, G.; Tao, N.; Lindsay, S.M. STM contrast, electron-transfer chemistry, and conduction in molecules. *J. Phys. Chem. B.* **1997**, *101*, 10719–10725.

[10] Xue, Y.; Datta, S.; Hong, S.; Reifenberger, R.; Henderson, J.; Kubiak, C. Negative differential resistance in the scanning-tunneling spectroscopy of organic molecules. *Phys. Rev. B.* **1999**, *59*, R7852.

[11] Chen, H.; Jia, C.; Zhu, X.; Yang, C.; Guo, X.; Stoddart, J.F. Reactions in single-molecule junctions. *Nat. Rev. Mater.* **2023**, *8*, 165–185.

[12] Zhang, J.; Wang, Z.; Niu, T.; Li, Z.; Chen, W. Single molecule tunneling spectroscopy investigation of reversibly switched dipolar vanadyl phthalocyanine on graphite. *Appl. Phys. Lett.* **2014**, *104*, 113506.

[13] Li, Z.; Borguet, E. Determining charge transport pathways through single porphyrin molecules using scanning tunneling microscopy break junctions. *JACS. 2012*, *134*, 63–66.

[14] Tsutsui, M.; Taniguchi, M. Single molecule electronics and devices. *Sensors.* **2012**, *12*, 7259–7298.

[15] Wang, L.; Wang, L.; Zhang, L.; Xiang, D. Advance of mechanically controllable break junction for molecular electronics. *Molecular-Scale Electronics: Current Status and Perspectives.* **2017**, 45–86.

[16] Perrin, M.L.; Burzurí, E.; Van der Zant, H.S. Single-molecule transistors. *Chem. Soc. Rev. 2015*, *44*, 902–919.

[17] Xiang, D.; Jeong, H.; Lee, T.; Mayer, D. Mechanically controllable break junctions for molecular electronics. *Adv. Mater.* **2013**, *25*, 4845–4867.

[18] Tian, J.; Yang, Y.; Zhou, X.; Schöllhorn, B.; Maisonhaute, E.; Chen, Z.; Yang, F.; Chen, Y.; Amatore, C.; Mao, B. Electrochemically assisted fabrication of metal atomic wires and molecular junctions by MCBJ and STM-BJ methods. *ChemPhysChem.* **2010**, *11*, 2745–2755.

[19] Hong, W.; Valkenier, H.; Mészáros, G.; Manrique, D.; Mishchenko, A.; Putz, A.; García, P.; Lambert, C.; Hummelen, J.; Wandlowski, T. An MCBJ case study: The influence of π-conjugation on the single-molecule conductance at a solid/liquid interface. *Beilstein J. Nanotechnol.* **2011**, *2*, 699–713.

[20] Khireddine, A.; Bouhemadou, A.; Maabed, S.; Bin-Omran, S.; Khenata, R.; Al-Douri, Y. Elastic, electronic, optical and thermoelectric properties of the novel Zintl-phase Ba_2ZnP_2. *Solid State Sci.* **2022**, *128*, 106893.

[21] Xu, K.; Yi, G.; Wang, W.; Wang, J.; Wang, C.; Li, Q. Theoretical insights into the diverse and tunable charge transport behavior of stilbene-based single-molecule junctions. *Chem. Phys.* **2022**, *556*, 111478.

[22] Wang, Y.; Huang, H.; Yu, Z.; Zheng, J.; Shao, Y.; Zhou, X.; Chen, J.; Li, J. Modulating electron transport through single-molecule junctions by heteroatom substitution. *J. Mater. Chem. C.* **2020**, *8*, 6826–6831.

[23] Albrecht, K.F.; Wang, H.; Mühlbacher, L.; Thoss, M.; Komnik, A. Bistability signatures in nonequilibrium charge transport through molecular quantum dots. *Phys. Rev. B.* **2012**, *86*, 081412.

[24] Ojeda, J.H.; Duque, C.A.; Laroze, D. Electron–phonon interaction in quantum transport through quantum dots and molecular systems. *Physica B.* **2016**, *502*, 73–81.

[25] Solomon, G.C.; Andrews, D.Q.; Hansen, T.; Goldsmith, R.H.; Wasielewski, M.R.; Van Duyne, R.P.; Ratner, M.A. Understanding quantum interference in coherent molecular conduction. *J. Chem. Phys.* **2008**, *129*, 054701.

[26] Ojeda, J.H.; Duque, C.A.; Laroze, D. Shot noise and thermopower in aromatic molecules. *Physica E.* **2014**, *62*, 15–20.

[27] Vahedi, J.; Sartipi, Z. Effects of quantum interference on the electron transport in the semiconductor/benzene/semiconductor junction. *Mol. Phys.* **2015**, *113*, 1422-1432.

[28] Xu, K.; Yi, G.; Wang, W.; Wang, J.; Wang, C.; Li, Q. Theoretical insights into the diverse and tunable charge transport behavior of stilbene-based single-molecule junctions. *Chemical Physics* **2022**, *556*, 111478.

[29] Ojeda, J.; Duque, C.; Laroze, D. Electron–phonon interaction in quantum transport through quantum dots and molecular systems. *Physica B: Condensed Matter* **2016**, *502*, 73–81.

[30] Levstein, P. R.; Pastawski, H. M.; D'amato, J. L. Tuning the through-bond interaction in a two-centre problem. *J. Phys.: Condens. Matter.* **1990**, *2*, 1781.

[31] Pastawski, H. M.; Medina, E. 'Tight Binding' methods in quantum transport through molecules and small devices: From the coherent to the decoherent description. *Rev. Mex. Fis.* **2001**, *47 S1*, 1-23.

[32] Pastawski, H. M.; Torres, L. F.; Medina, E. Electron–phonon interaction and electronic decoherence in molecular conductors. *Chem. Phys.* **2002**, *281*, 257-278.

[33] Ojeda, J. H.; Duque, C. A.; Laroze, D. Electron–phonon interaction in quantum transport through quantum dots and molecular systems. Physica B. **2016**, *502*, 73-81.

[34] Zhang, C.; Yi, Y.; Yang, H.; Yi, Z.; Chen, X.; Zhou, Z.; Yi, Y. G.; Li, H.; Chen, J.; Liu, C. Wide spectrum solar energy absorption based on germanium plated ZnO nanorod arrays: Energy band regulation, Finite element simulation, Super hydrophilicity, Photothermal conversion. *Appl. Mater. Today.* **2022**, *28*, 101531.

[35] Li, W.; Xu, F.; Cheng, S.; Yang, W.; Liu, B.; Liu, M.; Yi, Z.; Tang, B.; Chen, J.; Sun, T. Six-band rotationally symmetric tunable absorption film based on AlCuFe quasicrystals. *Opt. Laser Technol.* **2024**, *169*, 110186.

[36] Li, W.; Liu, M.; Cheng, S.; Zhang, H.; Yang, W.; Yi, Z.; Zeng, Q.; Tang, B.; Ahmad, S.; Sun, T. Polarization independent tunable bandwidth absorber based on single-layer graphene. *Diamond Relat. Mater.* **2024**, *142*, 110793.

[37] Liang, S.; Xu, F.; Li, W.; Yang, W.; Cheng, S.; Yang, H.; Chen, J.; Yi, Z.; Jiang, P. Tunable smart mid infrared thermal control emitter based on phase change material VO2 thin film. *Appl. Therm. Eng.* **2023**, *232*, 121074.

[38] He, L.J.; Sun, Y.; Li, W.; Wang, J.; Song, M.X.; Zhang, H.X. Highly-efficient sensitizer with zinc porphyrin as building block: Insights from DFT calculations. *Sol. Energy.* **2018**, *173*, 283–290.

[39] Narra, V.; Ullah, H.; Singh, V.; Giribabu, L.; Senthilarasu, S.; Karazhanov, S.; Tahir, A.; Mallick, T.; Upadhyaya, H. D–π–A system based on zinc porphyrin dyes for dye-sensitized solar cells: combined experimental and DFT–TDDFT study. *Polyhedron.* **2015**, *100*, 313–320.

[40] Zhang, J.X.; Han, F.M.; Liu, J.C.; Li, R.Z.; Jin, N.Z. Self-assemblies formed by isonicotinic acid analogues axially coordinating with zinc porphyrin via pyridyl unit: Synthesis and application in dye sensitized solar cells. *Tetrahedron Lett.* **2016**, *57*, 1867–1872.

[41] Sallam, G.; Shaban, S.Y.; Nassar, A.; El-Khouly, M.E. Water soluble porphyrin as optical sensor for the toxic heavy metal ions in an aqueous medium. *Spectrochim. Acta, Part A.* **2020**, *241*, 118609.

[42] Han, Q.; Wang, C.; Liu, P.; Zhang, G.; Song, L.; Fu, Y. Achieving synergistically enhanced dual-mode electrochemiluminescent and electrochemical drug sensors via a multi-effect porphyrin-based metal-organic framework. *Sens. Actuators, B.* **2021**, *330*, 129388.

[43] Perrin, M.L.; Verzijl, C.; Martin, C.; Shaikh, A.; Eelkema, R.; Van Esch, J.; Van Ruitenbeek, J.; Thijssen, J.; Van Der Zant, H.; Dulić, D. Large tunable image-charge effects in single-molecule junctions. *Nat. Nanotechnol.* **2013**, *8*, 282–287.

[44] Souza, A.M.; Rungger, I.; Schwingenschlögl, U.; Sanvito, S. The image charge effect and vibron-assisted processes in Coulomb blockade transport: a first principles approach. *Nanoscale. 2015*, *7*, 19231–19240.

[45] Al-Galiby, Q.H.; Sadeghi, H.; Algharagholy, L.A.; Grace, I.; Lambert, C. Tuning the thermoelectric properties of metallo-porphyrins. *Nanoscale.* **2016**, *8*, 2428–2433.

[46] Ojeda, J.H.; Rey-González, R.R.; Laroze, D. Quantum transport through aromatic molecules. *J. Appl. Phys.* **2013**, *114*, 213702.

[47] Toscano-Negrette, R.G.; León-González, J.C.; Vinasco, J.A.; Ojeda Silva, J.H.; Morales, A.L.; Duque, C.A. Theoretical Study of Thermoelectric Properties of a Single Molecule of Diphenyl-Ether. *Condens. Matter.* **2023**, *8*, 1–21.

[48] Soto-Gómez, E.Y.; Ojeda Silva, J.H.; Gil-Corrales, J.A.; Gallego, D.; Hurtado Morales, M.F.; Morales, A.L.; Duque, C.A. Theoretical Study of Electronic and Thermal Transport Properties through a Single-Molecule Junction of Catechol. *Condens. Matter.* **2023**, *8*, 1–19.

[49] Rivera Mateus, M.A.; Ojeda, J.H.; Gallego, D. Thermoelectric properties through a wire composed of isoprene molecules. *AIP Adv.* **2020**, *10*, 065021.

[50] Sadeghi, H.; Sangtarash, S.; Lambert, C.J. Electron and heat transport in porphyrin-based single-molecule transistors with electro-burnt graphene electrodes. *Beilstein J. Nanotechnol.* **2015**, *6*, 1413–1420.

[51] Ojeda, J.H.; Cortés, J.C.; Gómez, J.A.; Duque, C.A. Current's fluctuations through molecular wires composed of thiophene rings. *Molecules.* **2018**, *23*, 881.

[52] Yang, N. X.; Yan, Q.; Sun, Q. F. Linear and nonlinear thermoelectric transport in a magnetic topological insulator nanoribbon with a domain wall. *Phys. Rev. B.* **2020**, *102*, 245412.

[53] Ojeda, J. H.; Laroze, D.; Maiti, S. K. Thermoelectric phenomena of the molecular structure of a Thiolated Arylethynylene with a 9, 10-Dihydroanthracene (AH) core. *Eur. Phys. J. Plus.* **2022**, *137*, 553.

Conclusions

The nonlinear optical response of ZnS/CdS/ZnS quantum dots was studied, considering the effects of geometry, external fields, and a donor impurity. The results show that these factors influence absorption and refractive coefficients, with potential applications in the design of optoelectronic devices in the terahertz region (1.5–20 meV).

We studied optical transitions in ZnTe/CdSe and CdSe/ZnTe quantum dots under electric/magnetic fields and varying internal radii. Transition energies and absorption spectra shift with field strength and geometry, affecting oscillator strength. The model agrees with experiments and shows potential for application in optoelectronic and photonic devices.

The electrical and thermoelectric properties of a diphenyl ether molecule connected to metal electrodes were analyzed. Significant variations were observed depending on the coupling site. Model (c) showed the best performance, with a high Seebeck coefficient and $ZT \geq 1$.

The ZnPTPPdT molecule connected to metal electrodes was studied using non-equilibrium Green's functions and the Landauer-Büttiker formalism. The results agree well with DFT and experimental $I - V$ data, and show high Seebeck coefficients and ZT values, indicating strong potential for thermoelectric applications.

Appendix

This appendix presents a representative example of how to calculate thermoelectric properties in a system composed of a single molecule connected between two metallic electrodes. In particular, the case of model (a) corresponding to a Diphenyl-Ether molecule is considered.

The calculation is carried out using a script written in the Python programming language. This script employs the Landauer formalism to describe coherent electronic transport and allows the computation of various quantities of interest as a function of the molecular energy level and the system temperature.

Among the properties calculated are the current–voltage (I–V) characteristic curve, electrical conductance, electronic thermal conductance, the Seebeck coefficient, and the thermoelectric figure of merit ZT. These quantities make it possible to evaluate the performance of the system as a potential nanoscale energy conversion device.

This example is intended to illustrate the basic procedure followed in the more general studies presented in the main body of this thesis. Although the model is simplified, it provides a conceptual and computational foundation for understanding the methods applied to more complex molecular systems.

It is worth noting that this example can be extended to other molecular systems, provided that the equations for the decimated Green's functions are known. These functions effectively describe the interaction between the molecule and the electrodes in terms of self-energies, thus allowing the generalization of the approach to a wide variety of molecular architectures.

Dephenyl-Ether

1 Model (a)

[1]:
```
import numpy as np
import cmath
import matplotlib.pyplot as plt
from scipy import integrate
import sympy as sp
import time

EC   =  0.0 # Site energy for the Carbon atom    (eV)
EO   = -2.2 # Site energy for the Oxygen atom    (eV)
tC   =  1.0 # Carbon - Carbon hopping parameter  (eV)
tO   = -1.0 # Carbon - Oxygen hopping parameter  (eV)
Gamm =  0.2 # Electrode-Molecule coupling energy (eV)
EF   =  0.0 # Fermi energy (eV)
k    =  8.617333262*10**-5 # Planck constant (eV/K)
T    =  300 # Temperature (K)
ee   = 1
```

[2]:
```
# Local Green's Functions for Carbon and Oxygen

def gC(w):
    return 1/(w-EC-0.0000001j)

def gO(w):
    return 1/(w-EO-0.0000001j)
```

[3]:
```
# Decimation at two effective sites of the Benzene molecule

def g1(w):
    return (gC(w) - gC(w)**3 * tC**2) / (1 - 3*gC(w)**2 * tC**2)

def v1(w):
    return (2*gC(w)**2 * tC**3) / (1 - gC(w)**2 * tC**2)
```

[4]:
```
# Green's functions of sites 1 and 5

def G11a(w):
    return (g1(w)*(1 - g1(w)**2*v1(w)**2 - 2*gO(w)*g1(w)*tO**2 +␣
 ↪gO(w)*g1(w)**3*v1(w)**2*tO**2))/((1 - g1(w)**2*v1(w)**2)*(1 -␣
 ↪g1(w)**2*v1(w)**2 - 2*gO(w)*g1(w)*tO**2))

def G15a(w):
```

```
    return (g0(w)*g1(w)**4*v1(w)**2*t0**2)/((1 - g1(w)**2*v1(w)**2)*(1 -␣
↪g1(w)**2*v1(w)**2 - 2*g0(w)*g1(w)*t0**2))
```

[5]:
```
# Total Green's function

def G(w):
    return (G15a(w)) / ((1+(1j*Gamm*G11a(w))/2)**2 + ((Gamm*G15a(w))/2)**2)
```

[6]:
```
# Transmission probability

def Tr(w):
    return (Gamm*abs(G(w)))**2
```

1.1 Calculation of the probability of transmission

[7]:
```
start_time = time.time()

# Generate an array for the incident electron energy values
w_values = np.linspace(-4, 3, 10000)

# Calculate Transmission values for each energy value
Tr_values = [Tr(w) for w in w_values] # Calcular los valores de gc1 para cada␣
↪valor de x

# Make the graph of Transmission vs energy on a linear scale
plt.figure(figsize=(12, 4))
plt.subplot(1, 2, 1)
plt.plot(w_values, Tr_values, label='Transmission', color='red')
plt.xlabel('energy (eV)')
plt.ylabel('Transmission')
plt.title('T vs E')
plt.legend()
plt.grid(True)

# Make the graph of Transmission vs energy on a logarithmic scale
plt.subplot(1, 2, 2)
plt.semilogy(w_values, Tr_values, label='Transmission', color='red')
plt.xlabel('energy (eV)')
plt.ylabel('Transmission')
plt.title('T vs E')
plt.legend()
plt.grid(True)
plt.show()

end_time = time.time()
execution_time = end_time - start_time
```

```
print("Process completed successfully")
print(f"The calculation took {execution_time:.4f} seconds.")
```

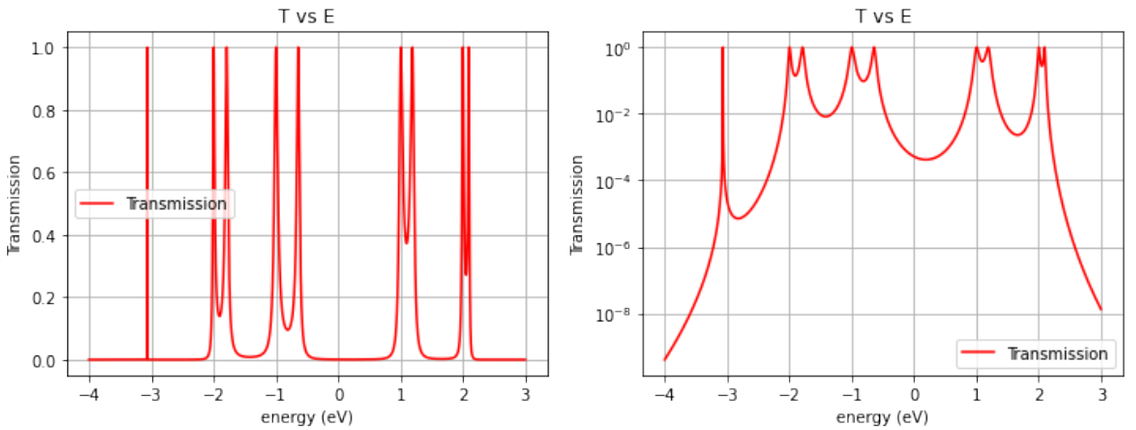


```
Process completed successfully
The calculation took 2.9160 seconds.
```

1.2 Calculation for current-voltage characteristic curve

[8]:
```
# Expression for the chemical potential for the Left (L) and Right (R) electrode.

def muL(Vi):
    return EF + ee*Vi/2

def muR(Vi):
    return EF - ee*Vi/2

# Expression for the Fermi probability function for the Left (L) and Right (R)␣
 ↪electrode.

def fL(w,Vi):
    return 1/(1 + np.exp((w - muL(Vi))/(k*T)))

def fR(w,Vi):
    return 1/(1 + np.exp((w - muR(Vi))/(k*T)))

# Expression to calculate the current-voltage characteristic curve

def I(w,Vi):
    return (fL(w,Vi) - fR(w,Vi)) * Tr(w)
```

[9]:
```
start_time = time.time()

Vii = np.linspace(-4, 4, 1000)
```

```
wini = -4
dw = 0.01

def IC(Vi):
    I0 = []
    for i in range(0,2000):
        wp = wini + i*dw
        fun = I(wp,Vi)
        I0.append(fun)
    Resul = sum(I0)*dw
    return Resul

IC_re = [7.75*10**-5*IC(i)/10**-6 for i in Vii]


plt.figure(figsize=(10, 6))
plt.plot(Vii, IC_re, label='IvsV', color = 'red')
plt.xlabel('V (volt)')
plt.ylabel('I ($\mu$A)')
plt.title('I vs V')
plt.legend()
plt.grid(True)
plt.show()

end_time = time.time()
execution_time = end_time - start_time

print("Process completed successfully")
print(f"The calculation took {execution_time:.4f} seconds.")
```

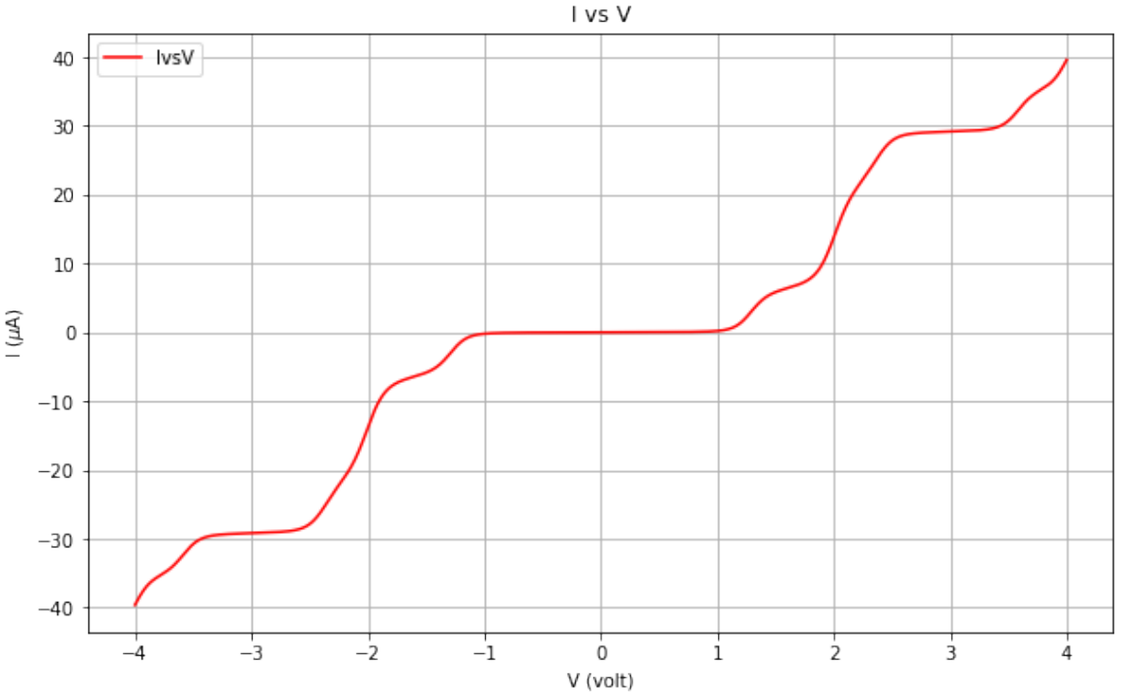


```
Process completed successfully
The calculation took 76.2656 seconds.
```

1.3 Calculation for electrical conductance

[10]:
```
start_time = time.time()

def df(w,Ef1):
    return -(np.exp((w-Ef1)/(k*T)))/(k*T*(1 + np.exp((w-Ef1)/(k*T)))**2)


def L0(w,Ef1):
    return -df(w,Ef1)*Tr(w)

Eff = np.linspace(-4, 3, 1000)

wini = -4
dw = 0.01

def L01(Ef1):
    I1 = []
    for i in range(0,910):
        wp = wini + i*dw
        fun = L0(wp,Ef1)
        I1.append(fun)
    Resul = sum(I1)*dw
```

```
    return Resul

L0_re = [L01(i) for i in Eff]

plt.figure(figsize=(10, 6))
plt.subplot(1, 2, 1)
plt.plot(Eff, L0_re, label='Cond. Electrica', color = 'red')
plt.xlabel('E_F (eV)')
plt.ylabel('G/G_0')
plt.title('G vs EF')
plt.legend()
plt.grid(True)

plt.subplot(1, 2, 2)
plt.semilogy(Eff, L0_re, label='Cond. Electrica', color = 'red')
plt.xlabel('EF (eV)')
plt.ylabel('G/G_0')
plt.title('G vs EF')
plt.legend()
plt.grid(True)
plt.show()

end_time = time.time()
execution_time = end_time - start_time

print("Process completed successfully")
print(f"The calculation took {execution_time:.4f} seconds.")
```

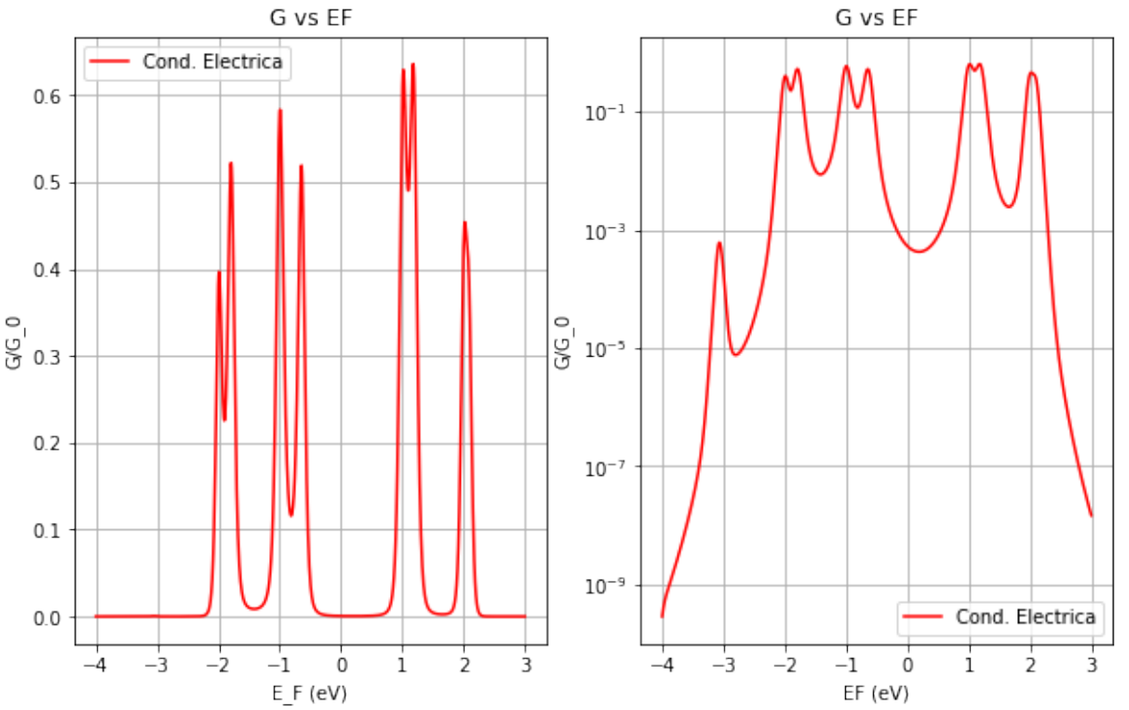


```
Process completed successfully
The calculation took 35.0941 seconds.
```

1.4 Calculation for the Seebeck Coefficient

[11]:
```
start_time = time.time()

def L1(w,Ef1):
    return -df(w,Ef1)*(w - Ef1)*Tr(w)

wini = -4
dw = 0.01

def L11(Ef1):
    I2 = []
    for i in range(0,910):
        wp = wini + i*dw
        fun = L1(wp,Ef1)
        I2.append(fun)
    Resul = sum(I2)*dw
    return Resul

L1_re = [L11(i) for i in Eff]
```

```
S = [(- b) / (a*T) for a, b in zip(L0_re, L1_re)]


plt.figure(figsize=(10, 6))
plt.plot(Eff, S, label='Seebeck', color = 'red')
plt.xlabel('E_F (eV)')
plt.ylabel('S/S_0')
plt.title('S vs EF')
plt.legend()
plt.grid(True)
plt.show()

end_time = time.time()
execution_time = end_time - start_time

print("Process completed successfully")
print(f"The calculation took {execution_time:.4f} seconds.")
```

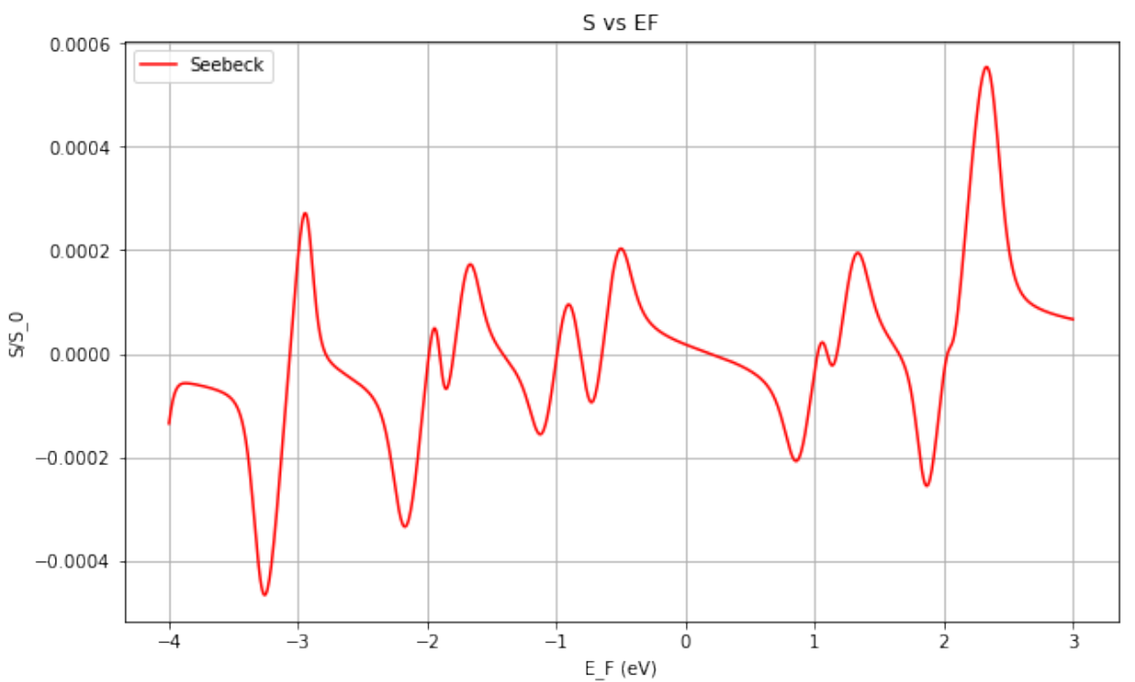


```
Process completed successfully
The calculation took 34.0080 seconds.
```

1.5 Calculation for thermal conductance

[12]:
```
start_time = time.time()

def L2(w,Ef1):
    return -df(w,Ef1)*(w-Ef1)**2*Tr(w)

wini = -4
dw = 0.01

def L21(Ef1):
    I3 = []
    for i in range(0,910):
        wp = wini + i*dw
        fun = L2(wp,Ef1)
        I3.append(fun)
    Resul = sum(I3)*dw
    return Resul

L2_re = [L21(i) for i in Eff]


kk =  [ (c*a - b**2)/(a*T) for a, b, c in zip(L0_re, L1_re, L2_re)]


plt.figure(figsize=(10, 6))
plt.plot(Eff, kk, label='Cond. Termica', color = 'red')
plt.xlabel('E_F (eV)')
plt.ylabel('k/k_0')
plt.title('k vs EF')
plt.legend()
plt.grid(True)
plt.show()

end_time = time.time()
execution_time = end_time - start_time

print("Process completed successfully")
print(f"The calculation took {execution_time:.4f} seconds.")
```

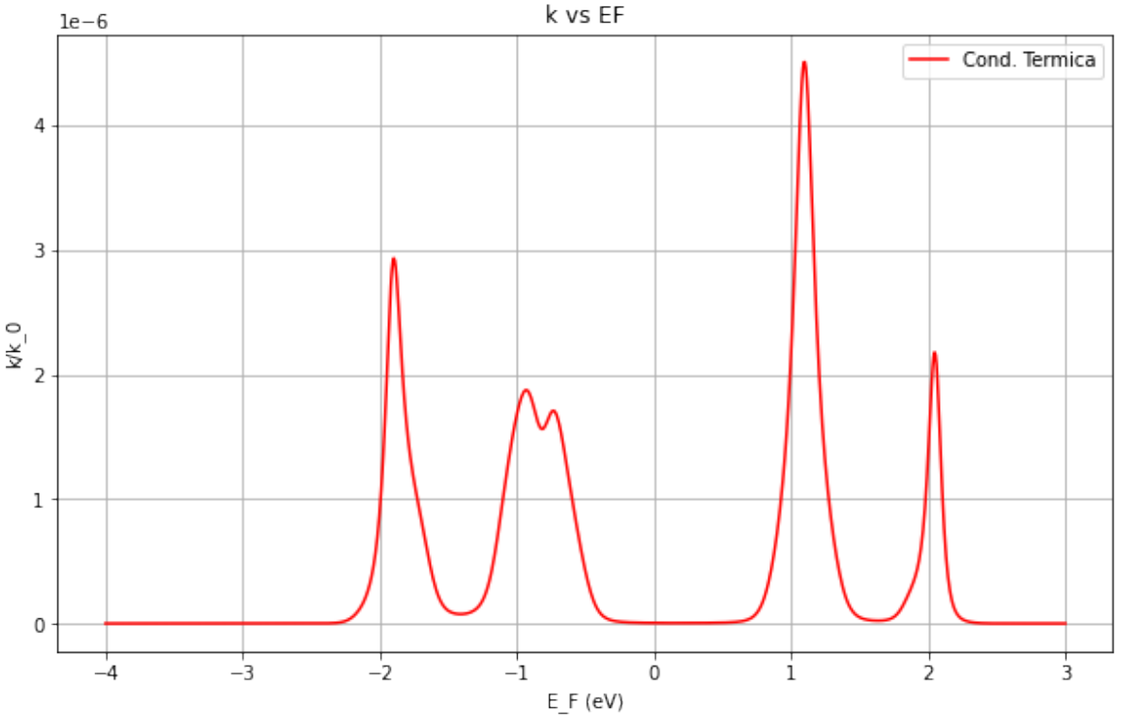


```
Process completed successfully
The calculation took 33.2374 seconds.
```

1.6 Calculation for the figure of merit (ZT)

[13]:
```
ZT = [ b**2 / ( a*c - b**2) for a, b, c in zip(L0_re, L1_re, L2_re)]


plt.figure(figsize=(10, 6))
plt.plot(Eff, ZT, label='ZT', color = 'red')
plt.xlabel('E_F (eV)')
plt.ylabel('ZT')
plt.title('ZT vs EF')
plt.legend()
plt.grid(True)
plt.show()
```

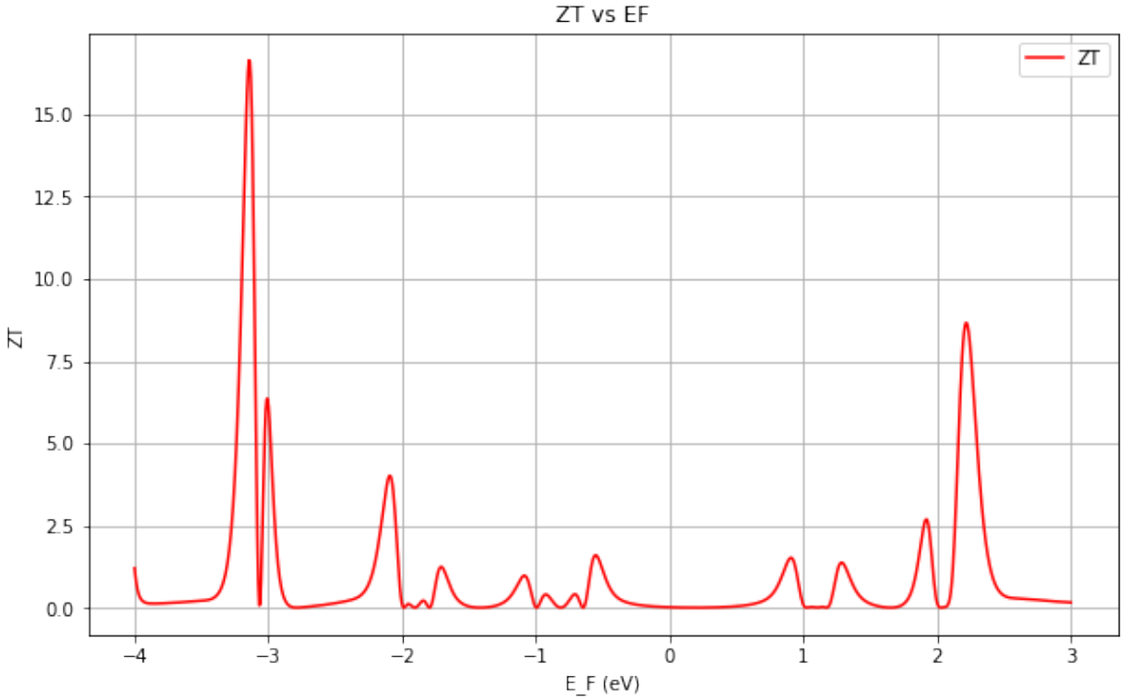
ZT vs EF
ZT
15.0
12.5
10.0
7.5
5.0
2.5
0.0
ZT
−4
−3
−2
−1
0
1
2
3
E_F (eV)

[ ]: